Investigation of hybrid organic-inorganic lead halide perovskites by modulated surface photovoltage spectroscopy

Vorgelegt von

M.Sc.

Celline Awino Omondi

Geb. in Siaya (Kenia)

Von der Fakultät IV – Elektrotechnik und Informatik

der Technischen Universität Berlin

zur Erlangung des akademischen Grades

Doktor der Naturwissenschaften

Dr. rer. nat.

genehmigte Dissertation

Promotionsausschuss:

Vorsitzender:	Prof. Dr. Bernd Szyszka
Gutachter:	Prof. Dr. Bernd Rech (TUB)
	Prof. Dr. Roland Scheer (Martin Luther Universität, Halle)
	PD Dr. Thomas Dittrich (TUB / HZB)

Tag der wissenschaftlichen Aussprache: 05. Juli 2018

Berlin 2018

Abstract

Hybrid organic-inorganic metal halide perovskites (called here perovskites) have emerged as a new group of materials for highly efficient solar cells (SCs) based on earth abundant elements which can be processed from solutions at low temperature. $CH_3NH_3Pb(I_{1-x}Br_x)_3$ perovskite films were studied in the thesis since it belongs to the materials which are of great interest for top SCs in tandem SCs with c-Si bottom SCs due to its tunable band gap. Electronic properties of $CH_3NH_3Pb(I_{1-x}Br_x)_3$ perovskite films sensitively depend on crystallization and defect formation and are crucial for the performance and stability of SCs. The band gap (E_g), exponential tail states (E_t) and the diffusion length (L) are decisive parameters for absorbers in SCs since they give principle limitations for photo-generation and Fermi-level splitting. In $CH_3NH_3Pb(I_{1-x}Br_x)_3$ perovskites, E_g, E_t and L are not necessarily constant and can depend, for example, on the preparation conditions and degradation. Therefore, E_g, E_t and L of $CH_3NH_3Pb(I_{1-x}Br_x)_3$ perovskites were studied with respect to stoichiometry, interfaces, degradation and temperature. Modulated surface photovoltage (SPV) spectroscopy was used as the main characterization technique. Modulated SPV spectroscopy allows for the contactless and very sensitive characterization of E_g, E_t, direction of charge separation and L (after Goodman) without the requirement of the preparation of contacts after or during different stages of layer preparation, light soaking etc. Vegard's law was applied to obtain the composition of $CH_3NH_3Pb(I_{1-x}Br_x)_3$ films. The E_g of $CH_3NH_3Pb(I_{1-x}Br_x)_3$ films varied between 1.59 eV to 2.30 eV depending on the stoichiometry whereas the bowing parameter was 0.36 eV. The influence of the substrate on E_g and E_t of $CH_3NH_3PbI_3$ films was investigated. It has been found, for example, that E_g and E_t of $CH_3NH_3PbBr_3$ sensitively depend on the substrate and on soaking in nitrogen atmosphere and that light soaking has strong influence on the direction of modulated charge separation. $CH_3NH_3PbI_3$ deposited on double layers of TiO_2-PCBM and SnO_2-PCBM showed a constant band gap of 1.58 eV and a low scatter in E_t. This was attributed to the modification of the TiO_2 or SnO_2/$CH_3NH_3PbI_3$ interfaces by PCBM allowing for efficient charge separation and transfer and well reproducible conditions for the layer formation. A decrease of L with light soaking was observed and can be attributed to light induced degradation due to charging and discharging of trap states and formation of defects at the TiO_2/ $CH_3NH_3PbI_3$ interface. Furthermore, E_g and E_t of $CH_3NH_3PbI_3$ stabilized with PMMA increased with increasing temperature, i.e. thermal expansion gives the predominant contribution to the temperature dependence of E_g of $CH_3NH_3PbI_3$ whereas dynamic disorder was limited by phonons. A jump-like increase of E_g in the region of phase transition was attributed to the phase transition from the tetragonal to the cubic phases.

Zusammenfassung

Hybride organisch-anorganische Metallhalidperovskite (hier kurz Perovskite genannt) sind eine neue Materialgruppe für hocheffiziente Solarzellen, welche auf in der Erdkruste reich verfügbaren Elementen basieren und welche bei niedrigen Temperaturen aus Lösungen hergestellt werden können. Perovskitschichten aus $CH_3NH_3Pb(I_{1-x}Br_x)_3$ wurden in der Doktorarbeit untersucht, da diese für Anwendungen als Topzellen in Tandemsolarzellen mit c-Si-Bottomzellen aufgrund der einstellbaren Bandlücke von großem Interesse sind. Die elektronischen Eigenschaften von Perovskitschichten aus $CH_3NH_3Pb(I_{1-x}Br_x)_3$ hängen empfindlich von der Kristallisation und der Bildung von Defekten ab und sind kritisch für die Leistung und Stabilität von Solarzellen. Die Bandlücke (E_g), die exponentiellen Bandausläufer (E_t) und die Diffusionslänge (L) sind entscheidend für Absorber in Solarzellen, da sie die Photogeneration und die Aufspaltung der Fermi-Niveaus limitieren. E_g, E_t und L sind in Perovskitschichten aus $CH_3NH_3Pb(I_{1-x}Br_x)_3$ nicht zwingend konstant und hängen z.B von der Präparation und der Degradierung ab. Deshalb wurden E_g, E_t und L mit Hinblick auf die Stöchiometrie, Grenzflächen, Degradierung und Temperatur untersucht. Als Hauptuntersuchungsmethode wurde die modulierte Oberflächenphotospannungs-spektroskopie (SPV) eingesetzt. Die SPV erlaubt eine kontaktlose und außerordentlich empfindliche Bestimmung von E_g, E_t, Richtung der Ladungstrennung und L (nach Goodman) nach oder während verschiedener Schritte der Präparation oder Degradierung, z.B. unter Beleuchtung. Anhand des Vegard'schen Gesetzes wurde die Stöchiometrie von $CH_3NH_3Pb(I_{1-x}Br_x)_3$ ermittelt. E_g von $CH_3NH_3Pb(I_{1-x}Br_x)_3$ variierte zwischen 1.59 und 2.30 eV, wobei der Bowingparameter 0.36 eV betrug. Starke Einflüsse des Substrates und der Lagerung in Stickstoffatmosphäre auf E_g, E_t und die Richtung der modulierten Ladungstrennung wurden u.a. in $CH_3NH_3PbBr_3$ festgestellt. E_g betrug für auf TiO_2/PCBM oder SnO_2/PCBM abgeschiedenes $CH_3NH_3PbI_3$ 1.58 eV und E_t zeigte nur geringfügige Variationen, PCBM hat also kaum Einfluss auf E_g und E_t. und trägt sehr zur effizienten Ladungstrennung und zur gut reproduzierbaren Herstellung von Perovskitschichten bei. Die beobachtete Abnahme von L in $CH_3NH_3PbI_3$ unter Beleuchtung kann der Umladung von Defekten sowie der Generation zusätzlicher Defekte besonders im Bereich der Grenzfläche zwischen TiO_2 und $CH_3NH_3PbI_3$ zugeordnet werden. E_g und E_t stiegen mit steigender Temperatur für mit PMMA stabilisiertes $CH_3NH_3PbI_3$ an, was auf den dominanten Einfluss der thermischen Ausdehnung und der Limitierung der dynamischen Unordnung durch Phononen zurückzuführen ist. Ein sprunghafter Anstieg von E_g bei etwas höheren Temperaturen wurde dem Übergang der tetragonalen Phase von $CH_3NH_3PbI_3$ in die kubische Phase von $CH_3NH_3PbI_3$ zugeordnet.

Contents

CHAPTER 1

Introduction

With growing population, there is an unprecedented sharp rise in the energy demand of mankind. The increasing energy demand leads to the depletion of fossil fuels. Furthermore, the adverse climatic changes coupled with global warming due to the emission of greenhouse gases from fossil fuels are growing. Therefore, the societies are faced with challenges to develop and incorporate energy technologies based on renewable energy sources that can replace fossil fuels. The sun is the largest source of energy with about 3.9 x 10^{24} J of solar energy annually reaching the earth's surface [1]. This qualifies solar energy as the most viable candidate that can supply and meet the energy demand required by the growing population.

Photovoltaic or solar cells (SCs) convert solar light directly into electricity. Earth abundant materials are key for the development and sustainable production of reliable and efficient solar cells. Material concepts for SCs can be classified as large silicon crystals (wafer based crystalline silicon), epitaxial layer systems of group III - V compounds, thin films on foreign substrates and nanocomposites. The PV market is dominated by crystalline silicon (c-Si), based on p-n junctions and account for more than 90% of the PV module production [2]. Silicon is naturally abundant, reliable and c-Si solar cells are very stable with a life span of more than 25 years [3]. c-Si solar cells have record power conversion efficiencies of up to 26.7 % [4]. A disadvantage with silicon based wafer technology is the relatively high energy demand for the production of very pure silicon crystals.

The absolutely highest power conversion efficiency was reached under concentrated sunlight for SCs based on epitaxial layers of group III – V compounds (46% for multi-junction SCs) [5]. Despite high efficiencies, the use of SCs based on group III-V semiconductors is limited to space applications, and concentrator SCs due to the high cost of production [2]. Thin film technologies are developed to reduce manufacturing costs and material usage. Thin absorber layers are deposited on foreign substrates. However, disadvantages with thin film SCs are, for example, a low efficiency for amorphous silicon (a-Si:H) and material scarcity (tellurium in cadmium telluride and indium in copper gallium indium diselenide SCs) [6]. Nanocomposites are materials with interpenetrating different phases which are combined together to achieve a desired combination of properties. Dye-sensitized solar cells [7] are the most prominent nanocomposite SCs. However, the use of a liquid electrolyte prevented a broad penetration of this technology.

For the further strong improvement of the efficiency of c-Si solar cells, their implementation into tandem and other multi-junction SCs will be necessary. The Shockley-Queisser limit is 33 % [8] for single junction SCs and the efficiency is limited to 44 % [5] for tandem SCs at air

mass 1.5 global (AM 1.5G).Therefore, there is the need to produce tandem solar cells with a large band gap material (E_g about 1.7 eV) for the top cell and c-Si (E_g = 1.1 eV) for the bottom cell. The top cell absorbs photons with high energies and transmits photons with low energies to the bottom cell.

Quite recently, hybrid organic - inorganic metal halide perovskites (in this thesis also called perovskites) emerged as a new group of materials for highly efficient SCs based on earth abundant materials which can be processed at low temperature. The material has emerged as a potential low cost alternative for top cells due to its flexibility, tunable band gap and it can be deposited from solution processes with high efficiency.

A perovskite has a ABX_3 structure, where A can be, for example, methyl ammonium ($CH_3NH_3^+$) (MA^+) or formamidinium [$HC(NH_2)_2^+$] (FA^+) or cesium (Cs^+) cation; B is commonly a lead (Pb^{2+}) or tin (Sn^{2+}) cation and X is a halide anion (Cl^-, Br^-, or I^-) [9]. The material combines properties of both organic and inorganic materials and can be deposited from solution processes leading to opto- electronic properties of perovskites well reliable for SCs. In 1990s, Mitzi et al. [10] studied the semiconducting properties of hybrid organic-inorganic halide perovskite in field effect transistors. The 3-D $CH_3NH_3SnI_3$ perovskite revealed a low charge carrier density with a Hall mobility of 50 $cm^2/V.s$ at 300 K [11]. In 2009, Kojima et al. studied the photovoltaic function of $CH_3NH_3PbI_3$ and $CH_3NH_3PbBr_3$ on TiO_2 as a light sensitizer in photo electrochemical cells and realized a power conversion efficiency of 3.81 and 3.13%, respectively [12]. Since then, lead halide perovskites have attracted increasing attention and present a very promising technology for further development of SCs.

Perovskite material poses excellent absorption properties [13], an intrinsic material with moderate charge carrier mobilities [14], large carrier diffusion length of more than 1 μm [15], shallow defect levels [16] and a direct band gap resulting in high efficiencies up to 22.1 % [5]. Furthermore, perovskite materials have a band gap that can be tuned between 1.17 [17] and 2.3 eV [18] by varying the composition of ions (mixed cations and mixed anions) [9,19].

Perovskites undergo degradation when exposed to moisture, light and heat. A stabilized power conversion efficiency (PCE) of about 21.1 % has been realized on mixed perovskite based on the so-called triple cations (contains Cs^+, MA^+ and FA^+) and upon light soaking for 250 h, PCE decreased to about 18% [9]. Formation of light induced traps and halide segregation for $CH_3NH_3Pb(I, Br)_3$ films upon light soaking has also been observed [20]. For comparison, c-Si SCs are very stable (degradation rates are about 0.5 – 0.7 %) [21].Therefore, the stability of perovskite SCs has to be further improved. Based on this, there are open questions that need to be addressed to increase the understanding of the fundamental properties of perovskite.

- What is the nature of band structure of perovskite?
- How do interfaces influence disorder in the bulk of perovskite materials?

- What are the mechanisms behind stabilization of perovskites?

The band gap (E_g), exponential tail states (characterized by E_t, the tail energy, or E_u, the so – called Urbach energy which is obtained from absorption spectra) and the diffusion length (L) are decisive parameters for absorbers for SCs since they give the principle limitations for photo-generation and Fermi level splitting. In perovskites, E_g, $E_{t\,(u)}$ and L are not necessarily constant and can depend, for example, on preparation and degradation. Therefore, E_g, E_t and L are studied in this work with respect to stoichiometry, interfaces, degradation and temperature. For example, E_g is an important parameter that reflects on the nature of chemical bonding of a material, E_t gives information about the disorder in a material whereas L gives information about photo-generation of charge carriers in SCs. Furthermore, light induced defects are important because photo-generated electrons can change the chemical bonds. Also, knowledge of the transport length of photo-generated charge carriers and their dependence on light soaking is of interest for the development of efficient and stable solar cells.

In order to study the E_g, E_t and L, a sensitive method that depends on photo-generation, charge transport and separation is needed for characterization. Modulated surface photovoltage (SPV) spectroscopy was used as the main characterization technique. SPV is the difference between the surface potential of a semiconductor material under illumination and in the dark [22]. SPV signals are generated whenever photo-induced charge carriers are separated in space [23]. The technique is contactless, non-destructive and surface sensitive. Modulated SPV allows for the characterization of electronic properties related to the band gap (E_g), exponential tail states close to the band edges (E_t), deep defect states and transport or diffusion length (L). Furthermore, SPV analysis does not require the preparation of contacts and can be performed after different stages of layer preparation, light soaking etc.

The reproducibility of perovskites depends very much on the preparation conditions. For example, the bandgap (E_g) for $CH_3NH_3PbI_3$ perovskite can vary between 1.5 to 1.6 eV [19,24,25] depending on the conditions of preparation. Furthermore, the prototypical perovskite, i.e. $CH_3NH_3PbI_3$, undergoes a phase transition from tetragonal to cubic at a temperature of about 55° C [26] which can affect the performance and stability of perovskite based devices. Depending on annealing time, $CH_3NH_3PbI_3$ layers can be p-type or n-type doped [27]. The excess of CH_3NH_3 and iodine (I) leads to p-type doping of $CH_3NH_3PbI_3$ layers, whereas the deficiency of CH_3NH_3 and I leads to the formation of the PbI_2 phase on the surface of $CH_3NH_3PbI_3$ films and to n-type doping. Reduced disorder has been observed when a small amount of ammonium valeric acid iodide ($AVAI$) is added into solution containing $PbCl_2$ and CH_3NH_3I [28]. This caused the formation of a stabilized precipitate of $CH_3NH_3PbCl_3$ that supported controlled crystallization of $CH_3NH_3PbI_3$ which further led to a reduction of disorder. Perovskite is known to be unstable when exposed to moisture, oxygen, continuous illumination

and high temperature. Degradation of $CH_3NH_3PbI_3$ leads to the formation of other phases such as PbI_2 [29]. The resulting PbI_2 can form a passivating layer on the $CH_3NH_3PbI_3/PbI_2$ interface during moderate heating which is beneficial for solar cells [29].

The temperature dependence of the band gap of $CH_3NH_3PbI_3$ perovskite layers gives information about the nature of the semiconductor, i.e. whether it is dominated by electron-phonon interaction or by thermal expansion. For example, for conventional semiconductors such as silicon, E_g decreases monotonically with temperature whereas for perovskites, E_g, increases linearly with temperature [30,31] . The monotonic decrease of E_g with temperature is due to dominant contribution of electron- phonon interaction [30] whereas the linear increase of E_g with temperature is due to the dominant contribution of thermal expansion of the lattice [31]. Furthermore, under operating conditions, the temperature of a solar cell can vary over a relatively wide range up to 70° C. Temperature fluctuations affect the efficiency of perovskite based solar cells. Therefore, the precise knowledge of the temperature dependence of the band gap for methyl ammonium lead iodide and related perovskites is essential for deeper understanding of the temperature dependence of solar cells and origins behind.

This thesis is divided into 7 chapters where chapter 1 and chapter 7 are the introduction and summary, respectively. Chapter 2 covers the fundamentals of perovskite and its electronic, optical and structural properties. Models of temperature variation of the band gap of semiconductors are explained and the temperature dependence of the band gap of selected semiconductors are compared. Stoichiometry of perovskites in relation to Vegard's law is described. A systematic description of different charge selective contacts with various chemical, electric and transport properties is presented. Issues of stability under moisture, oxygen, heat, light soaking, ultra violet (UV) illumination and charge selective contacts are discussed.

Chapter 3 describes the fundamentals of modulated surface photovoltage (SPV) spectroscopy. The principle of modulated SPV is explained. Modulated SPV signals such as in-phase signals, phase shifted by 90° signals, amplitude and phase angles are explained and the components of set-ups for modulated SPV spectroscopy measurements are described. The chapter explains how the parameters E_g, E_t and L were obtained. E_g, for example, was analyzed as an onset energy (E_{on}), as energy of inflexion point ($E_{g\text{-}ip}$) and as a Tauc gap ($E_{g\text{-}Tauc}$) for direct semiconductors.

The experimental methods are described in chapter 4. This includes substrate and sample preparation, characterization and analysis methods. The fabrication method for $CH_3NH_3PbI_3$, $CH_3NH_3PbBr_3$, stoichiometric variations of $CH_3NH_3Pb(I_{1-X}Br_X)_3$ layers as well as preparation of various charge selective contacts are explained. The chapter explains how E_g, E_t, as well as L after Goodman [32] were analyzed. Supporting methods such as UV-vis spectroscopy,

photothermal deflection spectroscopy (PDS) and grazing incidence x-ray diffraction (GIXRD) are also described in the chapter.

Chapter 5 gives the results on the properties of $CH_3NH_3Pb(I, Br)_3$ and their dependence on aging and light soaking. The band gap of $CH_3NH_3Pb(I_{1-X}Br_X)_3$ films was tuned from 1.59 eV to 2.30 eV by varying the stoichiometry of the perovskite. Vegard's law was used to obtain the composition of $CH_3NH_3Pb(I_{1-X}\ Br_X)_3$ films. The lattice constant decreased linearly with increasing $CH_3NH_3Pb(I_{1-X})Br_X)_3$ composition. Furthermore, the bowing parameter of 0.36 eV in $CH_3NH_3Pb(I_{1-X}\ Br_X)_3$ perovskite films measured by SPV correlated well with the values of 0.33 and 0.29 eV obtained by Noh et al. [19] and Jacobsson et al. [33] respectively.

The values of E_u and E_t were observed to be lower for pure tri-iodide and tri-bromide perovskite but higher for mixed perovskites. The influence of the substrate on E_g and E_t of the $CH_3NH_3PbI_3$ films was investigated. $CH_3NH_3PbI_3$ deposited on double layers of TiO_2-PCBM and SnO_2-PCBM showed a constant band gap of 1.58 eV and low scatter in the value of E_t. This was attributed to the modification of theTiO_2 or SnO_2/$CH_3NH_3PbI_3$ interfaces by the PCBM, to allow for efficient charge separation and transfer [34]. Effects of light soaking on the transport length of $CH_3NH_3PbI_3$ were studied using SPV. A decrease in the transport length with light soaking time was observed. The decrease in the value of transport length was attributed to light induced degradation which arises due to trap states and charging- discharging effect at TiO_2/ $CH_3NH_3PbI_3$ interface.

Chapter 6 covers the results of the temperature dependence of the band gap of $CH_3NH_3PbI_3$ perovskite layers measured by modulated SPV. In order to avoid degradation in vacuum during temperature dependent SPV measurement, a poly (methyl methacrylate) (PMMA) layer has been deposited on $CH_3NH_3PbI_3$ films and optimized in order to stabilize $CH_3NH_3PbI_3$. The temperature dependence of E_g and E_t were investigated using modulated SPV spectroscopy. E_g and E_t of $CH_3NH_3PbI_3$ increased with increasing temperature. The results showed that thermal expansion gives the predominant contribution to the temperature dependence of the band gap of $CH_3NH_3PbI_3$ whereas dynamic disorder is limited by phonons. A jump in the value of E_g near the region of phase transition has been observed and was related to the phase transition from the tetragonal to the cubic phases. The temperature dependence of E_t was fitted with a model taking into account phonon-induced disorder and phonon energy E_{ph} of 150 ± 40 was obtained.

CHAPTER 2

Fundamentals of perovskites

2.1. Perovskite structure

The term perovskite is related to the structure of the mineral called calcium titanate oxide ($CaTiO_3$). It was collected in the Ural Mountains of Russia by Perovski and described for the first time by Gustav Rose in 1839. He named the mineral as 'Perovskite' in honor of Russian mineralogist Lev Alekseevich Perovski (1792-1852). The structure of hybrid organic-inorganic perovskite family is ABX_3, where A is a monovalent cation such as $CH_3NH_3^+$ (methylamonium cation), $HC(NH2)_2^+$ (formamidium cation), Rb^+, Cs^+; B is the inorganic component usually divalent metal cation such as Mg^{2+}, Ca^{2+}, Sr^{2+}, Ba^{2+}, Sn^{2+}, Pb^{2+} and X is anion such as O^{2-} Cl^-, I^-, Br^- [9,35,36,37].

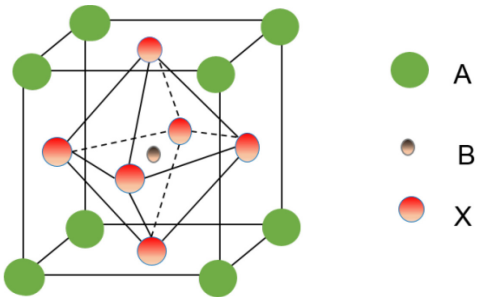

Figure 2.1: ABX_3 perovskite structure.

The size of cation A has a strong influence on the structure of perovskite. Furthermore, cation A compensates the charge within the lattice and has only minor influence on the electronic properties of the perovskite. The size of cation A can cause distortion in the B-X bonds, thereby affecting the symmetry [38]. Assuming a rigid sphere model for all ions, Goldschmidt's equation [39] can be used to calculate a tolerance factor (TF) for hybrid perovskites from the effective radii of ions.

$$TF\sqrt{2(r_B + r_X)} = r_A + r_X \qquad 2.1$$

where *TF* is tolerance factor, r_A, r_B and r_X are the radii of the ions A, B and X respectively. It is assumed that the values r_A+r_X and r_B+r_X are the approximate distances of between the anion X and the cations A and B, respectively. For an ideal cubic perovskite structure, *TF* is equal to unity. For *TF* > 1, the structure distorts towards the tetragonal structure. For *TF* < 1, the structure distorts towards the bulk of the octahedral structure [40]. Therefore physical properties such as magnetic, electronic and dielectric ones depend highly on distortions. For

instance, the $CH_3NH_3^+$ cation has a permanent electric dipole moment which changes the dynamic orientations of these ions thereby contributing to the dielectric properties [41].

A hybrid organic-inorganic lead halide perovskite, such as $CH_3NH_3PbX_3$, consists of a divalent inorganic cation, a monovalent organic cation and halide anion. If the size of the organic cation is too large, then the 3-D network is broken and a 2-D network is formed (see figure 2.2). *TF* is equal to 1 for a perfect 3-D network. In reality, as found empirically, *TF* varies between 0.8 and 1.0 for most of the cubic perovskite structures [42]. This implies that a small organic cation consisting of two or three atoms with one carbon atom and one nitrogen atom can fit into the space provided between nearest neighbours of the anion X [41,43]. On the other hand, for a 2-D network, cation A is too large to fit into the space provided by the nearest neighbours of the anion X within the inorganic sheet resulting in the distortion of the cubic structure resulting in *TF* > 1. In such a situation, the organic cation is kept away from the inorganic sheets by a spacer such as alkyl chains. A commonly used structure of a 2D perovskite, given by $(R\text{-}NH_3)_2BX_4$, is shown in figure 2.2 (b), where cation A is an organic component of $(R\text{-}NH_3)_2$ with R being an aromatic ammonium or aliphatic cation. The layers of the relatively large organic cations form barriers whereas the inorganic structures (BX_4) form wells for charge carriers so that the whole network form a self-organized quantum well structure [43].

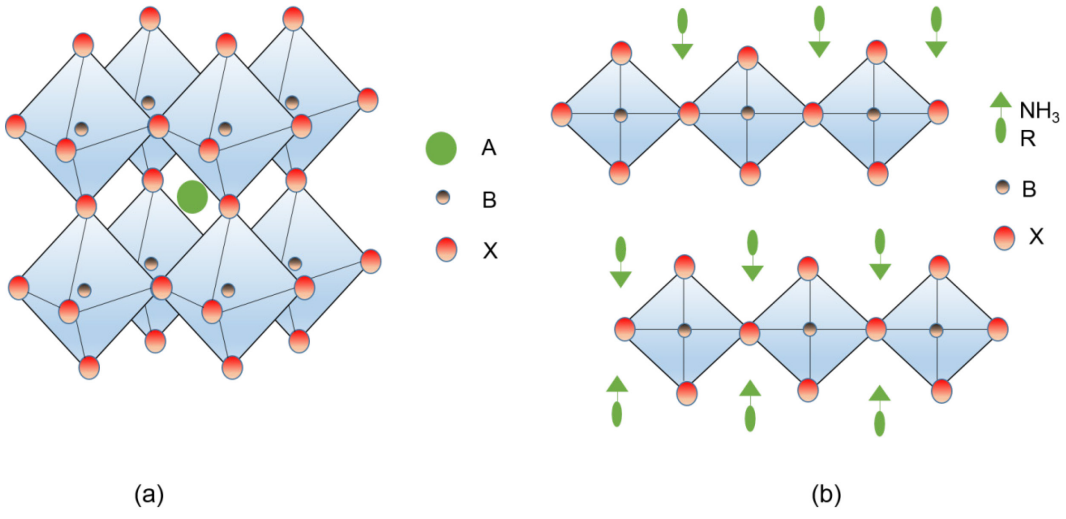

Figure 2.2: Schematics of (a) the 3-D octahedral and (b) the 2-D perovskite structures.

The 3-D crystal structure of hybrid organic-inorganic lead halide perovskites is of primary interest for reaching very high efficiencies in SCs. This work is focused on methylammonium lead iodide ($CH_3NH_3PbI_3$), methylammonium lead bromide ($CH_3NH_3PbBr_3$) and stoichiometric variations of $CH_3NH_3Pb(I_{1-X}Br_X)_3$ layers. Perovskites with mixed cations can result in higher efficiencies. Perovskites with three different A cations can also be called triple cation, for

example, $[Cs_{0.05}(FA_{0.83}MA_{0.17})_{0.95}]Pb(I_{0.83}Br_{0.17})_3$ where Cs, FA ($CH_3(NH_2)_2$ and MA (CH_3NH_3) stand for cesium, formamidium and methylammonium cations, respectively.

Early crystallographic studies identified three phases of $CH_3NH_3PbI_3$: orthorhombic, tetragonal and cubic phases [41]. X-ray diffraction (XRD) and calorimetric measurements have confirmed two phase transitions of $CH_3NH_3PbI_3$ at 162 K (orthorhombic / tetragonal) and 327 K (tetragonal / cubic) [44].

The orthorhombic phase of $CH_3NH_3PbI_3$ occurs at temperature of about 160 K [45]. The initial space group of orthorhombic phase was $pna2_1$ which was later reclassified into pnma by neutron powder diffraction [46]. In the pnma space group, $CH_3NH_3^+$ cations are fixed with rotation restricted along the C-N axis. Furthermore, the $CH_3NH_3^+$ cations are fully ordered whereas the PbI_6 octahedra are slightly distorted. The behaviour makes the average Pb-I-Pb bond angle to be 154.5°, with the individual bond angle of Pb-I_1-Pb being 161.94° along the b axis and Pb-I_2-Pb = 150.72° along both the a- and c- axes. These tilts enable iodide ions to move towards the $–NH_3$ end of the $CH_3NH_3^+$ cations and away from the $–CH_3$ end of the unit cell [47]. On the other hand, the orthorhombic phase of $CH_3NH_3PbBr_3$ exists at temperatures below 144.5 K having a space group of $pna2_1$ with the lattice parameters of a= 7.979 Å, b = 8.58 Å and c = 11.849 Å. The unit cell occupies a volume of 811 Å³ [41] . In the $pna2_1$ space group, the $CH_3NH_3^+$ cation is highly ordered because the ions are in a frozen state by mechanical strain or electric field [48]. As a remark, the orthorhombic phase of both $CH_3NH_3PbI_3$ and $CH_3NH_3PbBr_3$ perovskite crystals possesses ferroelectric and anti-ferroelectric properties because the symmetry of the unit cell changes from a centrosymmetric to an acentric system making the ions within the lattice to be off-centred due to the rotation of $CH_3NH_3^+$ cation within the unit cell [41].

The tetragonal phase of $CH_3NH_3PbI_3$ occurs at temperatures between 162.2 K and 327.4 K [41]. In the tetragonal structure, NH_3^+ moves closer to iodide (I^-) thus lowering the electrostatic energy due to rotation of the PbI_6 octahedron along the c-axis. In addition, the super lattice reflection increases in the tetragonal phase most probably due to ordering and disordering of $CH_3NH_3^+$ cations and I^- anions. The $CH_3NH_3PbBr_3$ perovskite has two tetragonal phases, i.e. the beta (β) and the gamma (γ) phases. At temperatures between 155.1 and 236.9 K, the β phase of the $CH_3NH_3PbBr_3$ tetragonal structure has the space group of *I* 4/mcm. In this phase, the unit cell has the following lattice parameters: a = 8.322 Å and c = 11.83 Å. The γ phase of $CH_3NH_3PbBr_3$ occurs at temperatures between 149.5 and 155.1 K, has a space group of P4/mmm and the following lattice parameters: a= 5.894 Å and c= 5,861 Å. The unit cell of the tetragonal phase of $CH_3NH_3PbBr_3$ possess the largest volume of 819 Å³ [41].

The cubic phase of $CH_3NH_3PbI_3$ occurs at temperature above 327.4 K and has a space group of pm3m with the lattice constant of the unit cell of a = b = c = 6.3285 Å. The unit cell of the cubic phase of $CH_3NH_3PbI_3$ occupies a volume of 253.5 Å³ [41]. In the cubic phase, the

orientation of the $CH_3NH_3^+$ cation is highly disordered in order to satisfy the cube symmetry. Furthermore, $CH_3NH_3^+$ poses two forms of orientational disorder whereby the first one involves motion of the cation along the C-N axis with respect to the crystal axis whereas the second one involves rotation of the cation around the C-N axis [44].

$CH_3NH_3PbBr_3$ has a cubic structure at temperatures above 239.6 K with a space group of pm3m. In this space group, the positions of $CH_3NH_3^+$ cations are not fixed but possess an eightfold disordered state in order to preserve the cubic symmetry of the lattice. The lattice parameters in the cubic phase are as follows: a = 5.901 Å with the unit cell occupying a volume of 260 Å [41], implying that in the cubic phase, there is rapid re-orientation of $CH_3NH_3^+$ cation along the C-N axis.

The lattice constant is a fundamental parameter of any crystalline material. The lattice constant can help to identify a particular material and to provide information about the structural properties of a material. Vegard's law can be used to give an empirical relation between the lattice constant and the composition of constituent elements. Vegard's law states that the crystallographic lattice parameters of a continuous solid solution vary linearly with composition at a fixed temperature for constituent phases having the same bonding [49]. This means that, when the influence of electronic effects is negligible, the lattice parameters of a unit cell in an alloy shall vary linearly with the composition of a solid solution. The atoms or ions in the solid solution are randomly distributed in order to substitute for each other. The relative size of the atoms or ionic species controls the crystallographic lattice parameters making the law valid for ionic compounds. In a binary solid solution of the compounds A and B, Vegard's law can be expressed as:

$$a = a_A(1-x) + a_B(x) \qquad 2.2$$

where x is the mole fraction of compound B and a_A and a_B are the lattice constants of the pure compounds A and B, respectively.

Figure 2.3 shows the dependence of the lattice constant of pseudo-cubic $CH_3NH_3Pb(I_{1-x}Br_x)_3$ as a function of the content of bromide. The data points were acquired after Noh et al. 2013 [19]. The lattice constant decreased with an increase of the content of bromide in the solution. According to Vegard's law, the lattice constant in the alloy varies linearly with composition at constant temperature and negligible electronic effects. Therefore, the linear dependence of the lattice constant on x indicates the formation of a pseudo-cubic $CH_3NH_3Pb(I_{1-x}Br_x)_3$ compound in the complete range of $0 \leq x \leq 1$ by a simple solution process. Therefore, vice versa, the measurement of the lattice constant can be used for a precise determination of x in $CH_3NH_3Pb(I_{1-x}Br_x)_3$ compounds.

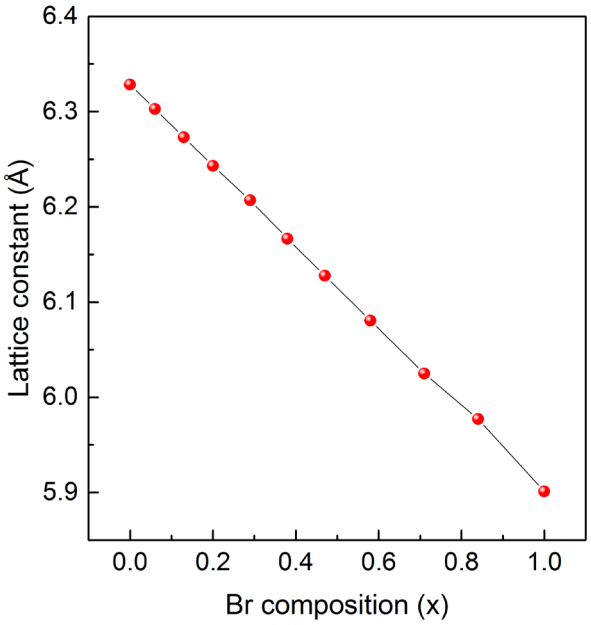

Figure 2.3: Dependence of the lattice constant of pseudo-cubic $CH_3NH_3Pb(I_{1-x}Br_x)_3$ as a function of bromide composition (x). Data point were taken after Noh et al. [19].

2.2. Band gap of hybrid organic-inorganic metal halide perovskites

2.2.1. Formation and origin of the band gap

The band gap (E_g) of a semiconductor is the difference between the valence band maximum and conduction band minimum. A free electron is generated by exciting a valence electron with energy equal or larger than E_g. An electron excited from the valence into the conduction band leaves a mobile hole in the valence band. According to a periodic potential, energy levels of free electrons and holes are arranged in bands.

The origin of E_g has been explained by different theories. In general, E_g originates from the difference between bonding and anti-bonding states of hybrid orbitals. In the free electron model, electrons move freely within the lattice, experiencing only potential barriers at the boundaries [50]. Figure 2.4 (a) shows the energy of free electrons as a function of the electron wave number. In the free electron model, all values of energy are allowed. On the other hand, an electron travelling through a crystal lattice experiences periodic variation of potential energy. This periodic variation of potential energy affects the behavior of conduction electrons. The Bloch wave-function can be used to describe the periodic nature of an electron passing through a periodic lattice. Electrons are considered as plane waves of the form exp(i**k**·**r**) travelling through a periodic lattice with the solution of the form

$$\varphi(\mathbf{r}) = V_k(\mathbf{r}) \exp(i\mathbf{k} \cdot \mathbf{r}) \qquad 2.3$$

where $V_k(\mathbf{r})$ has the periodicity of the lattice [50]. The wave functions of the form of equation 2.3 are called Bloch functions [50].

Figure 2.4 (b) shows the energy of electrons in a lattice as a function of the wave number. Forbidden band gaps are those regions where solutions representing electrons passing through a crystal lattice do not exist whereas allowed bands are the regions where electrons can exist. For example, in the first Brillion zone, the allowed energy gap is between $-\frac{\pi}{a} < \mathbf{k} < \frac{\pi}{a}$. Therefore the allowed energy bands can be represented by the wavenumber k within the Brillion zone such that k = $\frac{n\pi}{a}$, where a, is the atomic spacing and n = ± 1, ± 2… which can be seen as an overlap of atomic states. On the other hand, a forbidden band gap is obtained where propagating waves are absent (see figure 2.4(b)).

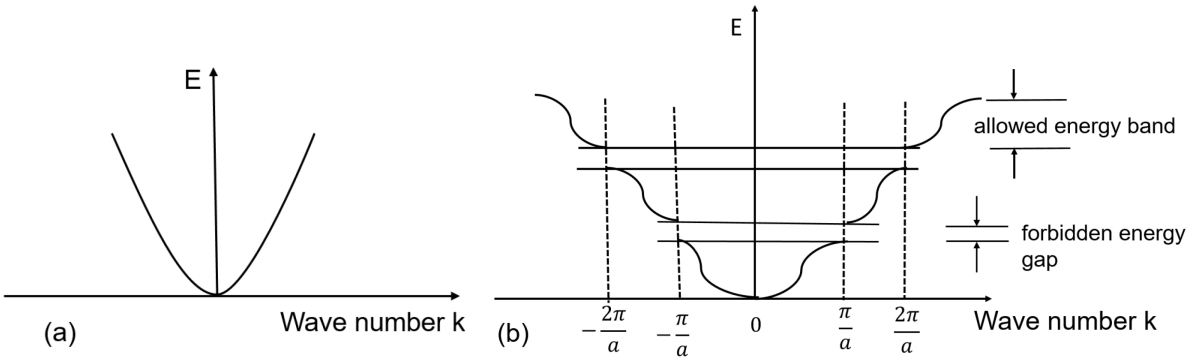

Figure 2.4: Energy as a function of wave number for a free electron (a) and for an electron in a periodic potential (b).

2.2.2. Direct and indirect band gap of hybrid organic-inorganic perovskite

Direct band gap semiconductors are those materials in which an electron is excited by a photon of energy larger than the band gap to make transition from valence band maximum to conduction band minimum (see figure 2.5 a). In such transitions, the crystal momentum or k-vector is the same in both the valence band maximum and conduction band minimum. On the other hand, indirect transition occurs when the energy of valence band maximum and conduction band minimum takes place at different values of crystal momentum (see figure 2.5 b). In such transitions, a phonon is needed to supply the crystal momentum equal to the difference between the minimum of the conduction band and valence band maximum.

It has been reported that $CH_3NH_3PbI_3$ behaves like a direct band gap semiconductor since a photon is needed in the absorption and emission processes via allowed transitions [51]. This behaviour differs from indirect transitions in silicon in which absorption and recombination processes involve a photon as well as a phonon. This explains why perovskite has high

absorption coefficients with slower recombination rates in comparison to silicon [52]. However, theoretical calculations have also revealed the indirect nature of the $CH_3NH_3PbI_3$ perovskite absorber materials in which the conduction band minimum is slightly shifted relative to valence band maximum [53]. The indirect nature is proposed to be due to Rashba splitting of the bands due to electron –phonon coupling which lead to the formation of spin allowed and spin forbidden transitions. Spin forbidden transition results in a reduced recombination rate due to momentum and spin mismatch while searching for phonon with the required momentum [54].The reduced recombination results into longer lifetime for enhanced photovoltaic performance.

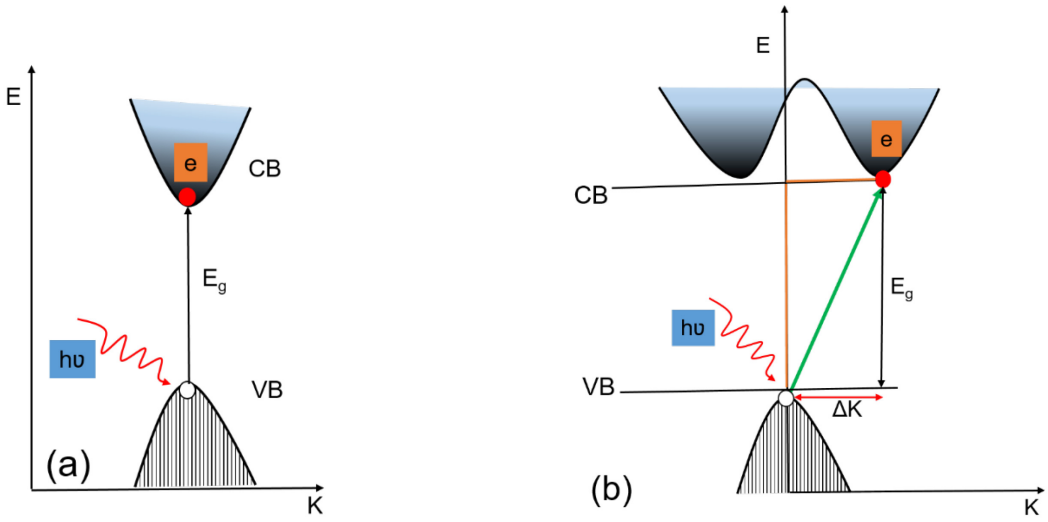

Figure 2.5: Schematic illustration of (a) direct and (b) indirect band gap semiconductors.

2.2.3. Band gap of perovskite as a function of lattice constant and stoichiometry

The band gap of hybrid organic-inorganic halide perovskite materials can feasibly be tuned by chemical substitution of alloys, enabling a wide range of parameters to be explored. Comparing reported experimental values suggests that the band gap of perovskites can feasibly be tuned from 1.17 eV for $CH_3NH_3(Sn_xPb_{1-x})I_3$ [17] about 2.3 eV [55] for $CH_3NH_3PbBr_3$ and even higher energies for chloride containing compounds [56]. However, the experimental data sets obtained by different researchers are quite diverging suggesting the existence of thermodynamic instability as well as miscibility gap for halide based compounds [57].Therefore the band gap of perovskite based compound can be tuned following Vegard's law.

Figure 2.6 (a) shows the dependence of band gap E_g as a function of lattice parameter of pseudo-cubic $CH_3NH_3Pb(I_{1-X}\ Br_X)_3$. The data points were acquired from the publication of Noh

et al. [19]. E_g decreases with increasing lattice parameter suggesting a lattice contraction due to increase in potential energy of the electrons in the orbitals of an atom.

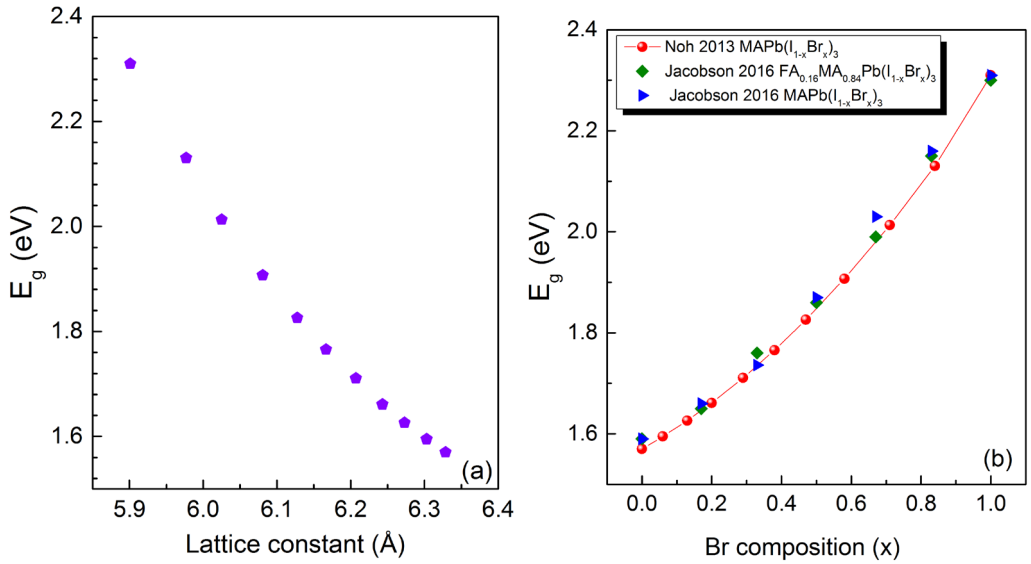

Figure 2.6: Dependence of the band gap (a) on the lattice constant of pseudo-cubic $CH_3NH_3Pb(I_{1-X}Br_X)_3$ (data points acquired after Noh et al. [19]) and (b) on the bromide composition for pseudo-cubic $MAPb(I_{1-X}Br_X)_3$ [19] and $FA_{0.16}MA_{0.84}Pb(I_{1-X}Brx)_3$ [33].

Figure 2.6 (b) relates the reported band gap as a function of bromide composition for $CH_3NH_3Pb(I_{1-X}Br_X)_3$ and $FA_{0.16}MA_{0.84}Pb(I_{1-X}Brx)_3$ with data points acquired from Noh et al [19] and Jacobsson et al. [33]. The non-linear variation of band gap as a function of bromide (Br) composition can be obtained using the relation:

$$E_g\ [CH_3NH_3Pb(I_{1-x}\ Br_x)_3] = E_g\ [CH_3NH_3PbI_3] + E_g\ ([CH_3NH_3PbBr_3] - [CH_3NH_3PbI_3] - c) + cx^2 \qquad 2.4$$

where c is the bowing parameter [58] which measures the degree of non-linear deviations arising from the anisotropy in the binding energy. After substitution of the bowing parameter of 0.33 according to [19], equation 2.4 reduces to quadratic equation of the form:

$$E_g = 1.57 + 0.39\ x + 0.33\ x^2 \qquad 2.5$$

where x is the bromide concentration

Jacobson et al. [33] also applied equation 2.4 for band gap tuning of $FA_{0.16}MA_{0.84}Pb(I_{1-X}Br_X)_3$ and $CH_3NH_3Pb(I_{1-X}Br_X)_3$ as a function of bromide concentration in the range between $0 \leq x \leq 1$. A non-linear increase of E_g with increasing content of bromide has been observed. The change in E_g with x did not significantly depend on the ratio between FA and MA cations due to the fact that the organic cations have a small influence on the band gap because of a negligible density of states near the band gap.

2.2.4. Band gap as a function of temperature

The band gap is a fundamental parameter of any semiconductor in relation to its electrical and optical properties. It reflects the bond energies such that an increase in temperature affects the chemical bonding when electrons are excited from the top of the valence band to bottom of the conduction band [59]. The first experimental and theoretical work on electronic band gap dated back to the dawn of the semiconductor era. Both the theoretical and experimental studies have over many decades, successfully explained the normal behavior of the temperature dependence of band gap for various types of semiconductors such as silicon (Si) [60], germanium (Ge), gallium arsenide (GaAs) [61], indium phosphide (InP) [62], cadmium selenide (CdSe) etc. In the conventional semiconductors, the band gap decreases monotonically with increasing temperature, with the behavior being non-linear at low temperatures and linear at higher temperatures [30]. For the inorganic semiconductors, the contribution of electron-phonon interaction to the band gap change with temperature is more dominant in comparison to dilation of the lattice [63,64]. However, there are some exceptional semiconductors with unusual temperature behaviors where the band gap decreases with decreasing temperature. An early example was PbTe in which a blue shift in energy gap was reported in the temperature range between 50 and 300 K [65]. Recently, a similar unusual behavior has been observed for lead sulphide (PbS) in which there is a strong increase in band gap energy with increase in temperature, a behavior opposite to what is observed in most common semiconductors .The increase was attributed to isotopic effect of the mass of sulphur which led to the cancellation of the zero point motion of lead and sulphur [66]. $CsSnI_3$ perovskite is another semiconductor with the anomalous behavior of the band gap with temperature. A strong linear increase of the band gap energy with increasing temperature in $CsSnI_3$ perovskite was attributed to thermal expansion contribution which dominates over electron-phonon interaction [31].

Several models have been reported in literature to describe temperature variation with band gap energy. The first model was reported by Varshni in which he reported on empirical model for the temperature dependent of the band gap energy in semiconductors [30]. The proposed Varshni relation is of the form:

$$E_g(T) = E_g(0) - \frac{AT^2}{B+T} \qquad 2.6$$

where $E_g(T)$ is the band gap energy as a function of temperature and the gap may be direct or indirect, $E_g(0)$ is the band gap at 0 K, A is a constant whereas B is fitting parameter related to Debye temperature θ_D .Theoretical treatment of equation 2.6 leads to the form:

$$\text{At } T \leq \theta_D;\ \Delta E_g(T) \propto T^2 \text{ and } T \gg \theta_D,\ \Delta E_g(T) \propto T \qquad 2.7$$

where $\Delta E_g(T)$ is the change in band gap as a function of temperature.

Expression 2.7 shows that the variation of band gap is non-linear at low temperatures and linear at higher temperatures. At lower temperatures, the expression 2.7 indicates that there is a quadratic temperature dependent which makes the fitting parameter B negative for some semiconductors such as diamond and hydrogenated silicon (6H SiC) [67]. The quadratic behavior at low temperature contradicts with the experimental findings which showed an approximate temperature independence of the band gap hence the inadequacy of the Varshni model. This led to the development of The Bose-Einstein (*BE*) model which relates the shift in the temperature dependent of energy gap with the Debye energy [68, 69]. Therefore, *BE* model considers the contribution of both lattice dilation as well as electron –phonon vibrations. According to this model, the change in band gap energy with temperature can be obtained from the relation 2.8:

$$E_g(T) = E_g(0) - \alpha_E \left[1 + \frac{2}{e^{\frac{\emptyset_E}{T}} - 1}\right] \qquad 2.8$$

where α_E is parameter related to the strength of electron – phonon interactions in the crystal lattice; $\emptyset_E$ is Einstein characteristic temperature of interacting phonons within the system and is related to the Debye temperature through the relation: $\theta_D = 1.33\ \emptyset_E$ [70].

Bose –Einstein model has been used to obtain a better fit for Cu_2ZnSnS_4(CZTS) absorber material with the experimental data [71]. The results suggested that a small shift of atoms or ion arising due to lattice vibration would damage lattice periodic field which in turn affect chemical bond length and energy of the band gap. In addition, temperature increase promotes more active phonon population modes which results to more electron-phonon interaction leading to shrinkage of the band gap [71]. However, the BE model could only be conceived in rather low temperature regime and this led to the development of a model which is most commonly used; the Pässler model.

Pässler model [72, 73] describes the variation of band gap with temperature based on the dominant contribution of electron- phonon interaction. The model can be represented by the following equation 2.9:

$$E_g(T) = E_g(0) - \frac{\alpha\theta}{2}\left(\left(\sqrt[x]{1 + \left(\frac{2T}{\theta}\right)^x}\right) - 1\right) \qquad 2.9$$

Where $E_g(T)$ and $E_g(0)$ are the energy gaps at temperature T and 0 K, respectively.

$$\text{As } T \to \infty, \quad \alpha = \frac{dE_g(T)}{dT} \qquad 2.10$$

θ is the temperature of phonon specific to a particular material whereas x is empirical parameter which is related to the shape of electron-phonon function usually confined to a range of $x > 2$ [73].

In general the Varshni model presents three parameters whereas the Pässler model presents 4 parameters that can be adjusted to fit the experimental data. Both models assume that the dominant factor in the temperature dependent of the band gap is due to electron-phonon interaction. However, the Varshni model shows some deviations in the low temperature region with the experimental data in which the model predicts quadratic (T^2) behavior in the low temperature region and does not produce T^4 temperature dependence behavior observed in bulk silicon [74]. On the other hand, the Pässler model considers the contributions of phonons with various energies. However, it ignores the contributions from the thermal dilation of the lattice causing a significant deviations at higher temperatures. BE model has been shown to fit in very well with the observed experimental trends at all temperatures since it involves both the lattice dilation and electron-phonon interactions.

The contribution of the lattice dilation on the shift of band gap can be described by thermal expansion based on the so called quasi harmonic approximation which assumes a harmonic interatomic potential but takes into consideration zero point effects [31]. The periodic lattice dilation of the temperature dependence of the energy band gap is given by the relation:

$$\left(\frac{dE_g}{dT}\right)_{lattice} = -\left(\frac{\partial E_g}{\partial P}\right) B_o \frac{\Delta V(T)}{V_o} \qquad 2.11$$

where $\frac{\partial E_g}{\partial P}$ is pressure dependent at constant volume but independent of temperature, $\Delta V(T)$, volume expansion term of the quasi harmonic approximation including zero-point effect. V_o is the volume of the lattice at temperature T and B_o is the bulk modulus. The strongest temperature variation appears through the term $\frac{\Delta V(T)}{V_o}$.

Therefore, at $T << \theta_D$

$$\frac{\Delta V(T)}{V_o} = \frac{V(T)-V(0)}{V_o} = \frac{c_V \gamma_G}{B_o} T \qquad 2.12$$

where c_V and γ_G are the specific heat capacity and Grüneisen parameter respectively [75]. On the other hand, at $T \gg \theta_D$

$$\frac{\Delta V(T)}{V_o} = \frac{V(T)-V(0)}{V_o} = \frac{c_V \gamma'_G}{4B_o} T \qquad 2.13$$

where γ'_G is an average of the Grüneisen parameters for the three branches of acoustic phonons.

Generally, in most common semiconductors such as Si, GaAS, electron-phonon interaction is the dominant factor that contributes to the shift in band gap with respect to temperature. In these semiconductors, an increase in temperature promotes more phonon population modes which increases more electron-phonon interaction leading to shrinkage of the band gap. However, this is not the case for hybrid organic –inorganic lead halide perovskite which shows a reversed behaviour. The reports investigated in the literature indicate that the contribution of direct electron-phonon interaction is negligible and the variation of band gap with temperature is dominated by the thermal expansion contribution [31]. Thermal expansion effects produces unusual signs which causes the anomalous behaviour in the energy band gap with temperature. The unusual behaviour was first observed in PbTe and was attributed to the interplay between lattice dilation and electron-phonon interaction in which the former was thought to produce anomalous sign and contributed to half of the temperature dependence of the band gap [76].

Figure 2.7 shows the dependence of the band gap energy with temperature. For common semiconductors such as Si, GaAs, InP, the band gap decreases monotonically with increase in temperature. The behavior is observed to be linear at higher temperatures and becomes non-linear at low temperatures. However, $CsSnI_3$ exhibited an exceptionally opposite behavior in which the band gap increases monotonically with increasing temperature. For the former, the major contributor to the variation of band gap with respect to temperature has been reported to be mainly due to electron-phonon interaction with thermal expansion accounting only for a small fraction of the total variation energy gap with temperature [30]. In contrast, for the latter, the major contribution to variation of energy gap with temperature is mainly due to lattice dilation as a result of thermal expansion of the lattice brought about by the anomalous large electron effective mass [31]. In summary, the temperature variation of energy band gap in semiconductors is mainly due to periodic lattice dilation [77] and electron-phonon interaction [30].The dominant contribution in most semiconductors comes from electron-phonon interaction which accounts for almost 80-90% of the shift in energy gap with temperature. This is because lattice phonons have extremely small energies which make them readily excited in large numbers at moderate temperature [59] and results into the shrinkage of the band gap with increasing temperature.

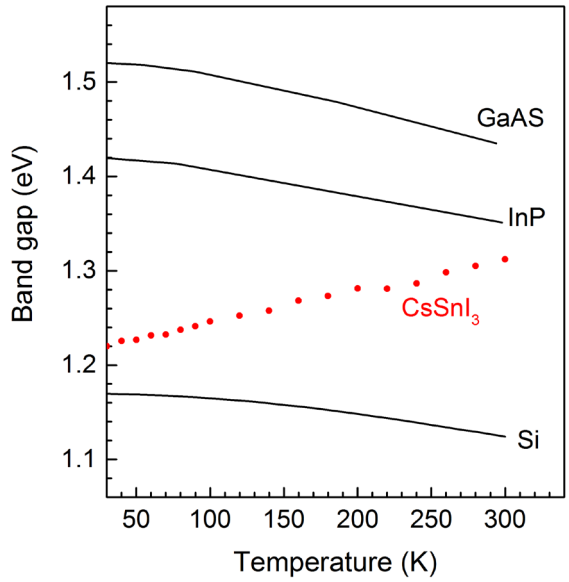

Figure 2.7: Energy band gaps as a function of temperature for silicon (Si), gallium arsenide (GaAS), indium phosphide (InP) and caesium tin iodide ($CsSnI_3$) (red circles). The data for Si is obtained after [60], GaAs [61], InP [62] and $CsSnI_3$ [31]

Table 2.1 summarises some of the most commonly used parameters for different compounds. The second column shows the ratio of electron effective mass to the rest mass for Si, Ge, GaAS, InP, CdSe, CdTe and $CH_3NH_3PbI_3$. Table 2.1 shows that GaAs has the lowest effective mass whereas $CsSnI_3$ compound has the largest value of electron effective mass. The unusually large effective mass of $CsSnI_3$ explain the unusual behaviour in the temperature dependence of the band gap. Moreover, the temperature coefficient is of significant importance since it enables the quantification of the temperature sensitivity of the photovoltaic devices. As can be seen from table 2.1, dE_g/dT is negative for common semiconductors and positive for $CH_3NH_3PbI_3$ and $CsSnI_3$ semiconductors. The negative value of dE_g/dT for common semiconductors is due to strong electron-phonon interaction which dominates over the thermal lattice dilation. On the other hand, for ionic semiconductors such as $CH_3NH_3PbI_3$ and $CsSnI_3$, lattice dilation due to thermal expansion and intra-band interaction is the dominant interaction in the temperature dependent of the band gap resulting into $dE_g/dT < 0$.

Figure 2.8 shows band gap energy and the slope of the linear approximation of the band gap (dE_g/dT) at 300 K for various semiconductors. For common semiconductors such as Ge, Si, GaAs, CdTe, InP and CdSe, dE_g/dT is negative. This is because for these semiconductors, the electron-phonon interaction is stronger than intra-band interaction and thermal expansion of the lattice resulting into $dE_g/dT < 0$. On the other hand, for ionic semiconductors such as $CH_3NH_3PbI_3$ and $CsSnI_3$, intra-band interaction and lattice dilation are the dominant parameters responsible for positive temperature coefficient. It has also been reported in

literature that band gap of $CH_3NH_3PbI_3$ increases with increasing temperature due to reverse band ordering of the electronic states such that the valence band maximum is constituted of p-like states whereas the conduction band minimum is constituted of s-like states [78]. This reverse ordering of band edge states are the main reason for the anomalous behavior of the band gap with temperature $CH_3NH_3PbI_3$ perovskite materials and hence the positive temperature coefficient. Yu et al reported that the anomalous behavior of the temperature dependence of the band gap of $CsSnI_3$ perovskite was dominated by thermal expansion contribution with negligible contribution from electron- phonon interaction due to unusually large electron effective mass (0.734 m_o) [31].

compounds	$\frac{m_e^*}{m_0}$	Band gap (E_g) (eV) at 300 K	Temperature Coefficient $\left(\frac{dE_g}{dT}\right) \times 10^{-4}$ eV/°K	References
Si	0.19	1.12	-4.73	[60,79, 80]
Ge	0.082	0.66	-4.4	[79, 81]
GaAS	0.067	1.424	-4.45	[82, 83, 84, 85]
InP	0.077	1.347	-2.88	[86, 87, 88]
CdSe	0.13	1.7	-3.3	[89, 90, 91]
CdTe	0.11	1.529	-4.3	[92, 81]
$CH_3NH_3PbI_3$	0.32	1.55	3.2	[93, 17, 94]
$CsSnI_3$	0.74	1.316	3.5	[31]

Table 2.1: Electron effective masses, band gaps at room temperature and values of temperature coefficient ($\frac{dE_g}{dT}$) from a linear fit at 300 K.

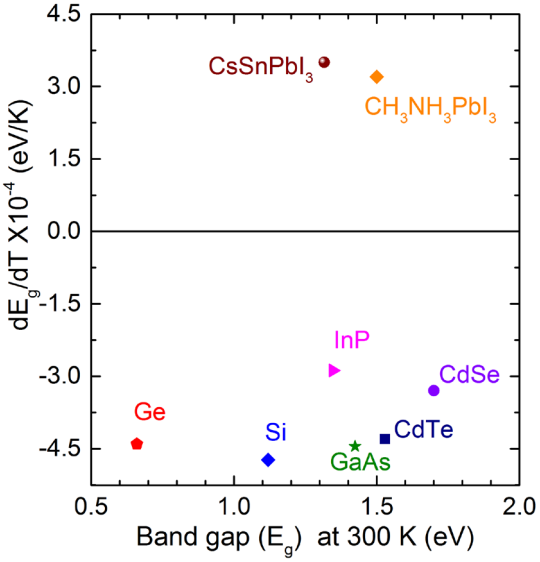

Figure 2.8: Dependence of the temperature coefficient of band gap (dE_g/dT) as a function of band gap energy at 300 K for various semiconductors. See table 2.1 for references.

2.2.5. Influence of distortions in a lattice on absorption spectra near the band gap

A periodic lattice potential can be distorted by lattice vibrations and/or distortions in bond lengths and bond angles due to defects such as lattice defects, impurities and dislocations. Distortions in the periodic lattice potential cause fluctuations in the edges of the valence and conduction bands and therefore of the band gap. In disordered semiconductors, such as amorphous silicon (a-Si: H), local variations of bond lengths and bond angles are so strong that the translation symmetry is lost. Furthermore, bond configurations change abruptly near interfaces and surfaces of a semiconductor leading often to disorder in interface regions.

Fluctuations in the band gap result in a deviation of absorption spectra from those of ideal direct or indirect semiconductors. These deviations are described by an exponential increase of the absorption coefficient (α) with increasing photon energy near the band gap. The exponential increase of α is characterized by the energy parameter E_t (t stands for tails) or E_u (u stands for Urbach who described the exponential absorption tails in semiconductors and insulators for the first time [95]).

$$\alpha \propto \exp(E - E_o)/E_{t(u)} \qquad 2.14$$

E_u is also called the Urbach energy and is obtained by measuring the absorption spectrum. $E_{t(u)}$ characterizes the degree of fluctuations or disorder in a semiconductor due to the structure, composition and temperature. Compositional disorder can be due to variations in stoichiometry, doping, hydrogenation, etc.

The characteristic energy describing the exponential increase of α with increasing photon energy, i.e. $E_{t(u)}$, depends on temperature and structural disorder and is described by the relation 2.15:

$$\frac{1}{E_{t(u)}} = \frac{\sigma}{K_B T} \qquad 2.15$$

where σ is the steepness parameter of the absorption edge (depends on the nature of the material), T is absolute temperature and K_B is the Boltzmann constant. As an example, figure 2.9 shows the influence of temperature on E_u for a-Si:H. The values of E_u increase with increasing temperature from about 55 meV at -150° C to about 67 meV at 60° C.

Figure 2.10 shows a typical absorption spectrum of a $CH_3NH_3PbBr_3$ layer in the range near the band gap. Three regions (A, B and C) can be distinguished in the absorption spectrum. At lower photon energies, the absorption is caused by relatively deep defects states in the band gap of $CH_3NH_3PbBr_3$ films (region A). At photon energies between 2.24 and 2.3 eV (region B), α shows an exponential absorption tail energy described by the relation 2.16: [96]

$$\alpha(E,T) = \alpha_o \exp\frac{E-E_o}{E_{t(u)}} = \alpha_o \exp\frac{\sigma(E-E_o)}{K_B T} \qquad 2.16$$

Where E_o, is the optical band gap and α_o is the convergence point of the Urbach bundle.

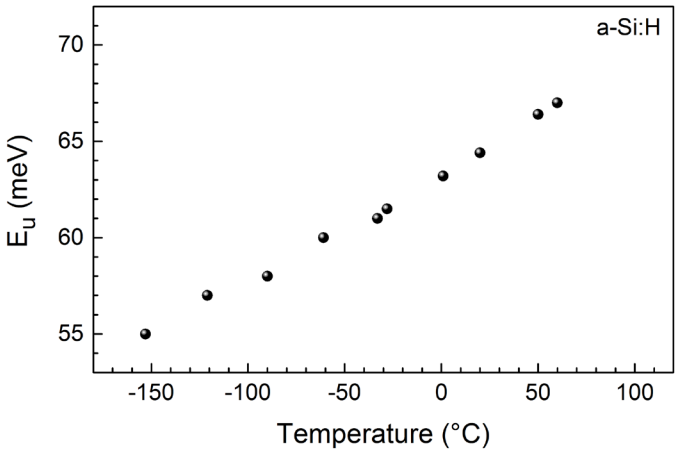

Figure 2.9: Example for the temperature dependence of the Urbach energy of a-Si:H (data points after Cody et al. [63]).

At higher photon energies, α is directly proportional to the square root of the photon energy. This region of absorption spectrum marks the direct optical band gap of $CH_3NH_3PbBr_3$ perovskites at about 2.3 eV (region C).

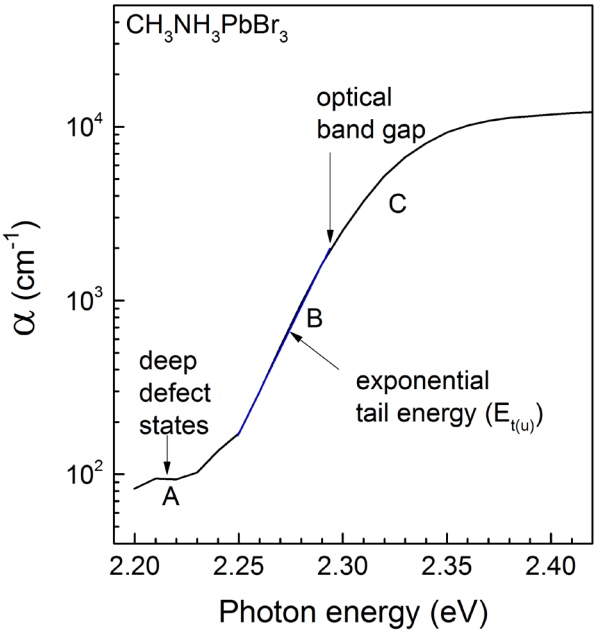

Figure 2.10: Schematic of absorption spectrum of $CH_3NH_3PbBr_3$.

2.3. Electronic and optical properties of hybrid organic-inorganic lead halide perovskites

2.3.1. Transport length

The transport length is one of the most important properties of any absorber material for solar cells. For a high short-circuit current, photo-generated charge carriers should be able to travel to the charge-selective contact over a distance longer than the absorption length before recombination takes place. Photo-generated charge carriers can travel by diffusion or drift. Therefore, the diffusion length or the drift length should be longer than the absorption length. The transport length corresponds to the dominating transport mechanism, i.e. the drift or diffusion length. In case of very thin absorber layers, such as $CH_3NH_3PbI_3$ with a typical thickness between 200 and 300 nm [97, 98] the transport length should be as long as the layer thickness in order to achieve a very high efficiency. This means, in the case of drift, there is an electric field across the absorber layer. The electric field can be caused, for example, by a p-i-n structure like in amorphous silicon (a-Si:H) solar cells [99].

The diffusion length is defined as the square root of the product of the lifetime and diffusion constant $L = \sqrt{\tau D}$ [15, 100].The diffusion constant and the lifetime can be obtained from the measurement of the mobility $D = \mu \frac{K_B T}{q}$ and of the decays of photocurrent or photoluminescence transients [15], respectively. However, this is an indirect method to obtain the diffusion length. A direct method to measure the diffusion length is related to the dependence of the illumination intensity on the absorption length at a constant surface photovoltage. As remark, this method gives the drift length in case of very thin absorber layers with a homogeneous electric field.

In $CH_3NH_3PbI_3$, most studies have been done on the measurement of the diffusion length by the indirect method based on lifetime and mobility measurements of charge carriers with values of transport length up to 175 µm [101] and 1 µm [15] having been reported for single crystals as well as thin films of perovskites. However, there is relatively little literature on direct method of measurement of diffusion length after Goodman [32] for perovskite based devices. So far, only Dittrich et al. have reported on the direct method of the determination of the transport length after Goodman using surface photovoltage (SPV) and obtained values ranging between 200 nm to tenths of µm for perovskite layers and powders respectively [102]. In order to apply the Goodman method to measure transport length of perovskite layers, accurate and precise knowledge of absorption coefficient and hence absorption length need to be known. The preceding section will discuss briefly the absorption coefficient of some semiconductors determined using different methods of measurement.

2.3.2. Absorption coefficient

For measurement of transport length, the absorption length of the material at different wavelengths need to be accurately known. The absorption coefficient is the reciprocal of absorption length. De Wolf et al. [13] determined effective absorption coefficient of $CH_3NH_3PbI_3$ films at room temperature and compared this with other semiconductor photovoltaic materials such as CdTe, CIGS, GaAS and c-Si. They found out that $CH_3NH_3PbI_3$ had an unusually sharp shoulder appearing at 1.57 eV with no presence of deep states. They used photothermal deflection spectroscopy (PDS) as well as Fourier transform photocurrent spectroscopy (FTPS) to obtain an absorptance spectrum featuring an exponential increase for $CH_3NH_3PbI_3$ layers. FTPS enabled measurement to be done without the contribution of the substrate as opposed to PDS. Xing et al [103] measured the absorption coefficient of $CH_3NH_3PbI_3$ films based on optical reflectance and transmittance method on quartz substrate. However, this technique does not allow separation of band to band absorption from parasitic absorption. Barugkin et al [104] used spectrally resolved PL measurements to determine band to band absorption coefficient of $CH_3NH_3PbI_3$ films in the wavelength range between 675-1400 nm. Absorption coefficients as low as 10^{-14} cm^{-1} were obtained at room temperature for long wavelengths.

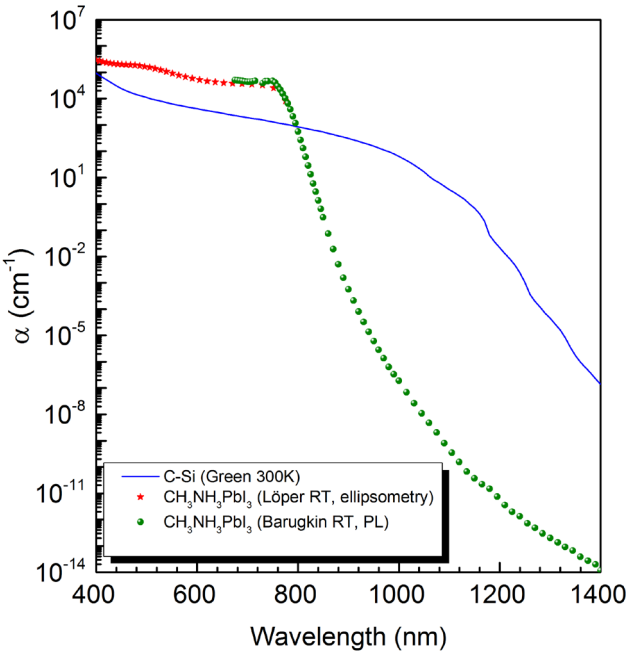

Figure 2.11: Absorption coefficient of $CH_3NH_3PbI_3$ from ellipsometry measurements by Löper et al [105] (red stars), spectrally resolved PL by Barugkin [104] (olive spheres). For comparison absorption coefficient of c-Si (blue line) obtained by Green et al. [106]. All measurements were obtained at room temperature.

In the wavelength region close to the band gap, the absorption coefficient of $CH_3NH_3PbI_3$ decays exponentially suggesting high structural order and low density of deep defect states.

In this region, the absorption coefficient of $CH_3NH_3PbI_3$ films obtained by PL and ellipsometry methods matches very well (see figure 2.11). Furthermore the absorption coefficient obtained by spectrally resolved PL technology can extend to longer wavelengths up to 1400 nm. For comparison, the absorption coefficient of c-Si with data points acquired from Green et al. [106] is included (blue line in figure 2.11). It should be noted that close to the sub band gap region of $CH_3NH_3PbI_3$ layers, both spectra show a sharp absorption edge with steep slopes in comparison to that of c-Si.

2.3.3. Mobility and doping of hybrid organic-inorganic lead halide perovskites

Considerable attention has been drawn in the past towards the development of photovoltaic technology which can be determined by controlled doping. The intentional doping techniques has been widely used in inorganic semiconductors such as silicon [107] as well as in the organic semiconductors [108]. For example, p-n junction has been reported to be formed via boron diffusion into the n-type silicon wafer to enhance charge separation and carrier collection efficiencies in the solar cell. Doping in semiconductors are beneficial since they directly alter the electrical properties such as conductivity, mobility, rate of charge carrier recombination, charge carrier diffusion length, interface energy barrier and contact resistance. For example, doping can help shift the position of the fermi level towards transport states that can help reduce ohmic losses and ease charge carrier injection to the contacts thereby improving device performance. Unlike, inorganic semiconductors, hybrid organic-inorganic perovskite semiconductors are usually processed in un-doped form. However, controlled and stable doping is favorable for high efficient devices.

Recently hybrid organic inorganic lead halide perovskite in particular $CH_3NH_3PbI_3$ has been reported to be self-doped through defect engineering. $CH_3NH_3PbI_3$ can either be p-type or n-type self-doped, depending on the ratio of CH_3NH_3I to PbI_2 during the formation process of perovskite in the precursor solution. $CH_3NH_3PbI_3$ rich in CH_3NH_3I were found to be p-type self-doped whereas those films rich in PbI_2 were n-type doped [109].Annealing can help transform p-type doped perovskite into n-type doped perovskite by removing excess CH_3NH_3I. Naikaew et al. demonstrated self-doping on the $CH_3NH_3PbI_3$ perovskite film using modulated surface photovoltage (SPV) technique [27]. They demonstrated that as-deposited samples annealed under nitrogen conditions inside a glovebox at 15, 30 and 45 minutes were p-type doped whereas perovskite samples annealed at 60 and 90 minutes showed n-type doping. The appearance of PbI_2 marked the transition from p to n-type doping [27].

First principle density functional theory (DFT) calculations also revealed that electrical conductivity of $CH_3NH_3PbI_3$ layers could be tuned from p-type to n-type doping by proper choice of precursor composition during fabrication process [16]. For example, CH_3NH_3I and

PbI_2 form Schottky defects which do not create traps states within the band gap. However, Frenkel defects such as Pb, I and CH_3NH_3 vacancies form shallow states near the band gap and causes un-intentional doping [16]. Furthermore, $CH_3NH_3PbI_3$ possess unusual defect physics with the dominant defects being p-typed doped lead vacancies and n-type doped CH_3NH_3I interstitials. The defects with low formation energies create shallow defects whereas those with high formation energies create deep defects. The unusual defect physics could be due to strong lead lone pair of s orbital and iodine p-orbital which form anti-bonding states and ionic property of $CH_3NH_3PbI_3$ layers [110].

Electronic transport properties of conventional semiconductor materials usually have a high "$\mu\tau$"product which is defined at the product of the charge carrier mobility, μ, and carrier lifetime τ. The relation is closely related to the diffusion length L, given by $L = (D\tau)$, where D is the charge carrier diffusion coefficient given as $D = (\mu k_B T/q)$, with q being the electronic charge, k_B is the Boltzmann constant, and T is the absolute temperature. Long charge carrier lifetimes could imply slow charge carrier recombination with low trapping probabilities, however that does not automatically imply high mobility's, which are limited by scattering. Charge carrier mobilities in hybrid organic-inorganic lead halide perovskite are often moderate and comparable to those of organic semiconductors but lower by several orders of magnitudes to Si, GaAS and some other inorganic semiconductors like CdTe as indicated in table 2.2.

semiconductor	Effective mass	Electron mobility (cm^2/VS)	Hole mobility (cm^2/VS)	References
Silicon	0.19	1500	500	[60, 111]
GaAS	0.067	8000	400	[82, 111]
CdTe	0.11	≤ 1000	≤100	[92, 111]
Rubrene	0.77	≤0.1	≤ 15	[110, 112]
$CH_3NH_3PbI_3$	0.32	800	164	[93, 113] [101]
$CH_3NH_3PbBr_3$		≤ 100	≤ 100	[114]
$CH_3NH_3SnI_3$			200-300	[114]

Table 2.2: Electron effective masses, electron and hole mobilities at room temperatures of selected semiconductor materials used as photovoltaic absorbers.

As a remark, mobility is usually proportional to charge carrier lifetime and indirectly proportional to carrier effective mass. If effective masses of perovskite are indeed comparable

to those of inorganic semiconductors (see table 2.2), then it means that the mobility of perovskite is limited by the scattering of acoustic phonons [115] and polaronic effects [116]. Polarons are quasi particles in which a phonon could screen charge carriers from conducting thereby lowering their mobilities. Therefore, the observation of a long carrier lifetime coupled with the indirect power dependence of mobility with temperature, suggest that there is negligible scattering from impurity and defects at room temperature but the main scattering are caused by phonons. This therefore, imply that the origin of polaronic effect may be due to mechanical and vibrational properties of perovskite material as a 'soft material', given a very small bulk and young modulus.

2.4. Solar cells based on hybrid organic-inorganic lead halide perovskite

Unlike silicon solar cells, perovskite-based solar cells are usually not doped hence there is no p-n junction in such devices. Since there is no p-n junction in perovskite solar cells, there is a need for electron transporting material (*ETM*) and hole transporting material (*HTM*) to transport charge carriers from absorber material to the ohmic contacts. Therefore this section will discuss the solar spectrum and work-function of different charge selective contacts and their role in charge carrier transport in perovskite based devices.

2.4.1. Solar spectrum

Solar energy is one of the inexhaustible renewable energy source with a large potential on the surface of the earth. Approximately 1.08×10^{18} KWh of the solar energy strike the earth's surface per year [1]. Practically about 600 TW of global terrestrial solar energy is provided with about 30% being reflected by the earth's atmosphere. In comparison, the annual global electricity consumption in 2016 was estimated as 22000 TWh indicating the average power consumption of around 2.4 TW [117]. Therefore, photovoltaic solar energy received on the earth's surface is significantly able to fully cover the electricity demand around the globe.

Engineering efficient photovoltaic devices comprising of absorber materials with different band gap energies is of crucial importance for making efficient multi-junction based devices which can match the solar spectrum. One way to realize high efficiencies is to make a multi-junction solar cells, whereby multiple absorber layers are used to divide the solar spectrum into different parts. This allows multi-junction solar cells to reach high efficiencies which cannot be achieved by a single junction based technologies.

The solar irradiance is standardized by the American society for testing of materials (ASTM). Therefore, the solar irradiance reaching the earth' surface is described by the ASTM-

173-03 standard designated by AM 1.5G [118].This standard correspond to the hemispherical global irradiance that consist of both direct and diffuse reflections. Figure 2.12 shows the normalized solar spectrum as a function of photon energy for the air mass of 1.5 global (AM 1.5 G) corresponding to the angle of incidence of 48°.19°. AM 1.5 G is the most commonly used solar spectrum with the irradiance normalized to an integrated power density of 1000 Wm^{-2} in order to calibrate and characterize solar cells [119]. The ultra-violet and visible irradiance roughly covers the spectral region from about 4.4 to about 1.6 eV and near infra-red roughly denotes the spectral region from 1.6 - 0.89 eV hence most spectral regions of solar spectrum is fully covered. Therefore the spectral regions match the optimal absorption region for a solar cell devices. The blue arrows in the figure 2.12 shows the band gap of Si, GaAS and $CH_3NH_3PbI_3$ perovskite absorber materials to be about 1.12 eV [60], 1.42 [84] and 1.55 eV [17] respectively. Therefore tandem solar cells comprising silicon as bottom cells with perovskite or GaAS as top cell can have potential to exceed the state of the art high efficiency single junction solar cells.

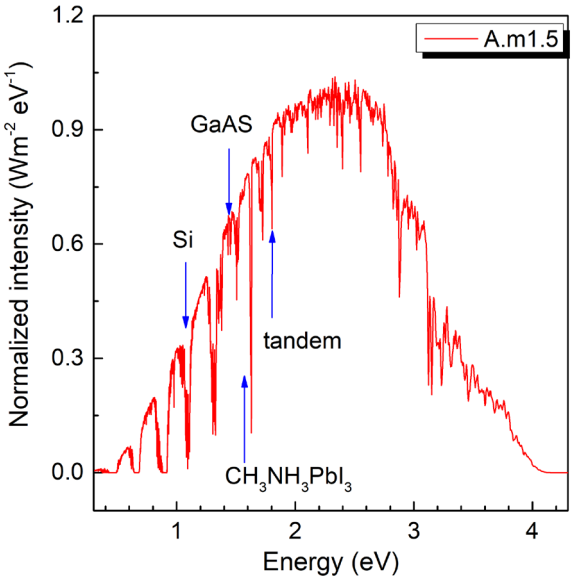

Figure 2.12: Solar spectrum with irradiance normalized to an integrated power density of 1000 Wm^{-2} (AM 1.5G). The arrows indicate the band gap of Si, GaAS, $CH_3NH_3PbI_3$ and tandem solar cells relevant for photovoltaic applications [120].

2.4.2. ETM and HTM layers used in perovskite solar cells

The electronic levels such as work function (Φ), fermi levels (E_F), vacuum level (E_{vac}), ionization energy (*IE*) and activation energy (*AE*) are fundamental parameters for controlling charge transport properties across different material interfaces. These electronic levels are sensitive to the structure, morphology and chemical compositions of a material. For example, a small amount of impurity on the surface of a metal or a semiconductor can significantly

change the work function and position of vacuum level [121].

The work function (Φ) can be defined as the minimum amount of energy required to remove an electron originally at E_F deep into the material and place it at vacuum level (E_{vac}) [121]. Therefore for a metal surface, Φ corresponds to energy difference between Fermi-energy (E_F) and vacuum level (E_{vac}) (see figure 2.13 (a)). Figure 2.13 (a) shows schematic energy diagram of a metal in which the valence band is filled with electrons up to the Fermi-energy (E_F). Φ is equal to energy difference between E_F and E_{vac} which is also similar to the difference between the ionization energy (*IE*) and electron affinity (*EA*) of a metallic material. *IE* can be defined as the work done in removing an electron at zero temperature or in the case of a molecule, *IE* can be defined as the standard enthalpy of ionization at 0 K [122].

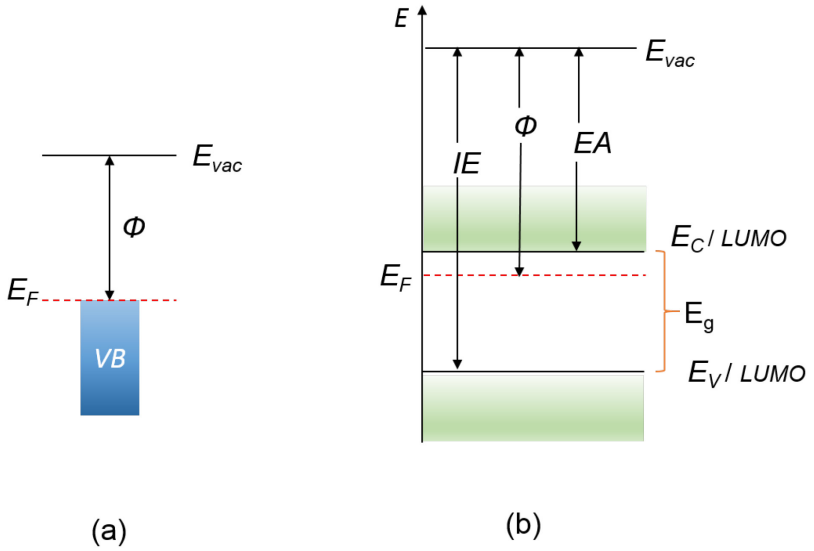

Figure 2.13: Schematic energy diagram of (a) metal with valence band (VB) filled with electrons up to the Fermi energy (E_F), vacuum level E_{vac} and work function (Φ) (b) in-organic and organic semiconductors with the band edges E_V, *Ec* and *LUMO*, *HOMO* respectively. E_V and *Ec* are the energies of the valence band maximum and conduction band minimum respectively, whereas *LUMO* and *HOMO* are the lowest unoccupied and highest occupied molecular orbitals of organic semiconductors. Vacuum level E_{vac}, work function (Φ), energy gap (E_g), ionization energy (*IE*), and electron affinity (*EA*) are as defined.

Figure 2.13 (b) shows schematic energy levels of inorganic and organic semiconductors. For inorganic semiconductors, Φ depends directly on E_F and position of the E_{vac} such that $\Phi = E_{vac} - E_F$. Ionization energy $IE = E_{vac} – E_V$, whereas electron affinity (*EA*) can be given by the relation: energy $EA = E_{vac} – E_c$. The band gap energy E_g is the energy difference between the energy of conduction band minimum (E_c) and valance band maximum (E_v), i.e. $E_g = E_c – E_v$. The energy levels of organic semiconductors are described by the lowest unoccupied molecular orbitals (*LUMO*) and highest occupied molecular orbital (*HOMO*) for a neutral

molecule in a ground state energy. The band gap E_g is equivalent to the difference in Energy between the LUMO and HOMO levels I.e. $E_g = LUMO\text{-}HOMO$.

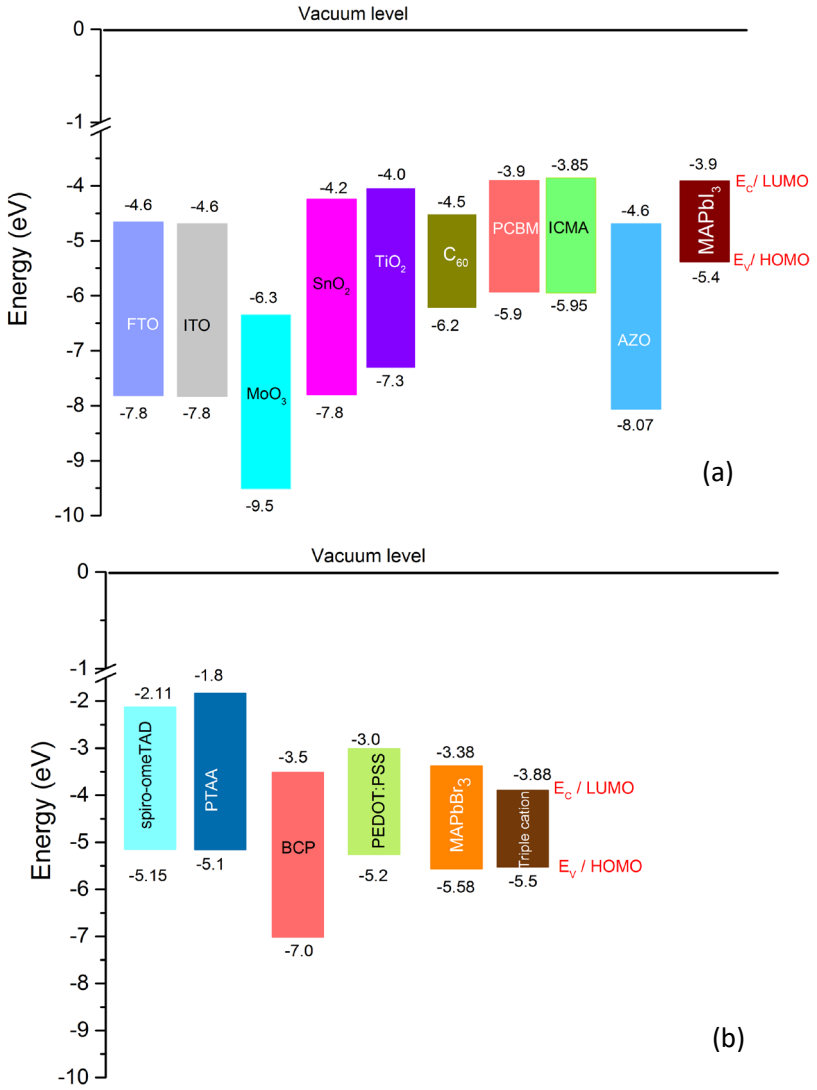

Figure 2.14: Energies of the conduction and valence band edges (a) different electron selective contacts, perovskite and transparent conductive oxides and (b) hole selective contacts and perovskites. The band gap with corresponding references are as shown in table 2.3.

The work function of charge transport layers has a strong influence on device performance (see table 2.3). This is because it significantly affects the open circuit voltage (V_{oc}) of perovskite based solar cells. It has been shown that V_{oc} of regular (*n-i-p*) structure is higher than that of inverted structure (*p-i-n*). The band gap of inorganic metal oxides used as electron selective materials (*ETL*) is very wide. For example, for SnO_2 the band gap is 3.5 eV, that ofTiO_2 (3.2 eV) and for ZnO: Al (3.3-3.7 eV). These wide band gaps enable *ETLs* to absorb higher photon energies without themselves contributing to photocurrents thus minimizing *ETL* induced current losses. As can be seen in figure 2.14 (a) for metal oxide *ETLs*, SnO_2 has the highest

band gap. This implies that it possesses a favourable band alignment with perovskite photoactive layer hence reduced current losses than TiO_2 and ZnO : Al. Furthermore, these wide band gap metal oxide have ionization energies of about 2 eV larger then perovskite active layers. This property enables for distinct hole extraction barrier at the interface with perovskite active layer. In contrast, fullerene derivatives used in the thesis as *ETLs*, have 1 eV lower ionization energies than inorganic metal oxide hence substantially have an increased hole blocking capability (see figure 2.14 (a)).

substrate	Work function (eV)	Band gap (eV)
FTO	4.4	3.2 [123]
ITO	4.4 [124]	4.2 [125]
PEDOT:PSS	4.9 [126]	1.4 - 2.5 [127]
TiO_2	4.2	3.2 [128]
SnO_2	4.75	3.5 [129]
C_{60}	4.7	2.0 [130]
PCBM	4.3 [131]	2.0 [130]
ZnO: Al	4.62 [132]	3.32 - 3.77 [133]
ICMA	4.3	2.1 [134]
MoO_3	6.9	3.2 [135]
PTAA	5.1	1.95 - 3.3 [136, 137]
BCP	6.7 [138]	3.5 [130, 139]
$MAPbI_3$	4.8 [140]	1.6 [130]
$MAPbBr_3$	4.0 [141]	2.3 [136]
Triple cation		1.61 [142]

Table 2.3: work function and band gap of various substrates and perovskite absorber materials

In this thesis, the Spiro-OmeTAD was used as hole transporting material (*HTM*) in the n-i-p structure whereas PEDOT: PSS and PTAA were employed in inverted structure. The work function of PEDOT: PSS is 4.9 eV (see table 2.3) and from the energy level diagram (figure 2.14 (b)), the highest molecular orbital (HOMO) level was higher in comparison to perovskite material. This implied that low work function coupled with high HOMO level make PEDOT: PSS energetically unfavourable for efficient charge carrier transport with perovskite absorber materials. Poly-triarylamine (PTAA) is another *HTL* used in the study with a work function of

5.1 eV slightly higher than PEDOT: PSS (see table 2.3). The favourable band alignment between PTAA and perovskite absorber material may lead to improvement in the open circuit voltage of perovskite-based solar cells.

2.4.3. Tandem solar cells

Tandem solar cells are double junction solar cells with an optimum combination of band gap values. The device consists of a low band gap bottom cell and a higher band gap top cell. In ideal case, the bottom cell absorbs all the light transmitted by the top cell [143]. Studies have shown through device modelling that for efficient tandem device, the top cell should have a band gap between 1.7 eV to 1.9 eV whereas for bottom cell, the band gap should range between 0.9 eV to 1.2 eV [144]. Halide perovskite based on tin (Sn) and lead (Pb) demonstrate excellent band gap tenability across the solar spectrum. For example, Pb- perovskite based on mixed iodide and bromide cover a band gap range from 1.5 eV [145] for pure iodide to 2.3 eV [19] for pure bromide. On the other hand, mixed Pb and Sn perovskites based on iodide can cover a band gap range of 1.17 [17] for 50% Sn and 50% Pb to 1.5 eV [145] for pure Pb. This makes Pb perovskite based on mixed halide suitable as a top cell whereas mixed Pb and Sn perovskite based on iodide as a bottom cell for tandem solar cells. Furthermore, both the low band gap and wide band gap halide perovskites can be fabricated via low temperature processing thus preventing undesirable damage during fabrication of tandem devices [143].

Albrecht et al. [143] fabricated a monolithic tandem solar cells based on silicon as bottom cell and perovskite as top cell and realized a power conversion efficiency of 18%. The monolithic integration was realized via low temperature processing of perovskite absorber layer, electron selective contacts (SnO_2) and hole transporting material (spiro-OMeTAD). The low temperature processing of the top cell ensured that optical and transport properties of bottom cell (silicon) was not damaged [143]. Zhao et al. fabricated an all metal halide perovskite 4-terminal tandem solar cells with a low band gap (1.25 eV) bottom cell based on mixed Sn and Pb halide perovskite and demonstrated a high power conversion efficiency (PCE) of 17.6 % and PCE of 21% when stacked together with wide band gap (1.58 eV) top cell [146]. Eperon et al. [147] reported on the 2 and 4 terminal all perovskite tandem solar cells [147]. For the two terminal tandem device, a low band gap (1.2 eV) bottom cell was used which consisted of $FA_{0.75}Cs_{0.25}Sn_{0.5}Pb_{0.5}I_3$ and demonstrated a PCE of 14.8% with *Voc* greater than 1.65 eV and PCE of 17% when stacked with a wide band gap (1.8 eV) top cell.

Figure 2.15 shows energy level diagram of a two terminal tandem solar cell. Light travels through ITO and spiro-OMeTAD layer before being absorbed in the perovskite layer. The perovskite layer transmits a large proportion of near infra-red light (NIR) to generate high

photocurrent in the silicon bottom cell which can absorb near infra -red light. ITO/SnO_2 is used as a recombination/interfacial layer for electrical contact between the cells. However, ITO acts as a transparent layer as well as an intermediate reflector so as to significantly decrease the light that is passed to the bottom silicon solar. SnO_2 is used as electron selective contact given that it has a favourable energy level aligned with the conduction band of perovskite [143].

Hybrid Organic-inorganic lead halide perovskite has evolved rapidly over the years with power conversion efficiency reaching 22.1% [5] in a span of less than 10 years. However the stability issue remains a challenge for commercial utilization. Long term operational stability of perovskite-based devices is important for practical applications. There have been remarkable improvements in the stability of halide perovskite with some studies having recorded measurements in thousands of hours. This improvements have been realized through interface engineering [34], device architecture & optimization [148] and using mixed halide perovskite [33, 19].

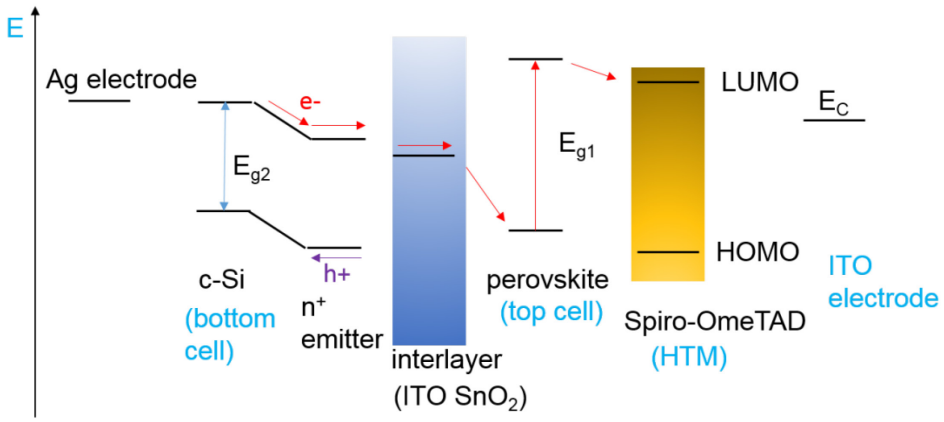

Figure 2.15: Energy level diagram of a 2-terminal solar cell

2.5. Stability of hybrid organic-inorganic lead halide perovskite

Stability studies are required in order to gain a deeper understanding of the reasons for degradation of devices and possible ways to enhance the long-term stability of solar cells based on hybrid organic-inorganic lead halide perovskites. For instance, chemical interaction between a perovskite and an electrode could lead to device instability as well as photo-induced degradation. Metals such as aluminium, silver and gold may react or induce chemical reactions with perovskite film under humid conditions resulting into degradation of perovskite absorber layer. Furthermore, metals can also diffuse into charge-selective contact layers, which gives additional reasons for the degradation of solar cells. For example, aluminium can diffuse into PCBM layers during evaporation causing local shunts [149].

2.5.1. Stability under moisture and oxygen

Humidity is regarded as one of the major causes of degradation in perovskite, however humidity alone is not the main degradation component but rather the quantity of photons in combination with humidity triggers instability. Leijtens et al. established that by applying a weak field of 600 Vcm^{-1} near gold electrodes coated with perovskite film in the presence of moisture led to irreversible degradation [150]. The irreversible degradation in the presence of moisture was attributed to the ion movement in the electric field [150]. Furthermore, trap charges also play a significant role in the irreversible degradation of perovskite films under moisture [151] by causing the deprotonation of the $CH_3NH_3^+$ cation. The deprotonation of the $CH_3NH_3^+$ cation induces local electric fields that distort the structure of the perovskite when octahedral PbI_6 interacts with $CH_3NH_3^+$ and water.

Although most reports indicate that moisture causes degradation of perovskite films, it has been revealed that mild moisture could have a positive impact on the perovskite film formation. Due to the hygroscopic nature of methyl ammonium iodide, exposing the precursor solution of perovskite to moisture during film formation could lead to accumulation of moisture in the grain boundaries causing grain- boundary creep that could lead to a merger of corresponding grain boundaries. The effect increases the size of the grains and subsequent reduction of pin-holes. In addition, mild moisture levels (35% ±5%) could also result into a significant enhancement in perovskite device performance with a power conversion efficiency of 17.1% and fill factor of 80% with an intense and sharp XRD diffraction [152].

De Wolf investigated moisture induced degradation of methyl ammonium lead iodide using photothermal deflection spectroscopy (PDS) [13]. A sharp onset of the absorption spectrum of methyl ammonium lead iodide perovskite at 1.5 eV has been observed during the initial state suggesting a low density of deep defect states. However, with exposure to a relatively high humidity in the range of 30-40 %, there was a significant drop in the absorptance spectrum towards high energy at about 2.3 eV corresponding to the band gap of PbI_2 [153].

2.5.2. Stability of perovskite in UV- light and light soaking

Ultra violet (UV) illumination can reduce the performance of devices based on perovskite due to the generation of defects by different mechanisms. In contact with TiO_2, degradation induced by UV-light can be explained by chemical reactions activated by photo-generation at the surface of TiO_2. Oxygen vacancies, the concentration of which can be high at the surface of TiO_2, act as efficient electron donating deep sites. The electrons from such deep sites interact with oxygen from the atmosphere, which in-turn adsorbs to the oxygen vacancy sites forming a charge transfer complex [154].

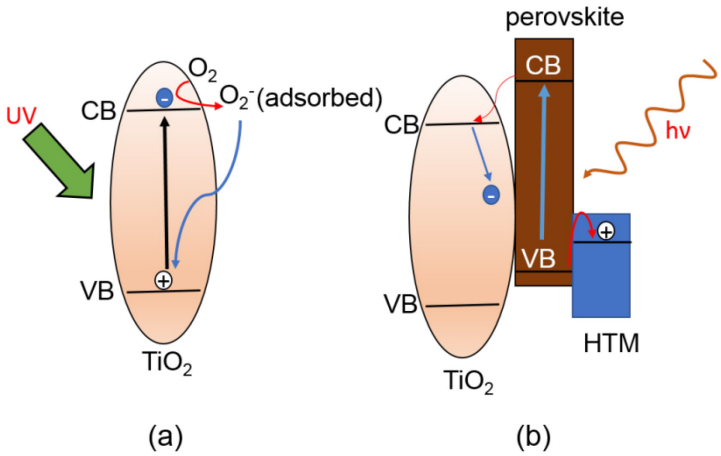

Figure 2.16: Mechanism for ultraviolet (UV) induced degradation [154]. Band diagram of TiO_2 surrounded by oxygen (O_2) from atmosphere; upon UV absorption electron-hole pair is created in which the photo-generated electrons from TiO_2 react with O_2 to generate oxygen radical called superoxide (O_2^-). The holes in the valence band of TiO_2 recombine with electrons present at the oxygen adsorbed site thereby desorbing the oxygen (a). Excitation of the perovskite absorber material sandwiched between TiO_2 (*ETM*) and spiro-MeOTAD (*HTM*), electrons are injected into the conduction band (CB) of TiO_2 for where they become deeply trapped while holes are attracted to the valence band (VB) of *HTM* (b).

Photo-generation of electron-hole pairs under UV illumination leads to recombination of holes from the valence band of TiO_2 with electrons trapped at adsorbed oxygen. As consequence of recombination, oxygen is desorbed (figure 2.16 a). This means that free electrons in the conduction band of TiO_2 as well as unfilled positively charged oxygen vacancies are left on the surface of TiO_2. Upon excitation of the perovskite absorber material, electrons are injected into the conduction band of TiO_2 from where they are deeply trapped whereas holes in the absorber are attracted towards hole transporting material e.g. spiro-OMETAD (see figure 2.16 b).Therefore, by considering perovskite absorber material sandwiched between TiO_2 (*ETM*) and spiro-OMeTAD (*HTM*), excess holes in the spiro-OMeTAD will recombine with trapped electrons from TiO_2 leading to device degradation.

Chemical models of photo-induced degradation

Light induced degradation of $CH_3NH_3PbI_3$ in dry air can be initiated when an iodide anion undergoes oxidation and donates an electron to the surrounding oxygen. In the presence of light, the surrounding oxygen forms a free radical of superoxide (O_2^-) which deprotonates the methyl ammonium cation to form a highly volatile methylamine molecule that escapes from the surface of perovskite leaving behind lead iodide. The transformation equation is shown in 2.17 and 2.18:

$$CH_3NH_3PbI_3 \rightleftharpoons CH_3NH_3I + PbI_2 \quad (2.17)$$

$$2CH_3NH_3I + 1/2\ O_2 \longrightarrow 2CH_3NH_2 + H_2O + I_2 \quad (2.18)$$

Recent similar reports show that illumination of $CH_3NH_3PbI_3$ films with or without the presence of oxygen results into dissociation of methyl ammonium ($CH_3NH_3^+$) cations into methylamine (CH_3NH_2) and molecular hydrogen which at room temperature can easily diffuse out of the perovskite sample [155]. Illumination of $CH_3NH_3PbI_3$ layers with a photon energy greater than the band gap of perovskite in the presence of oxygen leads to the creation of electron-hole pairs. The free electron in the conduction band of $CH_3NH_3PbI_3$ could easily be captured by an oxygen molecule forming a superoxide (O_2^-) (equation 2.19). The superoxide formed reacts with a $CH_3NH_3^+$ cation and forms methylamine (CH_3NH_2) and hydroperoxyl (HO_2) (see equation 2.20). Because CH_3NH_2 has a low boiling point of -6.7 °C [156], it evaporates easily from the sample surface resulting in the breakdown of the $CH_3NH_3PbI_3$ lattice. The unstable hydroperoxyl dissociates into oxygen and hydrogen gas as shown in equation 2.21 [155].

$$O_2 \xrightarrow{light} O_2^- \quad (2.19)$$

$$CH_3NH_3^+ + O_2^- \longrightarrow HO_2\uparrow + CH_3NH_2\uparrow \quad (2.20)$$

$$2HO_2 \longrightarrow 2O_2\uparrow + H_2\uparrow \quad (2.21)$$

Perovskite also degrades rapidly in the presence of light. For example, the air stability of pure $CH_3NH_3PbI_3$ and $CH_3NH_3PbI_3$ embedded on poly-vinylpyrrolidone (PVP) both deposited on mesoporous TiO_2 were compared. Minor degradation was observed for the film stored in the dark and humid environment, but rapid degradation was found for films exposed to light in the presence of humidity. This was attributed to surface defects at the $TiO_2/CH_3NH_3PbI_3$ interface which were initiated by the light and caused charge imbalance in the perovskite films [157].

A reversible red shift of the photoluminescence (PL) spectrum (peak at 1.68 eV) as well as a splitting of X-ray diffraction peaks for $CH_3NH_3Pb(Br_xI_{1-x})_3$ films upon light soaking have been recently demonstrated [20]. This finding was ascribed to photoexcitation that induces migration of halides. The migration of halides causes phase separation into domains of iodide (lower band gap) and bromide (higher band gap). The iodide precipitates act as traps for holes from the valence band offset. The electrons trapped in the conduction band at the Br^- site and the holes in the valence band of the I^- site recombine and the energy of the emitted photons corresponds to the difference between [valence band edge of iodine and the conduction band edge of bromine. The increased recombination resulted also in a reduced splitting of the quasi Fermi levels and therefore to a reduced Voc [20].

It has also been reported that UV illumination of the Pb-X bond could generate halogen free radicals that break down the perovskite structure resulting in the irreversible formation of PbX_2 [20]. Christian et al. [158] suggested that after light soaking of perovskite films, organic cations, such as $CH_3NH_3^+$, may become less tightly bound to the PbI_6^{4-} octahedra due to weak hydrogen bonds. Furthermore, light soaking of perovskite films in the presence of moisture induced irreversible degradation. As main reasons for this irreversible degradation, reduced hydrogen bonding that occur after photo-excitation and trapping of charge carriers along grain boundaries were suggested [158].

Grain boundaries act as accumulation sites for trapped charges and provide pathways for infiltration of water molecules [151]. The formation of hydrates (for example, $(CH_3NH_3)_4PbI_6.2H_20$), which may be triggered by trapped charge carriers, was suggested as a further scenario for irreversible decomposition of perovskite films [158]. The PbX_6 octahedra within the hydrated perovskite interact with both organic cations and water causing trapped charges at the defect site, which induce local electric fields and deprotonate organic cations. Such a deprotonation process in the presence of water molecules yields volatile molecules that can evaporate at room temperature [151]. The deprotonation takes place via the following reaction 2.22:

$$2CH_3NH_3^+ + 2e \longrightarrow 2CH_3NH_2 + H_2 \qquad 2.22$$

The two molecules formed (i.e. methylamine and molecular hydrogen are highly volatile hence diffuse easily outside the sample surface leading to breakdown of the perovskite lattice.

2.5.3 Thermal stability

Supasai et al. [29] used SPV and GIXRD to characterize $CH_3NH_3PbI_3$ layers annealed under vacuum conditions to temperatures up to 160°C. GIXRD showed no PbI_2 diffraction peaks for $CH_3NH_3PbI_3$ layers annealed at 100°C. However, the impurity peak of PbI_2 was observed for $CH_3NH_3PbI_3$ layers annealed inside a glovebox under nitrogen conditions at 140 °C and 160° C. SPV spectra showed a change of sign in the in-phase and phase shifted by 90° signal for $CH_3NH_3PbI_3$ layers annealed at 100° C and above. The change of sign was correlated to the onset of defect states at the surface of $CH_3NH_3PbI_3$ layers which changes the electronic properties of the perovskite layers. Furthermore, there was a strong change of SPV signals at photon energies of 2.36 eV after annealing at 140°C corresponding to PbI_2 phase, which was in agreement with GIXRD measurements indicating onset of degradation process [29].

Recently Zhang et al. [159] studied photovoltaic behaviour of $CH_3NH_3PbI_3$ perovskite solar cells over a wide temperature range from 80-360 K and observed a maximum open circuit voltage of about 1.15 V at 200 K close to phase transition from tetragonal to orthorhombic

symmetry. On the contrary, the photocurrent was remarkably stable from 360-240 K but drops abruptly below 220 K indicating that there is inefficient charge generation in the orthorhombic perovskite structure [159]. Habisreutinger et al. [160] subjected $CH_3NH_3PbI_{3-x}Cl_x$ to a temperature of 80° C in air and observed fast degradation in the perovskite films, characterized by color change from dark brown to yellow indicating degradation to PbI_2.

GIXRD diffraction peak at 12.65° was observed for $CH_3NH_3PbI_3$ layers annealed in nitrogen filled atmosphere in a glovebox at 100° C for 60 min, with the intensity of the diffraction peak increasing strongly at 90 min. The diffraction peak at 12.65° was attributed to appearance of PbI_2 which was the onset of degradation of $CH_3NH_3PbI_3$ films [27]. Kim et al. [161] also employed in-situ synchrotron radiation analysis to monitor thermal degradation of perovskite solar cells. $CH_3NH_3PbI_3$ films changed to intermediate phase before it degrades to CH_3I, NH_3 and PbI_2 after short exposure to heat stress for 20 min at 100° C and after longer exposure to heat stress at 80°C for more than one hour.

2.5.4. Role of interfaces for stability

Hybrid organic inorganic perovskite are susceptible to degradation under moisture, oxygen, heat and light due to their low formation energies. In this respect, charge selective contacts play an important role in protective perovskite absorber layers from such environmental exposure. Therefore charge selective layers are crucial for energy level matching, charge transport and for high stability. You et al [149] reported on solution processed $CH_3NH_3PbI_3$ solar cells with p - i - n structure, employing NiO_x and ZnO as hole & electron transporting material respectively. The solar cell had improved stability against degradation from water and oxygen given that ZnO separates perovskite and Al layers thus preventing infiltration of Al layers into perovskite films.

Perovskite solar cells with planar TiO_2 as electron transporting material (*ETM*) have been demonstrated to exhibit un-stabilized power conversion efficiencies (PCE) with high hysteresis. The anomalous hysteresis in the I-V curves may be due to large contact resistance for electron transfer between TiO_2 and perovskite interface [162]. Hysteresis-free perovskite solar cells have also been reported using SnO_2 as *ETM*, attaining PCE of above [163]. SnO_2 has been chosen because it has favorable conduction band alignment with perovskite as compared to TiO_2 which showed energy band mismatch with perovskite. Furthermore, SnO_2 has a deeper conduction band and can be fabricated via low temperature processing conditions hence can facilitate the realization of long term air stability devices with enhanced hysteric behavior. Electron injection dynamic behavior from $CH_3NH_3PbI_3$ into TiO_2 and SnO_2 based devices has also been studied with SnO_2 exhibiting better electron extraction property in comparison to TiO_2 indicating a favorable energetic band alignment for the former [163].

Anaraki et al. [164] reported on planar perovskite-based solar cell on SnO_2 ETM prepared by simple, low temperature deposition process through a combination of spin coating and chemical bath techniques; attaining PCE of 20.7% at stabilized maximum power point tracking after storage in the dark under aging conditions. Their work demonstrated the importance of electron selective contacts as a means of achieving high efficiency and stability in perovskite based devices. In the p - i - n structure, the *ETM* is the topmost layer exposed to ambient air if metal electrode is excluded. For example, PCBM could absorb water or oxygen onto its surface resulting into the formation of dipole moment and high resistance that lead to decomposition of the perovskite photoactive layer [149].

CHAPTER 3

Modulated surface photovoltage (SPV) spectroscopy

3.1 Principle of modulated surface photovoltage spectroscopy

Modulated surface photovoltage (SPV) spectroscopy is a contactless non-destructive technique for investigating semiconductors and semiconductor surfaces by examining modulated illumination that induces changes in the surface potential [22]. The SPV is defined as the difference between the surface potentials of a semiconductor under illumination and in the dark [165]. A nonzero SPV implies that photogenerated free charges are redistributed in the space [22].

SPV signals are measured between two electrodes, the sample and the reference electrodes (figure 3.1 (a)). For modulated SPV measurements, both electrodes are electrically connected via a very high resistance. Electrons flow from the electrode with lower work function to the electrode with the higher work function until equilibrium of the Fermi-level (E_F) is achieved. The difference in the work functions of the reference and sample electrodes is called the contact potential difference (CPD). The sample electrode is covered with the semiconductor. Under illumination of the semiconductor (figure 3.1 (b)), free charge carriers are photogenerated. The separation of photogenerated charge carriers in space results in the change of the surface dipole and leads to the change of the semiconductor work function (ΔCPD). The SPV is defined as the negative change of the CPD, i.e. - ΔCPD.

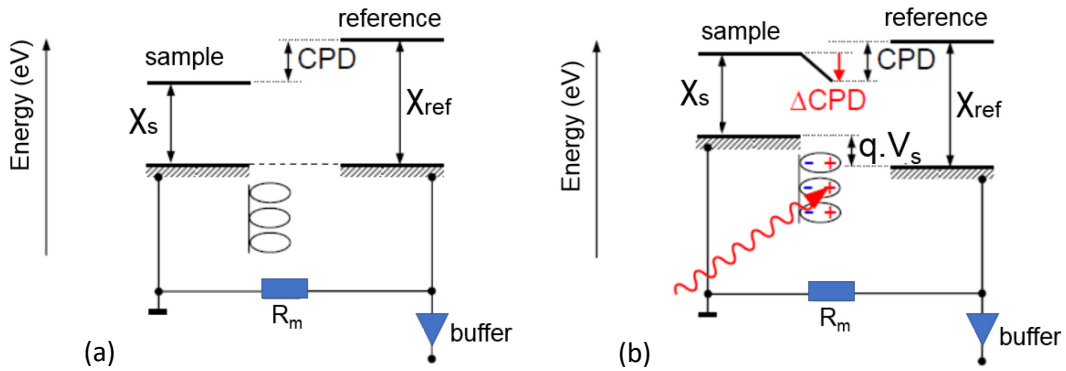

Figure 3.1: Energy schemes of a sample electrode with a surface layer and reference electrode in the dark (a) and under illumination (b). Both the electrodes are connected with a measurement resistance. The reference electrode is connected to a high impedance buffer. The work functions of the sample and reference electrodes are χ_s and χ_{ref}, respectively. The contact potential difference (CPD), the light induced change of the CPD (ΔCPD) and the light induced voltage between the electrodes (V_s) are indicated.

The change in the surface work function induces a current flow through the very high measurement resistance (R_m) between the sample and reference electrodes until the Fermi-levels are re-aligned. In modulated SPV measurements, the measurement capacitance (C_m) between the sample and reference electrodes is fixed (fixed capacitor arrangement, figure 3.2). Therefore, the Fermi-levels re-align within the R_mC_m time constant. If R_mC_m is much longer than the modulation period, the CPD is preserved and a positive voltage corresponding to a lower electron potential is obtained. On the other hand, if the measurement time is longer than R_mC_m, the potential at the external contacts drops to zero voltage due to discharging of the capacitor with respect to ΔCPD [166, 167].

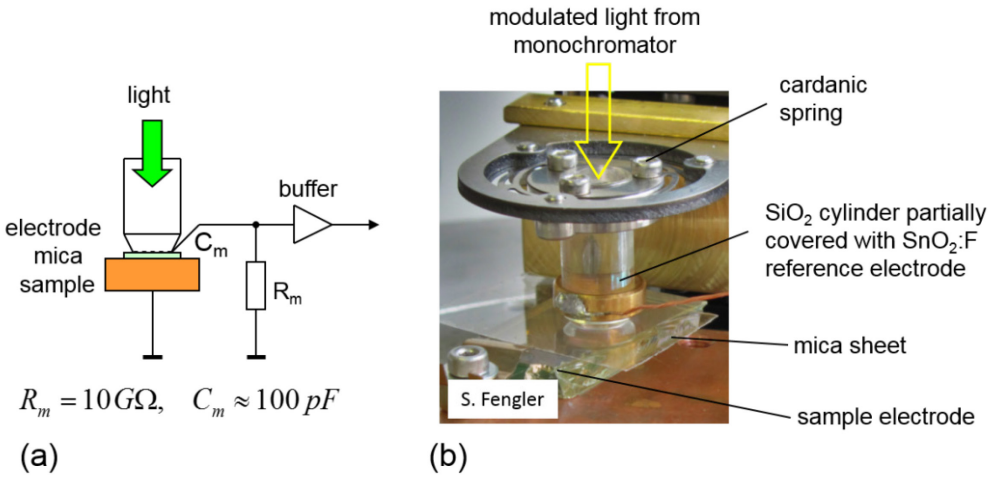

Figure 3.2: Schematic of the fixed capacitor arrangement for modulated SPV measurements (a) and a photo of a given reference electrode with a sample and a mica spacer (b).

The sign of modulated SPV signals gives the direction of modulated charge separation. A positive SPV signal is obtained when electrons are separated towards the sample electrode (equivalent to charge separation in the surface space charge region of an n-type doped semiconductor in depletion), whereas a negative SPV signal is measured for separation of electrons towards the surface of the sample (equivalent to charge separation in the surface space charge region of a p-type doped semiconductor in depletion).

In modulated SPV measurements with a double phase lock-in amplifier, the in-phase (also called x-signals) and phase-shifted by 90° (also called y-signals) signals are distinguished (figure 3.3). The x- and y-signals correspond to the sine or cosine components of the modulated signals (in figure 3.3, the coefficients m_x and m_y are used for explanation). For a positive increasing (light on) and decreasing (light off) signals, the x- and y-signals are positive and negative, respectively (on dominating mechanism of charge separation). Therefore, the in-phase signal gives the information about the direction of charge separation.

The x- and y-signals correspond to the fast and slow response in relation to the modulation period, i.e. the y-signal is zero if the increase and the decay of the signal is much faster than the modulation period and the x-signal is zero if the increase and the decay of the signal is much slower than the modulation period [28].

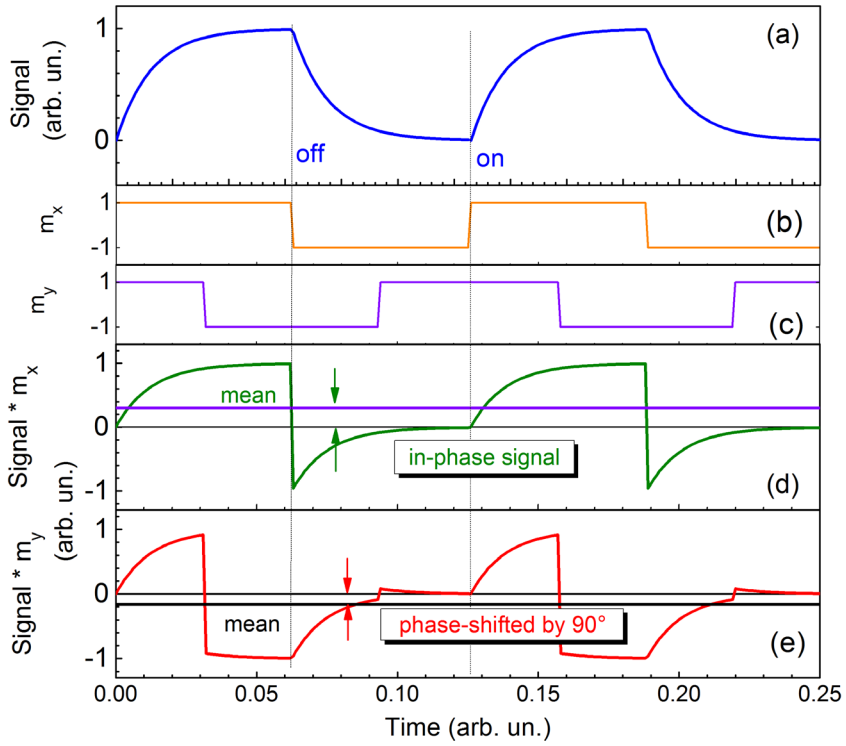

Figure 3.3: Example of modulated signal (a), coefficients for analyzing the in-phase and phase shifted by 90° signals (m_x and m_y, (b) and (c) respectively) and the products of the modulated signal with m_x and m_y ((d) and (e), respectively). The in-phase and phase shifted by 90° signals are indicated.

The amplitude of modulated SPV signals (R) is defined as the square root of the sum of the squared x- and y-signals:

$$R = \sqrt{x^2 + y^2} \qquad 3.1$$

The tangent of the phase angle (φ) is defined as

$$tan\phi = \frac{y}{x} \qquad 3.2$$

Modulated SPV spectroscopy is an ideal method for the characterization of electronic properties of hybrid organic-inorganic lead halide perovskites since it does not require the preparation of contacts and since it can be performed after every step of layer preparation, light soaking etc. For example, the passivating behavior [29] and hole blocking [168] of the $CH_3NH_3PbI_3$ / PbI_2 interface, the dependence of the electronic properties of the $CH_3NH_3PbI_3$ / TiO_2 interface on the presence [28] and thickness of amino valeric acid (AVAI) during

deposition [169], the role of phase composition of electronic states in $CH_3NH_3PbI_3$ prepared from $CH_3NH_3I/PbCl_2$ solution [27], the determination of the transport length (L) of $CH_3NH_3PbI_3$ after Goodman in layers and powders [102], dependence of L on light soaking of $CH_3NH_3PbI_3$ powders [170] and its dependence on the grain size in $CH_3NH_3PbI_3$ layers [171] and the modulated charge transfer at interfaces between carboxylated multi-walled carbon nanotubes and $CH_3NH_3PbI_3$ [172] were investigated by modulated SPV spectroscopy. In this thesis, modulated SPV spectroscopy is applied in order to investigate the behavior of the band gap (E_g), exponential tail states close to the band edges (E_t), deep defect states, charge separation and transport or diffusion length (L).

3.2 Components for modulated SPV spectroscopy measurements

Figure 3.4 shows the block scheme for measurements by modulated SPV spectroscopy. A lamp with a monochromator is used for spectral-dependent illumination. The light passes an optical chopper for modulation and is directed onto the sample and reference electrodes (measurement capacitor). The impedance of the measurement capacitor is matched with the input impedance of the lock-in amplifier by a high-impedance buffer. The SPV signal passes the high impedance buffer and is measured with the double-phase lock-in amplifier. A personal computer is used for adjusting the wavelength via the stepper driver control unit and for measuring the modulated SPV spectra.

A quartz prism monochromator was used for measuring SPV spectra from the near infrared to the ultraviolet range without the need for changing order filters and gratings, i.e. without breaking points in the spectra. Incidentally, SPV spectra measured over a wide spectral range cannot be simply normalized to the photon flux as is be done, for example, for the measurement of the quantum efficiency.

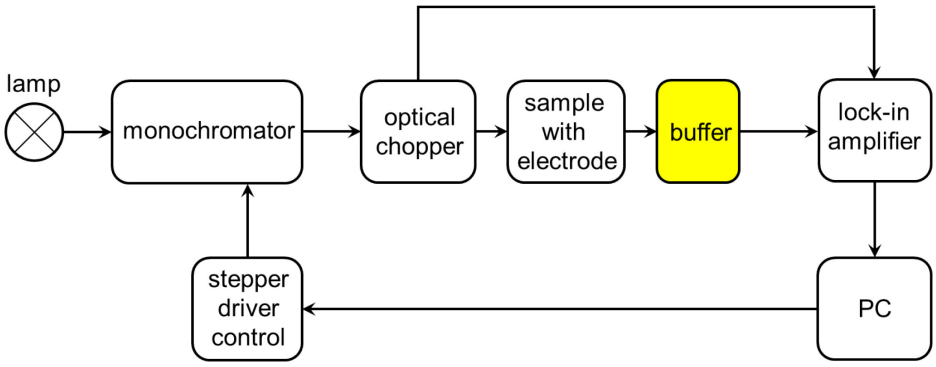

Figure 3.4: Block diagram of the set-up for measurement by modulated SPV spectroscopy.

Figure 3.5 (a) shows a measurement capacitor connected directly with a lock-in-amplifier. The relatively low input resistance of the measurement device (kΩ to MΩ) acts as a shunt. As a consequence, a current flow will be measured as a potential drop across the input resistance of the measurement device, i.e. the measured signal is not directly related to the SPV. Therefore, a device matching the impedance of the measurement capacitor with the impedance of the measurement device is required (figure 3.5 b).This device is called a high-impedance buffer because the input resistance of a high impedance buffer is extremely high in order to match the impedance of the measurement capacitor. On the other side, the output resistance of the high impedance buffer is usually 50 Ω. For ideal high-impedance buffers, the input resistance is infinitely high and the input capacitance is zero and the output resistance is much lower than the input resistance of the measurement device so that the input potential is equal to the output potential.

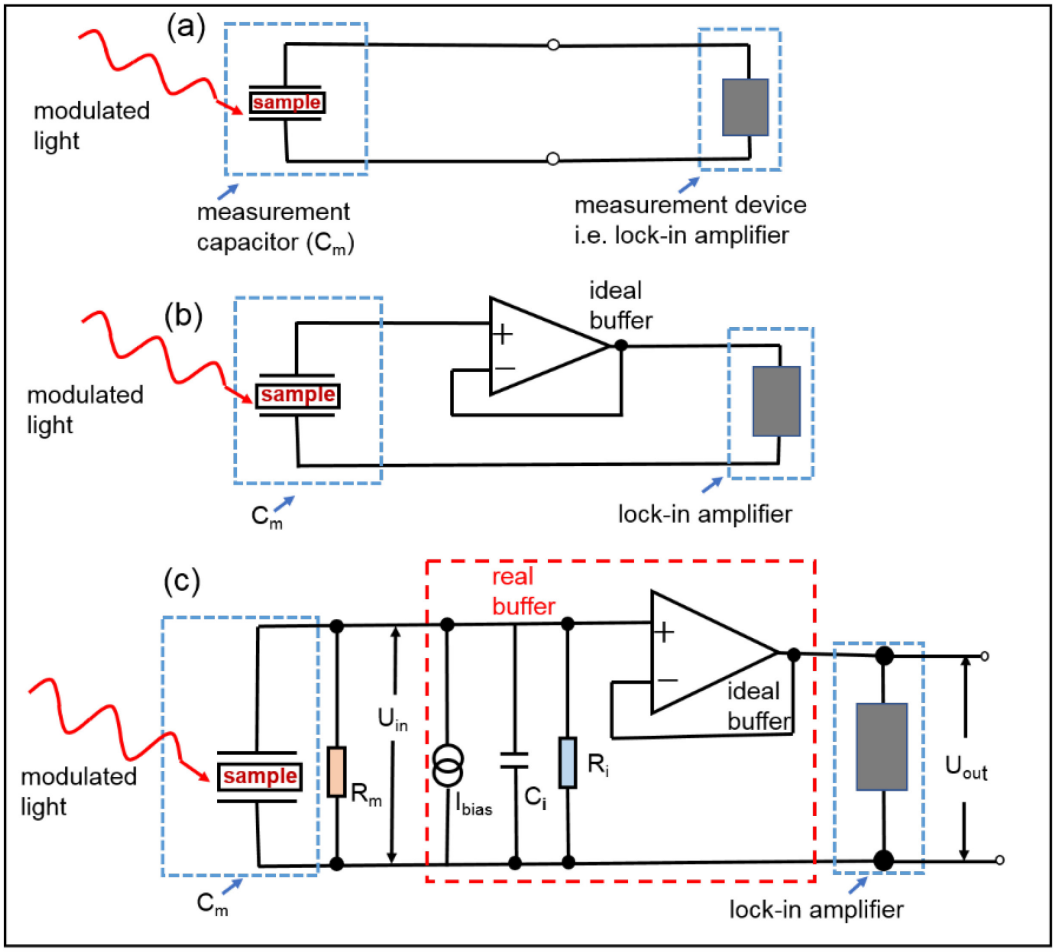

Figure 3.5: Equivalent circuits of a measurement capacitor connected directly with a measurement device (a) and connected with a measurement device via an ideal (b) or real (c) high-impedance buffer.

In real high impedance buffers, however, the input resistance cannot be infinitely high and the input capacitance cannot be zero. This has consequences for the measurements of SPV

signals. Figure 3.5 (c) shows an equivalent circuit of a real high impedance buffer consisting of an ideal high impedance buffer connected in parallel with an input resistance (R_i), input capacitance (C_i)and a bias current source (I_{bias}) at the input and connected in series with an output resistance (R_{out}) at the output. For the buffer used in our experiments, an operational amplifier (OPA565) with I_{bias} equal to 2 fA and C_i of the order of 3-4 pF was used.

Both measurements capacitance C_m across the sample and input capacitance C_i form a capacitive voltage divider which reduces the output voltage U_{out}.

$$U_{out} = \left({C_m}/{C_m + C_i}\right) U_{in} \qquad 3.3$$

The product of I_{bias} and R_i is high because R_{in} is very high (of the order of TΩ for OPA565).

$$\Delta U_{in} = I_{bias}.R_i \qquad 3.4$$

The high bias voltage (ΔU_{in}) is reduced by implementing a measurement resistance (R_m), which is of the order of GΩ. In addition, I_{bias} charges the C_m and a potential drift (U_{ib}) appears:

$$\frac{d\,U_{ib}}{dt} = {I_{bias}}/{C_m} \qquad 3.5$$

The measurement resistance R_m charges and discharges C_m with the time constant given by:

$$\boldsymbol{\tau} = R_m C_m \qquad 3.6$$

This has the consequence that SPV signals can be measured only at times significantly shorter than the $R_m C_m$.Therefore, the modulation period of the chopped light should be significantly shorter than $R_m C_m$ [166]. For more detailed analysis, the response function of a given high-impedance buffer shall be simulated (see, for example, [173]).

3.3 Determination of the band gap and exponential tails by SPV

Modulated SPV amplitudes may not be linked directly to the photon flux since different processes may contribute to charge separation, for example, with opposite direction of charge separation and/or with different dependencies on light intensity. Furthermore, SPV signals, in analogy to the open circuit voltage of a solar cell, can depend logarithmically on the light intensity (at high light intensity), can saturate at very high light intensity or can depend linearly on the light intensity (at low light intensity, limitation by the shunt resistance). Therefore, SPV signal may result into a non-linear response [174].

Measurements by modulated SPV spectroscopy are performed at low light intensities, which are of the order of tens of μW/cm². Therefore, measurements are performed in the low signal case, for which the response is linear if there is no change in the mechanisms of charge separation and relaxation within the considered spectra range. The phase angle is very sensitive to the change of the mechanisms of modulated charge separation and relaxation. As a criterion, the spectra of the modulated SPV amplitudes can be analyzed in analogy to optical

measurements if the phase angle is constant (or nearly constant) in the considered spectral range. Incidentally, the value of E_t obtained by SPV is not necessarily equal to the value of E_u obtained by UV-vis spectroscopy because charge carriers excited into localized states do not participate in charge transport and do therefore not contribute to the SPV signal. This is shown schematically in figure 3.6 for fundamental absorption (process A), for which both the photogenerated electron and hole are mobile, for excitation from a delocalized into a localized state (process B), for which one of the photogenerated charge carriers is not mobile, and for excitation from a localized into a localized state (process C), for which both photogenerated charge carriers are not mobile.

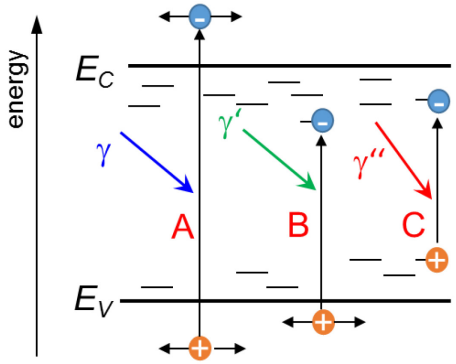

Figure 3.6: Schematic of photogeneration in fundamental absorption (A), for excitation from a delocalized into a localized state (B) and from a delocalized into a delocalized states (C).

If there is only one mechanism of charge separation and relaxation, the distribution of exponential defect states below the band gap can be analyzed by dividing the SPV amplitude by the photon flux (Φ_{ph}). The value of E_t was obtained by fitting the leading edge of the SPV amplitude normalized Φ_{ph} with an exponential function.

$$R/\Phi_{ph} = B \cdot exp\left(\frac{h\upsilon - E_g}{E_t}\right) \qquad 3.7$$

where B is a proportionality factor, $h\upsilon$ is the photon energy, E_g denotes the band gap at the onset energy.

SPV spectra of the amplitude or of the in-phase or phase-shifted by 90° signals can be used to determine the approximate band gap of semiconductors. In most semiconductors, there is a pronounced increase of the absorption coefficient closer to the band gap (E_g). Therefore, SPV signals are directly proportional to the absorption coefficient of a semiconductor as long as the absorption length, i.e. the reverse absorption coefficient, is shorter than the diffusion length of minority charge carriers [22] an as long as there is only one dominating process of charge separation and relaxation involved into the formation of the SPV signals.

SPV or absorption spectra around the band gap of a thin semiconductor layer do often not correspond to those of ideal semiconductors. There are different opportunities to define a band gap or an onset energy for SPV spectra. The easiest way is to get the onset energy (E_{on}) of a SPV spectrum (figure 3.7 (a)). The onset energy can be acquired from the spectra of the modulated SPV amplitude by extrapolating the leading edge of the SPV signal to the photon energy scale and reading out the photon energy at the point of intersection with photon energy axis. For ordinary semiconductors, E_{on} of the SPV signal is depicted by the signature near the band gap and corresponds to a strong increase in the magnitude of the SPV signal [175]. As an example, Lagowski et al. [176] applied a similar method to define an onset energy in order to study the SPV response of silicon-on-sapphire films.

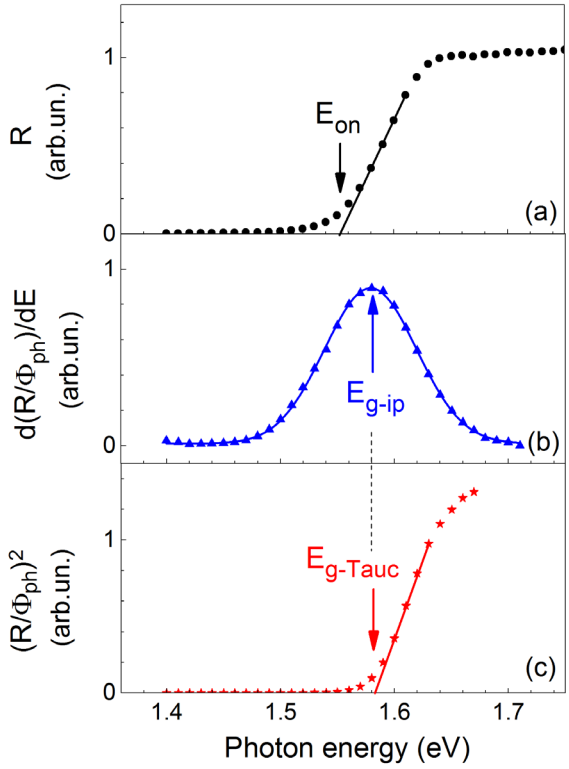

Figure 3.7: Analysis of the band gap as the onset energy (a), energy in the inflection point (b) and Tauc gap for a direct semiconductor (c).

Another way to define a band gap is the analysis of the inflection point of the spectrum normalized to the photon flux ($E_{g\text{-}ip}$). In this case, the band gap is close to the maximum of the spectrum of the first derivative as suggested by Lassabatere et al. [177] (figure 3.7 (b)). The inflection point analysis is the most general approach, which does not depend on the nature of the band gap and which does only weakly depend on the exponential tails. As an example, Lassabatere et al. [177] used maximum derivative of wavelength dependent modulated SPV

to determine the $E_{g\text{-}ip}$ of GaAs films, which was in excellent agreement with E_g resulting from conventional optical measurements [85].

The nature of the band gap is considered in the analysis of the so-called Tauc gap ($E_{g\text{-}Tauc}$). This method of determining $E_{g\text{-}Tauc}$ was introduced by Tauc [178] who demonstrated that amorphous germanium has an indirect transition in its optical absorption spectrum. For a semiconductor with a direct band gap, the Tauc gap is found from the extrapolation of the linear region of the squared spectrum normalized to the photon flux to the axis of the photon energy (figure 3.7 (c)).

3.4 Measurement of the diffusion length after Goodman

The diffusion or transport length (L) is the average distance over which excess charge carriers can travel before they recombine. It can be measured by direct and indirect methods. The direct method is related to the dependence of the intensity on the absorption length at a constant SPV [32]. The indirect method, on the other hand, involves the dependence of L on the lifetime (τ) and diffusion constant (D) [15] through the relation

$$L = \sqrt{\tau \cdot D} \qquad 3.8$$

The lifetime can be obtained from the measurement of the decays of photocurrent or photoluminescence transient whereas D can be found from the mobility [15] by using the Einstein equation:

$$D = \mu \frac{K_B T}{q} \qquad 3.9$$

In order to measure the diffusion length after the method developed by Goodman [32], a modulated SPV signal between an illuminated surface and a non-illuminated back surface is kept constant at each wavelength by adjusting the light intensity. The constant SPV signal provides a constant Fermi-level splitting during the measurement and therefore avoids an influence of the spectral-dependent surface recombination velocity. By plotting the light intensity versus the absorption length and extrapolating to zero light intensity, a straight line, the negative intercept of which is equal to the diffusion length (L), is obtained (see figure 3.8).

Following the original equation of Goodman [32], the intensity is equal to a constant multiplied by a functional dependence of the absorption coefficient α, such that,

$$I_0(\lambda) = const.\,(\alpha(\lambda)^{-1} + L) \qquad 3.10$$

with the condition that

$$L, \alpha^{-1} \gg d \qquad 3.11'$$

$$L, \alpha^{-1} \ll t \qquad 3.11''$$

$$\Delta p \ll n_0 \qquad 3.11'''$$

where α^{-1} is the absorption length, t is the thickness of the absorber layer, d is the depletion width of the space charge region, n_0 is the majority charge carrier density and Δp the minority charge carrier density. Equations (3.10 and 3.11) can be applied if a low level of charge injection was considered, when trapping and recombination processes in the space charge region was neglected and when there is only a small variation of the quantum efficiency and of the reflectance with the wavelength.

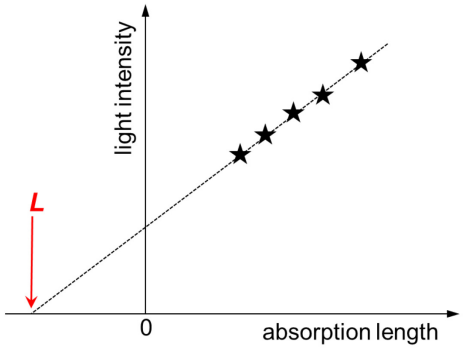

Figure 3.8: So-called Goodman plot, which gives the dependence of the light intensity on the absorption length by keeping SPV constant.

The knowledge of the precise absorption spectrum of the investigated semiconductor is needed for a direct analysis of the diffusion length. In contrast to c-Si, precise data of absorption spectrum for $CH_3NH_3PbI_3$ and other perovskites are rare. In this thesis, the data of Löper et al., which was obtained with from ellipsometry measurements [105], were fitted with cubic spline function and used in the analysis of the transport length.

CHAPTER 4

Experimental and characterization methods

Electronic, structural and optical properties of hybrid organic-inorganic lead halide perovskite depend on the preparation conditions, crystallization methods and defect formation. Solution based techniques are most commonly used. The formation of perovskites depends on the solvents, additives, temperature and substrates. Furthermore, electronis properties change as a function of time and additional factors such as light soaking, coating and temperature treatments, which are important factors for the stability of perovskite solar cells.

Grazing incidence X-ray diffraction (GIXRD), surface photovoltage spectroscopy (SPV), optical (UV-vis) spectroscopy and photothermal deflection spectroscopy (PDS) were used for characterization. GIXRD gives information about the phase composition of perovskite whereas SPV allows for the characterization of the exponential tail states (E_t) close to the band edge, the band gap (E_g), defects below the band gap and the diffusion length (L). UV-vis spectroscopy allows for the characterization of the optical properties of the perovskite layer. In this thesis, material properties related to degradation, stoichiometry, band gap (E_g), E_t and L were investigated.

By varying different halide compositions, the band gap of perovskite could be changed. Similarly diffusion length after Goodman can provide a useful information about the lifetime of solar cells. Furthermore, temperature dependent measurement of the band gap as well as investigation of the role in interfaces in the evolution of defect states will be determined by SPV. In the study of interfaces, different electron selective as well as hole selective contacts will be varied and their influence on perovskite properties determined.

4.1. Preparation of substrates and of hybrid organic-inorganic lead halide perovskites

4.1.1. Preparation of the substrates and preparation routes for deposition of hybrid organic-inorganic lead halide perovskites

Substrates consisted of glass coated with bare transparent conductive oxides (TCOs) or coated with a TCO and an electron or hole selective contact material. The substrates were subsequently cleaned in acetone, 2% mucasol (detergent), deionized water and isopropanol for 15 minutes each. After each step, the samples were dried with nitrogen and thereafter

treated with ozone (generated by UV light) for 20 minutes in order to activate the surface. The TCOs were SnO_2: In (indium doped tin oxide, ITO), SnO_2: F (fluorine doped tin oxide, FTO), MO_3 (molybdenum oxide, MO), In_2O_3: H (hydrogen doped indium oxide, IOH). The used electron selective contact materials were TiO_2 (titanium oxide, sputtered), np-TiO_2 (film of TiO_2 nanoparticles spin coated from a suspension), np-SnO_2 (film of SnO_2 nanoparticles spin coated from a suspension), np-ZnO:Al (aluminium doped zinc oxide nanoparticles spin coated from a suspension), PCBM (Phenyl-C_{60}-butyric acid methyl ester), C_{60} (Buckminster-fullerene) [179], BCP (Bathocuproine) and indene C_{60}-mono adduct ($IC_{60}MA$). The used hole-selective contact materials were PEDOT: PSS (poly (3, 4-ethylenedioxythiophene)polystyrene sulfonate) and PTAA (poly (triaryl amine)).

The substrates (size 2.5x2.5 cm^2) with ITO contacts (Lumtec) had the following specification: LTG001 plane ITO glass with a resistivity of about 15 Ω/sq and LT-G001 PT, patterned ITO with a resistivity of about 15 Ω/sq. The substrates (size 5x5 cm^2, thickness 2.2 mm) with FTO contacts (Solaronix) had the following specification: co022-7/LI, resistivity of 7Ω/sq. The substrates were cut into pieces of 2.5x2.5 cm^2. The substrates coated with MO_3 were provided from PVcomB (size: 10x10 cm^2). The Mo substrates were cut into pieces of 2.35×2.35 cm^2, which was suitable for spin coating (with another spin coater). IOH was prepared by sputtering (TU Berlin) with the following sputter specification: A600V7 from Leybold Optics, pulsed DC, from a ceramic target of 0.6 kW with a power ratings (P/A) of about 0.8 W/cm^2. The oxygen pressure during sputtering was maintained at about 3×10^{-4} Pa. The obtained layers of IOH (thickness about 200 nm) were annealed in vacuum at 200°C for 1 hour.

Nanoparticles of TiO_2 were prepared as reported elsewhere [180]. 0.25 ml of anhydrous $TiCl_4$ (99.9 %, Sigma-Aldrich) was added drop-wise while stirring in a vial containing 1 ml of anhydrous ethanol (Sigma-Aldrich) and 5 ml of anhydrous benzyl alcohol (99.8 %, Sigma-Aldrich). The solution was stirred for 9 h at a temperature of 80 °C. Thereafter, the solution was cooled down to room temperature before being mixed in diethyl ether at a volume ratio of 1:9 in order to form precipitates of TiO_2 nanoparticles. 10 ml of the precipitate was centrifuged at 6000 rpm for 5 min, washed with acetone and then re-dispersed in 20 ml of anhydrous ethanol. Lastly, 5 µl of Titanium diisopropoxide bis (acetylacetonate) (Tiacac) was directly added for each 20 ml of the dispersion to form TiO_2 nanoparticles. TiO_2 nanoparticles were spin coated twice over ITO glass substrate at 1000 rpm for 40 seconds in ambient air. For each subsequent spin coating, the sample was thermally annealed at 150 °C for 30 min, before repeating the procedure for a double final film thickness [34]. Nanoparticles of SnO_2 were prepared by dissolving 4 mg of $SnCl_2.2H_2O$ (> 99.995% Sigma-Aldrich) in 1 ml of anhydrous ethanol (sigma-Aldrich). The precursor solution was stirred at room temperature for 30 minutes

and thereafter spin-coated on a pre-cleaned ITO substrate at 2000 rpm for 40 s and then annealed for 1 hour at 180°C as reported by Ke et al. [181].

A $PC_{60}BM$ solution was prepared by dissolving phenyl-C_{60}-butyric acid methyl ester ($PC_{60}BM$, 99.5% Solenne BV) into anhydrous chlorobenzene at a concentration of 10 mg/ml and stirred in a glovebox overnight at 60° C. The solution was spin coated on a ITO substrate at 2000 rpm for 30 s in a nitrogen filled glovebox [34].Indene C_{60}- mono Adduct ($AC_{60}MA$, >> 99 %, Lumtec) was dissolved in anhydrous chlorobenzene at a concentration of 10 mg/ml, stirred overnight at 60° C and spin coated at 2000 rpm, 30 s in a nitrogen filled glovebox. C_{60} was thermally evaporated at a pressure of 1×10^{-6} mbar with crucible temperature maintained at 385° C at an evaporation rate of 0.2 Å yielding a film which is 35 nm thick. Bathocuproine (BCP), which acts as an exciton blocking layer [139], was deposited using thermal evaporation as well as using solution spin coating method. For the case of thermally evaporated BCP, the base pressure and deposition rate were 1×10^{-6} mbar and 1.0 Å/min. For BCP deposited from a solution, 0.5 mg of BCP was dissolved in 1 ml of anhydrous ethanol at room temperature while stirring. The solution was then spin coated onto a substrate in a nitrogen filled glovebox at 4000 rpm for 60 s [182].

Commercially purchased PEDOT:PSS (Clevious AI 4083, Heraus) was spin coated on UV-ozone treated ITO glass substrate at 3000 rpm for 60 sec and thereafter annealed at 135°C for 20 minutes [183]. PTAA was dissolved in toluene at 15 mg/ml solution. 13.6 µl Li-bis(trifluoromethanesulfonyl)imide (Li-TFSI) , 28.3 mg/ml of acetronile and 3.4 µl of 4-tert-butylpyridine (TBT) were added to the solution and spin coated at 3000 rpm for 30 s [184].

Perovskites such as $CH_3NH_3PbX_3$ (X = I, Cl, Br or mixed halides) can be prepared by reaction of an organic halide precursor salt (for example, CH_3NH_3I) with an in-organic halide precursor salt (for example, PbI_2). Layers of $CH_3NH_3PbI_3$ were prepared by different techniques: the solution process technique [185], the two step sequential deposition [186] , two step inter-diffusion method [187] and the vapour assisted deposition [188].The solution based process by single step preparation is the most commonly and widely used due to its simplicity and short processing time. For the case of $CH_3NH_3PbI_3$, one mole of CH_3NH_3I (159 mg) and one mole of PbI_2 (461 mg) were dissolved in 700 µl of dimethylformamide (DMF) and 71 µl dimethyl sulfoxide (DMSO). The solution was dissolved overnight at 60° C in a nitrogen filled glovebox. To prepare $CH_3NH_3PbI_3$ films, the solution was spin coated onto a substrate (2.5x 2.5 cm^2).

A summary of different preparation routes used for the deposition of perovskite on different substrates were as shown in figure 4.1. For example, in the temperature dependent measurement of $CH_3NH_3PbI_3$ by modulated surface photovoltage, the perovskite precursor solution was deposited on a Mo substrate, annealed and thereafter coated with a thin layer of poly methyl methacrylate (PMMA) as a capping layer on the surface of the perovskite films

(process 2). On the other hand, for transport/diffusion length measurements after Goodman, perovskite films were deposited on electron selective contacts (*ETM*) such as SnO_2 and TiO_2 while PEDOT/PSS and PTAA were used for hole-selective contacts (*HTM*). The TCOs used for this deposition were ITO (textured or plane) and IOH (Process 3). For studying the role of interfaces on the evolution of defects during light soaking by SPV, perovskite was deposited on either *ETM* or *HTM* with or without a capping layer (Process 3). Perovskite was also deposited on ITO, FTO and Mo substrates and the properties were studied and compared (Process 1). Electronic properties of a solar cell (without ohmic contacts) were studied by SPV and results were compared with the device performance (process 4).

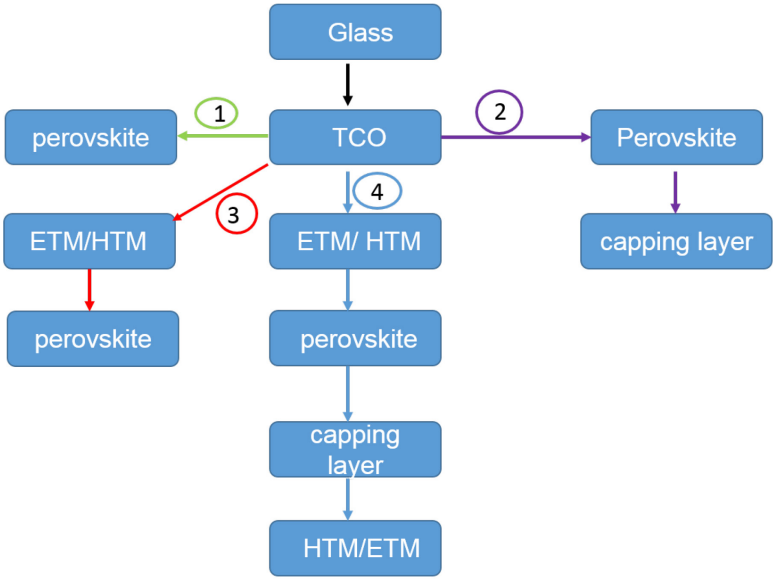

Figure 4.1: Perovskite preparation routes used in this work.

4.1.2. Single step preparation of hybrid organic-inorganic lead halide perovskites

Figure 4.2 shows a summary of a scheme illustrating some preparation routes of the active perovskite layer. The precursor salts used in the synthesis of hybrid organic-inorganic lead halide perovskites were: methyl ammonium iodide, CH_3NH_3I (MAI, Dyenamo); lead iodide, (PbI_2, 99.99 %, TCI), methyl ammonium bromide, CH_3NH_3Br (MABr, Dyenamo); lead bromide ($PbBr_2$, Alfa Aesar); formamidinium iodide, (FAI) and cesium bromide (CsBr). Different types of salts were used for different perovskite compositions. For example, in the preparation of pure methyl ammonium lead iodide, $CH_3NH_3PbI_3$, the films were prepared according to the modified procedure as reported by Jeon et al. [185]. The precursor solutions of $CH_3NH_3PbI_3$ were prepared by dissolving 1 M MAI and 1M PbI_2 in γ-butyrolactone (GBL, ≥ 99 %, Sigma Aldrich) and dimethyl sulfoxide (DMSO, Sigma-Aldrich) at a volume ratio of 7:3. The precursor

solutions were stirred at 60°C for 12 h in a nitrogen filled glovebox. Before perovskite deposition, the temperature of the atmosphere in the glovebox was kept constant at around 28 C. Three consecutive steps of spin coating at 1000 rpm for 10 s, 2000 rpm for 20 s and 5000 rpm for 10 s were used to spin precursor solutions on the sample substrates with a final dripping of 150 µl of toluene while spinning was continued (third or final stage). After that, the $CH_3NH_3PbI_3$ films were formed during annealing at 100°C for 10 min.

Similarly, $CH_3NH_3PbBr_3$ films were prepared from a precursor solution containing 1M MABr and 1M $PbBr_2$ dissolved in DMSO and DMF at a volume ratio of 1:4. Before spin coating, the solution was placed on a hot plate at a temperature of 60°C and stirred overnight in a nitrogen filled glovebox. Perovskite precursor solutions were spin coated on pre-cleaned ITO substrates at 4000 rpm, acceleration of 5 m s^{-2} for 30 s [55]. During the spin coating process, 100 µl of chlorobenzene (Sigma Aldrich) was dripped on the spinning sample 10 s prior to the end of the spinning program. Similarly, the spin coated film was left in the glovebox ground for 3-5 minutes before annealing at 100°C for 10 min [136] in the glovebox.

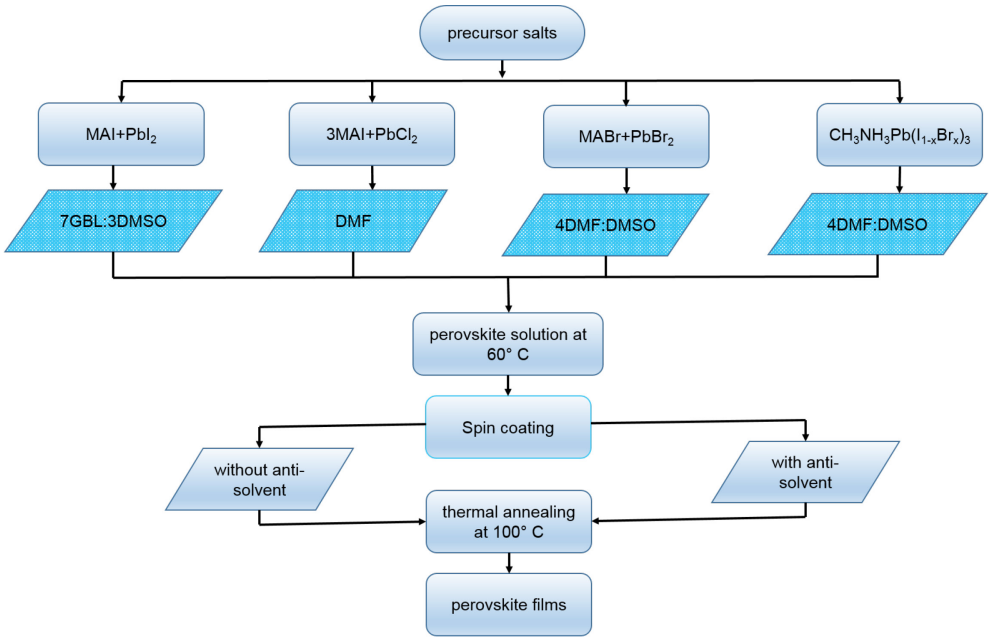

Figure 4.2: Parameter variation for single step preparation of perovskite

To prepare mixed perovskites based on iodide and chloride, precursors of $PbCl_2$ and CH_3NH_3I with a molar ratio of 1:3, respectively [189] were spin coated using a two-step spin coating process at 2000 rpm for 10 s followed by 3000 rpm for 30 s onto the substrates and the perovskite film was formed during annealing at 100°C for 60 min directly after the spin coating. Finally, $CH_3NH_3Pb(I_{1-x}Br_x)_3$ solutions were prepared by stoichiometric mixing of synthesized solutions of $CH_3NH_3PbI_3$ and $CH_3NH_3PbBr_3$ at 60° C for 60 min as reported by Noh et al. [19]. The solutions of $CH_3NH_3Pb(I_{1-x}Br_x)_3$ were then spin coated on pre-cleaned ITO

substrates at 4000 rpm, acceleration of 5 m s^{-2} for 30 s. 10 s prior to the end of the spinning program, 100 µl of chlorobenzene (Sigma Aldrich) was dripped on the spinning sample. The spin coated sample was annealed at 100° C for 10 min.

Spin coating is a rapid solution based process for depositing thin films on substrates. The process involves the preparation of the solution with the desired concentration of the precursor salt(s), applying a quantity of the solution to a substrate and then spinning the substrate. As the solution spreads, it dries and leaves a film. Deposition parameters consist of choice of the substrate, deposition temperature, solvent, and concentration of the hybrid in the solvent and speed of spin [190]. Spin coating enables formation of highly oriented perovskite films on a substrate while solvent evaporates off (see figure 4.3).

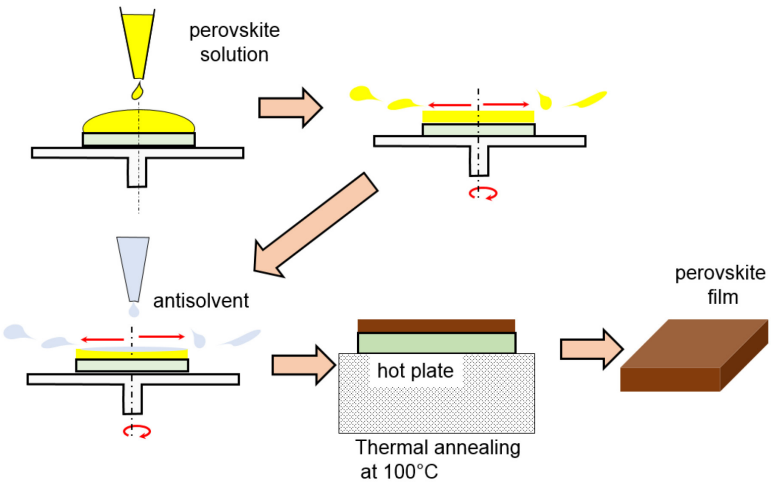

Figure 4.3: Scheme of spin coating and annealing with anti-solvent dripping for single step preparation of perovskites.

In this thesis different spin coating parameters were used to spin coat hybrid organic-inorganic metal halide perovskite. Layers of $CH_3NH_3PbI_3$, based on PbI_2 and CH_3NH_3I, three consecutive spin coating steps of 1000 rpm for 10 s, 2000 rpm for 20 s and 5000 rpm for 10 s were used to spin precursor solutions on the substrate with 150 µl of toluene dripped while spinning in the third stage. Toluene was used as anti-solvent to aid in the formation of a uniform, dense and homogeneous perovskite film thus controlling the morphology of the film. In this sense, the toluene is used as a capping layer on top of a perovskite film since it does not dissolve the perovskite material and miscible in DMF, DMSO and GBL which are solvents commonly used in perovskite preparation [185]. During the spin coating process, the solvent evaporates and self-orientation of the films occurs and induces the formation of a crystalline perovskite layer due to ionic interaction between metal cations and halide anions. On the other hand, mixed perovskite based on iodide and chloride, (precursors of $PbCl_2$ and CH_3NH_3I),

were spin coated using a two-step spin coating process at 2000 rpm for 10 s followed by 3000 rpm for 30 s. In this process, no anti-solvent was used.

Thermal annealing at 100°C for different times has been applied in various preparation conditions of perovskite films in order to reach high solar energy conversion efficiencies [9, 34, 191] . In this thesis, $CH_3NH_3PbI_3$, based on PbI_2 and CH_3NH_3I was annealed at 100°C for 10 min, $CH_3NH_3PbI_3$, based on $PbCl_2$ and CH_3NH_3I was annealed at 100°C for 60 minutes, triple cation of $FA_{0.85}$ $MA_{0.15}$ $Cs_{0.17}Pb$ $(I_{0.83}$ $Br_{0.17})_3$ was annealed at 100°C for 20 min and $CH_3NH_3PbBr_3$ annealed at 100°C for 10 min.

For some investigations, perovskite layers have been stabilized with a capping layer (PMMA (Sigma Aldrich): poly methyl methacrylate). The capping layer can have different functions, for example, it can avoid the penetration of moisture into the perovskite during the transfer of samples out from the glovebox and it can slow down the decomposition of the perovskite during temperature-dependent measurements. For this purpose, PMMA was dissolved in butyleacetate (Sigma Aldrich) and heated to 60°C in a nitrogen filled glovebox. The stability of the perovskite layer was optimized by varing the concentration of PMMA in the butylacetate (0, 20, 40, 60, 80, and 100 mg/ml). After annealing of the perovskite, the hot solution of PMMA and butylacetate was spin coated (2000 rpm for 60 s) onto the perovskite layer as described by Yu et al. [192].

4.2 Morphology and architecture of hybrid organic-inorganic lead halide perovskites

4.2.1. Morphology of TCOs (transparent conductive oxide)

Figure 4.4 shows SEM (secondary electron microscopy) micrographs of bare FTO (a), ITO (b), IOH (c) and MO (d), substrates. The SEM images of FTO shows different facets of crystallites on the surface. The facets are relatively large indicating that the FTO surface is quite rough. FTO is known to be very rough with reported root mean square roughness of the order of 70 – 90 nm [193]. The high roughness is beneficial for the enhancement of light trapping in the solar cell. On the other hand, the Mo substrate poses elongated structures of facets which are uniform and compact suggesting that the surface is also rough. However, the surface roughness is smaller compared to FTO due to smaller grain sizes. The morphology of ITO shows small grains in comparison to the FTO and MO substrates indicating the formation of a smoother surface with smaller grains. IOH has the smoothest surface with very small grains. In general, the roughness of the substrate can have a strong impact on the homogeneity of perovskite films.

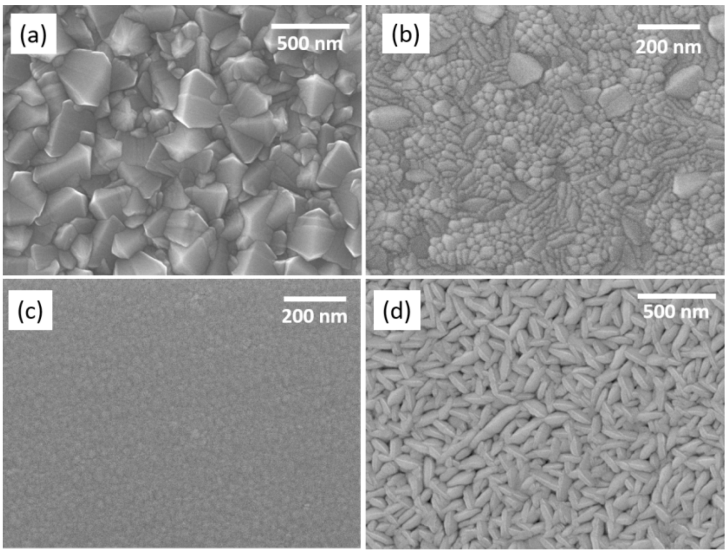

Figure 4.4: SEM micrographs of used substrates (FTO (a), ITO (b), IOH (c) and MO (d)

4.2.2. Morphology of hybrid organic-inorganic lead halide perovskites deposited on transparent conductive oxides and electron and hole selective contact materials

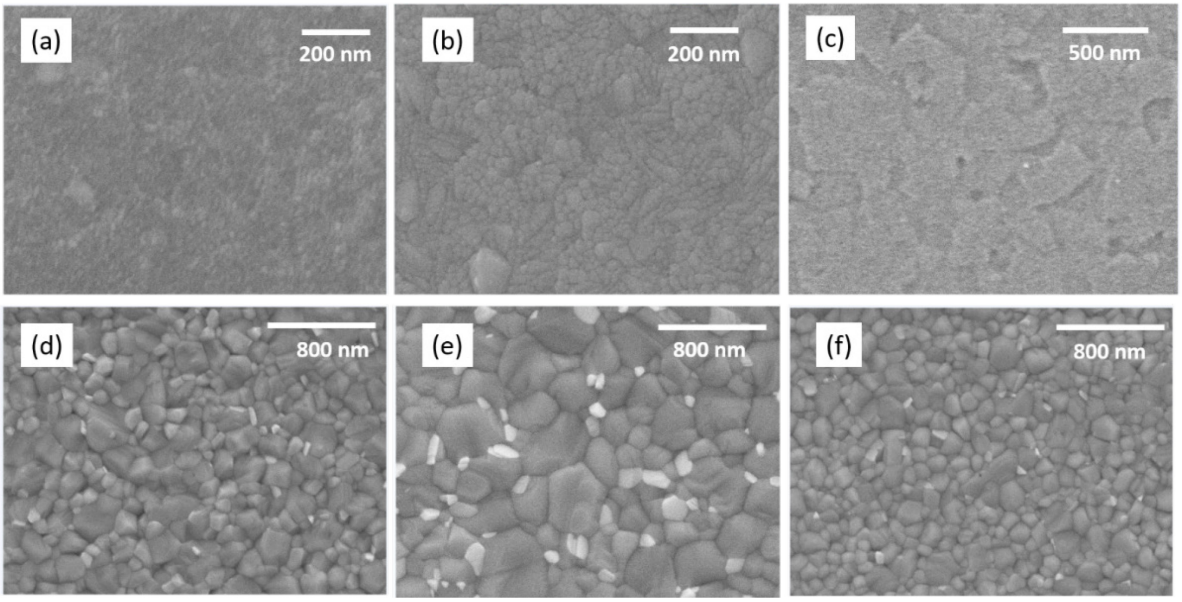

Figure 4.5: SEM images of np-TiO_2 (a) sputtered np-TiO_2 (b), np-SnO_2 (c), np-TiO_2/ perovskite (d), sputtered np-TiO_2/, perovskite (e) and np-SnO_2 /perovskite (f).

Figure 4.5 the SEM micrographs of np-TiO_2 (a), sputtered TiO_2 (b), np-SnO_2 (c), np-TiO_2/ perovskite (d), sputtered np-TiO_2/ perovskite (e) and np-SnO_2 /perovskite (f). The SEM top views show that the sputtered TiO_2 has a larger grain size than spin coated np-TiO_2 and spin coated np-SnO_2 suggesting that perovskite films with larger grains can be formed on sputtered

np-TiO_2 in comparison to spin coated films. SEM images of annealed perovskite active layers on np-TiO_2 and np-SnO_2 did not show major differences in grain sizes. The average grain size of perovskite absorber layers was about 240 nm on spin coated substrates and about 470 nm on sputtered substrates. Perovskite absorber layers with larger grain sizes are desirable for longer diffusion length due to the reduced recombination rates at grain boundaries [102].

Figure 4.6 presents SEM micrographs of annealed perovskite active material on various fullerenes; ICMA (a), PCBM (b), C_{60} (c) and a cross-section image of perovskite on C_{60}. The SEM micrograph of annealed perovskite active layers on various fullerenes did not show a pronounced difference in the grain size which was of the order of 240 nm. Figure 4.6 (d) illustrates a SEM cross section image of annealed perovskite active material deposited on C_{60}. The cross section image revealed remarkable appearance of horizontal grain boundaries in the perovskite layer with an average thickness of about 350 nm.

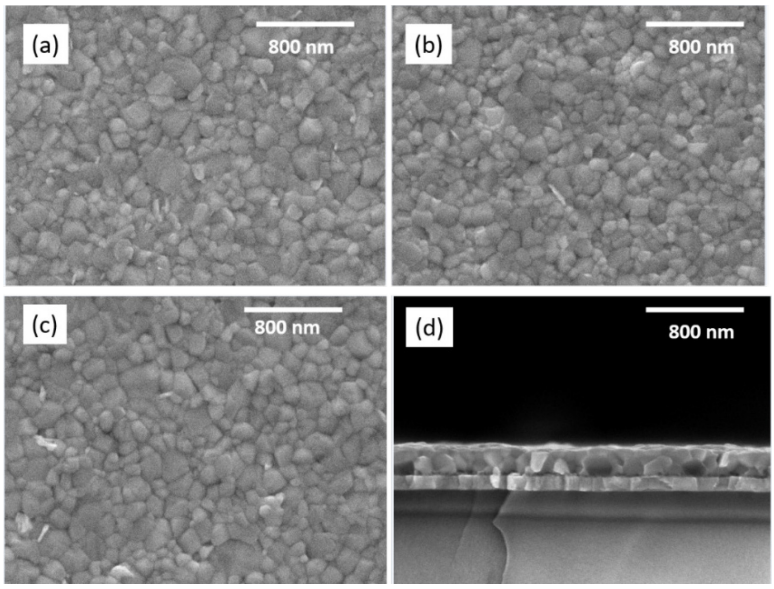

Figure 4.6: SEM images of perovskite on fullerenes, ICMA (a) PCBM (b) C_{60} (c) and cross-section image of perovskite on C_{60} (d)

Figure 4.7 shows SEM micrographs of PEDOT: PSS (a), PTAA (b), annealed perovskite on (c) PEDOT: PSS and (d) PTAA respectively. The PEDOT: PSS layer on ITO substrate showed a blurred morphology whereas for PTAA, the morphology of ITO was conserved at the surface. This suggests that the layer of PEDOT: PSS on the ITO substrate was a significantly thicker in comparison to the PTAA layer. The size of perovskite grains on both PEDOT: PSS (c) and on PTAA (d) was of about 125 nm.

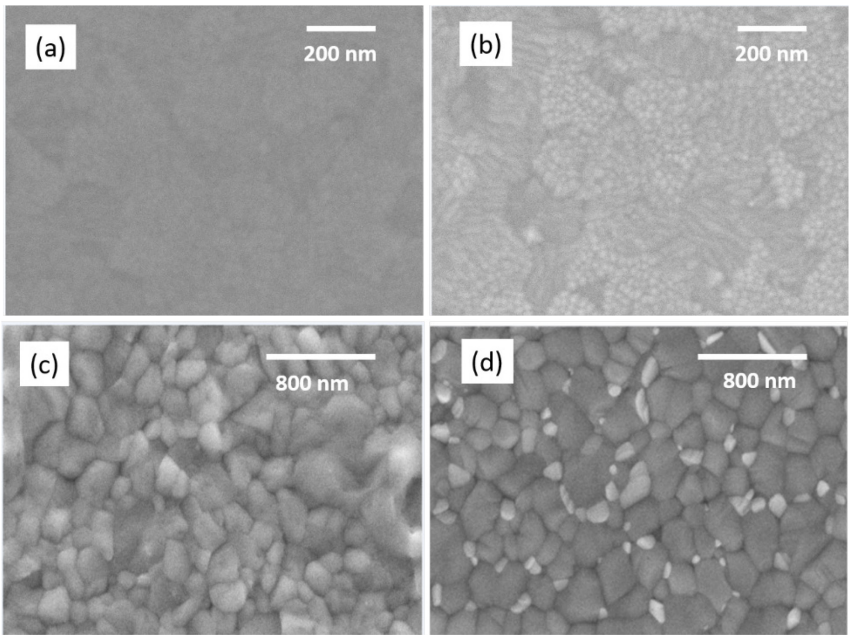

Figure 4.7: SEM images of PEDOT: PSS (a), PTAA (b), annealed perovskite on (c) PEDOT: PSS (d) and PTAA, respectively.

4.2.3. Layer structures used for characterization

Figure 4.8 shows different layer structures of perovskite films used for the characterization. For the investigation of material properties at room temperature, hybrid organic-inorganic lead halide perovskite layers were deposited onto glass substrates coated with a TCO (usually ITO) layer (figure 4.8 a).

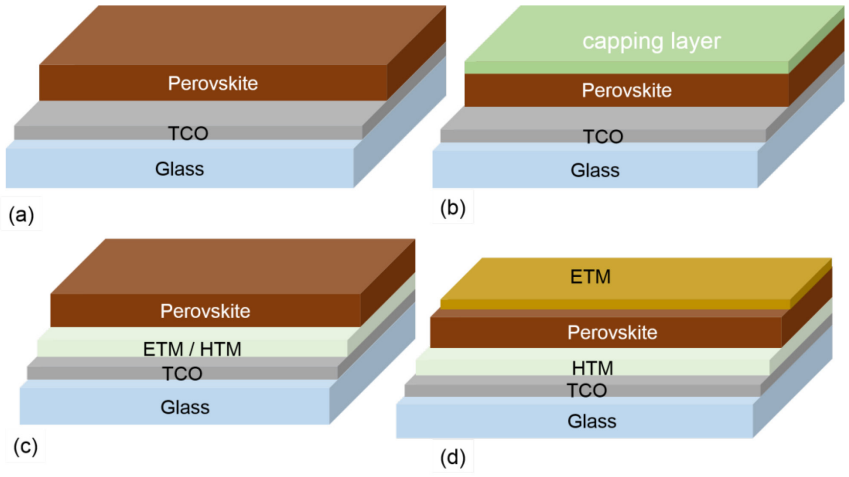

Figure 4.8: Layer structures of investigated perovskite samples. Glass / TCO / perovskite (a) Glass / TCO / perovskite / capping layer (b); Glass / TCO / HTM or ETM / perovskite (c) and Glass / TCO / HTM / Perovskite / ETM (d).

For the investigation of the temperature dependence of the band gap of $CH_3NH_3PbI_3$ by SPV, the layer architecture glass/Mo/perovskite/PMMA (figure 4.8 b) was used. In order to investigate the influence of charge-selective contacts on charge separation, different hole- or electron-selective contacts were deposited onto the TCO layer before the perovskite layer was deposited (glass/ITO/*HTM*/perovskite or glass/ITO/*ETM*/perovskite, (figure 4.8 c). For some SPV measurements, the perovskite layer was sandwiched between an *HTM* (PEDOT: PSS or PTAA) bottom and an *ETM* (double layers of PCBM/BCP, C_{60}/BCP and IPH/C_{60}) top layers (glass/ITO/*HTM*/Perovskite/ *ETM* (see figure 4.8 d)).

4.3 Phase analysis by grazing incidence X-ray diffraction (GIXRD)

Grazing incidence x-ray diffraction (GIXRD) is a powerful and non-destructive technique for characterizing films with thicknesses of a few atomic layers [194]. The method was originally developed in 1979 by Marra et al. for studying ordered interfaces and surface phenomena for atomic layers of Al and GaAs [195]. In this technique, the detector was placed horizontal to the plane parallel to the surface of the film in order to record diffraction patterns from lattice planes that are perpendicular to the film surface. At an angle of incidence near or above the critical angle, total internal reflection occurs, giving rise to x-rays with highly enhanced intensities and a small penetration depth [196].

Figure 4.9 shows a schematic diagram of GIXRD geometry in which the incident x-ray beam of the wave vector $\mathbf{k_i}$ impinges on the film surface at a glancing angle of $\alpha_i < 1°$. The diffracted wave vector $\mathbf{k_s}$ was detected at an angle α_s with respect to the sample surface and at an angle of 2θ with respect to the transmitted beam. The investigated sample rotates around its surface in a so-called ω scan (see figure 4.9).

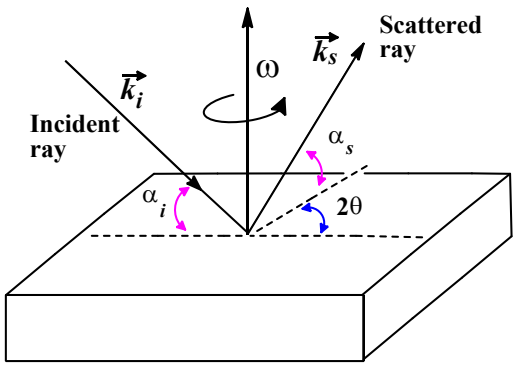

Figure 4.9: Schematic diagram of GIXRD geometry

The GIXRD beam irradiates the sample surface in a grazing incidence with α_i close to the critical angle for total internal reflection to occur. The incident x-ray beam gives rise to a diffracted beam from the lattice planes that are perpendicular to the surface. The diffracted beam encloses an angle of 2θ which was fixed with respect to the detector and leaves the

surface at a grazing angle α_s [194].The grazing incidence x-ray diffraction pattern was measured by Bruker AXS (D8 Advance) for thin films analysis with a Cu Kα radiation source of wavelength 0.154065 nm. The instrument was equipped with a 9-fold sample changer. For the investigation of the perovskite thin films, the angle 2θ was scanned from 10° to 70° using a step size of 0.02° and acquisition time of 4 s deg^{-1}.

The measured GIXRD patterns enabled to gain information about the phases in the layers by comparing with the reference data. The international center for diffraction data base was installed at the PC in the lab xlabd8bb, room PT006 of Helmholtz Zentrum Berlin. Bruker diffraction EVA software version 4.1.1 in combination with free powder diffraction data base (COD 7218931) was used for phase analysis and structure determination.

Figure 4.10 shows GIXRD patterns of $CH_3NH_3PbI_3$ films for as-prepared, 7 and 43 days of storage in air (a, b & c respectively). For the as-prepared sample (figure 4.10 (a)), the GIXRD pattern showed diffraction peaks at 14.2°, 20.01°, 23.48°, 24.5°,28.5°, 31.89° and 43.5° corresponding to the (110), (112),(211), (202), (220),(310) and (314) diffraction planes of the tetragonal phase of $CH_3NH_3PbI_3$ [12]. After 1 week of storage in air (figure 4.10 (b)), $CH_3NH_3PbI_3$ undergoes a phase change with the appearance of a new phase with an additional peak at 12.67°. This new phase characterized by the appearance of the peak at 12.67° corresponds to PbI_2 [197] which did occur due to decomposition of $CH_3NH_3PbI_3$ to its constituent precursor compounds. After continuous storage in air for 43 days (figure 4.10 (c)), the intensity of the PbI_2 peak at 12.67° continued to increase whereas the intensity of the $CH_3NH_3PbI_3$ peak at 14.2 ° decreased strongly. Therefore, the $CH_3NH_3PbI_3$ continued to degrade to PbI_2, due to evaporation of CH_3NH_3I from the surface of the sample [192].

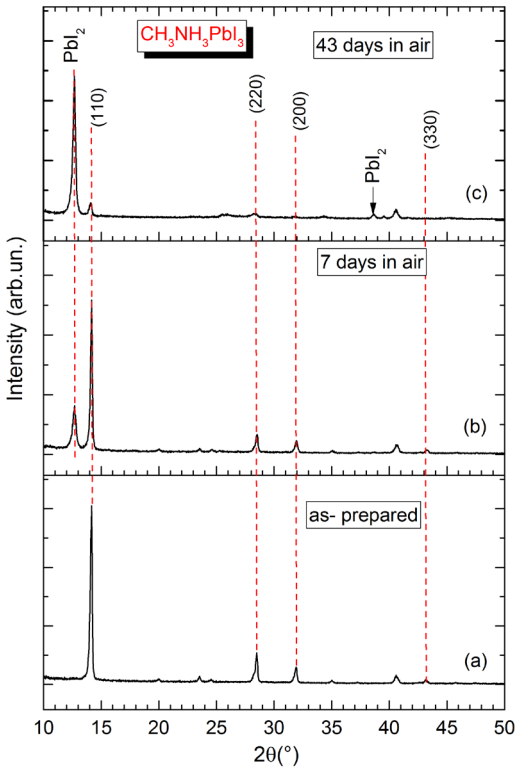

Figure 4.10: Grazing incidence x-ray diffractogram (GIXRD) of as-prepared $CH_3NH_3PbI_3$ (a), and of $CH_3NH_3PbI_3$ after storage in air for 7 days (b) and after 43 days (c)

The GIXRD patterns of a $CH_3NH_3PbI_3$ and $CH_3NH_3PbBr_3$ thin films are compared in figure 4.11. A systematic shift in GIXRD peak patterns towards higher 2θ degrees was observed for $CH_3NH_3PbBr_3$ in comparison to $CH_3NH_3PbI_3$ thin films. This was attributed to volume contraction of the unit cell of $CH_3NH_3PbBr_3$ layers [41] due to smaller ionic radius of bromide ion which favors the formation of a cubic structure. The structural differences of $CH_3NH_3PbI_3$ and $CH_3NH_3PbBr_3$ thin films seem to originate from the ionic radius of iodine and bromide anion which according to reported values in literature are 2.2 and 1.96 respectively [19].This implies that smaller bromine atoms decreases the lattice spacing for $CH_3NH_3PbBr_3$ perovskite layer as compared to larger iodine atom in $CH_3NH_3PbI_3$ film.

For the case of $CH_3NH_3PbI_3$ layers deposited on an ITO substrate, two dominant peaks at 14.12° and 28.45° were observed. These peaks corresponded to (110) and (220) diffraction planes of tetragonal lattice [12].The GIXRD analysis for $CH_3NH_3PbBr_3$ thin films reveals characteristic diffraction peaks of cubic perovskite phase with a preferential orientation at 14.98° corresponding to (100) plane of cubic perovskite [198]. Other peaks appear at 21.92°, 30.18°, 33.84°, 37.18°, 43.204° and 45.97° corresponding to (110), (200), (210) (112) (220) and (300) planes respectively of crystalline cubic phase of perovskite [41]. Lattice constant was calculated to be 5.93 Å and 6.32 Å for $CH_3NH_3PbBr_3$ and $CH_3NH_3PbI_3$, respectively, which agrees well with previously reported value [12].

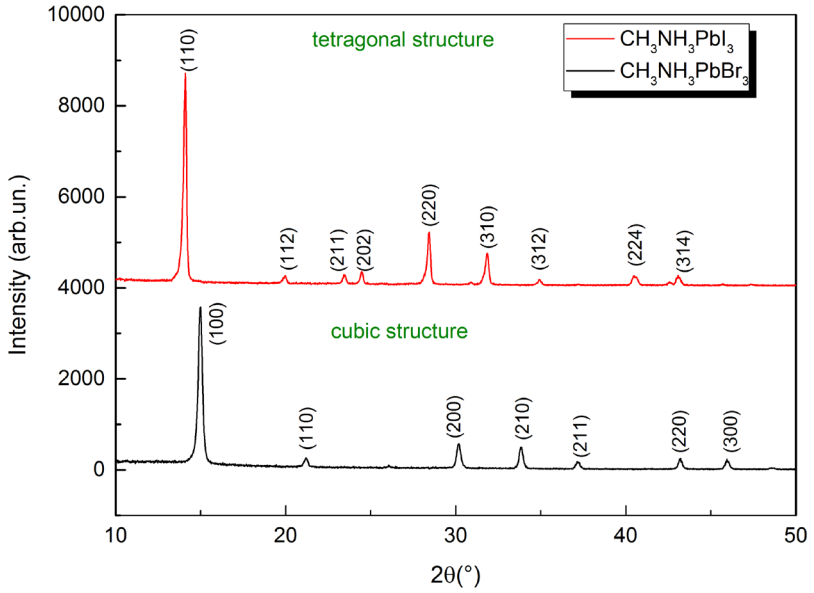

Figure 4.11: GIXRD of as- prepared $CH_3NH_3PbI_3$ and $CH_3NH_3PbBr_3$ (red and black lines, respectively).

4.4 Ultraviolet-visible light spectroscopy (UV-vis)

Ultraviolet-visible (UV-vis) light spectroscopy is an optical method allowing for the measurement of reflected and transmitted light. The intensity of the absorbed light is obtained from the difference between the intensity of the incident light and of the intensities of the transmitted and reflected light. For thin planar samples, the intensities of the reflected and transmitted light can be simply measured by placing the detector in line with the reflected or transmitted light beams (figure 4.12 (a)). However, perovskite layers are deposited onto substrates containing additional layers, for example, for contacts and/or passivation. Furthermore, perovskite layers consist of grains with different size so that the layer thickness is not constant and light is partially scattered (figure 4.12 (b)). Therefore, perovskite layers are not ideal for optical measurements and sophisticated optical models are needed for the detailed analysis of transmission and reflectance spectra. This is out of the scope of this thesis. Here, the measurement of the band gap and of the Urbach tails is desired for a large variety of perovskite samples.

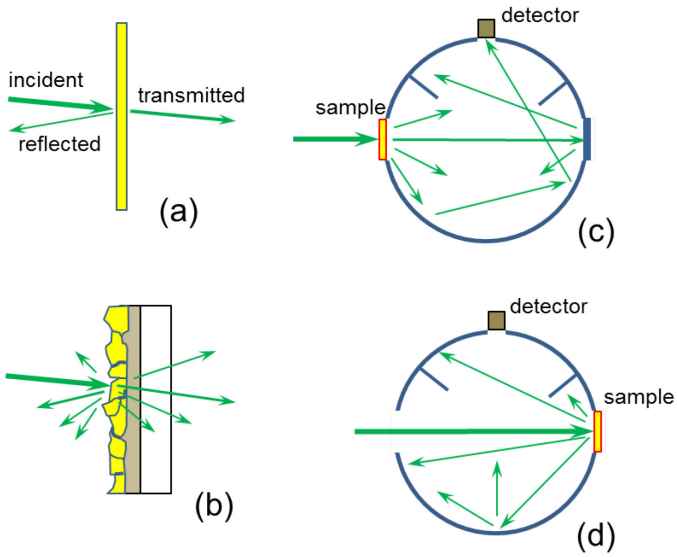

Figure 4.12: Schematic of transmission and reflection of an ideal sample (a) and of a sample with a layered structure and with partial light scattering (b); arrangement of the measurement of transmitted (c) and reflected light with an Ulbricht or integrating sphere.

The completely transmitted and reflected light can be measured with an Ulbricht or integrating sphere. In an ideal integrating sphere, light is not absorbed but scattered into all directions with the same probability (white Lambertian surface). For this purpose, the internal surface of an integrating sphere is coated with, for example, barium sulfate ($BaSO_4$) or Teflon (PTFE). For the measurement of the complete intensity of transmitted light, the sample is placed at the entrance of the integrating sphere (figure 4.12 (c)). A baffle shields the detector from direct incoming light so that only light which is scattered in the integrating sphere can be detected. Therefore, the detector is sensitive to the complete intensity of transmitted light. For the measurement of the complete reflected light, the sample is placed at the edge of the opposite surface of the integrating sphere (figure 4.12 (d)). Again, a baffle shields the detector from directly reflected light. UV-vis measurements are calibrated by measuring the spectra of the incident light without placing a sample into the positions for the measurement of transmission and reflection spectra.

As an example, figure 4.13 shows reflectance, transmittance and absorbance spectra of $CH_3NH_3PbBr_3$. The absorbance increases steeply in the range of the band gap. The values of the band gap and of the Urbach tails were obtained from the absorbance spectra by applying the analysis explained before.

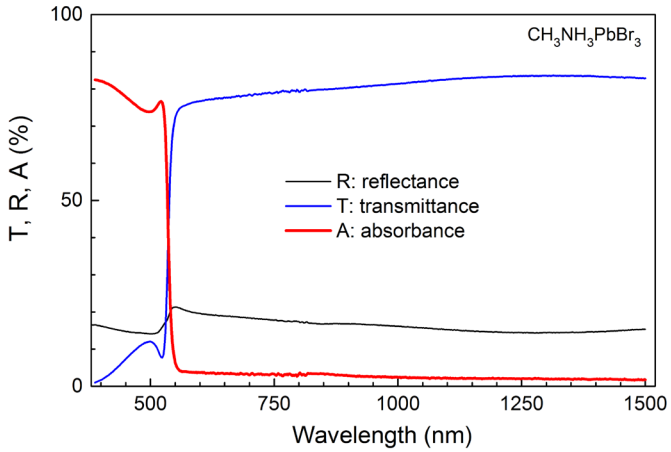

Figure 4.13: Spectra of the reflectance, transmittance and absorbance (black, blue and red lines, respectively) of a $CH_3NH_3PbBr_3$ layer deposited on glass.

Absorbance spectra of hybrid organic-inorganic perovskite layers were measured with a commercial UV-vis spectrometer (Perkin Elmer Lambda 1050 spectrophotometer) in the spectral range from 175 nm to 3300 nm. In this spectrometer, a grating monochromator is used. The spectrophotometer uses two detectors inside the integrating sphere. One detector is a photomultiplier (PMT) in combination with InGaAs as a cathode covering the spectral range between 860 to 1800 nm and wide band covering between 860-2500 nm. The second detector is a PbS detector which is sensitive in the wavelength range between 1800/ 2500-3300 nm.

4.5 Photothermal deflection spectroscopy (PDS)

Photothermal deflection spectroscopy (PDS) is an optical technique allowing for the characterization of the absorption spectrum near the band gap of a thin semiconductor layer [199]. PDS is based on the absorption of a periodically modulated light beam (pump beam, figure 4.16). The light from the pump beam (see figure 4.16) is absorbed by the sample and transformed into heat [199]. This causes a small modulated increase of the temperature at the surface of the sample. The sample surface is in contact with a liquid. Therefore, the liquid is periodically heated by the heated surface of the sample and a modulated temperature gradient arises in the liquid. The liquid is a material with a strong temperature dependence of the refractive index (for example, tetradecafluorohexane, C_6F_{14}). The resulting change of the gradient of the refractive index is detected by the deflection of a probe beam (usually a He-Ne laser) which is aligned in parallel to the sample surface and perpendicular to the pump beam [200]. The deflection of the probe beam is detected with a position-sensitive photodiode.

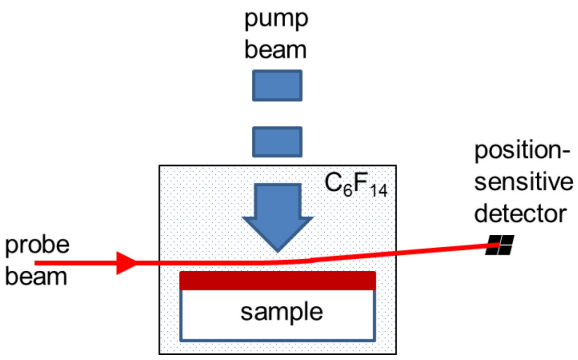

Figure 4.16: Working principle of PDS.

By probing the gradient of the refractive index with a probe beam, its deflection can be related to the optical absorption of the sample whereas the degree of deflection corresponds to the optical absorption of the sample [201]. In order to increase the sensitivity, the sample is immersed in a transparent liquid characterized by a relatively strong change of the refractive index with small changes of the temperature so that tiny increments of the temperature can be detected (of 10^{-4} K) [202]. However, one has to keep in mind that the liquid should not interact with the sample. This is the case for C_6F_{14} in contact with perovskites.

A typical PDS set-up consists, as shown in figure 4.17, of a halogen lamp with a monochromator and an optical chopper in order to create the wavelength-dependent modulated pump beam, a He-Ne laser (probe beam) and a position-sensitive detector (quadrant photodiode).

The deflection is detected with a lock-in amplifier (lock-in A) as the difference between the photocurrents of the quadrants of the photodiode. An oscilloscope is used for the alignment of the quadrant detector. The cuvette with the C_6F_{14} and the sample is placed on a x-y-z-Φ stage for alignment of the position and the orientation angle in relation to the He-Ne laser, respectively. The position of the quadrant detector is aligned with a x-y stage. A part of the pump beam is directed via a beam splitter onto a calibrated tandem detector for measuring the intensity of the pump beam. The tandem detector consist, for example, of a silicon photodiode and a lead sulfide (PbS) photoresistor (or a GaInAs photodiode). The intensity of the pump beam is measured with a second lock-in amplifier (lock-in B).

PDS measurements were performed on selected samples ($CH_3NH_3PbBr_3$) in the range between 0.7 and 2.7 eV. For the measurements, a home-made set-up was used.

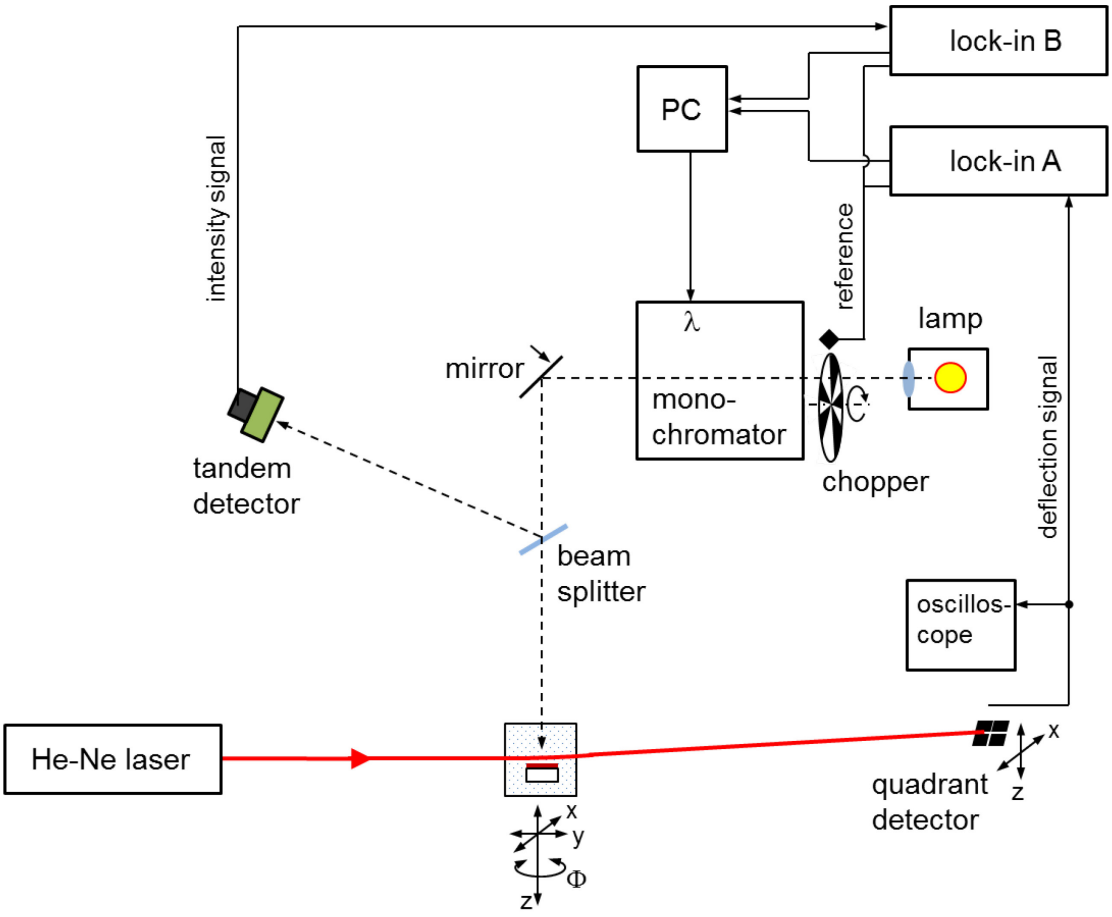

Figure 4.17: Set-up for PDS measurements.

4.6 Experiments with modulated surface photovoltage (SPV) spectroscopy

Two setups were used for modulated SPV spectroscopy. In both setups, illumination was performed with a halogen lamp (100 W) and quartz prism monochromator (SPM2). The modulation frequency was usually 8 Hz. The reference electrodes consisted of a quartz cylinder partially coated with conductive SnO_2:F (band gap about 3.6 eV). The reference electrode was gently pressed onto the sample surface with a cardanic spring whereas a thin mica sheet (thickness 20 – 30 µm) was placed between the sample surface and the reference electrode in order to form the measurement capacitor [203]. The capacitance of the measurement capacitor was between 10 and 20 pF. The sample electrode was grounded. The reference electrode was connected with the high-impedance buffer.

For temperature-dependent measurements, a home-made high vacuum chamber (figure 4.18, base pressure below 2 x 10^{-5} mbar) was used. The high-impedance buffer (R_m = 50 GΩ) was placed outside the chamber (BNC feedthrough). A Pt100 placed directly underneath the sample was used for temperature measurement. A temperature controller with a current source was applied for regulating the temperature. For routine SPV measurements at very low

noise levels, a second home-made chamber (figure 4.19), in which a battery powered high-impedance buffer (R_m = 150 GΩ) was placed inside the chamber, was used. The noise levels were about 1 – 2 µV and 0.2 – 0.3 µV for the temperature-dependent and routine SPV measurements, respectively, for standard measurement conditions (integrating time constant 300 and 500 ms, respectively; 10 averages). For routine SPV measurements, the chamber was pumped to vacuum with a rotary pump (base pressure below 10^{-2} mbar) and filled with nitrogen gas to a pressure of about 700 mbar. During SPV measurements with the routine chamber, the pump was switched off. EG&G 5210 and EG&G 7260 lock-in amplifiers were used in the set-ups for temperature-dependent and routine measurements, respectively.

The transfer of the sample from the glovebox to the chamber took about 2 min during which the sample was exposed to air. Usually, SPV Spectra were measured in a wide range (0.4 – 4.0 eV, step 50 meV) and in a narrow (around the band gap, step 10 meV) range. A widths of the entrance and exit slits of the monochromators were set to 0.3 mm (spectral resolution better than 10 meV).

For the measurement of the diffusion length after Goodman, the modulated SPV signals were kept constant by keeping constant the output signal of the lock-in amplifier (lock-in A in figure 4.19) with a power supply and an integrated feedback unit (Electronic Manufaktur Mahlsdorf).

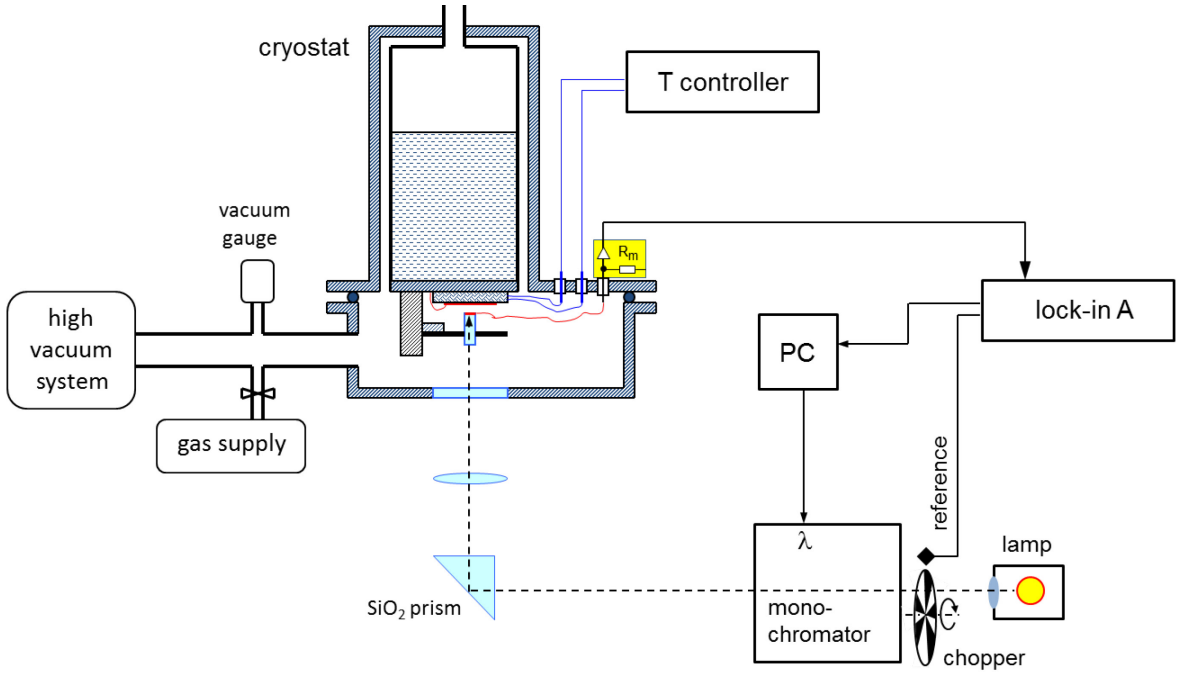

Figure 4.18: Scheme of the experimental set-up for temperature-dependent modulated SPV spectroscopy.

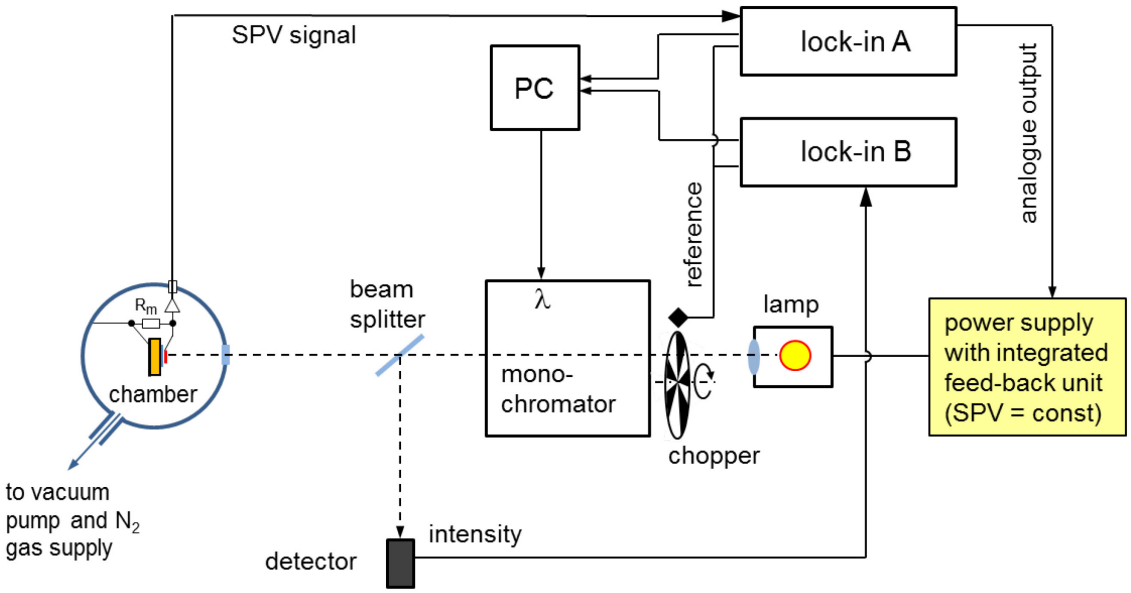

Figure 4.19: Scheme of the experimental set-up for modulated SPV spectroscopy (routine measurements and measurement of the diffusion length after Goodman).

The intensity was measured by coupling out a part of the light with a beam splitter and using a photodetector (Elektronik Manufaktur, Mahlsdorf) and a second lock-in amplifier (lock-in B in figure 4.19). The shape of the spectral response function of the detector was calibrated separately with a pyrodetector.

For quasi in-situ monitoring of the degradation of perovskite films, a LED lamp (see figure 4.20) was used. For this purpose the parabolic mirror, which is used for focusing the light from the monochromator onto the electrode, was moved out from the optical path and replaced by a LED (separate red / green / blue, about 1 mW).

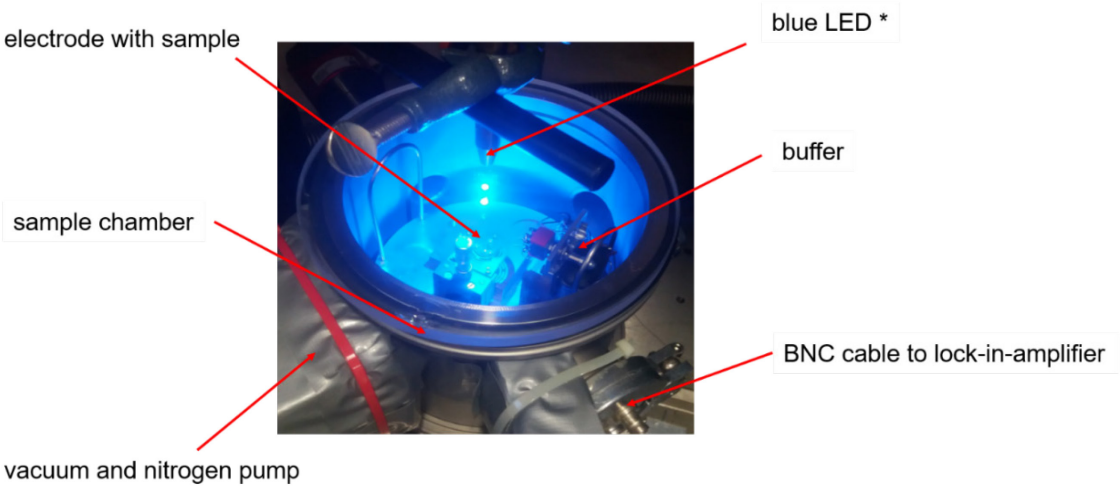

Figure 4.20: Chamber of SPV measurements during light soaking with a blue LED.

CHAPTER 5

Properties of $CH_3NH_3Pb(I, Br)_3$ and their dependence on aging and light soaking

The investigation of electronic properties of $CH_3NH_3Pb(I, Br)_3$ and their dependence on aging and light soaking is important for better understanding of the stability of solar cells based on related materials. Some of the results presented in this chapter were published in [34, 204].Modulated surface photovoltage spectroscopy (SPV) allows for ex-situ and quasi in-situ characterization of the band gap, tail states, direction of charge separation and diffusion length. In this thesis, material properties related to degradation, stoichiometry, the band gap (E_g), exponential tail states (E_t) and diffusion length (L) were investigated. By varying different halide compositions, the band gap of perovskite was tuned. Similarly, the measurement of the diffusion length after Goodman [32], can provide useful information in accordance to the lifetime of minority charge carriers in solar cells. In the study of interfaces, different electron selective as well as hole selective contacts were varied and their influence on perovskite properties were determined. It has been found, for example, that the Tauc gap and energy of exponential tail states sensitively depend on the substrate and on soaking in nitrogen atmosphere and that light soaking has strong influence on the direction of modulated charge separation. In this chapter, the effect of stoichiometry and light soaking on transport length, exponential defects and E_g of $CH_3NH_3Pb(I_{1-X})Br_X)_3$ will be investigated using SPV.

5.1. Mixed lead halide perovskite: $CH_3NH_3Pb(I_{1-X}Br_X)_3$

5.1.1. Equivalence between surface photovoltage (SPV) and photothermal deflection spectroscopy (PDS) for $CH_3NH_3PbBr_3$

Disorder in semiconductor leads to defect states below the band gap that participate in the absorption process (optical) or charge separation (SPV). For example, disorder results in a decrease of SPV signals towards lower photon energies [205]. For the optical absorption process, the absorption coefficient can be expressed using the Urbach relation [63]:

$$\alpha = \alpha_o \, exp\left(\frac{h\nu - E_0}{E_u}\right) \qquad 5.1$$

where $E_0 = 2.3$ eV for $CH_3NH_3PbBr_3$, $\alpha_o = 2.9 \times 10^4$ cm^{-1} and E_u is the Urbach energy which is equal to the reverse of the absorption edge slope.

$$\frac{1}{E_u} = \frac{\Delta(ln\alpha)}{\Delta h\nu} \qquad 5.2$$

In order to investigate defect states below the band gap by SPV, the amplitudes (R) of the SPV signals were measured in the energy range between 2.0 to 2.5 eV, step width of 0.01 eV with an average of 20 data points and then plotted on a logarithmic scale. The energy of the exponential tail states (E_t) measured by SPV was obtained by fitting the amplitude of the SPV signals to the leading edge with an expression of the form:

$$R/\Phi_{ph} = A\ exp\left(\frac{h\nu - E_g}{E_t}\right) \qquad 5.3$$

where A is a proportionality constant and E_g is the approximate band gap. As a remark, a low value of E_t indicates a high level of electronic order in the perovskite absorber material with low sub band gap states near the band edge.

Figure 5.1 shows the absorption spectrum of a $CH_3NH_3PbBr_3$ layer measured by the photothermal deflection spectroscopy (PDS) and the SPV spectrum of the same sample on a logarithmic scale. The absorption coefficient (α) exhibited a sharp shoulder near the band gap at about 2.3 eV. Below the shoulder i.e. between 2.2 to 2.3 eV, α follows an exponential behavior. E_u amounted to 18 meV, which was consistent with the value of 18.9 meV, as reported by Wenger et al. [206].

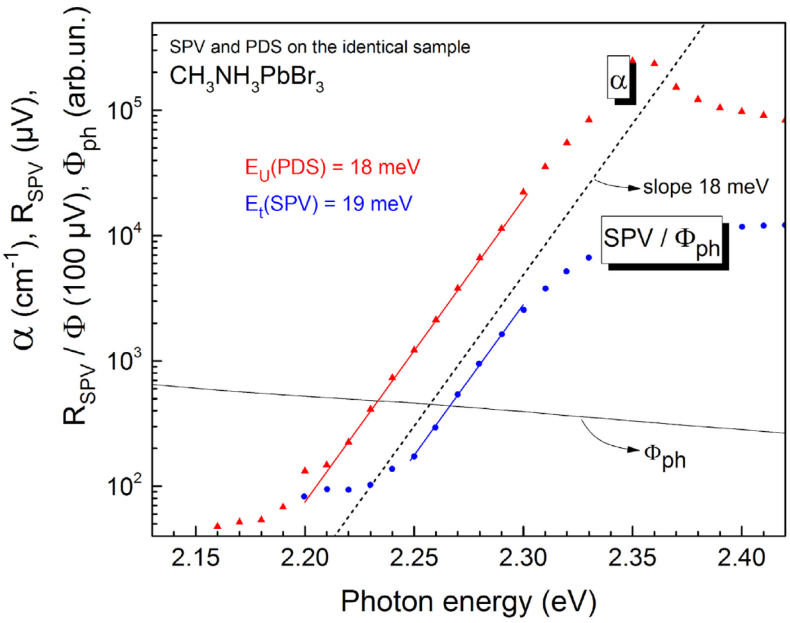

Figure 5.1: Absorption spectrum measured by PDS (red triangles) and spectrum of the PV amplitude on a logarithmic scale (blue circles) for the same $CH_3NH_3PbBr_3$ perovskite film. The solid lines are the slope of the Urbach tails (E_u) (red line) and exponential tail energy (E_t) (blue line). The dotted line marks the slope of 18 meV. The black line represents the photon flux Φ_{ph}.

Below photon energies of 2.2 eV, α was characterized by sub band gap absorption which revealed the population of sub band gap states. The sub-band gap states may be due to a contribution of the substrate which was limited by the defects present in the glass substrate

[13]. E_t was obtained to be 19 meV for $CH_3NH_3PbBr_3$ perovskite films. The value of E_t by SPV was comparable with E_u with a slight deviation of about 1 meV. The discrepancy was brought about by the difference in the sensitivity of each measurement method. As a remark, both methods are sensitive to different regions of measurements. For instance, SPV is sensitive to the measurement region where charge separation takes place whereas PDS probes the whole region of the sample volume where absorption takes place. In addition, SPV is not a pure optical method and detects separation of charge carriers excited from localized to delocalized states. To characterize the material in more detail, the band gap in terms of Tauc gap was determined using both PDS and SPV.

The Tauc model [178] was used to determine the band gap energy as shown in figure 5.2. For PDS, the Tauc gap was obtained by plotting the squared product of the absorption spectrum and photon energy i.e. $(\alpha.hv)^2$against the photon energy (see figure 5.2 red triangle and a line). The exponent 2 was used because $CH_3NH_3PbBr_3$ has a direct band gap [207] [208]. The band gap (E_g) of $CH_3NH_3PbBr_3$ measured by PDS was about 2.295 eV. The Tauc gap obtained was in excellent agreement with that reported in literature [207].

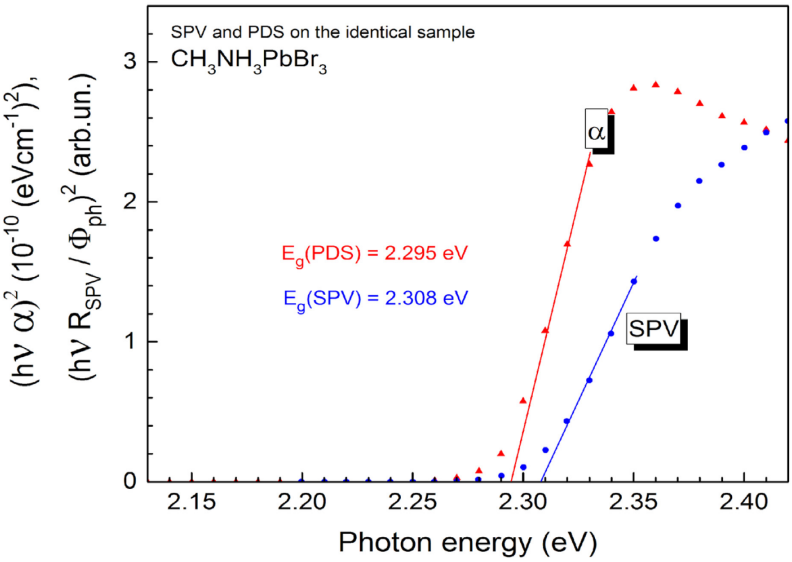

Figure 5.2: Tauc plots of the absorption spectrum measured by PDS (red triangles) and of the SPV spectrum (amplitudes, blue circles) of the same $CH_3NH_3PbBr_3$ sample. The red and blue lines mark the linear fits to the band gaps.

For comparison with optical absorption from PDS, SPV was used to determine the band gap in the spectral range near the direct band gap. The analysis of the Tauc plot of the amplitude signal was done with the presumption that the amplitude signal was proportional to the absorption coefficient, that the penetration depth was much shorter than the charge carrier diffusion length and that the modulated SPV signals could be treated as small signals [209]. The E_g measured by SPV (figure 5.2 with blue circles and a line) was same as for PDS. The

band gap measured by SPV was found to be 2.308 eV which was in good agreement with values obtained in literature [55, 18]. The E_g obtained by SPV and that obtained from PDS differed by about 13 meV. The discrepancy is due to uncertainty in the analysis, i.e. it cannot be completely assumed that the SPV signals are proportional to α, what is not surprising. As a remark, modulated SPV signals are not necessarily directly proportional to the photon flux as assumed for the small signal case, since the generation of SPV signals may involve many processes taking part during charge separation. However, the signals are practically proportional to the photon flux in the low signal regime when the dominant mechanism of charge separation and relaxation do not change [205,175]. In addition, there is an interface of perovskite with the liquid which might also influence the electronic states near the band gap.

5.1.2. Vegard's law in $CH_3NH_3Pb(I_{1-x}Br_x)_3$

Vegard's law maintains at constant temperature a linear relationship between the crystal lattice parameter (constant) and the composition of the constituent elements. Such a linear relation exists in an ensemble of a random mixture of substitutional solid solutions. An accurate knowledge of the dependence of the lattice parameter on the concentration of the constituent elements allows for the determination of the composition of an alloy by simple measurement of the lattice constant.

Figure 5.3 shows the GIXRD diffraction patterns for $CH_3NH_3Pb(I_{1-X}Br_X)_3$ perovskite films between $0 \leq x \leq 1$ in the 2θ range of 13 – 15.5°.The $CH_3NH_3PbI_3$ at x = 0 had a peak located at 14.12° which corresponded to (110) planes for the tetragonal 14/mcm phase [12]. The tetragonal phase of $CH_3NH_3PbI_3$ was maintained until x = 0.13 and then changed to cubic phase at about x = 0.2 [19]. A systematic shift in the GIXRD peak patterns towards higher 2θ angles was observed with increasing bromide composition x. The systematic shift towards higher 2θ angles was due to the gradual substitution of the larger iodine atoms with the smaller bromine atoms which led to the decrease of the lattice spacing. For example, 2θ was equal to 14.12, 14.24, 14.32, 14.41, 14.46, 14.54, 14.65, 14.80 and 14.91° at x = 0, 0.13, 0.2, 0.29, 0.38, 0.47, 0.58, 0.84 and 1 respectively. Since the iodine atom is larger than the bromine atom, the lattice undergoes contraction when I^- anion was substituted for Br^- anion. Therefore, according to Bragg's law $n\lambda = 2d\sin\theta$; a corresponding shift of diffraction peaks to higher 2θ angles was observed with increasing x.

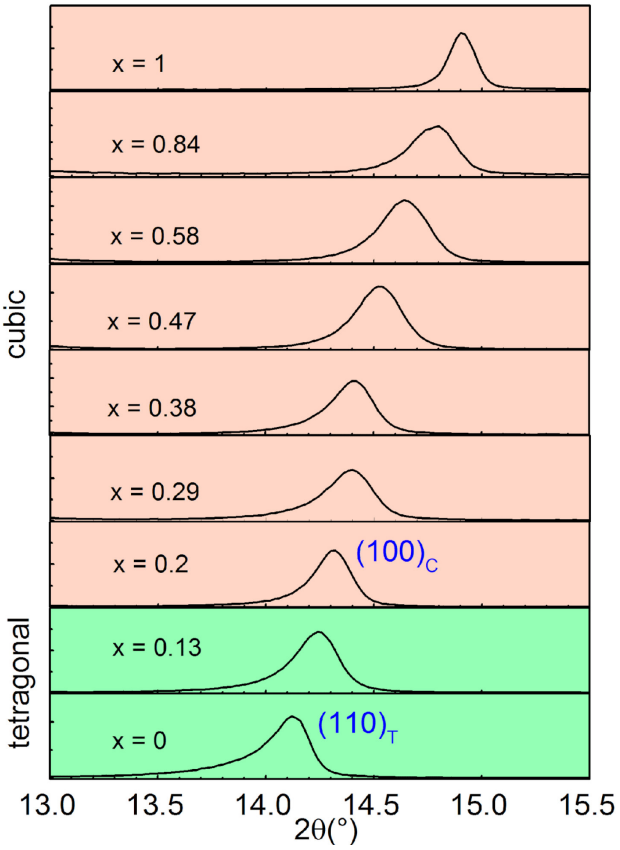

Figure 5.3: GIXRD patterns of the $CH_3NH_3Pb(I_{1-x}Br_x)_3$ films at x = 0, 0.13, 0.2, 0.29, 0.38, 0.47, 0.58, 0.84, and 1; magnified in the region of the tetragonal $(110)_T$ and cubic $(100)_C$ peaks for 2θ between 13.0 to 15.5.

Under slight rotation of the PbX_6 octahedra along the (110) planes, while maintaining the corner sharing structure, changed the tetragonal phase to the cubic phase in the ideal $CH_3NH_3PbX_3$ perovskite structure. This implied that the tetragonal phase could be described by the pseudo-cubic lattice [19] as shown in figure 5.4. Figure 5.4 (a) shows the dependence of the lattice parameter as a function of bromide composition x for the pseudo-cubic $CH_3NH_3Pb(I_{1-X}\ Br_X)_3$ films. The values of lattice constant correlated well with x, and showed a linear relationship with x. The values were, 6.26, 6.245, 6.22, 6.195, 6.165, 6.137, 6.09, 6.04, 6.02, 5.99 and 5.94 at x = 0, 0.13, 0.2, 0.29, 0.38, 0.47, 0.58, 0.84 and 1 respectively. The values compared well with the findings of Noh et al. [19].

According to Vegard's law, the lattice parameter in the alloy varies linearly with composition under constant temperature and negligible electronic effects. Therefore, the linear variation indicated the formation of the cubic $CH_3NH_3Pb(I_{1-X}\ Br_X)_3$ compound in the complete range of $0 \leq x \leq 1$ by a simple solution mixing process. In addition, the lattice constant decreased with increasing x. This phenomenon occurred due to the substitution of the larger iodine atom with smaller bromine atom that decreases the lattice spacing. For comparison, the values of lattice constant from literature was shown [19]. The lack of significant deviations from

Vegard's law indicates the absence of significant phase segregation in the $CH_3NH_3Pb(I_{1-X}\ Br_X)_3$ films.

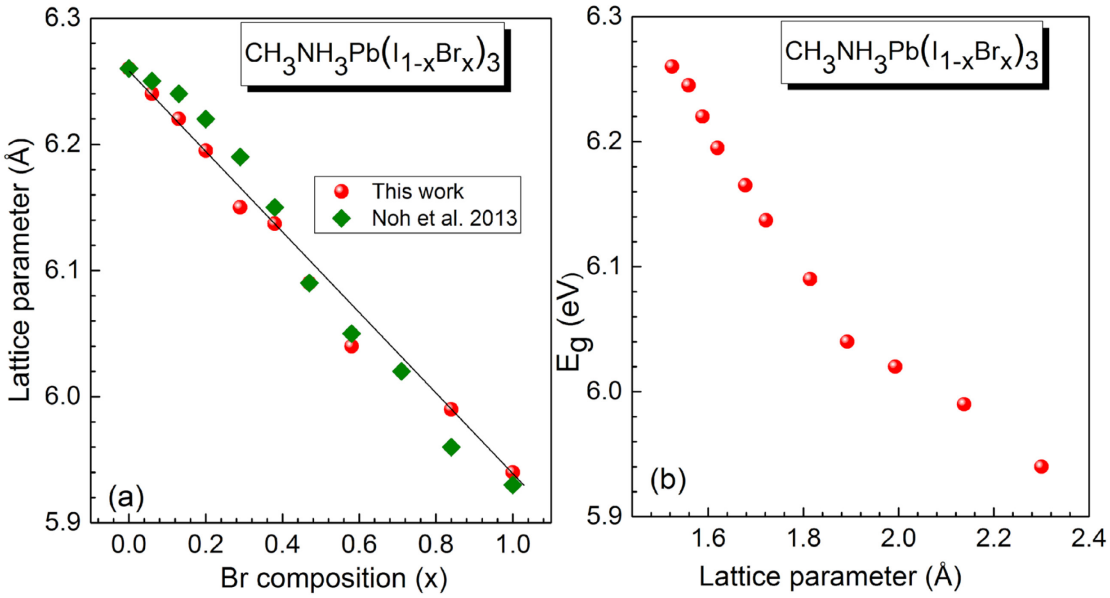

Figure 5.4: Dependence of the (a) lattice constant as a function of bromide composition x for samples used in this work and for values in the literature after Noh et al. [19]; (b) band gap on the lattice constant of pseudo-cubic $CH_3NH_3Pb(I_{1-X}\ Br_X)_3$ perovskite films.

Figure 5.4(b) shows the band gap as a function of lattice parameter for the pseudo-cubic $CH_3NH_3Pb(I_{1-X}\ Br_X)_3$ perovskite films. E_g was 1.52, 1.56, 1.59, 1.62, 1.68, 1.72, 1.81, 1.89, 1.99, 2.14, & 2.3 for lattice parameter of 6.26, 6.245, 6.22, 6.195, 6.165, 6.137, 6.09, 6.04, 6.02, 5.99 and 5.94 respectively. As observed, E_g increased with decreasing lattice parameter suggesting a lattice contraction due to increase in potential energy of the electrons in the orbitals of an atom. As the lattice parameter decreases, the interatomic distance reduces as well. This increases the binding force between valence electrons and the parent atom (i.e. the valence electrons become more bound to the parent atom). This means that more energy is required to make valence electrons move freely within the atom and become conduction electrons. A direct outcome of the decreasing lattice parameter is the increase in the energy gap.

5.1.3. Dependence of the band gap and of the exponential tail states on the stoichiometry of $CH_3NH_3Pb(I_{1-X}Br_X)_3$

For the approximate determination of the band gap, the so- called onset energy can be used. The onset energy (E_{on}) allows for the linear approximation of the SPV signals through the inflection point near the band gap to zero.

Figure 5.5 shows the SPV spectra of the $CH_3NH_3Pb(I_{1-X}\ Br_X)_3$ perovskite films with different halide compositions. For all samples, the in-phase signals were negative while the signals phase- shifted by 90° were positive. Negative values of in-phase signals implied that photo-generated electrons were preferentially separated towards the external surface while holes towards the bulk of the sample (i.e. like in a p-type semiconductor in depletion). The maximum of the in-phase signal was -0.86, -0.82, and -0.55 mV for x = 0, 0.58 and 1, respectively. This can imply, for example, that the band bending decreased with increasing bromide content. In contrast, the phase-shifted by 90° signals were 0.2, 0.3, and 0.35 mV, for x = 1, 0.58 and 0 respectively. This points to an increase of the influence of slow relaxation processes with increasing bromide content. Furthermore, in-phase and phase-shifted by 90° signals showed opposite signs which implied one dominating mechanism of charge separation in which electrons are preferentially separated towards the external surface. Mechanisms that lead to charge carrier separation with opposite signs may be due to charge separation across space charge regions and trapping of photo-induced charge carriers at interface states [28].

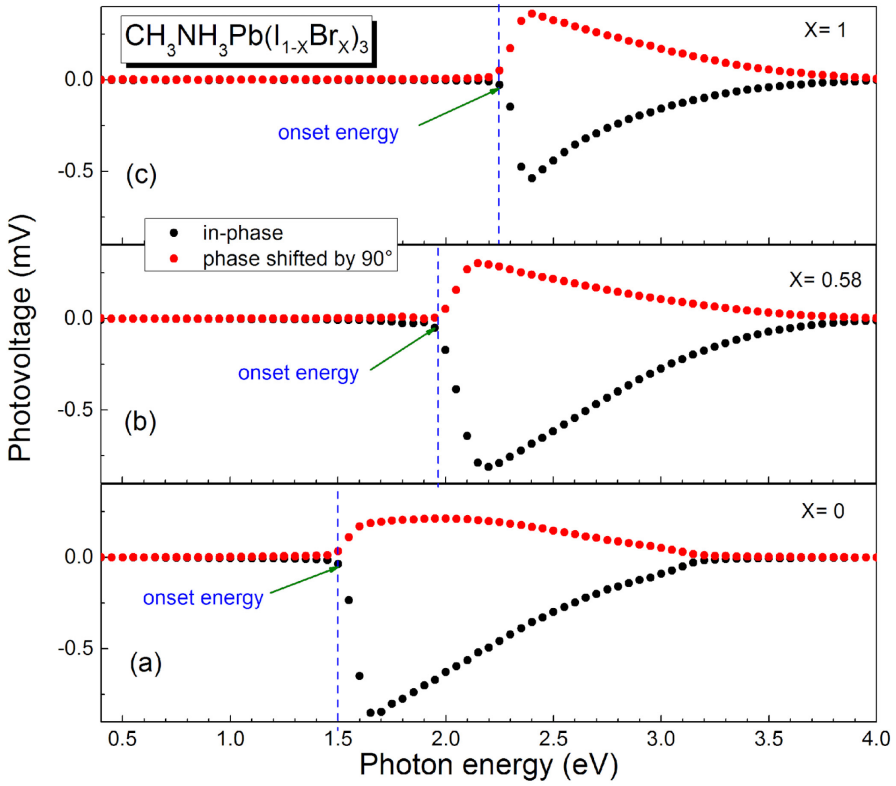

Figure 5.5: In-phase and phase-shifted by 90° SPV spectra (black and red circles, respectively) of $CH_3NH_3Pb(I_{1-X}\ Br_X)_3$ perovskite films for x = 1, 0.58 and 0 (a-c, respectively). The dashed lines mark the approximations to the onset energies.

The onset energy (E_{on}) of $CH_3NH_3Pb(I_{1-X}Br_X)_3$ perovskite films was tuned from 1.5 to 2.3 eV by varying different halide compositions. For pure $CH_3NH_3PbI_3$ in which x = 0, (figure 5.5

a), the onset energy was approximately 1.5 eV. This was consistent with both experimental and theoretical values reported in literature [28, 19] . When the bromide composition was varied to 58% of the initial amount i.e. x = 0.58 (figure 5.5 b), the onset energy shifted to approximately 1.92 eV. With pure bromide composition, i.e. $CH_3NH_3PbBr_3$ with x = 1) (figure 5.5 c), the approximate onset energy shifted further to about 2.30 eV which was also in agreement with reported values in the literature [210].

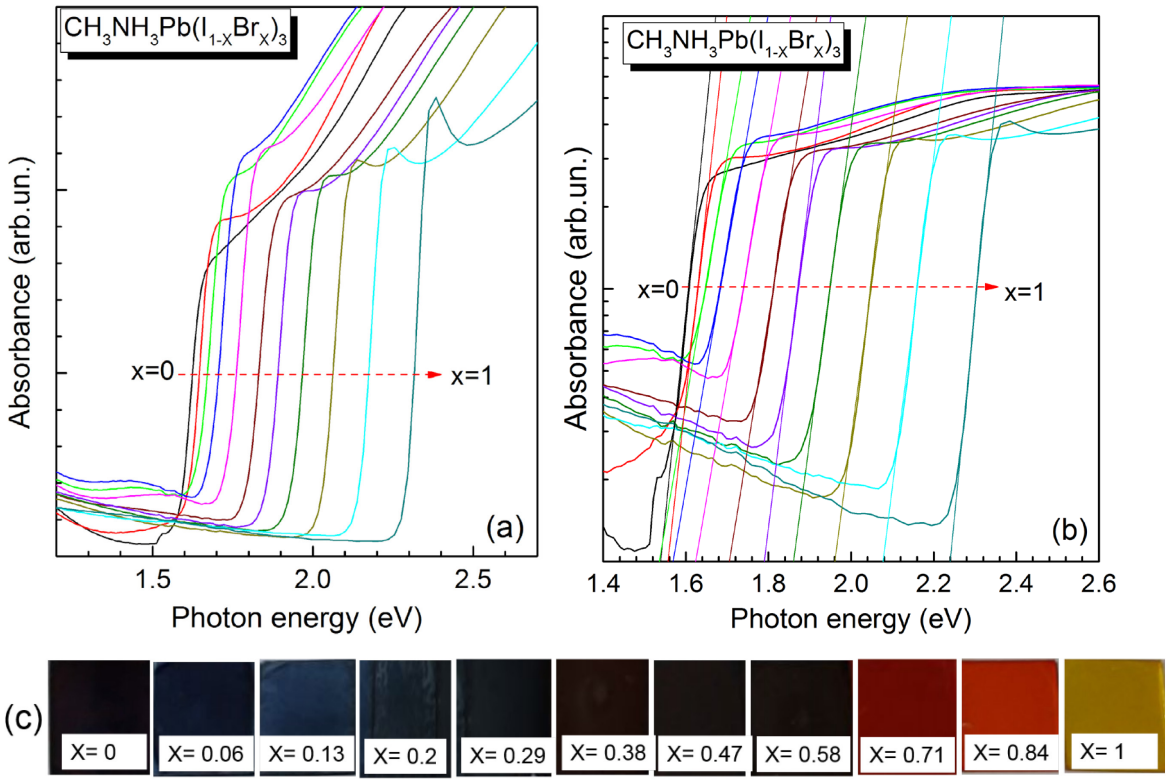

Figure 5.6: UV-Vis (a) absorption spectra on a linear scale, and (b) absorbance in logarithmic form for $CH_3NH_3Pb(I_{1-X}Br_X)_3$ films measured using an integrating sphere. For each spectrum in (b), the slope of the Urbach tail is shown. The photographs show, $CH_3NH_3Pb(I_{1-X}Br_X)_3$ films with different concentrations of bromide ions (c).

To check the variation of the optical properties of the perovskite absorber layers, UV-vis absorption spectra of $CH_3NH_3Pb(I_{1-X}Br_X)_3$ films were measured in the compositional range between $0 \leq x \leq 1$ (see figure 5.6 (a)). The onset of the absorbance spectra was tuned from an energy of 1.59 to 2.30 eV resulting in perovskite films of different colors. Figure 5.6 (a) shows a systematic shift of the absorbance spectra towards shorter wavelength with increasing bromide content i.e. the spectra blue shifted with increasing bromide content. The blue shift may be attributed to different spin- orbit interactions between lead-iodide and lead-bromide ions [19]. There was optical absorption for photon energies below the range influenced by the Urbach tails. This absorption may be ascribed to absorption of the perovskite or by free carrier

absorption in the ITO substrate. As a remark, the high background signals may also be influenced by scattering at the rough surface of the perovskite films which was observed to be higher for iodide rich perovskite films than for bromide rich films.

In order determine Urbach energy of $CH_3NH_3Pb(I_{1-X}Br_X)_3$ films; the absorbance in logarithmic form i.e. $log\left(\frac{2.303\,A}{d}\right)$ were plotted against photon energy as shown in figure 5.6 (b). A is the absorbance, and d is the film thickness. The spectra continuously blue shifted upon increasing x. All $CH_3NH_3Pb(I_{1-X}Br_X)_3$ films in this family showed strong absorption onsets. Moreover, all samples showed unusually sharp shoulder close to their corresponding onset energies. Below the shoulder, logarithmic form of absorbance for $CH_3NH_3Pb(I_{1-X}Br_X)_3$ films exhibited purely exponential trend. The slope of the exponential part gives the Urbach energy (E_u). E_u was obtained to be 28, 31, 48, 50, 50, 46, 35, 38, 38, 36 and 28 for x = 0, 0.06, 0.13, 0.20, 0.29, 0.38, 0.47, 0.58, 0.71, 0.84 and 1, respectively. The value of E_u was observed to be lower for pure tri-iodide and tri-bromide perovskite but higher for mixed perovskite. This observation was consistent with what was reported by Sadhanala et al. [211]. They observed E_u of about 90 meV for $CH_3NH_3Pb(I_{0.4}Br_{0.6})_3$ films with significant population of sub band gap states which was interpreted as the beginning of the formation of two species in perovskite films. The relatively high value of E_u for $CH_3NH_3Pb(I_{1-X}Br_X)_3$ films with $0 < x < 1$, might be attributed to the disordered lattice due to random distribution of iodide and bromide atoms in the lattice sites [212]. It is also postulated that the introduction of bromide ions into the mixed halide solution create more stress that induces more defect states hence the high disorder observed in the material [213]. In addition, increased disorder in the mixed halide perovskite tend to form localized states with a weak extended bonding. These localized states form sub-band gap states in bromide and relaxation of charge carrier processes in the perovskite films [214].

Figure 5.6 (c) shows the photographs of $CH_3NH_3Pb(I_{1-X}Br_X)_3$ films between $0 \leq x \leq 1$. By varying the composition of bromide content in the $CH_3NH_3Pb(I_{1-X}Br_X)_3$ films, the color was tuned from dark for $CH_3NH_3PbI_3$ at x = 0, red at x = 0.84 to yellow for $CH_3NH_3PbBr_3$ at x = 1. These arrays of colors may be desirable in the fabrication of colorful solar cells that can be used in rooftops, windows and walls [19].

Figure 5.7 (a) shows the variation of E_g as a function of bromide composition (x) in $CH_3NH_3Pb(I_{1-X}\,Br_X)_3$ perovskite films measured using SPV and UV-Vis spectroscopy. For both measurements, the values of E_g varied non-linearly with increasing Br composition x in the alloy. The E_g was estimated from Tauc plots. The values of E_g reported from literature are shown for comparison [19,33]. For example, the values of E_g obtained from SPV compared well with the E_g measured by optical methods after Noh et al. at x = 0, 0.06, 0.29, 0.38, 0.47, 0.58, 0.71, 0.84 and 1. However, E_g measured by SPV seemed to be underestimated at x = 0.13 and 0.2 in relation to E_g deduced from UV-vis after Noh et al. [19] and Jacobsson et al.

[33]. The values of E_g measured by UV-Vis spectroscopy in this work were a little bit over-estimated compared to the values obtained by Noh et al. but almost similar to the values obtained by Jacobsson et al. The over and under-estimation of E_g in the two measurements may be influenced by the formation of the perovskite and the interface with the substrate. In addition, SPV measurements are only sensitive to the sample region where charge separation takes place whereas UV-vis measurements probe the whole sample volume [215]. The non-linear increase of E_g with increasing Br content as measured using SPV was described with a quadratic equation 2.4 in chapter 2. List square fit of E_g reduced equation 2.4 into equation 5 .4 with a bowing parameter of 0.36 eV.

$$E_g = 1.5639 + 0.4\,x + 0.36\,x^2 \qquad 5.4$$

where $x = \frac{Br}{I+Br}$ 5.5

The bowing parameter is a measure of the degree of non-linear behavior in the crystal potential. The crystal potential in an alloy could be expressed as the sum of potential which was constant throughout the crystal and that which fluctuated with distance due to statistical variations of the alloy composition [216]. The bowing parameter of 0.36 eV in $CH_3NH_3Pb(I_{1-X}\ Br_X)_3$ perovskite films measured by SPV correlates well with the values of 0.33 and 0.29 eV obtained by Noh et al. [19] and Jacobsson et al. [33], respectively.

To characterize the mixed perovskite further in more detail, SPV measurements were performed on the samples to determine the electronic defect states close to the band edge of $CH_3NH_3Pb(I_{1-X}\ Br_X)_3$ absorber layers. The exponential tail states energy (E_t or E_u) near the band edge are a signature for disorder and may have a strong influence on electronic properties of the material. For example, E_t close to the band edge may contain information about charge separation from defects states whereas E_u measure the disorder in the Urbach tail.

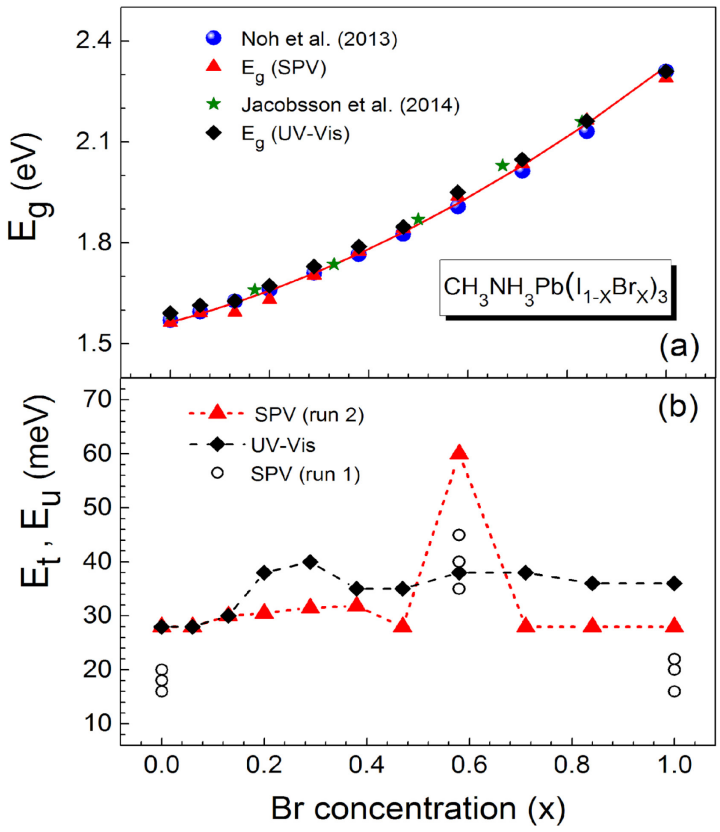

Figure 5.7: Dependence of the (a) band gap measured using SPV (red triangles), UV-Vis spectroscopy (black diamonds) in comparison to values from the literature [19], [33] (blue circles and olive stars, respectively) and (b) E_t, E_u (open circles in run 1, red triangles with dotted line in run 2 and black diamonds, respectively) on the stoichiometry of $CH_3NH_3Pb(I_{1-X}Br_X)_3$ films. Run 1 were measurements done previously in old glovebox whereas run 2 were measurements done in new hy-sprint perovskite baseline glovebox.

Figure 5.7 (b) shows the dependence of exponential tail states E_t and E_u on x. The values of E_t for $CH_3NH_3Pb(I_{1-X}\ Br_X)_3$ films were determined for measurements done in run 2; which was the glove box situated in new hy-sprint perovskite laboratory. The value of E_t was constant at 28 meV for x = 0 and 0.06 and thereafter increased to 30, 30.5, 31.5 and 31.8 meV for x = 0.13, 0.2, 0.29 and 0.38 respectively. E_t dropped to 28 meV for x = 0.47 meV before increasing strongly to 60 for x = 0.58. The values of E_t remained constant at 28 meV for x = 0.71, 0.84 and 1 respectively. The relatively low E_t in the films with higher iodide (i.e. x = 0, and 0.06) content and high bromide content (x = 0.71, 0.84 & 1) could be correlated with low disorder in those films. Similar trend was observed for E_u values of $CH_3NH_3Pb(I_{1-X}\ Br_X)_3$ films. E_u of 28 meV was obtained at x = 0 and 0.06 and increased to 30, 38, and 40 meV for x = 0.13 0.2 and 0.29, respectively. E_u dropped slightly to 35 meV for x = 0.38 and 0.47. E_u again increased to 38 meV at x = 0.58 and thereafter remains constant at 36 meV for x = 0.71, 0.84 and 1.

The disorder is high in lower iodide content films and low in higher iodide content films on both measurements. High disorder observed in $CH_3NH_3Pb(I_{1-X}\ Br_X)_3$ films may be due to the

introduction of bromide ion into the mixed halide solution which creates stress on its structure that induced more defects in the material [213]. Sadhanala et al. [211] observed similar behavior in which relatively large Urbach energy of about 90 and 60 meV was obtained for films with 20 and 40% bromide content respectively. They also observed low Urbach energies for pure tri-bromide films and perovskite films with 80 and 100% iodide content.

To demonstrate that the perovskite properties depend on the preparation conditions, values of E_t for perovskite prepared in the old glove box were also shown as run 1 in figure 5.7 (b). E_t values ranged from 16 – 20 meV for $CH_3NH_3PbI_3$, 35 – 45 meV for $CH_3NH_3Pb(I_{1-X}\ Br_X)_3$ films at x = 0.58 and 16 – 22 meV for $CH_3NH_3PbBr_3$ films. Lower values of E_t were observed in run 1 than in run 2. This means that the nature of the solvents present inside a glovebox significantly affects the electronic properties of perovskite films. At a given x, scatter of E_t, E_u is possible, hence very sensitive to the preparation conditions. This implied that; E_t, E_u can strongly be increased at a certain value of x.

5.2. The role of storage and light soaking on the degradation of $CH_3NH_3PbBr_3$ coated with PMMA

Figure 5.8 shows the in-phase SPV spectra for ITO/ $CH_3NH_3PbBr_3$/PMMA on day 1 and after 30 days of storage in air under blue light soaking. A change of the sign in the value of in-phase signal with blue light soaking on day 1 was observed. However, after 30 days of storage in air, there was no change of sign. The change of the sign on day 1 under blue light soaking might be attributed to photochemical reactions at the interface of $CH_3NH_3PbBr_3$ with PMMA given that not all solvents had completely evaporated from the film surface. After 30 days, no change of the sign was observed because all solvents had completely evaporated from the sample surface. At 0 h of light soaking, it was observed that the magnitude of the in-phase signal on day 30 increased compared to that in day 1.

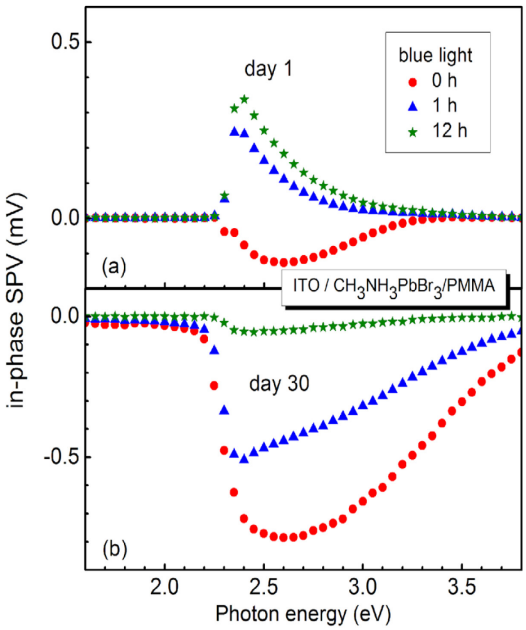

Figure 5.8. In-phase SPV spectra for ITO/ $CH_3NH_3PbBr_3$/PMMA on day 1 (a) and after 30 days of storage in air (b) under blue light soaking for 0 hour (red closed circles), 1 hour (blue triangles) and 12 hours (olive stars).

The maximum of the in-phase signal increased from -0.33 mV on day 1 to -0.79 mV on day 30. The increase in the signal intensity, might be due to passivating effect of $PbBr_2$ which cover the surface, thus preventing it from further degradation [217]. However, a pronounced reduction of the maximum in-phase signal intensity from -0.79, -0.51 and -0.05 mV corresponding to 0, 1 and 12 h of light soaking respectively was observed with light soaking after 30 days. The observed effect showed a reversible behavior suggesting that $CH_3NH_3PbBr_3$ had better stability compared to its counterpart $CH_3NH_3PbI_3$ [218, 219]. There was also defect generation with continued stay in air as indicated by the baseline which deviated from zero in comparison to practically zero baseline below the band gap on day 1. The defect may be induced by stress created by PMMA on $CH_3NH_3PbBr_3$ layers when in contact with impurities such as air, moisture and light. In addition, with continued storage in air, $CH_3NH_3PbBr_3$ layers degrade to $PbBr_2$ and other constituent precursor elements. This results in the formation of an interface region between $CH_3NH_3PbBr_3$ and $PbBr_2$ that introduces active defect states [220].

Figure 5.9 shows the exponential tail states (E_t) as a function of illumination time in hours for the $CH_3NH_3PbBr_3$ film measured on the day 1, 7, and after 30 days of storage in air.

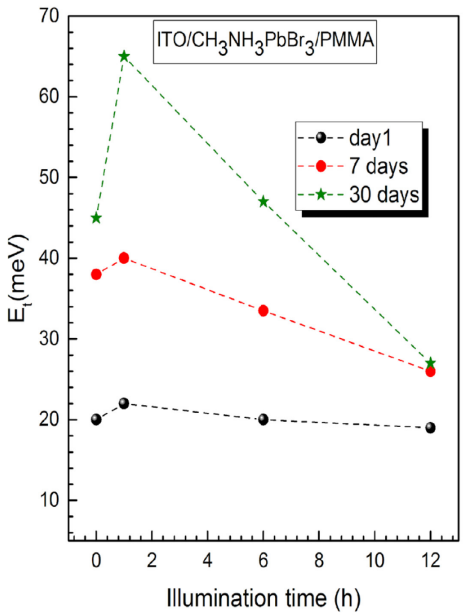

Figure 5.9: Tail states (E_t) as a function of illumination time in hours for $CH_3NH_3PbBr_3$ film measured on day 1 (black spheres with dashed line), 7 days (red circles with dashed line) and after 30 days (olive stars with dashed line) of storage in air.

E_t is a measure of the degree of disorder in $CH_3NH_3PbBr_3$ perovskite films. Disorder in a semiconductor results from defect states below or near the band gap that participates in charge separation. Disorder leads to an exponential decrease in the SPV signals towards lower photon energies [175]. E_t showed similar trends for all days such that the value was low before light soaking, increased after 1 h and thereafter decreases with prolonged light soaking for 12 h.

On day 1, E_t was lower compared to other days and amounted to 20, 22, 20 and 19 meV at 0, 1, 6 and 12 h of light soaking respectively. This was consistent with a practically constant baseline as shown in figure 5.8. E_t increased with storage time in air. For example, E_t amounted to 38, 40, 33.5 and 26 meV and 45, 65, 47 and 27 meV after 7 and 30 days respectively. Interestingly, 1 h of light soaking showed the highest E_t in all days whereas prolonged light soaking (12 h), showed the lowest E_t. The low value of E_t after 12 h of blue light soaking may be caused by activation of local ordering of trap states by the blue light. For comparison, exponential tail states for the $CH_3NH_3PbI_3$ coated with PMMA were of the order of 30 meV for front illumination [209].

To characterize $CH_3NH_3PbBr_3$ layers further, GIXRD was used in order to study the phase composition of the films after storage in air for 30 days. Figure 5.10 shows the GIXRD phase analysis for $CH_3NH_3PbBr_3$/PMMA thin films on day 1 and after 30 days of storage in air. On day 1, the GIXRD analysis revealed characteristic diffraction peaks of the cubic perovskite phase with a preferential orientation at 14.98° corresponding to (100) plane of cubic perovskite [198]. Other peaks appeared at 21.92°, 30.18°, 33.84°, 37.18°, 43.204° and 45.97° corresponding to (110), (200), (210) (112) (220) and (300) planes, respectively of the

crystalline cubic phase of perovskite [41]. However, after 30 days in air, some additional peaks were observed at 26.06° and 35.28°. These peaks corresponded to the $PbBr_2$ phase [221]. The peak intensity of the (100) at 14.98° decreased from 3576 to 2086 counts on day 1 and 30 respectively. Interestingly, there was an increase in the peak intensity for all the remaining peaks, suggesting a change in preferential orientation of the peaks with longer storage in air.

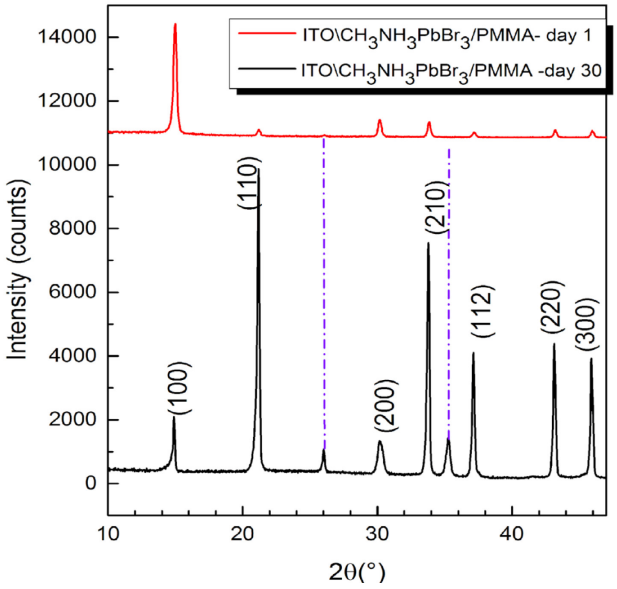

Figure 5.10: GIXRD phase analysis for $CH_3NH_3PbBr_3$/PMMA thin films on day 1 (red line) and after 30 days of storage in air (black line)

5.3. Influence of the substrate on the electronic properties of the $CH_3NH_3PbI_3$ films

The substrate has a strong influence on the electronic properties of perovskite solar cells. In this context, a substrate can be a bare substrate such as ITO or charge selective contacts such as TiO_2, PCBM, and SnO_2 etc. For example, poor charge extraction properties of TiO_2 were observed in TiO_2-based perovskite devices with a high hysteresis. On the other hand, SnO_2 poses favorable band alignment with perovskite, has high electron mobility and can be fabricated via low temperature processing [222].Besides, electron transporting fullerenes such as PCBM have good charge extraction properties as well as passivate defects at the interface with perovskite. PEDOT: PSS is an organic hole transporting material widely used in inverted structure of solar cells. However, it has a latent problem such as: highly hygroscopic, very acidic and has poor electron blocking properties. The acidic and hygroscopic nature of PEDOT: PSS may cause degradation and hence reduce device stability [223]. Therefore, the topography and chemical properties of the substrate can significantly influence perovskite absorber layer grown on it. Furthermore, chemical properties and surface roughness of the substrate may alter the interfacial energies that can have a strong impact on the nucleation of the perovskite films [34].

Figure 5.11 shows SPV overview spectra for $CH_3NH_3PbI_3$ deposited on SnO_2 and PEDOT: PSS. For ITO/SnO_2/$CH_3NH_3PbI_3$, both in-phase and phase shifted by 90° signals were positive indicating two mechanisms of charge separation in which photo-generated electrons were separated towards SnO_2 while holes towards the external surface.

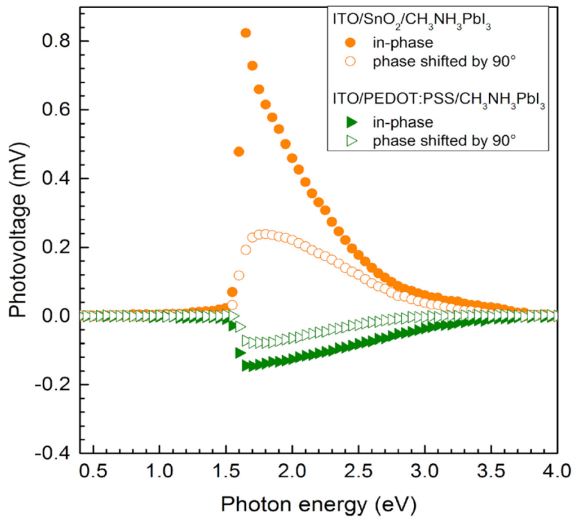

Figure 5.11: SPV overview spectrum for $CH_3NH_3PbI_3$ deposited on SnO_2 (orange circles) and PEDOT: PSS (olive stars)

For ITO/PEDOT: PSS/$CH_3NH_3PbI_3$, both in-phase and phase shifted by 90° signals were negative. This suggested that photo-generated electrons were separated towards the external surface while holes towards PEDOT: PSS. $CH_3NH_3PbI_3$ deposited in both the selective contacts i.e. SnO_2 and PEDOT: PSS, in-phase and phase shifted by 90° signals have the same signs which implied two mechanisms of charge separation. Two mechanism of charge separation occur when, for example, polarization of charge carriers significantly contributed to the SPV signals. Polarization and photo-generated charge carriers possess opposite signs that do not follow recombination of charge carriers when illumination was switched on and off [28].

Furthermore, for $CH_3NH_3PbI_3$ deposited on SnO_2, the in-phase signal was maximum at about 0.824 mV whereas for $CH_3NH_3PbI_3$ deposited PEDOT: PSS, the maximum was at -0.149 mV. Higher values of in-phase signals corresponded to faster transfer of photo-generated electrons from $CH_3NH_3PbI_3$ to SnO_2 in comparison to hole transfer to PEDOT: PSS. Similarly, the maximum value of phase shifted by 90°signal was 0.15 mV and -0.08 mV ITO/PSnO_2/$CH_3NH_3PbI_3$ and ITO/ PEDOT: PSS /$CH_3NH_3PbI_3$ respectively. This implied that slow charge separation and relaxation was relatively faster for electrons separated towards SnO_2 than for holes towards PEDOT: PSS.

Figure 5.12 shows a strong influence of the substrate on the band gap and disorder in the material for $CH_3NH_3PbI_3$ deposited on SnO_2 and PEDOT: PSS. The dependence of E_t on light

soaking time under nitrogen atmosphere for $CH_3NH_3PbI_3$ deposited on SnO_2 and PEDOT: PSS is shown in figure 5.12 (a). For the case of SnO_2 / $CH_3NH_3PbI_3$, E_t decreased with light soaking time and amounted to 30, 24, 21, 19, and 17 meV at 10, 20, 40, 60 and 120 min, respectively. On the other hand, for PEDOT: PSS/ $CH_3NH_3PbI_3$, E_t increased with light soaking time and amounted to 30, 31, 32, 35, 36 at 10, 20, 40, 60, and 120 min, respectively. The high value of E_t for $CH_3NH_3PbI_3$ deposited on PEDOT: PSS, may be attributed to acidic, hygroscopic and photo-oxidation nature of PEDOT: PSS [223] which increases the disorder and therefore the amount of defects in the material in comparison to $CH_3NH_3PbI_3$ deposited on SnO_2.

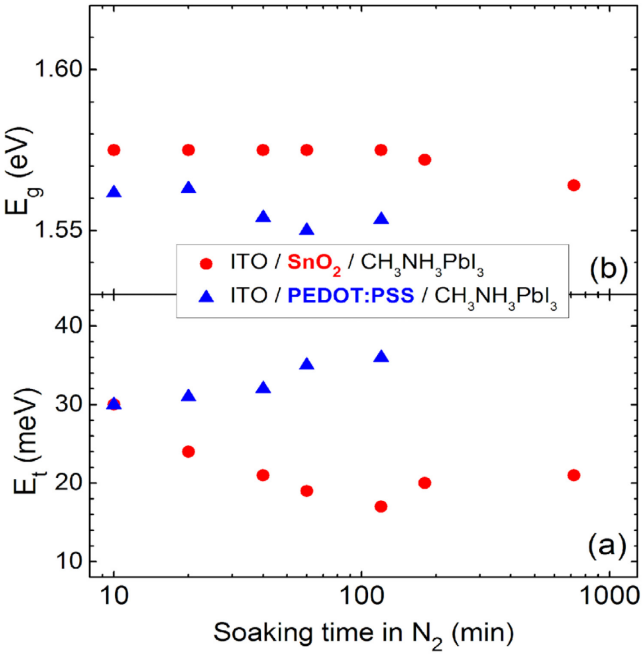

Figure 5.12: Dependence of light soaking on (a) E_t and (b) E_g measured for SnO_2 (red circles) and PEDOT: PSS (blue triangles).

The dependence of E_g on the light soaking time is also shown in figure 5.12 (b) for $CH_3NH_3PbI_3$ deposited on SnO_2 and PEDOT: PSS respectively. E_g was practically constant at 1.575 eV for light soaking up to 120 min for SnO_2 / $CH_3NH_3PbI_3$, but decreased slightly to 1.57 and 1.56 eV at 180 and 720 min, respectively. The almost constant E_g, show that SnO_2/ $CH_3NH_3PbI_3$ interface have well aligned energy levels, suggesting exceptionally better charge selectivity, low trap density, low degree of charge accumulation and low recombination rate and hence low exponential tail energy [164, 163]. However, there was gradual decrease of the band gap with longer light soaking time (i.e. at 180 and 720 min), an indication of defect generation due to degradation induced by illumination. On the other hand, E_g for PEDOT: PSS/ $CH_3NH_3PbI_3$, decreased with light soaking time and amounted to 1.563, 1.562, 1.55, 1.54 eV at 10, 20, 40, 60 min, respectively, of light soaking and increased slightly to 1.553 eV after 120 min of light soaking time. The reduced E_g may be due to some disorder at the interface between

$CH_3NH_3PbI_3$ and PEDOT: PSS. Furthermore, a high density of defect states present in PEDOT: PSS/ $CH_3NH_3PbI_3$ may be responsible for the reduced band gap. The acidic and hygroscopic nature of PEDOT: PSS creates stress at the interface with perovskite leading to the formation of defects.

To characterize $CH_3NH_3PbI_3$ absorber layers in more detail, SPV measurements were extended to study absorber properties with different electron transporting materials (*ETMs*) interfaces. The strong influence of the substrate and light soaking on the band gap, the exponential tail states and deep defect states of $CH_3NH_3PbI_3$ layers were demonstrated for TiO_2 and SnO_2 substrates by spectral dependent modulated SPV. Figure 5.13 shows layers of $CH_3NH_3PbI_3$ absorber layers deposited onto TiO_2 and SnO_2 substrates and investigated by spectral dependent modulated SPV. The influence of light soaking with blue light was studied at the $TiO_2/CH_3NH_3PbI_3$ and $SnO_2/CH_3NH_3PbI_3$ systems.

Figure 5.13 (a) shows the overview spectra for the $TiO_2/CH_3NH_3PbI_3$ interface.10 min after preparation, the in-phase signals were positive in the whole range of photon energies. On the other hand, the phase shifted by 90° were negative between 1.55 to 1.89 eV, changed the sign to positive up to photon energy of 3.1 eV and thereafter remained at 0 mV above 3.1 eV. After blue light soaking for 18 h, the in-phase signals changed the sign from positive to negative (see arrow A in figure 5.13 (a)), whereas the phase shifted by 90° signals increased in magnitude (i.e. an increase in slow response as indicated by the arrow B in figure 5.13 (a)). The change of the sign after 18 h of blue light soaking may be attributed to the interaction of light with TiO_2 which induced oxygen vacancies [224]. Such oxygen vacancies lead to accumulation of excess negative charge at the perovskite surface which results in a change of the sign. Furthermore, an increase in the slow response after 18 h of blue light soaking may be correlated to the presence of an amorphous region between the TiO_2 and $CH_3NH_3PbI_3$ interface which leads to slow charge separation and transport [225].

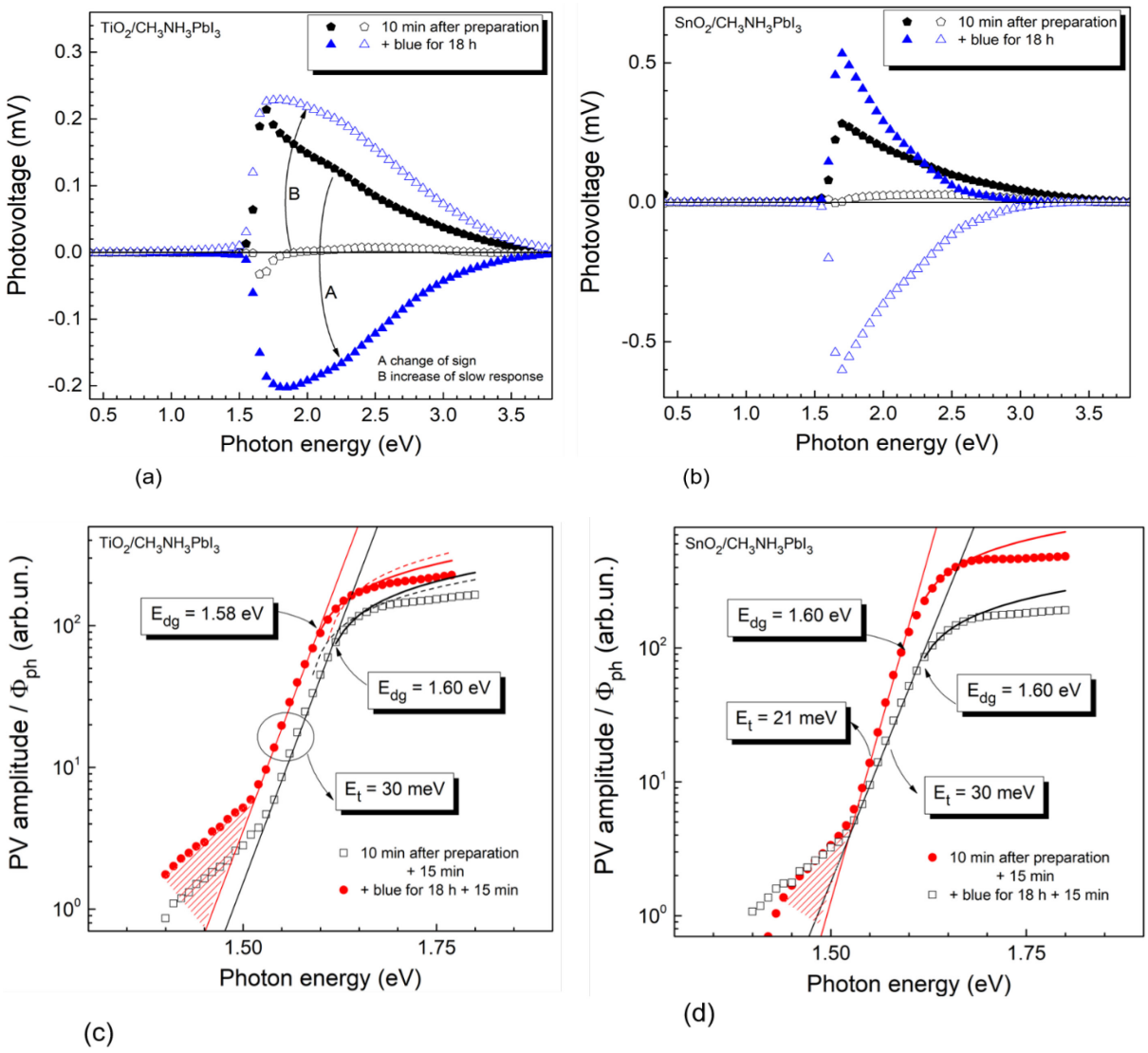

Figure 5.13: Spectral dependent modulated SPV for $TiO_2/CH_3NH_3PbI_3$ and $SnO_2/CH_3NH_3PbI_3$ systems. Figures (a) and (b) represent overview SPV spectra measured 10 min after preparation (black diamonds) and after 18 h of blue light soaking (blue triangles). The dependence of the PV amplitude divided by the photon flux as a function of photon energy for (c) $TiO_2/CH_3NH_3PbI_3$ and (d) $SnO_2/CH_3NH_3PbI_3$.

For $SnO_2/CH_3NH_3PbI_3$ (see figure 5.13 (b)), 10 min after preparation, the in-phase signals were positive indicating that the photo-induced electrons were preferentially separated towards the SnO_2 substrate whereas holes were separated towards the surface of perovskite. The phase shifted by 90° signals were slightly negative between 1.56 and 1.7 eV and thereafter change the sign to a positive value above 1.7 eV. After 18 h of light soaking, the magnitude of in-phase signals increased from 0.29 to 0.54 mV at a photon energy of 1.7 eV. In contrast, phase shifted by 90° signals changed the sign with the value increased from 0.02 mV at energy of 1.85 eV to -0.60 mV at 1.7 eV. As a remark, opposite signs of in-phase and phase shifted by 90° signals indicated one mechanism of charge separation, relaxation and transport [28].

For $TiO_2/CH_3NH_3PbI_3$, the band gap (E_g) reduced after light soaking with blue light from 1.60 to 1.58 eV. The tail states, i.e. the disorder, remained unchanged (i.e. E_t = 30 meV) whereas the SPV signals related to deep defects increased after light soaking (see figure 5.13 c). Figure 5.13 (d) shows $CH_3NH_3PbI_3$ deposited on SnO_2 substrate. The band gap E_g, remained constant at 1.60 eV. The value of E_t decreased from 30 to 21 meV after light soaking, i.e. the degree of disorder decreased. After light soaking with blue light, the SPV signals related to fundamental absorption strongly increased whereas the deep defects related signals remained constant.

The influence of the substrate on the microscopic structure of $CH_3NH_3PbI_3$ layers is shown in the figure 5.14. The SEM micrograph of $CH_3NH_3PbI_3$ perovskite active layers on TiO_2 showed a pronounced difference in the grain size which was of the order of 140 nm in comparison to that on SnO_2.

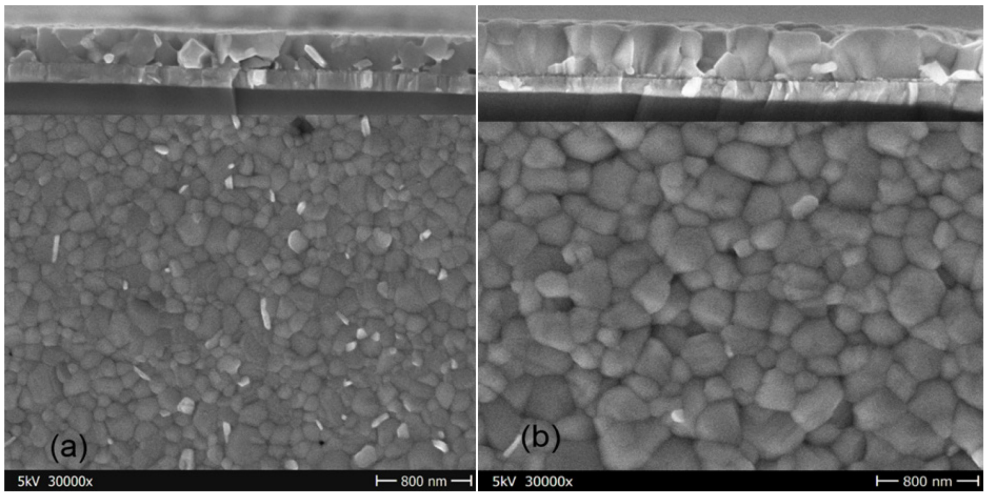

Figure 5.14: Cross-section and top view micrographs of $CH_3NH_3PbI_3$ perovskite layers deposited on (a) TiO_2 and (b) SnO_2 substrates. The upper parts in both figures represent the cross-section images whereas the lower part gives the top view images.

The thickness of $CH_3NH_3PbI_3$ deposited on $Ti0_2$ (see figure 5.14 (a)) was about 300 nm with TiO_2 itself having a thickness of about 15-30 nm. Since the average grain size of about 140 nm was much smaller than the thickness of perovskite layer, it indicated that the number of grain boundaries were significantly high. An increased number of grain boundaries is not desirable for photovoltaic devices because of increased recombination rate of charge carriers during transport.

For the case of $CH_3NH_3PbI_3$ deposited on SnO_2 (see figure 5.14 b), the thickness of the perovskite layer was about 400 nm with an average grain size of about 230 nm. The grain sizes were much larger compared to $CH_3NH_3PbI_3$ films deposited on TiO_2 substrate. This suggested that most of the grains were extended from the SnO_2 substrate to the perovskite

surface with the vanishing of grain boundaries that were parallel to the substrate, allowing for secondary grain growth that increased the size of the grains [16].

To further investigate the electronic properties, modulated SPV was extended to determine the energy of the exponential tail states at the interface of $CH_3NH_3PbI_3$ with different electron transport layers (*ETLs*). The *ETLs* used at the interface with $CH_3NH_3PbI_3$ were TiO_2, SnO_2, ICMA, C60, PCBM, and SnO_2-PCBM and TiO_2-PCBM.

Figure 5.15 shows the overview SPV spectra of $CH_3NH_3PbI_3$ deposited on SnO_2-PCBM, TiO_2-PCBM & TiO_2.For the as-prepared SnO_2-PCBM, TiO_2-PCBM, and TiO_2; the in-phase signals were positive, reached a maximum height at 5.13, 5.10 and 4.11 mV (see figures 5.15 (a-c), respectively). On the other hand, the phase-shifted by 90° signals were negative with a maximum photovoltage values of -0.69, -1.31 and -1.00 mV (a-c respectively).

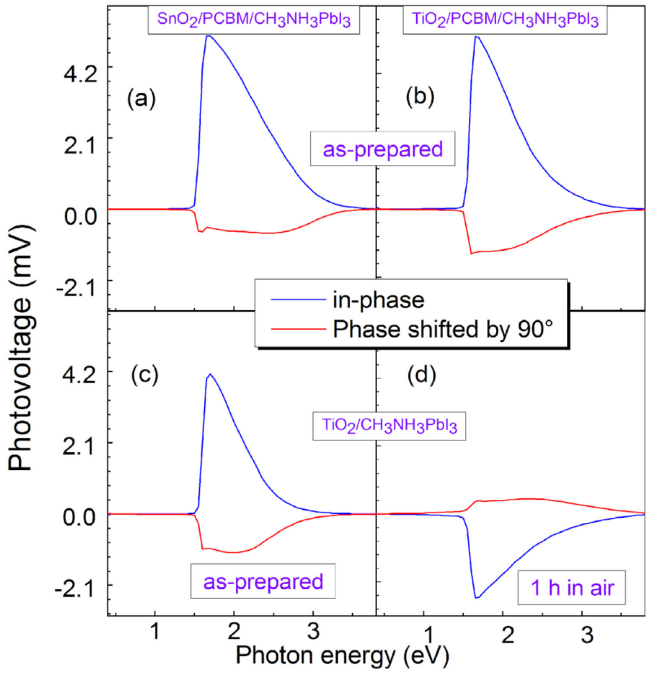

Figure 5.15: Examples for the overview SPV spectra of modulated in-phase (blue lines) and phase shifted by 90° (red lines) SPV spectra for as prepared SnO_2-PCBM (a), TiO_2-PCBM (b), TiO_2 (c) and TiO_2 after 1 h in air (d).

After the initial measurement, TiO_2 was placed in air for 1 h and additional measurement were performed. Interestingly, there was a change of the sign for both in-phase and phase shifted by 90° signals (figure 5.15 d). The in-phase signal changed the sign to negative while phase shifted by 90° signals became positive. The change of the sign was probably caused by polarization at the interface between TiO_2 and perovskite. The accumulation of electrons at $TiO_2/CH_3NH_3PbI_3$ interface creates charging and discharging effects which lead to polarization and is speculated to initiate degradation and hence the reason for the change of the sign of SPV signals. It can also be due to charge accumulation at $TiO_2/CH_3NH_3PbI_3$ interface which lead to slow charge extraction hence a change of the sign. In general, all samples showed a

dominant SPV onset at about 1.50 eV which was the band gap of $CH_3NH_3PbI_3$ as reported in the literature [24].

Figure 5.16 (a) shows spectra of the SPV amplitude on a logarithmic scale. The value of E_t for the double layer of ITO/SnO_2-PCBM/$CH_3NH_3PbI_3$ amounted to 18 meV. For comparison, E_t for single layer of ITO/SnO_2 or PCBM/$CH_3NH_3PbI_3$ has also been shown to be 23 meV. The values of E_t were comparable for $CH_3NH_3PbI_3$ deposited on single layer as well as on double layers. To further characterize the electronic properties, the so called Tauc plot which corresponds to the squared ratio of the product of the SPV amplitude and photon energy to the photon flux (see figure 5.16 (b). E_g was 1.58 eV which was comparable for both single as well as double layers of $CH_3NH_3PbI_3$ on SnO_2-PCBM.

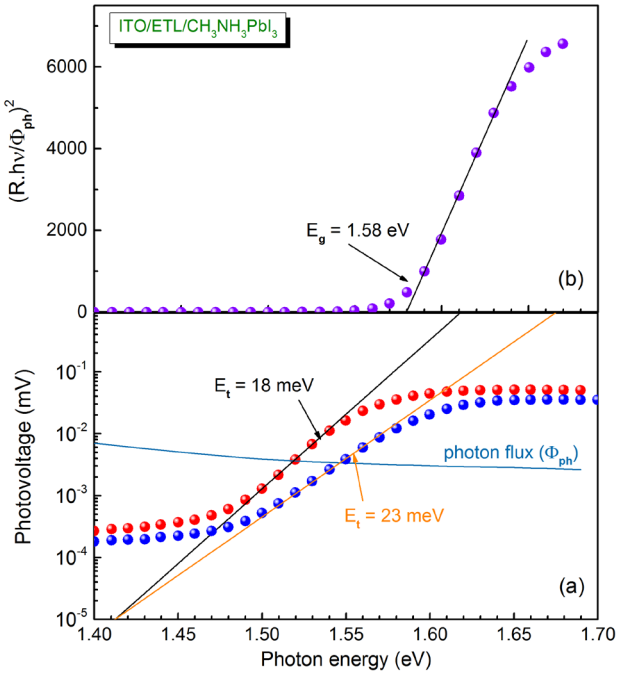

Figure 5.16: Spectra of the PV amplitude for ITO/SnO_2-PCBM/$CH_3NH_3PbI_3$ and ITO/SnO_2/$CH_3NH_3PbI_3$ (red and blue spheres, respectively) (a) and Tauc plot of ITO/SnO_2-PCBM/$CH_3NH_3PbI_3$ (b). The photon flux is shown for comparison (dark cyan line in (a)). The solid lines represent the fits for determining the corresponding E_t (a) and E_g (b).

Similarly, figure 5.17(a) shows the exponential tail slope parameter E_t measured for several batches of $CH_3NH_3PbI_3$ layers on glass/ITO/*ETL* substrates by SPV measurements. $CH_3NH_3PbI_3$ layers deposited on TiO_2, a scatter in the value of E_t was observed and ranged between 27 to 58 meV. The high value of E_t observed was proposed to be due to the presence of a thin amorphous layer at the interface of $CH_3NH_3PbI_3$/TiO_2 as reported in the literature for evaporated perovskite samples [225]. E_t ranged between 20 and 30 meV for $CH_3NH_3PbI_3$ deposited on SnO_2, whereas for ICMA, E_t amounted to 26, 38 and 18 meV for batch 1, 2 and 3, respectively. Low scatter was observed for $CH_3NH_3PbI_3$ deposited on C_{60}, PCBM, SnO_2-

PCBM and TiO_2-PCBM and amounted to 26, 22 and 20 meV; 24, 23, 19 meV; 23, 24 and 18 meV; 21, 24 and 23 meV in that order respectively. The value of E_t was comparable for fullerenes and double layers with some scatter for $CH_3NH_3PbI_3$ deposited on SnO_2, with pronounced scatter on TiO_2. $CH_3NH_3PbI_3$ coated on TiO_2, showed higher values of exponential tail states energy E_t with an average value of 40 meV and a lower value of 27 meV.

The relatively large value of E_t for $CH_3NH_3PbI_3$ deposited on TiO_2 may be correlated to the significant density of shallow traps in the TiO_2 which allows excitation of charge carriers from the valence band of perovskite into defect states at the interface with TiO_2. Another reason for high E_t for $CH_3NH_3PbI_3$ deposited on TiO_2 might be due to the presence of a thin amorphous layer within $CH_3NH_3PbI_3$ film on the surface of TiO_2 as reported in the literature for evaporated perovskite samples [225]. Moreover, there were several grain boundaries for $CH_3NH_3PbI_3$ deposited on TiO_2 (see SEM micrographs in figure 5.14).The grain boundaries acted as recombination centers which cause high E_t.

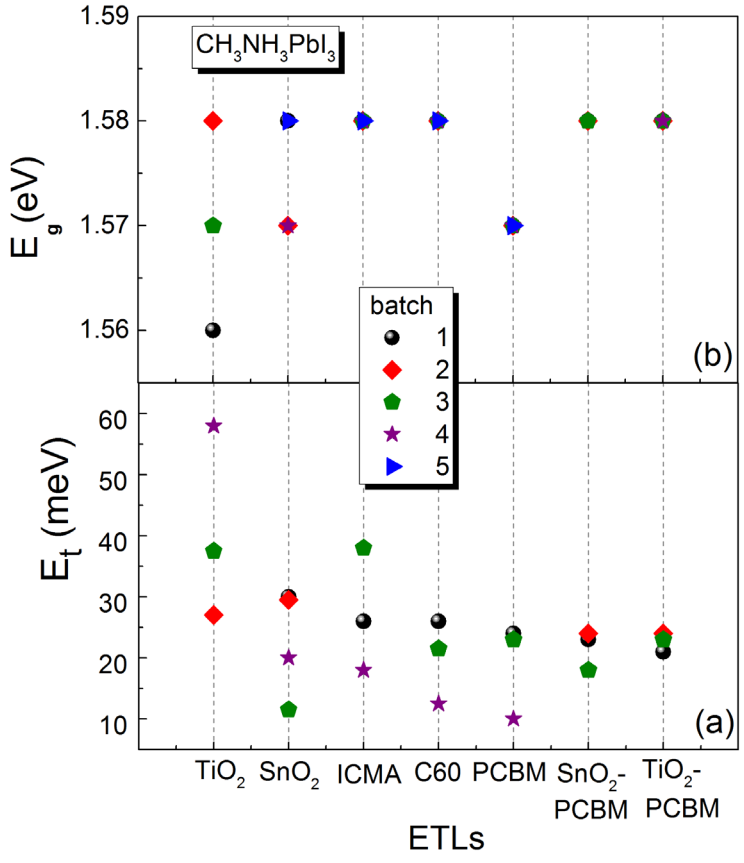

Figure 5.17: The Exponential tail states (E_t) (a) and the so called Tauc gap (E_g) obtained from SPV measurements of $CH_3NH_3PbI_3$ absorber layers grown on different *ETL* coated substrates.

Figure 5.17 (b) shows the Tauc gap (E_g) measured for several batches of $CH_3NH_3PbI_3$ layers deposited on glass/ITO/ETL substrates. E_g was assumed to be equivalent to the absorption processes in the optical measurements. E_g ranged from 1.56 to 1.58 eV for all

$CH_3NH_3PbI_3$ layers on every *ETLs* with ICMA, SnO_2 and TiO_2 showing slightly larger spread in comparison to other *ETLs*. The largest spread in E_g was observed in TiO_2 which may probably be due to the defect states near the interface which retarded charge transfer. The chemical potential at the $TiO_2/CH_3NH_3PbI_3$ interface may result in radical reactions which create instabilities at the interface. $CH_3NH_3PbI_3$ deposited on double layers of TiO_2-PCBM and SnO_2-PCBM showed a constant band gap of 1.58 eV. The constant band gap of the $CH_3NH_3PbI_3$ on double layers *ETLs* was deduced to be due to better charge transport and extraction properties of the bilayers. This observation could also be correlated to a smaller spread in the value of exponential tail states E_t. Generally, E_g is almost similar in all *ETLs* which was supported by the similar morphology across all *ETLs* as seen from scanning electron microscopy (SEM) (see figure 4.5 in methods section). This further promotes the assumption of a minor influence of the underlying substrate on the perovskite absorber grown on top of *ETLs*.

5.4. Effects of light soaking on the transport length of $CH_3NH_3PbI_3$

Figure 5.18 (a) shows Goodman [32] plots for TiO_2/ $CH_3NH_3PbI_3$ layers at SPV signals of 0.55, 0.75, 0.85, 0.95 and 1.05 mV under 20 min of blue light soaking. The corresponding diffusion length was extrapolated at negative intercepts of absorption length and amounted to 820 nm. For comparison, the diffusion length of c-Si of about 0.13 mm was obtained in figure 5.18 (b).

Figure 5.18 (c) correlates the values of the transport length of photo-induced charge carriers with values of SPV signals for $CH_3NH_3PbI_3$ layers and crystalline silicon wafers (c-Si). A certain scatter in the values of *L* for $CH_3NH_3PbI_3$ layers was observed in comparison to that of c-Si. The accuracy in determining *L* in $CH_3NH_3PbI_3$ layers is lower as compared to corresponding measurement of *L* in c-Si. This is because of the rough nature of $CH_3NH_3PbI_3$ layers as well as availability of very few data points of absorption coefficients from the literature [102].

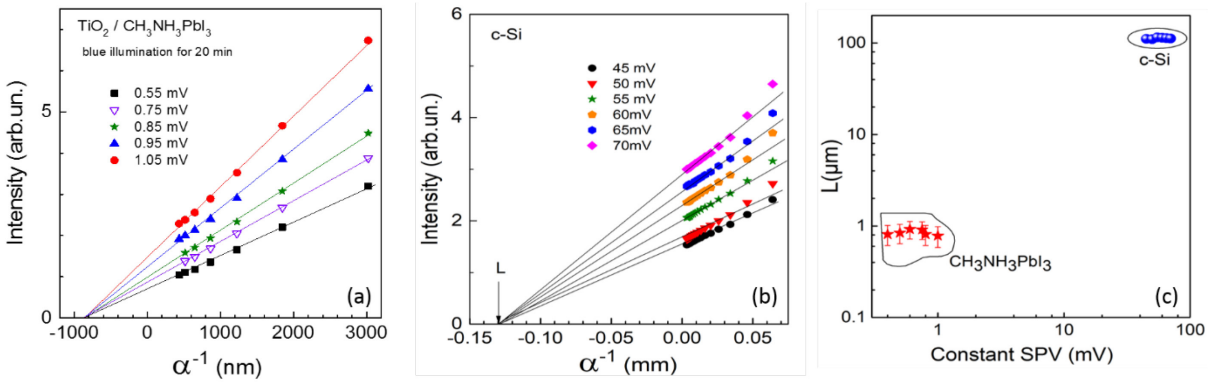

Figure 5.18. Goodman plot of (a) $TiO_2/CH_3NH_3PbI_3$ under blue light soaking for 20 minutes and crystalline silicon (c-Si) (b) measured at different constant SPV signal. The diffusion length photo-

generated charge carriers as a function of constant SPV signals obtained for $CH_3NH_3PbI_3$ layers (red) and c-Si (blue) (c).

For better understanding of the effect of light soaking on transport length, the sample was illuminated with blue light at different light soaking times from 0 min to 48 h (figure 5.19). The scatter in the value of the transport length with SPV was analyzed for the as-prepared sample, 20 min and 30 min of light soaking (figure 5.19 a-c). The scatter could be induced by the variation in the quasi Fermi levels over the absorber thickness and in-homogeneity of perovskite film. Dittrich et al. also observed a scatter in the value of transport length for both $CH_3NH_3PbI_3$ films and powders [102]. The scatter in the value of *L*, may also be attributed to the trapping of charge carriers at the $TiO_2/CH_3NH_3PbI_3$ interface which may influence transport hence limiting the diffusion length as well as the drift length.

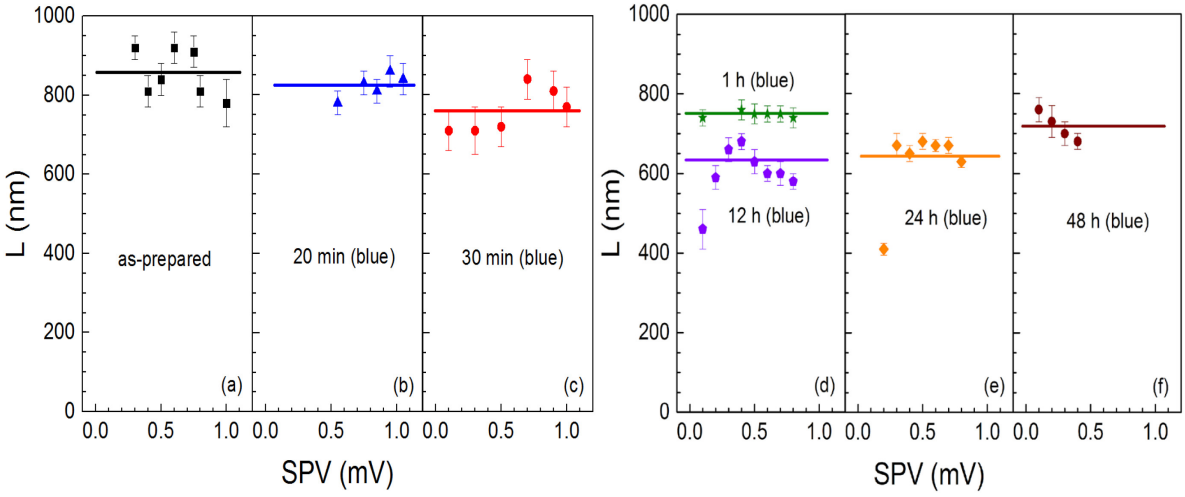

Figure 5.19. Dependencies of transport length of TiO_2/ $CH_3NH_3PbI_3$ as a function of different constant SPV signals for light soaking times at 0 min (a), 20 min (b), 30 min (c), 1 h –green star (d), 12 h- black symbols (d) , 24 h (e) and 48 h (f).

1 h of light soaking showed very low scatter (figure 5.19 d), while for 12 h, there was a dependence of the transport length *L* on the SPV signals (figure 5.19 d-violet symbols). This was a clear indication of the splitting of quasi Fermi level across the absorber layer. In general, there was a decrease in transport length within 12 h of light soaking time. The transport length decreased from 860, 820, 780 and 750 nm for as-prepared, 20 min, 30 min and 1h of light soaking, respectively. The decrease in the value of transport length might be due to light induced degradation which arises due to trap states and charging- discharging effect at TiO_2/ $CH_3NH_3PbI_3$ interface.

For prolonged light soaking i.e. 24 h and 48 h (figure 5.19 e and f), the diffusion length increased. The increase in the value of diffusion length with prolonged light soaking time was

probably analyzed by the change of the nature of trap states implying that less charge carriers were trapped leading to increase in transport length. Another possible explanation for a larger diffusion length under prolonged light soaking may be due to compensation of traps and defects states. There is a generation of defect states which neutralize the trap states leading to an increase of the diffusion length. Previous findings by electron beam induced current (EBIC), concluded that increased diffusion length due to illumination depended on the photo-generation of charge carriers [226].

In-homogeneities in the perovskite films led to the scatter of the diffusion length over a large range. For this reason, the mean transport length was taken as a representative value for the overall ability of charge carriers to diffuse in the material. The mean diffusion length was plotted as a function of illumination time (see figure 5.20).

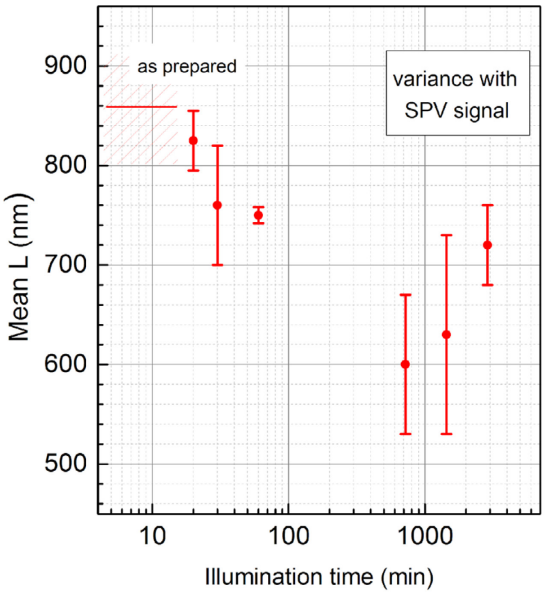

Figure 5.20: Mean transport length *L* of TiO_2/ $CH_3NH_3PbI_3$ as a function of illumination time.

A decrease in the mean *L* within 12 h of illumination time was observed. This decrease was probably caused by trap states and charging-discharging effects between TiO_2 and $CH_3NH_3PbI_3$. With longer light soaking time, *L* increased. The increase in *L* might be due to changing nature of the traps due to generation of compensating defects which neutralize the trap states. In addition, a strong variation of *L* with SPV signal indicated the in-homogeneous nature of the film which could lead to changes of the quasi Fermi levels over the whole range of film thickness.

A simplified model was designed to explain the behavior of the transport length with light soaking time. Figure 5.21 (a) presents an idealized band diagram in which an absorber material (perovskite) was sand-witched between hole transporting material (*HTM*) and the electron transporting material (*ETM*). In this model, photo-generated electrons are attracted towards

ETM while holes towards HTM. In such a case, the transport length *L* corresponds to the absorber layer thickness as illustrated in figure 5.21 (a). The scenario above is an ideal case which rarely occurs. In reality, disorder exists in materials and hinder transport of charge carriers.

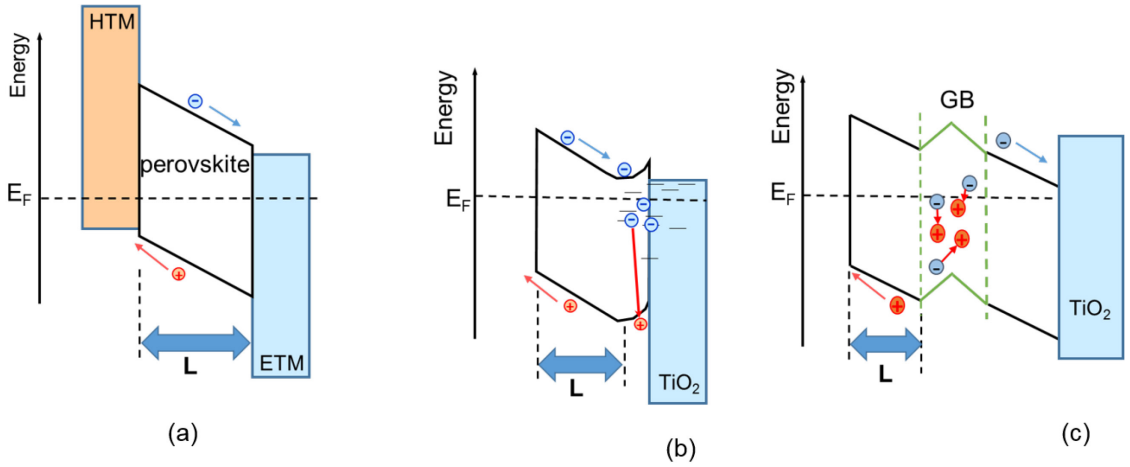

Figure 5.21: Ideal band diagram with absorber material (perovskite) sand-witched between hole transporting material (HTM) and electron transporting material (ETM) (a). Band diagram with traps near TiO_2 (b) and band diagram showing grain boundaries (GB) in perovskite (c).

Figure 5.21 (b) shows a band diagram in which traps appear between TiO_2 and $CH_3NH_3PbI_3$ or within the absorber material itself. In this study, there was no *HTM* and *ETM* was TiO_2.This means that photo-generated electrons will be attracted toward TiO_2 while holes towards the perovskite surface. This will create upward band bending at the TiO_2/ $CH_3NH_3PbI_3$ interface. Some photo-excited electrons become trapped at the TiO_2/ $CH_3NH_3PbI_3$ interface and others within the perovskite itself. These trap states will create defects that lead to charge carrier recombination hence the reduction in transport length. It was also speculated that the charging and discharging effect at the TiO_2/ $CH_3NH_3PbI_3$ interface may also lead to a reduction in the value of the transport length of $CH_3NH_3PbI_3$ layers. Prolonged light soaking may change the nature of trap states which can lead to the reduction of the defect density leading to increase in the transport length.

Grain bounderies contain large density of charge traps which act as recombination centres.In larger grains, photogenerated electrons travel freely without encountering grain bounderies hence reducing charge loss by recombination. On the other hand,smaller grain size reduce light harvesing efficiency due to recombination at grain bounderies leading to shorter diffusion length [171] as demonstrated in the figure 5.21 (c). As a remark, diffusion length can be long or short depending on the nature of grain sizes and grain bounderies.

5.5. Summary

Material properties of CH_3NH_3Pb (I, Br)$_3$ films that relate to degradation, stoichiometry, band gap (E_g), exponential tail states (E_t) or Urbach energy (E_u) and diffusion length (L) were investigated. For $CH_3NH_3PbBr_3$ perovskite films, E_t of 19 meV and E_u of 18 meV were obtained by SPV and PDS, respectively. The value of E_t obtained by SPV was comparable with E_u with a slight deviation of about 1 meV. The discrepancy was because both methods are sensitive to different regions of measurements. For instance, SPV is sensitive to the measurement region where charge separation takes place whereas PDS probes the whole region of the sample volume where absorption takes place.

Vegard's law was used to obtain the composition of $CH_3NH_3Pb(I_{1-X}\ Br_X)_3$ films. The lattice constant decreased linearly with increasing $CH_3NH_3Pb(I_{1-X})Br_X)_3$ composition. Similarly, E_g decreased with increasing lattice parameter suggesting a lattice contraction due to an increase in the potential energy of the electrons in the orbitals of an atom. The variations of E_g and E_t with the stoichiometry of the $CH_3NH_3Pb(I_{1-X}Br_X)_3$ perovskite films were investigated by modulated SPV and UV-Vis spectroscopies. E_g of $CH_3NH_3Pb(I_{1-X}Br_X)_3$ films was tuned from 1.56 eV to 2.30 eV by varying the bromide composition in $CH_3NH_3Pb(I_{1-X}Br_X)_3$ films. E_g blue shifted with increasing content of bromide and a bowing parameter of 0.36 eV was obtained. The blue shift was attributed to different spin- orbit interactions between lead-iodide and lead-bromide ions.

The values of E_u and E_t were observed to be lower for tri-iodide ($CH_3NH_3PbI_3$) and tri-bromide ($CH_3NH_3PbBr_3$) perovskites but higher for mixed perovskites. Higher disorder observed in $CH_3NH_3Pb(I_{1-X}\ Br_X)_3$ films may be due to the introduction of bromide ion into the mixed halide solution which creates stress on its structure that induced more defects in the material [213].

Light soaking studies under blue illumination on SnO_2/ $CH_3NH_3PbI_3$ and PEDOT: PSS /$CH_3NH_3PbI_3$ showed that there was a strong influence of the substrate on the band gap and disorder. On PEDOT: PSS, the disorder increased with increasing blue light soaking time in N_2, in contrast to SnO_2 substrates showing a constant band gap and decreasing disorder. The influence of blue light soaking was also investigated for $CH_3NH_3PbBr_3$ coated with and without PMMA. It was observed that there was a strong influence of light soaking on the direction of modulated charge separation since a change of sign occurred for $CH_3NH_3PbBr_3$ coated with PMMA.

The values of E_g and E_t depended sensitively on the kind of interface as shown by modulated SPV spectroscopy. $CH_3NH_3PbI_3$ deposited on double layers of TiO_2-PCBM and

SnO_2-PCBM showed a constant band gap of 1.58 eV and low scatter in the value of E_t. This was attributed to the modification of theTiO_2 or SnO_2/$CH_3NH_3PbI_3$ interfaces by the PCBM which allowed for efficient charge separation and transfer. In contrast, $CH_3NH_3PbI_3$ deposited on TiO_2 showed relatively large values of E_t which was correlated to the significant density of shallow traps in the TiO_2 that allowed for the excitation of charge carriers from the valence band of perovskite into defect states at the interface with TiO_2.

The diffusion or transport length (L) was measured for $CH_3NH_3PbI_3$ layers by the method after Goodman [32]. L was studied as a function of degradation under light soaking. A decrease of L with increasing time of light soaking was observed. The decrease was attributed to light-induced degradation which arises due to trap states and charging- discharging effect at the TiO_2/ $CH_3NH_3PbI_3$ interface. After 12 h of light soaking, L depended on the value of the modulated SPV signal, i.e. on the generation rate. The strong variation of L with modulated SPV signals was an indication of defects and/or inhomogeneity of the films which led to changes in the quasi Fermi levels over the whole range of film thickness.

CHAPTER 6

Temperature dependent, modulated surface photovoltage measurements on stabilized $CH_3NH_3PbI_3$ layers

The band gap and its dependence on temperature belong to the most important properties of a semiconductor material. Under operating conditions, the temperature of a solar cell can vary over a relatively wide range up to about 70°C. Temperature fluctuations affect the efficiency of perovskite based solar cells. The precise knowledge of the temperature dependence of the band gap for methyl ammonium lead iodide and related perovskites is essential for deeper understanding of the temperature dependence of solar cells and origins behind. Results of the temperature dependence of the band gap of $CH_3NH_3PbI_3$ perovskite layers measured by modulated SPV are presented in this chapter. Some of the results were published in [209].Bare $CH_3NH_3PbI_3$ is not stable in vacuum, which is required for measurements in a cryostat. For this reason, a protective PMMA layer was developed and tested for $CH_3NH_3PbI_3$, whereas the phase composition and electronic properties were characterized by GIXRD and modulated spectral-dependent SPV, respectively. The temperature dependence of SPV spectra was analyzed. The band gap and the energy parameter of the exponential tails of $CH_3NH_3PbI_3$ increased with increasing temperature. The results show that thermal expansion is the predominant contribution to the temperature dependence of the band gap of $CH_3NH_3PbI_3$ and that the dynamic disorder is limited by phonons.

6.1. Stabilization of $CH_3NH_3PbI_3$ with PMMA for temperature-dependent measurements

6.1.1. Criteria for PMMA as a protective layer

Hybrid organic-inorganic lead halide perovskites are known to be unstable in air [227], under moisture [13], heat [161,228], vacuum [229] and under illumination [155]. In order to enhance the stability in air, a protection polymer such as poly (methyl methacrylate) (PMMA) has been applied [192,230]. PMMA is a transparent polymer which can be dissolved in numerous organic solvents, for example, butyl acetate (BA) or toluene. These solvents are so-called anti-solvents for $CH_3NH_3PbI_3$ films, i.e. $CH_3NH_3PbI_3$ cannot be dissolved in these solvents. Furthermore, PMMA is an amorphous insulator and it can be assumed that PMMA does not (chemically) interact with the perovskite due to its inertness. These properties make PMMA a suitable material as a protective layer on the surface of $CH_3NH_3PbI_3$ perovskite films.

In order to use PMMA as a protective layer for temperature-dependent SPV measurements, different parameters were tested in order to test its influence on $CH_3NH_3PbI_3$ films.

First of all, a protective layer should act as a diffusion barrier for $CH_3NH_3PbI_3$, i.e. in-diffusion and out-diffusion of molecules shall be avoided (figure 6.1 (a)). For bare $CH_3NH_3PbI_3$ samples in air, there is in-diffusion of water and oxygen into the perovskite and out-diffusion of methylamine, hydroiodic acid and other components evolving during decomposition. For temperature-dependent measurements, a stable perovskite sample over a wide temperature range is needed at least for the time of measurements. A diffusion barrier at the surface of $CH_3NH_3PbI_3$ causes an increase of the concentration of reaction products at the interface with PMMA and reduces therefore drastically the decomposition rate of $CH_3NH_3PbI_3$ in the bulk or near surface region.

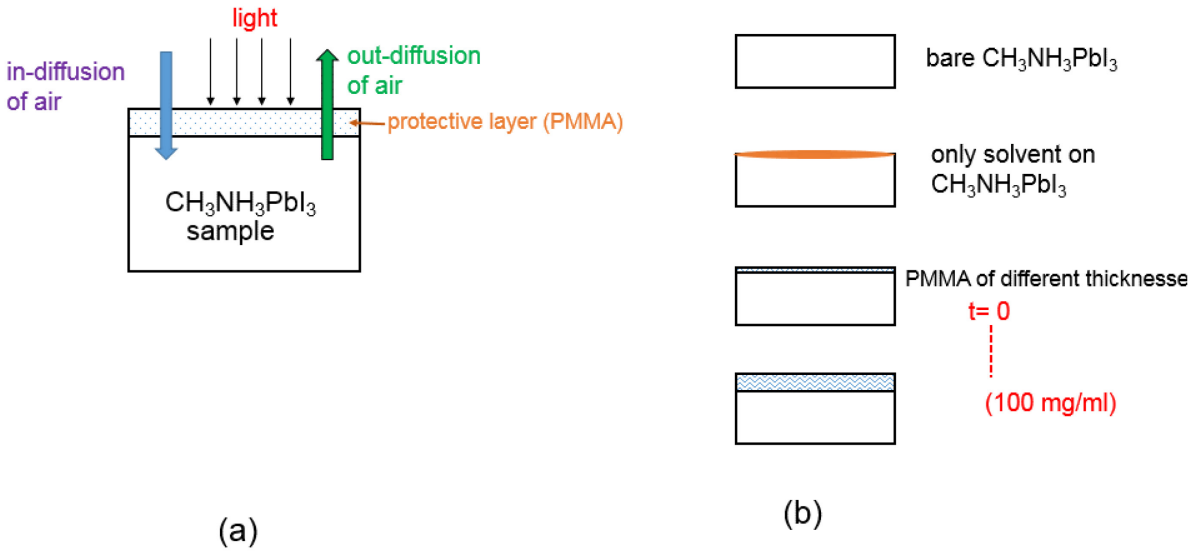

Figure 6.1: PMMA as a protective layer of $CH_3NH_3PbI_3$ for preventing in-diffusion and out-diffusion of molecules in different ambient (a), test samples for the influence of PMMA on degradation of $CH_3NH_3PbI_3$ (b).

The role of the PMMA for stabilization of $CH_3NH_3PbI_3$ was tested by comparing bare $CH_3NH_3PbI_3$ layers with $CH_3NH_3PbI_3$ layers treated in the solvent (BA) and $CH_3NH_3PbI_3$ layers with different thicknesses of the PMMA layer (see figure 6.1 (b)). The thickness of the PMMA layer can strongly influence the in- and out-diffusion of molecules since, if the polymer is too thin, molecules can penetrate through pores and, if the polymer is too thick, stress can lead to the formation of cracks during the evaporation of the solvent. In order to find out the optimum thickness of PMMA, the concentration of PMMA in BA was varied by dissolving 20, 40, 60, 80 and 100 mg in 1 ml of BA and the solutions were spin coated onto $CH_3NH_3PbI_3$ under identical conditions. The in- and out-diffusion of molecules was indirectly tested by investigating the degradation in air.

6.1.2. Influence of PMMA on the exponential tails in $CH_3NH_3PbI_3$ layers

Figure 6.2 shows the in-phase (x-signal) and phase shifted by 90°(y-signal) SPV spectra for the as-deposited sample without PMMA coating (a) and of samples (b) coated with PMMA before annealing (c), annealed but without PMMA coating and (d) coated with PMMA after annealing. As a remark, in-phase and phase shifted by 90° signals corresponded to fast and slow responses, respectively, in relation to periodic modulation of SPV signals.

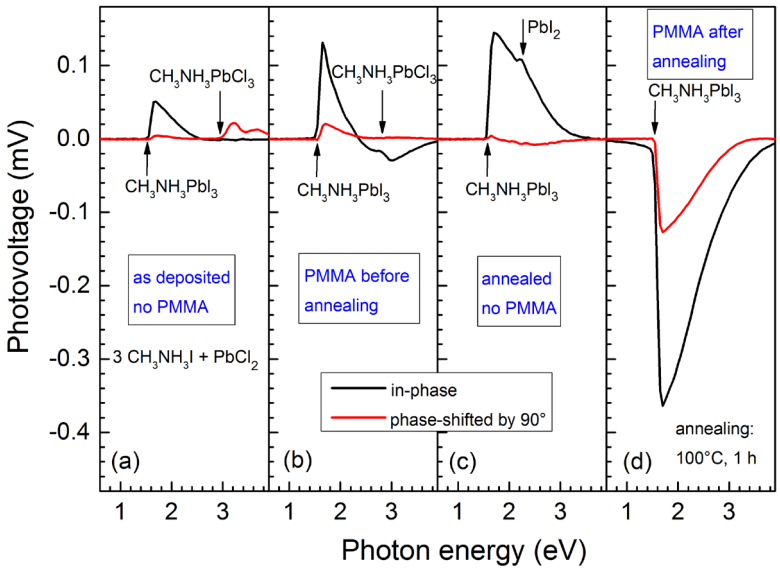

Figure 6.2: An overview spectrum of in-phase (black line) and phase shifted by 90° (red line) for CH3NH3PbI3 films (a) as-deposited without PMMA (b) with PMMA before annealing (c) annealed without PMMA and (d) with PMMA after annealing. The concentration of PMMA in BA was 40 mg/ml.

All samples showed a dominant onset of the SPV signals at around 1.55 eV which is close to the band gap of $CH_3NH_3PbI_3$ [24]. For the as-deposited sample with no PMMA coating (figure 6.2. (a)), the in-phase signals were positive around the onset energy, reached a maximum of about 0.05 mV at the photon energy of 1.66 eV and decreased to zero at about 2.5 eV. The positive value of in-phase signals shows that photo-generated electrons were preferentially separated towards the internal interface while holes towards the surface. A second onset at the energy of about 3.1 eV, which is close to the band gap of $CH_3NH_3PbCl_3$, was observed for the phase shifted by 90° signal. The absence of the onset at 3.1 eV in the in-phase signals shows that the modulated separation of charge carriers photo-generated in $CH_3NH_3PbCl_3$ was very slow.

For the sample coated with PMMA before annealing (figure 6.2 (b)), the in-phase signals were positive between energies of 1.51 to 2.3 eV and then became negative at energies above 2.3 eV. The change of sign at about 2.3 eV may be related to polarization of charge carriers at interface with PMMA which creates charging and discharging effects at the interface. An additional onset was observed in the in-phase signal at about 3.1 eV corresponding to the appearance of $CH_3NH_3PbCl_3$. Therefore, the modulated charge separation caused by photo-generation in $CH_3NH_3PbCl_3$ was much faster for the sample coated with PMMA before annealing.

For the annealed sample without the PMMA coating (figure 6.2 (c)), the in-phase and phase shifted by 90° signals showed an onset at about 1.58 eV, which was very similar to the onset of the as-deposited sample. An additional signature at about 2.3 eV, which is close to the band gap of PbI_2, was also observed in the spectrum of the in-phase signals. Therefore, annealing of the un-protected $CH_3NH_3PbI_3$ caused some degradation to PbI_2. No signature was observed for the $CH_3NH_3PbCl_3$ phase after annealing of the un-protected sample, i.e. chlorine species evaporated during the annealing [27]. The in-phase signals were positive and reached a maximum of 0.14 mV at 1.7 eV. The phase shifted by 90° signal were positive and rather low at about 1.5 eV and thereafter became negative at photon energies above 1.8 eV. The appearance of PbI_2 at the $CH_3NH_3PbI_3$ surface is a clear indication for the deficiency of methyl ammonium cation and iodide anion in the interface region which causes n-type doping of $CH_3NH_3PbI_3$ as demonstrated by positive in-phase signal [27] .

The SPV spectra of the sample onto which PMMA was deposited after annealing (figure 6.2 (d)), showed the largest signals related to charge separation in $CH_3NH_3PbI_3$ without any signatures for additional phases. Both in-phase and phase shifted by 90° were negative suggesting a change in the direction of charge separation in comparison to the other samples. Negative values of in-phase signals indicated the formation of a surface space charge region of a p-type doped semiconductor with a slight excess of methyl ammonium and iodide ions. Furthermore, the same sign of the in-phase and phase shifted by 90° were attributed to two mechanisms of charge separation with opposite directions in which trapping and de-trapping of charge carriers lead to slow modulation period [28].

Figure 6.3 (a) shows the PV amplitudes and photon flux on a logarithmic scale as a function of photon energy of the same samples shown in figure 6.2. Incidentally the amplitudes were dominated by the in-phase signals. The spectra were analyzed according to Chapter 3. The values of the band gap were about 1.58 eV and 1.57 eV for $CH_3NH_3PbI_3$ without and with PMMA respectively. PMMA coated on the $CH_3NH_3PbI_3$ reduced the band gap slightly, implying that the band gap of $CH_3NH_3PbI_3$ depends on the preparation condition. This is important for the analysis of SPV spectra at different temperatures. The exponential tails (E_t parameter) depended on the preparation conditions and PMMA coating. The values of E_t were 13, 15, 22

and 29 meV for as-deposited $CH_3NH_3PbI_3$ without annealing, annealed $CH_3NH_3PbI_3$, without PMMA, $CH_3NH_3PbI_3$ with PMMA before annealing and $CH_3NH_3PbI_3$ with PMMA after annealing, respectively. Therefore, the lowest degree of disorder was obtained for the as-deposited sample which was not annealed without PMMA coating. Furthermore, deposition of PMMA caused a strong increase of disorder in $CH_3NH_3PbI_3$ due to stress induced by the formation of the $CH_3NH_3PbI_3$/PMMA interface, and this stress has more influence on the disorder in the annealed $CH_3NH_3PbI_3$ layer.

The high disorder observed in samples coated with PMMA may be attributed to the interaction between PMMA and perovskite layers which increases the stress in $CH_3NH_3PbI_3$ films. It is speculated that, the formation of PMMA induces stress underneath which creates defects that lead to partial relaxation by introducing some disorder that increased the fluctuations among the PbI_6 octahedra. This implied that the rotation of PbI_6 octahedra depends on local stress induced by PMMA on $CH_3NH_3PbI_3$ layers. Furthermore, PMMA changed the nature of chemical bonds at and near the surface of $CH_3NH_3PbI_3$, which can also cause an increase of disorder and of surface defect states.

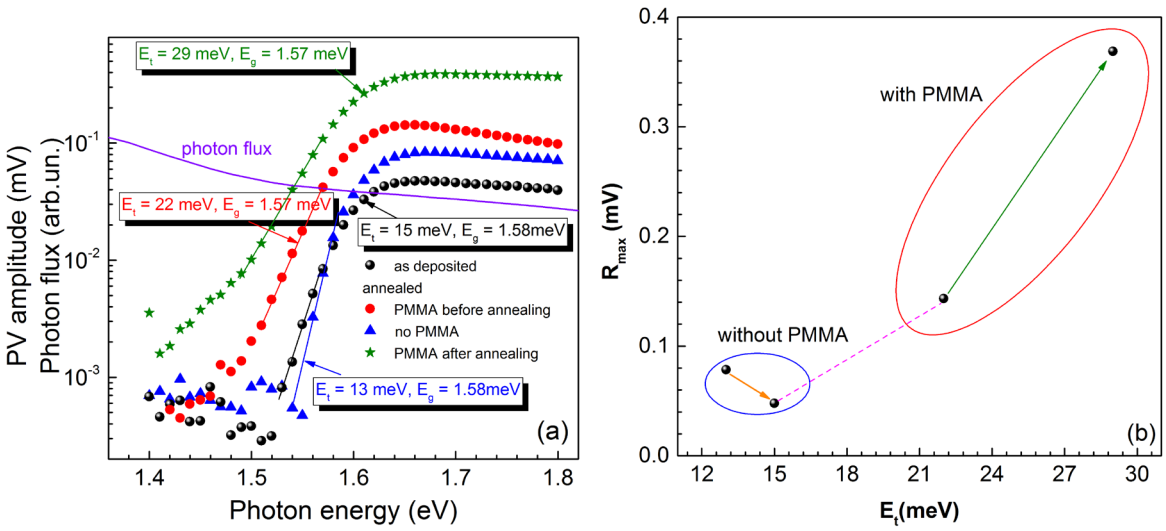

Figure 6.3: Spectra of the photovoltage amplitude near the band edge of $CH_3NH_3PbI_3$ and corresponding photon flux (a) and a plot of the maximum photovoltage amplitude as a function of the energy characterizing the exponential tails (E_t) (b)

The maximum photovoltage amplitude (R_{max}) tended to increase with the parameter describing the exponential tails (E_t). The corresponding values of R_{max} and E_t are correlated in figure 6.3 (b). R_{max} increased with increasing E_t (between 15 and 29 meV). $CH_3NH_3PbI_3$ without PMMA coating exhibited a low E_t, whereas $CH_3NH_3PbI_3$ coated with PMMA showed more defect states as demonstrated by the high value of R_{max}. The highest R_{max} was obtained for the highest E_t. For the as-deposited sample without PMMA coating, the value of R_{max} was 0.05 mV corresponding to E_t of 15 meV. For the annealed $CH_3NH_3PbI_3$ sample without PMMA coating,

R_{max} increased to 0.07 mV, whereas E_t increased from 13 to 15 meV. This implies that for bare $CH_3NH_3PbI_3$ samples, annealing lead to an increase of stress in the layers. R_{max} increased strongly by more than three times in comparison to $CH_3NH_3PbI_3$ coated with PMMA after annealing. This means that PMMA created more stress on the perovskite layer, hence more defects resulting into higher E_t of 29 meV.

During modulated SPV, separation of photo-generated electrons and holes takes place under illumination and recombination occurs in the dark. Recombination of charges separated in space is limited by transport in $CH_3NH_3PbI_3$, whereas the charge carriers have to overcome some barrier(s). As a result, some permanent charging occurs and only a certain part of photo-generated charge carriers contributes to the SPV signal. With an increasing density of defects states in the region of barrier(s), the probability for hopping increases so that recombination will become faster. As a result, the modulated photovoltage amplitude can increase with the density of defect states. For comparison, the effective densities of states are rather high at the conduction and valence band edges of c-Si (1–3 x 10^{19} cm^{-3}) [231] or a-Si:H (10^{20}–10^{21} cm^{-3} [232], E_t about 50–60 meV). Incidentally, the SPV signals decrease with increasing density of defect states if the recombination is not limited by transport. Furthermore, one has to keep in mind that an increase of E_t can distort the onset energy [27] and hence lower the band gap. This can explain the slightly reduced band gap for $CH_3NH_3PbI_3$ coated with PMMA in comparison to the uncoated sample.

6.1.3. Dependence of the phase composition of $CH_3NH_3PbI_3$ on PMMA coating and storage time in air

Figure 6.4 represents the GIXRD patterns of $CH_3NH_3PbI_3$ layers coated with PMMA deposited from solutions with the concentration of 0, 20, 40 60, 80 and 100 mg/ml for as-deposited samples. All samples exhibit similar perovskite peak except for $CH_3NH_3PbI_3$ coated with PMMA at a concentration of 80 and 100 mg/ml which showed additional peaks (represented by black arrows in figure 6.4). The GIXRD diffraction patterns were observed at about 14.2°, 20.01°, 23.5°, 28.5°, 31.9°, 35.07°, 37.27°, 40.5° and 43.5° which are the characteristics peaks of the tetragonal $CH_3NH_3PbI_3$ structure (COD 7218931). These diffraction peaks corresponded to (110), (112), (211), (202), (220), (310), (312),(321) (224) and (314) tetragonal planes of crystalline $CH_3NH_3PbI_3$, respectively [27, 12]. Two dominant peaks at 14.2° and 28.5° for the (110) and (220) planes respectively were observed in all the samples, indicating the formation of the crystalline perovskite in the tetragonal phase. Moreover, the samples had different diffraction intensities suggesting some differences in the preferential orientation of crystals in the $CH_3NH_3PbI_3$ layers. The peak intensity was relatively high for

$CH_3NH_3PbI_3$ coated with PMMA at a concentration of 40 mg/ml compared to other samples. This implied that 40 mg/ml seems to be an optimum concentration of PMMA.

The diffraction peaks at about 15.7° and 31.8° were also observed for all samples. These peaks could be correlated to the (100) and (200) diffraction peaks of $CH_3NH_3PbCl_3$ [192]. The peak intensity at 15.7° was relatively high for $CH_3NH_3PbI_3$ un-coated with PMMA at a concentration of 0 mg/ml and the intensity reduced with higher concentration of PMMA. On the other hand, the peak intensity for the (200) peak at 31.8° was relatively high for $CH_3NH_3PbI_3$ coated with 100 mg/ml of PMMA compared to other samples. Coating PMMA on top of $CH_3NH_3PbI_3$ layer could significantly increase the amount of $CH_3NH_3PbCl_3$ in the final perovskite films. This means that coating PMMA on the surface of $CH_3NH_3PbI_3$ prevented the evaporation of $CH_3NH_3PbCl_3$. Some weak extra peaks were also observed for $CH_3NH_3PbI_3$ coated with 100 mg/ml at 12.67° and 37.25° and these were ascribed to the (001) and (003) peak of PbI_2 [197, 233]. The additional peaks (shown by black arrows in figure 6.4) were observed for $CH_3NH_3PbI_3$ coated with 80 and 100 mg/ml of PMMA. For 80 mg/ml of PMMA, additional peaks appeared at 21.5°, 23.09°, 36.11°, 47.70° and 48.8°. Similarly, the non-identified peaks at 42.5°, 45.7°, and 47.5° were also observed for $CH_3NH_3PbI_3$ coated with PMMA at a concentration of 100 mg/ml. These peaks were not identified and can be related to intermediate phases that coexist with tetragonal perovskite phase [27].

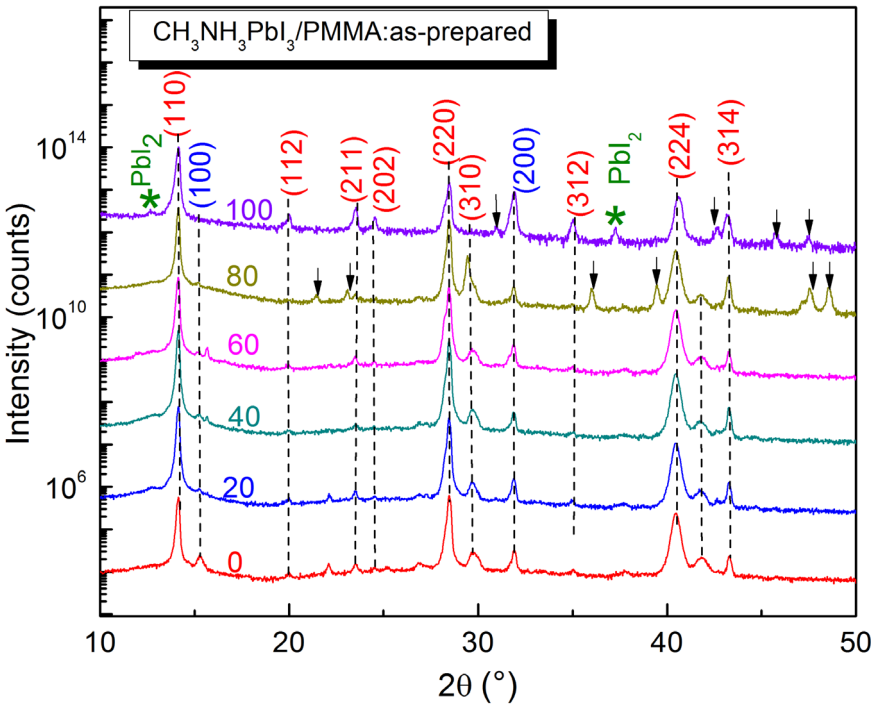

Figure 6.4: GIXRD of Mo/$CH_3NH_3PbI_3$ coated with PMMA at concentration varied from 0 to 100 mg/ml for as-deposited sample. The olive stars indicate PbI_2 peaks whereas black arrows indicate non identified peaks.

Figure 6.5 shows the GIXRD of $CH_3NH_3PbI_3$ coated with PMMA of at a concentration of 0, 20, 40, 60, 80 and 100 mg/ml after storage in air for 43 days. All samples showed $CH_3NH_3PbI_3$ peaks at 14.2°, 20.01°, 23.5°, 28.5°, 31.9°, 35.07°, 37.27° and 40.5° corresponding to (110), (112), (211), (202), (220), (310), (312), (321) and (224) respectively to tetragonal planes of crystalline $CH_3NH_3PbI_3$ [234, 12]. In addition, the intensity of the tetragonal $CH_3NH_3PbI_3$ peaks decreased for all samples with strongest reduction observed for $CH_3NH_3PbI_3$ coated with 0 and 60 mg/ml of PMMA. The decrease in the intensity of $CH_3NH_3PbI_3$ peaks in the tetragonal phase may be attributed to degradation of perovskite to constituent elements.

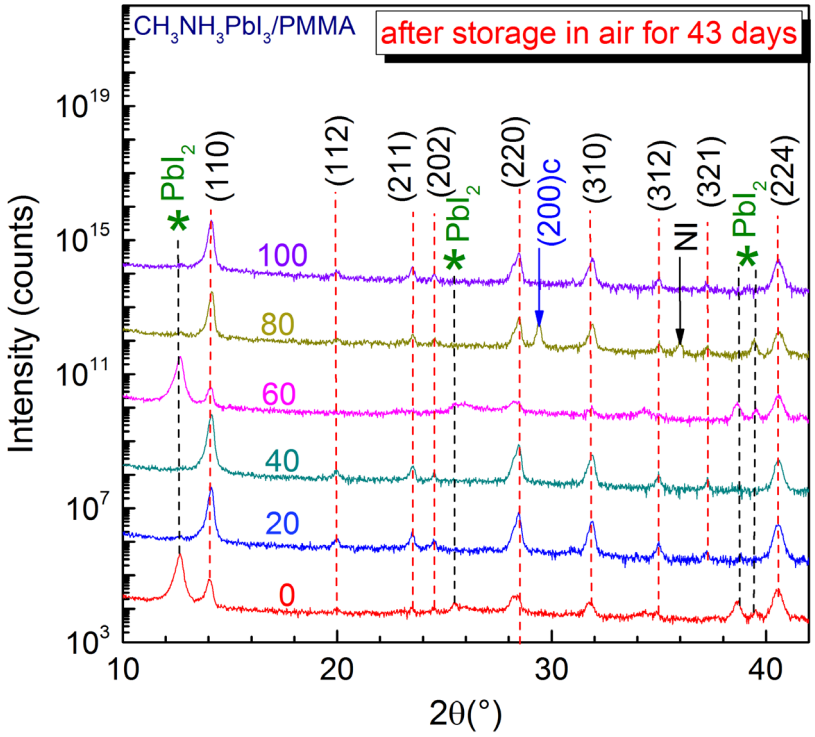

Figure 6.5: GIXRD of $CH_3NH_3PbI_3$ coated with PMMA at concentration varied from 0 to100 mg/ml after 43 days of storage in air. The olive stars indicate PbI_2 peaks, black arrows indicate non-identified peaks whereas blue arrow indicate the formation of (200) cubic peak of perovskite.

Some diffraction peaks at 12.67°, 25.5°, 38.77° and 39.5° corresponding to (001),(101), (003) and (110) planes of PbI_2 [235] were observed for $CH_3NH_3PbI_3$ coated with 0 and 60 mg/ml of PMMA. The (001) diffraction peak at 12.67° was observed for all samples except for $CH_3NH_3PbI_3$ coated with 40 mg/ml of PMMA. The intensity of the PbI_2 peak was higher for the samples with 0 and 60 mg/ml of PMMA. For the sample with 0 mg/ml of PMMA, it was speculated that the butyl acetate solvent chemically reacted with $CH_3NH_3PbI_3$ accelerating faster degradation into PbI_2 whereas $CH_3NH_3PbI_3$ coated with 60 mg/ml could have favored the growth of (001) peak of PbI_2. Some extra peaks at 29.42°and 37.45° corresponding to

(200) and (112) cubic phase of perovskite structure [12] were detected. For $CH_3NH_3PbI_3$ coated with 80 mg/ml of PMMA, this indicated that $CH_3NH_3PbI_3$ existed in two phases with continued storage in air, i.e. tetragonal and cubic perovskite phases. In addition, a non-identified (NI) peak at 36.03° was also observed $CH_3NH_3PbI_3$ coated with 80 mg/ml and absent in all samples. $CH_3NH_3PbI_3$ coated with 40 mg/ml of PMMA did not show any impurity phase even after storage in air for 43 days. This finding suggests that the optimum concentration of PMMA is 40 mg/ml for forming a protection layer on $CH_3NH_3PbI_3$.

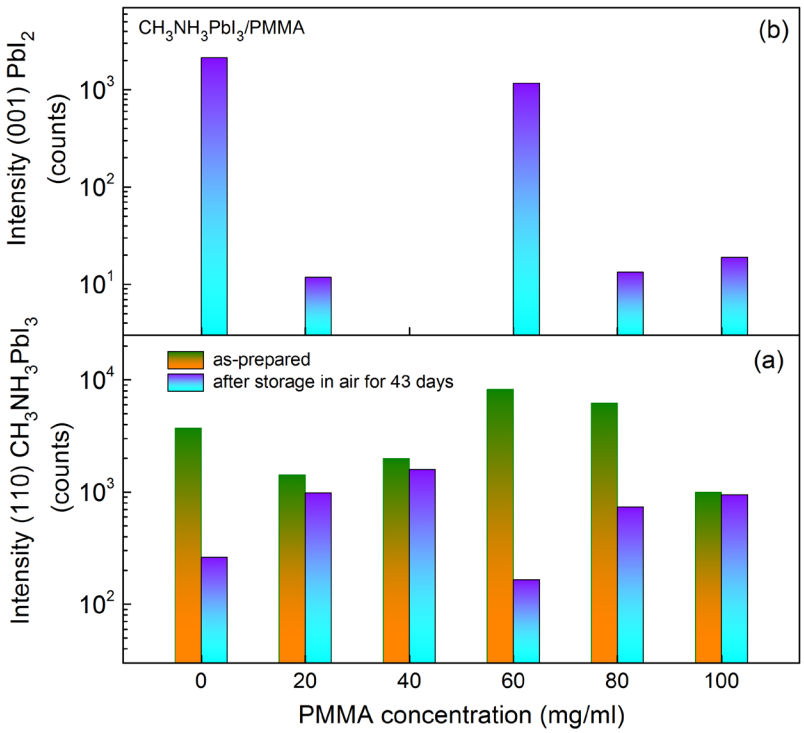

Figure 6.6: Dependence of the (110) $CH_3NH_3PbI_3$ (a) and (001) PbI_2 (b) peaks on the concentration of PMMA for as prepared (olive-orange bars) samples and for samples stored in air for 43 days (cyan-violet bars).

As a summary of the XRD measurements, figure 6.6 (a) shows the bar chart of the intensity of the (110) $CH_3NH_3PbI_3$ peak for as-prepared samples and for samples stored in air for 43 days. Incidentally, the GIXRD measurements were performed under identical conditions. The intensity of the (110) peak for the as-prepared samples were about 3721, 1429, 1989, 8218, 6218 and 1001 counts respectively. These quite large variations of the peaks were probably caused by fluctuations of the roughness (The dependence of the GIXRD signals on the preparation conditions was not investigated). After the samples have been stored in air for 43 days, the intensity of $CH_3NH_3PbI_3$ coated with PMMA reduced dramatically for some samples showing strong reduction in the magnitude of the (110) peak of $CH_3NH_3PbI_3$. $CH_3NH_3PbI_3$ coated with PMMA with 60 mg/ml showed the strongest drop of the peak intensity from 8218

counts (as-prepared) to 166 counts (after storage in air for 43 days). Un-coated perovskite (0 mg/ml of PMMA) also showed a stronger drop of $CH_3NH_3PbI_3$ peak intensity from about 3721 counts (as-prepared) to 263 counts (after storage in air for 43 days). The strong reduction in the intensity of the peak is mainly related to the ongoing decomposition of $CH_3NH_3PbI_3$ phase to other phases such as the formation of PbI_2 phase and in the presence of oxygen and light, the deprotonation of $CH_3NH_3^+$ to CH_3NH_2 and molecular hydrogen [155]. 40 mg/ml did not show any PbI_2 peak even after 43 days of storage in air hence the conclusion that 40 mg/ml was the optimum concentration of PMMA to be coated on the surface of $CH_3NH_3PbI_3$ layers.

Figure 6.6 (b) shows the bar chart for the (001) peak of the PbI_2. As can be seen, no PbI_2 peak was observed for the as-prepared samples. However, after storage of the samples in air for 43 days, the signature related to the (001) PbI_2 peak was observed for some samples. The highest intensities of the PbI_2 peak were observed for the un-coated $CH_3NH_3PbI_3$ (2139 counts) and for the $CH_3NH_3PbI_3$ coated with PMMA with 60 mg/ml (1169 counts). The intensities of the (001) PbI_2 peak were low for the $CH_3NH_3PbI_3$ samples coated with PMMA with 20, 80 and 100 mg/ml (12, 13 and 19 counts, respectively). The un-coated sample (0 mg/ml of PMMA) was equivalent to coating the solvent of butyl acetate on the surface of $CH_3NH_3PbI_3$ layer. Therefore, as the solvent evaporates, the reduction of the volume created stress in the layer and on the surface region of the $CH_3NH_3PbI_3$ layer. As a result, pores and cracks are developed in the $CH_3NH_3PbI_3$ layers, which enable penetration and diffusion of moisture and oxygen into the perovskite sample. $CH_3NH_3PbI_3$ in the presence of moisture decomposed to CH_3NH_3I and PbI_2 which further decompose to methylamine (CH_3NH_2) and hydroiodic acid (HI) [236].

6.1.4. Modulated SPV measurements of $CH_3NH_3PbI_3$ layers coated with PMMA

Figure 6.7 shows overview spectra of the modulated in-phase signals for $CH_3NH_3PbI_3$ thin films coated with PMMA deposited for different concentrations (0, 20, 40, 60, 80 and 100 mg/ml in butyl acetate). All samples showed the same onset energies of the SPV signals at about 1.5 eV, i.e. near the band gap of $CH_3NH_3PbI_3$ [24]. The existence of the $CH_3NH_3PbI_3$ phase is in agreement with the grazing incidence X-ray diffraction measurement (see figure 6.4). The concentration of the PMMA had no influence on the measured onset energy.

For $CH_3NH_3PbI_3$ coated with 0 mg/ml of PMMA, the in-phase signal was negative at photon energies below 1.5 eV, became positive at photon energy of about 1.5 eV, reached a maximum at 1.7 eV and again became negative at photon energies above 2 eV. The change of sign may be related to impurity phases. The sign of the in-phase-signals was positive over the whole spectrum for the other samples. A positive sign of the in-phase signal means that photo-generated electrons are preferentially separated towards the bulk while holes move

towards the surface. A precise analysis of the band gap and of the exponential tails is not possible if the sign of the SPV signal changes near the band gap.

For $CH_3NH_3PbI_3$ coated with 20 mg/ml of PMMA, the positive value of the in-phase signal reached maximum height at 0.5 mV corresponding to photon energy of 1.7 eV. Similarly, $CH_3NH_3PbI_3$ coated with 40 mg/ml of PMMA, the in-phase signal increased to the maximum height at 0.55 mV at photon energy of 1.7 eV. The magnitude of in-phase increased further for 60 mg/ml of PMMA with a maximum in-phase signal at 0.76 mV at photon energy of 1.7 eV. However, the magnitude of in-phase signal decreased to 0.41 mV at 1.7 eV for 80 mg/ml of PMMA. The value of in-phase signal decreased from 0.76 mV for 60 mg/ml of PMMA to 0.41 mV for 80 mg/ml of PMMA and continued to decrease further to 0.2 mV for 100 mg/ml of PMMA. In general, maximum value of in-phase signal was realized for $CH_3NH_3PbI_3$ coated with 60 mg/ml of PMMA, followed by 40 mg/ml of PMMA. However, as the concentration was increased i.e. for 80 and 100 mg/ml, the coating sample became thick and increasingly obscured the signal causing observed amplitude decrease.

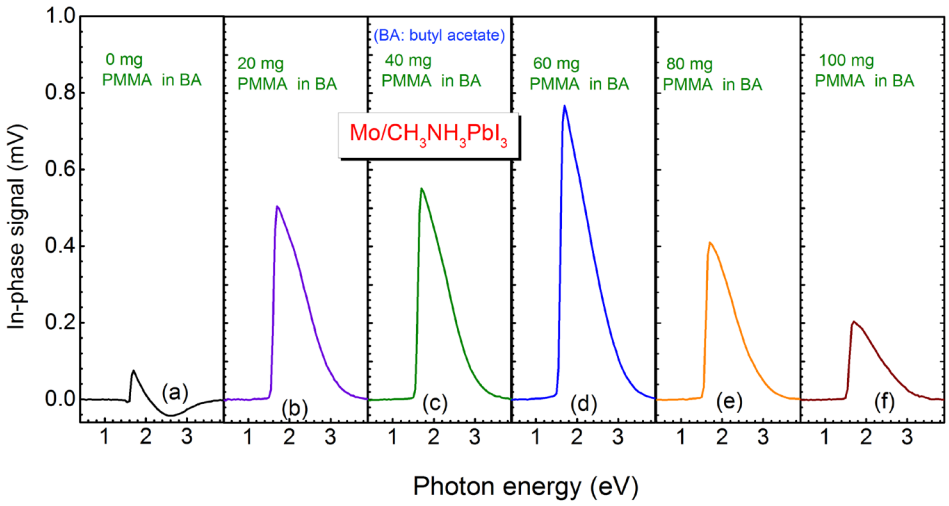

Figure 6.7: Modulated in-phase SPV signals for $CH_3NH_3PbI_3$ coated with PMMA at a concentration of 0, 20, 40, 60, 80 and 100 mg/ml of butyl acetate, (a) – (f) respectively.

Figure 6.8 shows the maximum in-phase SPV signals (X_{max}) plotted on a logarithmic scale versus storage time in air for 43 days. For $CH_3NH_3PbI_3$ coated with 0 mg/ml of PMMA, a change of sign occurred for as-prepared sample as well with continued storage in air. A kink was observed at about 2.3 eV corresponding to an impurity phase of PbI_2 [237]. The impurity phase of PbI_2 at about 2.3 eV was observed for all days which is consistent with the appearance of PbI_2 peak at 12.67 ° [238] as confirmed by the GIXRD spectrum (see figure 6.5). On the other hand, $CH_3NH_3PbI_3$ coated with 20 mg/ml of PMMA, showed no change of sign, but the sample exhibited a lot of variability in the value of maximum in-phase signal suggesting that the sample was not stable, hence not suitable for stability study.

Interestingly, the $CH_3NH_3PbI_3$ sample coated with 40 mg/ml of PMMA displayed no change of sign nor in the value of in-phase signal, however, there was a drop in the value of in-phase signal on the second day of measurement by more than one order of magnitude. Thereafter, X_{max} increased to 0.08 mV on the fifth day, 0.15 mV on the 9th day and 0.38 mV on the 19th day. After 19th day of storage in air, the value of X_{max} dropped slightly to 0.28 mV on the 32nd day of storage in air. The initial drop in the value of X_{max} could be postulated to be due to degradation when the sample was exposed to air initially. With continued exposure to air for several days, there was passivation of surface defects hence the increase in value of X_{max}. $CH_3NH_3PbI_3$ coated with 60 mg/ml of PMMA had the highest value of X_{max} at the beginning of about 0.75 mV. A sharp drop from 0.75 mV on the first day to 0.27 mV on the second day was observed and a further sharp drop to 0.12 mV on the 5th day. A change of sign occurred on the 9th day from positive to negative X_{max}. After 19th day, X_{max} changed sign to positive value at 0.016 mV and increased further to 0.028 mV on the 32nd day. The drop in the value of X_{max} together with the change of sign was attributed to the degradation of $CH_3NH_3PbI_3$ to its constituent precursor's salts. The increase in the value of X_{max} after 19th day was postulated to be as a result of charge separation of accumulated charges that pile up to cause a larger signal. A similar trend was observed also for $CH_3NH_3PbI_3$ coated with 80 and 100 mg/ml of PMMA, whereby there was a drop in the value of X_{max}, changed sign to negative on the 9th day of storage in air and thereafter changed sign again to positive on the 19th day.

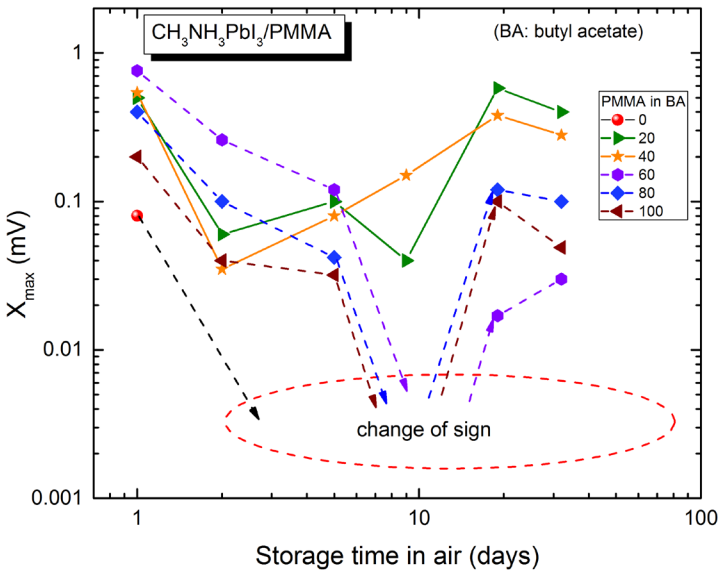

Figure 6.8: Evolution of the maximum in-phase SPV spectra with time for the perovskite coated with PMMA at a concentration of 0, 20, 40, 60, 80 and 100 mg/ml during storage in air for 43 days.

Figure 6.9 shows exponential tail states E_t as a function of PMMA concentration coated on $CH_3NH_3PbI_3$ films for as-prepared samples and for the samples stored in air for 43 days.

For as-prepared samples, the 0 mg/ml changed sign, hence precise analysis of E_t was not possible. The value of E_t increased from 18 to 25 meV as the concentration of PMMA increased from 20 to 100 mg/ml, respectively initially. After over 43 days of storage in air, E_t slightly increased to 22 and 20 meV for 20 and 40 mg/ml of PMMA respectively. On the other hand, $CH_3NH_3PbI_3$ films coated with PMMA at a concentration of 60, 80, and 100 showed slight decrease in E_t compared to as-prepared samples. In general, 40 mg/ml of PMMA had the lowest E_t in all the cases. The low value may be responsible for surface defect passivation which hinders degradation of the perovskite films to PbI_2. Therefore 40 mg/ml sample showed the least amount of tail states of about 18 meV which was relatively higher compared to the Urbach tail energy of about 15 meV, measured by De Wolf et al. [13]. The high value of E_t may be due to preparation conditions and the presence of the coating layer of PMMA which induced stress on $CH_3NH_3PbI_3$ layers creating defects. Since the criteria is to have a stable sample with no change of phase and low disorder, $CH_3NH_3PbI_3$ coated with 40 mg/ml of PMMA was chosen for the experiment and used to study temperature dependent measurement in the subsequent sections.

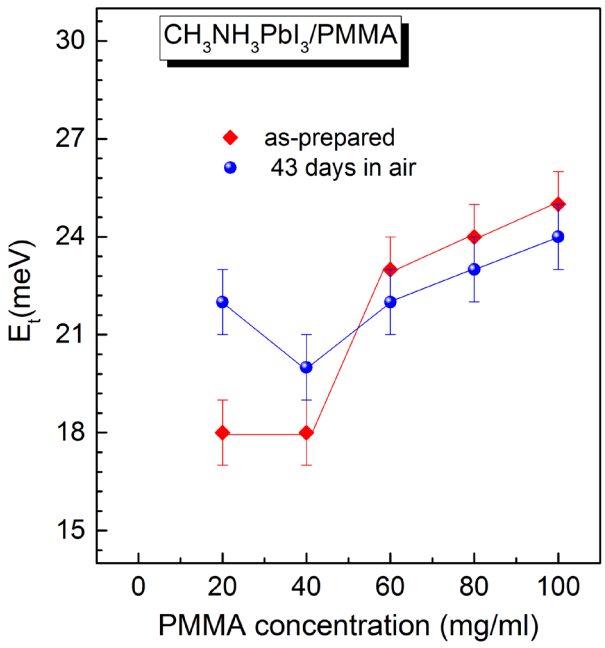

Figure 6.9: Exponential tail states E_t as a function of PMMA concentration coated on $CH_3NH_3PbI_3$ sample for as-prepared (red diamond) and after 43 days of storage in air (blue spheres).

6.2. Temperature dependent measurements of the modulated surface photovoltage for the band gap of $CH_3NH_3PbI_3$ stabilized with PMMA

6.2.1. Stability of $CH_3NH_3PbI_3$ over wide temperature range

For temperature dependent measurement by SPV, the sample to be investigated (i.e. $CH_3NH_3PbI_3$ coated with 40 mg/ml of PMMA) was connected to a temperature controller for the variation of temperature. A liquid nitrogen cryostat was used to vary the temperature between -182° C to 80°C. The SPV measurements at different temperature range were then undertaken.

Figure 6.10 shows the overview spectra of the in-phase and phase-shifted by 90° SPV signals measured at 32°C before starting and after finishing the temperature dependent measurements. All spectra showed a dominant SPV onset at photon energies between 1.5 and 1.6 eV with no impurity phase of PbI_2 observed.

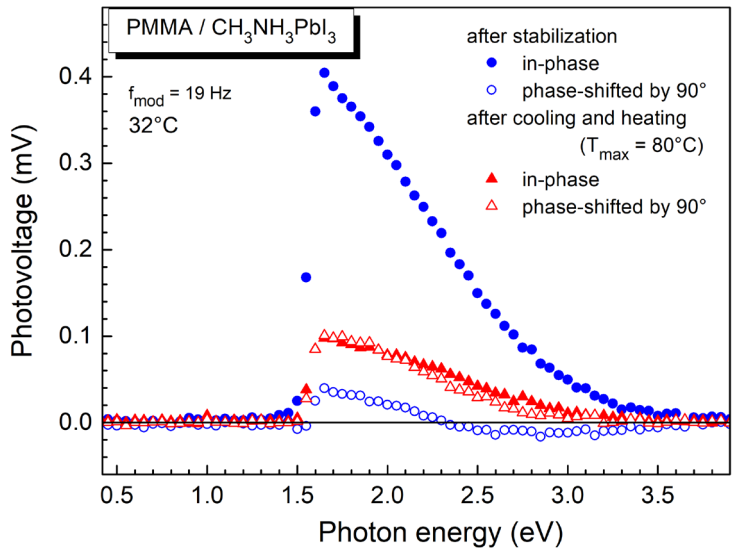

Figure 6.10: SPV overview spectra of the in-phase (filled symbols) and phase-shifted by 90° (open symbols) SPV signals measured at 32°C after stabilization (circles), and after cooling and heating cycles with a maximum temperature of 80°C (triangles).

Near the band gap E_g, the signs of the in-phase and phase-shifted by 90° signals were positive indicating two mechanism of charge separation in which photo-generated electrons were preferentially separated towards the substrate and holes to the sample surface [28]. Immediately after stabilization, in-phase signal was 0.41 mV, but after heating and cooling to 80°C, the value reduced to 0.1 mV. This implied that after complete temperature dependent measurements, the in-phase signals reduced by about four times their initial value. On the contrary, the signal of the phase shifted by 90° was 0.04 mV and 0.1 mV at the start and end

of temperature dependent measurement, respectively. Suggesting that phase shifted by 90° signals increased by more than two times its initial value. Charge separation under two mechanism may be caused by many processes including partial trapping and de-trapping of charge carriers at the interface of PMMA with $CH_3NH_3PbI_3$ [28]. This behaviour can be interpreted as a reduction of the diffusion length of photo-generated charge carriers due to degradation and defect generation.

The SPV phase angle gives information about the direction of charge separation in relation periodic modulation. For instance, a phase angle of 0° or 180° means a fast response relative to the periodic modulation of incident light. Whereas, a phase angle of 90° or -90° (270°) means a slow response with respect to the modulation period [205]. Figure 6.11 shows the phase angle measured at 32° C before starting temperature dependent measurement (violet star) and after cooling and heating cycles (red spheres). After stabilization, near the band gap at about 1.5 eV, the phase angle increased towards 0° and remains nearly constant from 1.6 eV to about 2.5 eV. Similar behaviour was demonstrated after cooling and heating cycles in which the phase angle increased towards 90° and remains constant at about 45° in the energy range between 1.6 and 2.5 eV. A shift in phase angle from 0° during stabilisation to 45° after cooling and heating cycles implied that there exist many mechanism of charge separation and relaxation in which photo-generated electrons are separated towards the bulk (internal) whereas photo-generated holes are preferentially separated towards the external surface.

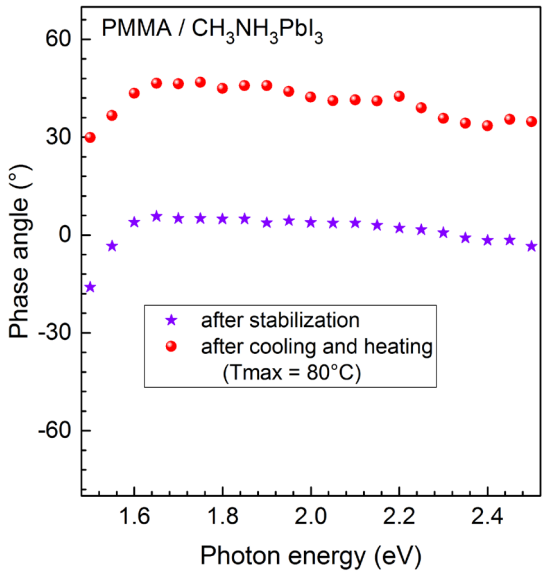

Figure 6.11: SPV phase angle measured at 32°C after stabilization (violet stars), and after cooling and heating cycles with a maximum temperature of 80°C (red spheres).

6.2.2. Temperature dependencies of the in-phase and phase shifted by 90° signals

Figure 6.12 (a) shows in-phase and the 90° phase shifted SPV signals measured at 32°C (room temperature) immediately after stabilization (blue circles),after cooling (red triangles) and after heating (black stars) as a function of photon energy. After stabilization, the in-phase signal was positive for all energies above 1.49 eV and peaked at 0.35 mV corresponding to an energy of 1.63 eV. The 90° phase shifted signal was negative for all energies below 1.56 eV and thereafter became positive. After cooling to room temperature (red triangles), in-phase signal remained positive, with the signal height increasing from 0.35 mV to 0.42 mV. Cooling enhances transport and separation of photo-generated charge carriers. The 90° phase shifted signal increased slightly after cooling and became positive for all values above 1.56 eV. After heating and cooling the sample to room temperature (black stars), the in-phase signal decreased by about 4 times the initial value whereas the phase shifted one increased by more than two times. This behaviour was interpreted to be due to degradation of the sample after exposure to high temperature measurements. The band gap remained constant at 1.51 eV for the stabilization, heating and cooling.

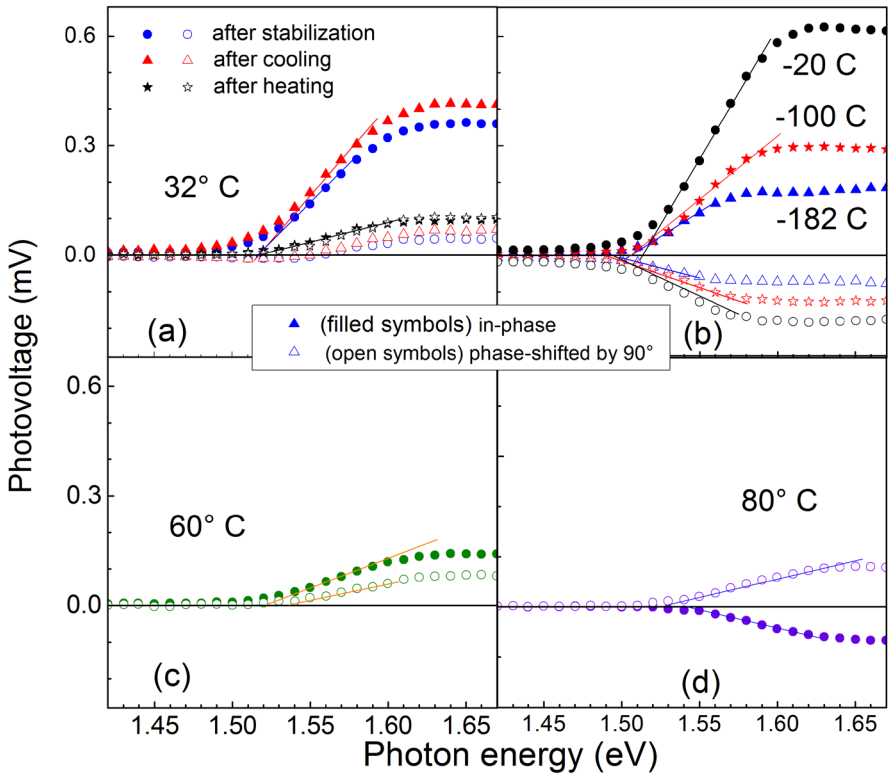

Figure 6.12: SPV spectrum of $CH_3NH_3PbI_3$ layers measured at 32°C (a), after cooling at -20°C,-100°C & -182° C (b), heating at 60°C (c) and at 80°C (d) measured in the energy range near the band gap between 1.42 to 1.67 eV

Figure 6.12 (b) shows the in-phase and the 90° phase shifted signals in the cooling regime. At -20°C, the in-phase signal was positive while the 90° phase shifted signal was negative. Opposite signs in the value of in-phase and phase shifted by 90° signals revealed a one mechanism of charge separation in which photo-generated electrons are preferentially separated towards the internal interface whereas holes towards external surface. The value of the in-phase and the 90° phase shifted signals had a maximum height of 0.64 corresponding to energy of 1.63 eV and -0.19 mV at photon energy of 1.62 eV, respectively. In-phase and the 90° phase shifted signals decreased further to 0.29 mV and -0.12 mV, respectively as the cooling continues to -100°C. On cooling further to -182°C,the in-phase and phase shifted by 90° decreased further to 0.17 mV and -0.07 mV respectively.

When the sample was heated to 60°C (figure 6.12 (c)), the in-phase signal decreased by 3 orders of magnitude i.e. from 0.36 mV (at 32° C) to 0.14 mV (at 60° C). Both the in-phase and the 90°phase shifted signals were positive at energies above 1.52 eV, with the onset energy at 1.52 and 1.54 eV, respectively. The positive value of the in-phase and the 90° phase shifted signals implied that there are two mechanism of charge separation with electrons preferentially separated towards the interface and holes to the surface and that trapping of charge carriers lead to charge separation with opposite directions [28].

For the sample heated to 80°C (figure 6.12 d), in-phase signal changed sign from positive to negative while the 90° phase shifted signal remained positive. The change of sign of the in-phase signal give evidence for the onset of degradation of $CH_3NH_3PbI_3$ at the interface with PMMA. This is because at about 80°C, recombination of charge carriers increases due to thermal activation and the cycle is non reversible. The degradation at this temperature has also been observed for PMMA based hole transporting materials that approach the glass transition temperature of the polymer [160].

Figure 6.13 illustrates the measurement regime showing the temperature dependencies of the maxima of the in-phase (X_{max}) and the 90° phase shifted (Y_{max}) signals. The temperature dependencies of X_{max} and Y_{max} follow similar trends independent of whether the signals were obtained in the low or high temperature cycles. For low temperature measurements (figure 6.13 (a)), the values of X_{max} reached a maximum at about 0°C and a minimum at about -160° C. Similarly Y_{max} reached a maximum at -60° C and changed sign between 20 and 32°C. During a cycle of low temperature measurements , the values of X_{max} and Y_{max} at 32°C increased by about 20%, with no change of sign of the X_{max} suggesting that there was no degradation at low temperatures.

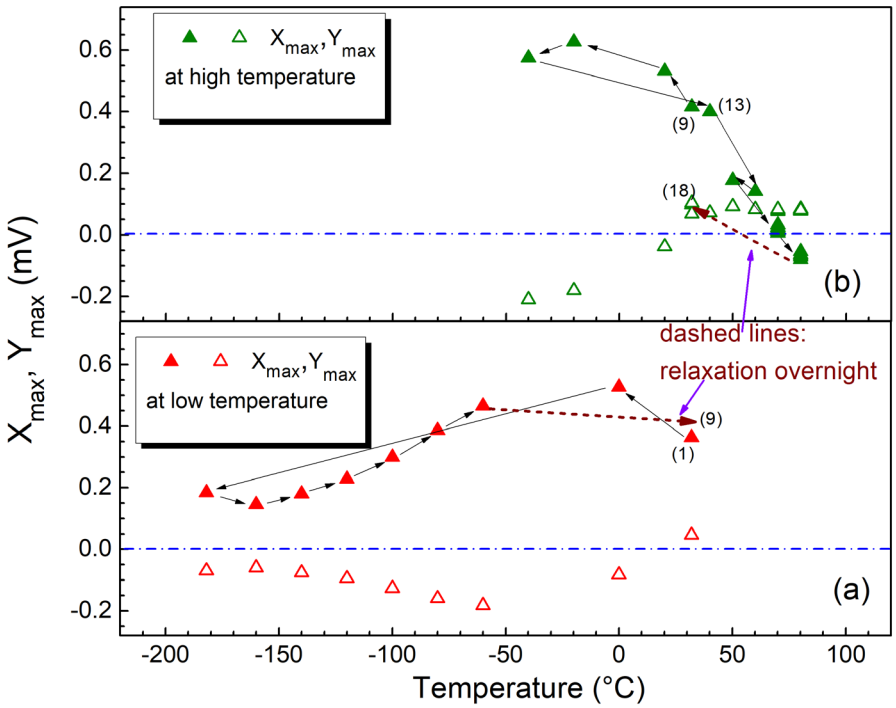

Figure 6.13: Temperature dependencies of the maxima of the in-phase (filled triangles, X_{max}) and the 90°phase shifted (open triangles, Y_{max}) SPV signals at low temperature (a) and high temperature (b) measurements, respectively. The arrows mark the regime of cooling or heating. The dashed arrows mark the relaxation overnight of X_{max} to the initial temperatures after the measurements at low (red symbols) or high (olive symbols) temperatures (to points (9) or (18), respectively).

However, for high temperature measurements (figure 6.13 (b)), X_{max} reaches a maximum at -20°C before its value starts to reduce during continued measurements up to 70°C and changes to negative at 80°C giving evidence of ongoing degradation at the PMMA / $CH_3NH_3PbI_3$ interface. Therefore a reliable analysis of the in-phase signals was only possible between -182 and 60°C. The value of Y_{max} increased linearly from -40° C to 20° C, changed the sign to positive value at about 30°C and thereafter remained constant with increasing temperature. The change of sign in both the value of in-phase and phase shifted by 90° signals may be related to the degradation at the interface between $CH_3NH_3PbI_3$ and PMMA.

Figure 6.14 (a) presents the SPV spectra of the in-phase and the 90° phase shifted SPV signals measured at 32° C after cooling. The onset energies of the in-phase and the 90° phase shifted signals ($E_{on\text{-}X}$ and $E_{on\text{-}Y}$, respectively) were obtained from the intersection points of the corresponding baselines and of the tangents in the inflection points of the spectra. For the given spectra, the values of $E_{on\text{-}X}$ and $E_{on\text{-}Y}$ were 1.518 and 1.539 eV, respectively.

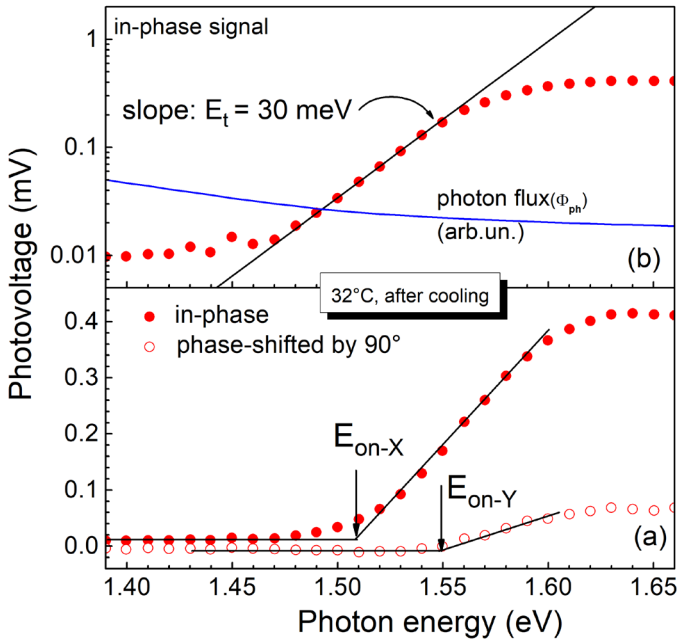

Figure 6.14: Spectra of the in-phase (filled circles) and phase-shifted by 90° (open circles) SPV signals measured around the band gap of $CH_3NH_3PbI_3$ at 32°C after cooling (a), of the in-phase SPV signals on a logarithmic scale (b). The solid lines in (a) describe the definitions of the onset energies (E_{on-X} and E_{on-Y}). The black and blue solid lines in (b) describe the slope of the exponential tails (E_t) and the photon flux, respectively.

Figure 6.14 (b) shows the in-phase SPV signals on a logarithmic scale. The exponential increase of the signal can be described by the energy of the band tails (E_t). The value of E_t amounted to 30 meV for the given spectrum which was significantly larger than for uncoated layers of $CH_3NH_3PbI_3$ (E_t can be as low as 15 meV, see, for example [13]). Therefore, the interaction between the PMMA and the $CH_3NH_3PbI_3$ layers resulted into an increase in the amount of disorder in the film. As remark, consideration of the spectrum of the photon flux would lead to a slight decrease of E_t due to the fact that different processes, some with even opposite signs of charge separation may contribute to SPV signals causing non-linear behaviour.

Figure 6.15 shows the temperature dependencies of the onset energies of the in-phase (E_{on-X}) and the 90° phase shifted (E_{on-Y}) signals between -182°C and 60°C. At temperatures between -182°C to -20°C, E_{on-X} and E_{on-Y} have similar dependencies even though the values of E_{on-X} were larger than the values of E_{on-Y} by about 0.01 eV. The values of E_{on-X} increased from 1.52 eV at -20° C to 1.522 eV at -60° C and thereafter decreased to 1.513 eV at -182° C. At 20° C, the value of E_{on-X} was 1.516 eV, increased to 1.518 eV at 32° C and became saturated for higher temperatures at 1.524 eV. On the contrary, the value of E_{on-Y} changed dramatically from 1.501 eV at 0°C to 1.548 eV at 40°C. Note that the reason for this strong change may be

due to variation in the dominating mechanisms of modulated trapping and de-trapping processes leading to a change of sign of the phase shifted by 90° signal as shown in figure 6.13. Moreover, above 40°C, the value of $E_{on\text{-}Y}$ decreased towards $E_{on\text{-}X}$ with the increase in temperature.

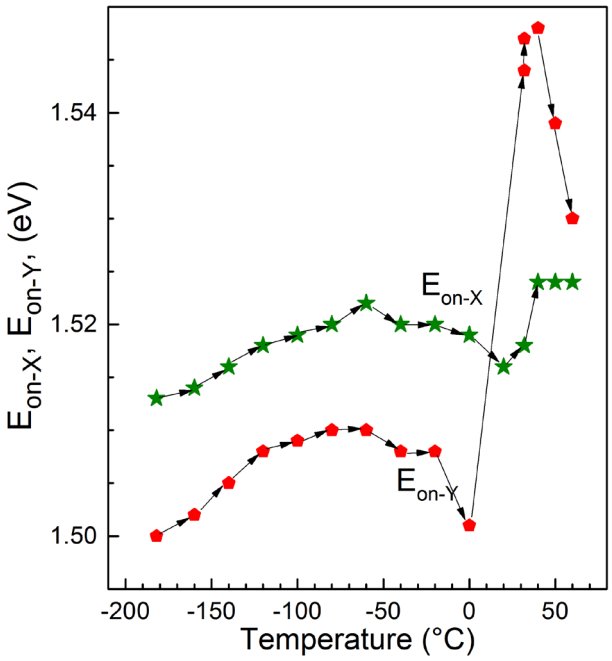

Figure 6.15: Temperature dependencies of $E_{on\text{-}X}$, and $E_{on\text{-}Y}$, (filled diamonds, and filled stars, respectively).The arrows describe the temperature dependencies from low to high temperatures.

6.2.3. Temperature dependence of the exponential tail states of $CH_3NH_3PbI_3$ stabilized with PMMA

The temperature dependence of the steepness parameter is used to deduce the physical origin of the exponential tail states during the charge separation process. Under this approach it is assumed that the dominant cause of exponential tail states is due to electron-phonon interaction as well as the contributions from charged defects [239].

Figure 6.16 (a) shows the temperature dependence of the exponential tail states E_t for $CH_3NH_3PbI_3$/PMMA. The value of E_t decreased monotonously with decreasing temperature from 24 meV at 0°C to 13 meV at -160 °C but scattered between 25 and 30 meV in the temperature range between 20 and 60 °C which can be correlated to an additional indication for the change of stress at the PMMA/ $CH_3NH_3PbI_3$ interface. Furthermore, disorder can increase in the tetragonal phase of $CH_3NH_3PbI_3$ with increasing temperature due to increased thermal vibration of $CH_3NH_3^+$ cations as well as continuous tilting of the average Pb-I-Pb bond angle towards 180° [47]. In addition, an increase in the disorder can be as a result of the re-organisation of photoferroic domains [236]. Further, the increase of E_t from 13 meV at −160°C to 18 meV at −182 °C gives evidence for an increase of disorder in $CH_3NH_3PbI_3$ with

decreasing temperature in this range and might be an indication for a starting phase transition to orthorhombic phase. The absence of a signature of the orthorhombic phase would not be surprising if taking into account that the orthorhombic phase of $CH_3NH_3PbI_3$ does not exist at pressures above 100 MPa [240] and that the reduced temperature of the phase transition from the tetragonal to the cubic phases of $CH_3NH_3PbI_3$ may be related to a pressure between 200 and 300 MPa.

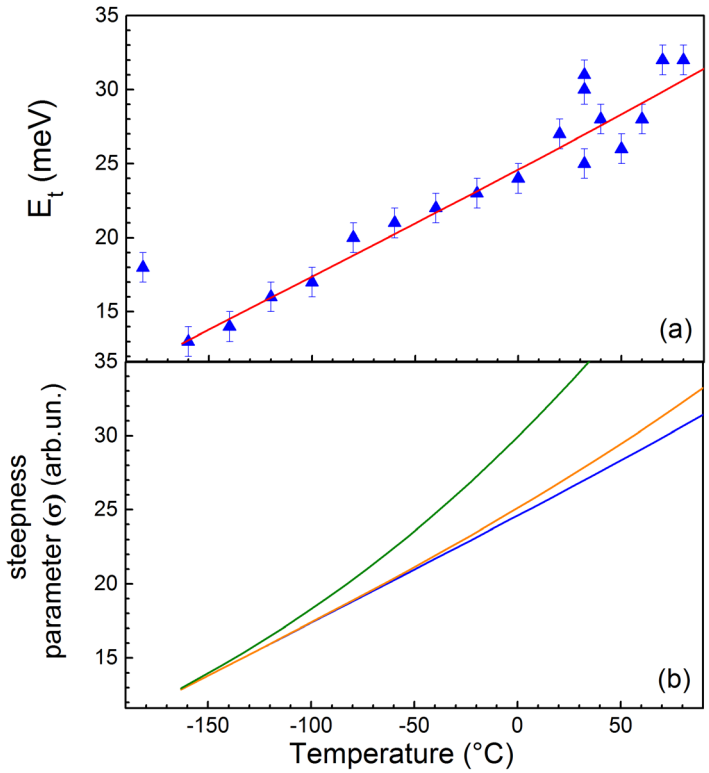

Figure 6.16: Dependence of E_t as a function of temperature. Solid line (red) is a fit whose value is given by equation 5.1.(a) and steepness parameter as a function of temperature at phonon energies of 150´meV (blue line), 100 meV (orange line) and 50 meV (olive line)(b) for $CH_3NH_3PbI_3$/PMMA.

An analysis of the temperature dependence of the slope, i.e. the steepness parameter of E_t was obtained (see the red line in figure 6.16 (a)). The variation of the steepness parameter was fitted with an empirical relation given by [96,241,242]:

$$\sigma = \sigma_0 \left(\frac{2k_BT}{E_{ph}}\right) tanh\left(\frac{E_{ph}}{2k_BT}\right) + E_{offset} \qquad 6.1$$

where σ_0 is a material dependent parameter which describes the excitation energy of $CH_3NH_3PbI_3$ layers, $E\mathrm{ph}$ is the phonon energy associated with E_t, k_B is the Boltzmann constant which is approximately 26 mV at 300 K while T is the absolute temperature. E_{offset} = 5 meV is an offset energy which arises due to coating PMMA on $CH_3NH_3PbI_3$ layers. The steepness

parameter increased with increasing temperature in the range of -160 to 80 °C. It reflects the thermal occupancy of phonon modes in the crystal and attributes E_t to electron phonon interaction as well as charged defects. The fittings yielded σ_o = 0.2475 and E_{ph} = 150 ± 40 meV. The value of E_{ph} was in agreement with the one obtained by Ledinski et al. [243] using Fourier transform photoelectron spectroscopy. The large value of phonon energy of about 150 meV may be attributed to longitudinal optical phonons which causes increased localization due to the tilting of the inorganic PbI_6 octahedral. Moreover disorder leads to the deformation of the energy bands forming exponential tail states E_t which influence the charge separation process at the band edge. Figure 6.16 (b) shows the dependence of steepness parameter (σ) on temperature. As phonon energy (E_{ph}) is decreased from 150 to 50 meV, the steepness parameter increased. It is evident that a decrease in phonon energy causes an increase in σ and hence an increase in E_t.

The band gap E_g was determined by analysing the intersection point in the Tauc plot [178] (i.e. the $E_{g\text{-}Tauc}$ in figure 6.17 (a)) and the inflexion point of the in-phase signals ($E_{g\text{-}ip}$, figure 6.17(b)). A linear dependence of the in-phase signal on the photon flux has been assumed for the Tauc plot. This reasonable assumption means that the limiting factors did not change within the analysed part of a given spectrum and that the SPV signals could be treated as small signals.

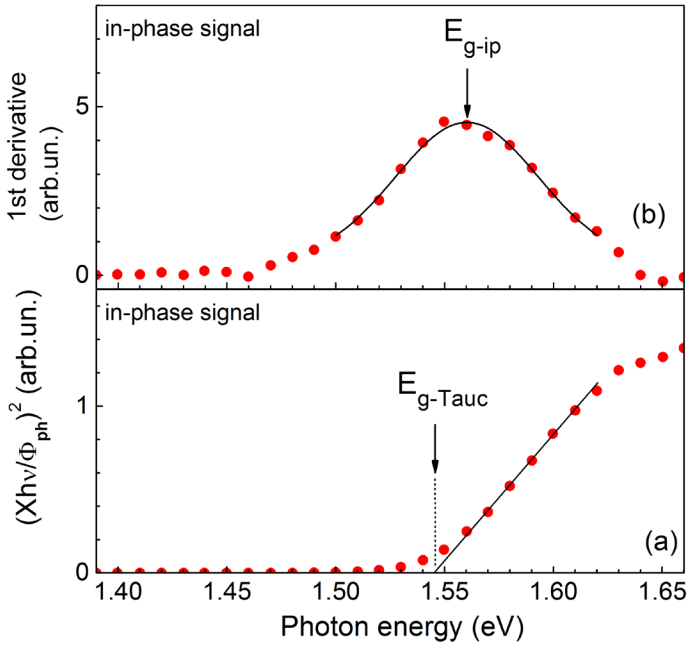

Figure 6.17: The so called Tauc plot from SPV measurements corresponding to the second power of the product of the in-phase (X) signal and photon energy divided by the photon flux (Φ_{ph}) plotted against incident photon energy (a); the first derivative of the in-phase SPV signals (b). The solid lines in (a) and (b) describe the determination of the $E_{g\text{-}Tauc}$, and the fit of the peak with a Gaussian function giving the value of $E_{g\text{-}ip}$ at the peak position respectively.

The Tauc gap was obtained by extrapolating the linear fit at photon energies above the exponential range to the photon energy axis. The inflexion point was obtained by fitting the first derivative with the Gaussian function. The values of $E_{g\text{-}Tauc}$ and $E_{g\text{-}ip}$ were 1.546 and 1.56 eV, respectively, for the given spectrum. The small deviations in the band gap can be attributed to different analysis methods employed in the determination of the band gap energy.

The temperature dependencies of $E_{g\text{-}ip}$ and $E_{g\text{-}Tauc}$ were given in figure 6.18. $E_{g\text{-}ip}$ and $E_{g\text{-}Tauc}$ decreased monotonously with decreasing temperature at temperatures below or equal to 32°C. This anomalous behaviour in which band gap increases with increase in temperature between -182° to 32°C may probably be due to lattice dilation which arises due to thermal expansion [31, 64] and consequently changes the energy band gap. $E_{g\text{-}ip}$ and $E_{g\text{-}Tauc}$ increased steeply by 0.01 eV between 32°C and 40°C and decreased to 1.569 at 50°C and 1.567 at 60°C.

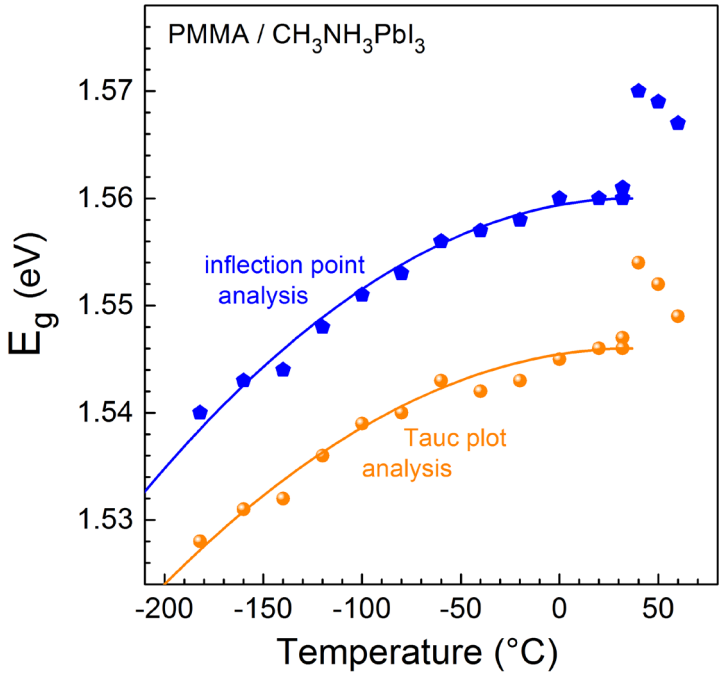

Figure 6.18. Temperature dependent of $E_{g\text{-}ip}$ and $E_{g\text{-}Tauc}$ (filled diamond and spheres, respectively). The solid lines describe the temperature dependencies of $E_{g\text{-}ip}$ and $E_{g\text{-}Tauc}$ below 30-40°C by the empirical function (equation (5.2)).

The steep increase of E_g between 32°C and 40°C is probably related to the phase transition from the tetragonal to the cubic phases if taking into account that the interaction between PMMA and $CH_3NH_3PbI_3$ could reduce the transition temperature. The decrease of $E_{g\text{-}ip}$ and $E_{g\text{-}Tauc}$ between 32 and 40 °C can be related to phase transition from tetragonal to cubic phases at 54°C [41].It is known from literature that the transition temperature of $CH_3NH_3PbI_3$ from tetragonal to cubic phases decreases with increasing pressure [240]. Therefore, the discrepancy between the transition temperatures measured for $CH_3NH_3PbI_3$ at normal pressure [44] and measured for $CH_3NH_3PbI_3$ coated with PMMA can be caused by an

interaction between PMMA and $CH_3NH_3PbI_3$ layers leading to an increase in stress in $CH_3NH_3PbI_3$. With respect to the phase diagram of $CH_3NH_3PbI_3$, the stress between $CH_3NH_3PbI_3$ and PMMA layers would be equivalent to a pressure between 200 and 300 Mpa in the $CH_3NH_3PbI_3$ layers.

The values of E_g above 32−40 °C can be related to the temperature dependence of E_g of the cubic phase of $CH_3NH_3PbI_3$. The decrease of E_g with increasing temperature by (1−2) × 10^{-3} eV/K between 40 and 60°C seems reasonable for the cubic phase of $CH_3NH_3PbI_3$ in comparison to conventional semiconductors [30].The decrease of E_g of the tetragonal phase of $CH_3NH_3PbI_3$ with decreasing temperatures can be empirically described by a quadratic dependency:

$$E_g(T) = E_g(T_0) - b \cdot k_B \cdot (T_0 - T)^2 \qquad 6.2$$

where T_0 is the temperature of the phase transition from the cubic to tetragonal phase (310 K has been chosen). The band and gap E_g can be $E_{g\text{-}ip}$ and $E_{g\text{-}Tauc}$ in which $E_{g\text{-}ip}(T_0)$ and $E_{g\text{-}Tauc}(T_0)$ are equal to 1.560 and 1.546 eV, respectively. k_B is the Boltzmann constant (8.62×10^{-5} eV/K) and b is a free parameter (about 0.0055 and 0.0048 for $E_{g\text{-}ip}(T)$ and $E_{g\text{-}Tauc}(T)$ respectively). No specific signature of E_g has been observed for the transition from the tetragonal to the orthorhombic phases at around −111 °C [240].

The shift of E_g is caused by the dilation of the crystal lattice due to thermal vibrations. This results in a lattice deformation potential [244] with respect to the volume of the unit cell. The lattice deformation potential is just the slope of E_g relative to the change in the volume of the unit cell. Given that, E_g of $CH_3NH_3PbI_3$ layers increases with increase in temperature, lattice dilation was the dominant parameter which contributed to positive temperature coefficient as well as positive band gap deformation potential of the system with respect to volume [236]. In the tetragonal phase of $CH_3NH_3PbI_3$ layers, the PbI_6 octahedron was tilted in the ab-plane resulting in the doubling of the volume of the unit cell [245]. A similar behavior was also observed in orthorhombic phase in which unit cell volume increases two times further along the c-axis. For the given temperature range, the change of E_g for the PMMA/$CH_3NH_3PbI_3$ system investigated by the surface/interface sensitive SPV was less by about 3 times in comparison to small (uncoated) single crystals of $CH_3NH_3PbI_3$ investigated by PL [246]. The lattice parameters perpendicular or along to the c-axis of the tetragonal phase of in $CH_3NH_3PbI_3$ decrease or increase, respectively, and the rotation angle of the PbI_6 octahedron increases monotonically with a decrease in temperature [247]. The corresponding increase of the Pb−I−Pb bond length along the c-axis with decreasing temperature and local variations in the rotation angle of the PbI_6 octahedron depended on the behavior of the $CH_3NH_3^+$ cation and of local stress. It can be supposed that the increase of the lattice constant along the c-axis with decreasing temperature was the reason for the unusual behavior of the temperature

dependence of E_g of the tetragonal phase of $CH_3NH_3PbI_3$ and that a reduced degree of freedom for local rotation of the PbI_6 octahedron may be the origin for changes in phase transitions toward the cubic phase at higher temperatures and toward the orthorhombic phase at lower temperatures.

6.3. Summary

Modulated SPV spectroscopy was used to investigate the temperature dependence of E_g and E_t for $CH_3NH_3PbI_3$ layers. To avoid the degradation of $CH_3NH_3PbI_3$ in vacuum during temperature dependent SPV measurements, a poly (methyl methacrylate) (PMMA) layer was deposited on $CH_3NH_3PbI_3$ films and optimized in order to stabilize the $CH_3NH_3PbI_3$ films. The stabilization of $CH_3NH_3PbI_3$ films with PMMA was necessary since a stable perovskite sample was required for temperature-dependent measurements over a wide temperature range.

Before the temperature dependent measurements were performed, the influence of PMMA on exponential tails (E_t parameter) of $CH_3NH_3PbI_3$ layers was studied using modulated SPV. E_t depended on the preparation conditions and PMMA coating. Low values of E_t of about 13 meV was obtained for the $CH_3NH_3PbI_3$ layers without PMMA coating whereas high values of E_t of about 28 meV was obtained for $CH_3NH_3PbI_3$ layers coated with PMMA. This means that the deposition of PMMA caused a strong increase of disorder in $CH_3NH_3PbI_3$ due to stress induced by the formation of the $CH_3NH_3PbI_3$/PMMA interface. The high disorder observed in samples coated with PMMA may be attributed to the interaction between PMMA and perovskite layers which increases the stress in $CH_3NH_3PbI_3$ films. It was speculated that the formation of PMMA induces stress underneath which defects are created that lead to partial relaxation by introducing some disorder that increased the fluctuations among the PbI_6 octahedra.

The temperature dependencies of E_g and E_t were investigated using modulated SPV spectroscopy. E_g and E_t of $CH_3NH_3PbI_3$ increased with increasing temperature. The results showed that thermal expansion gives the predominant contribution to the temperature dependence of the band gap of $CH_3NH_3PbI_3$. A jump in the value of E_g near the region of phase transition was observed and was related to the phase transition from the tetragonal to the cubic phases.The value of E_t increased monotonously with increasing temperature from 13 meV at -160 °C to 24 meV at 0°C but scattered between 25 and 30 meV in the temperature range between 20 and 60 °C. The scatter was related to stress at the PMMA / $CH_3NH_3PbI_3$ interface. Furthermore, with increasing temperature, disorder can increase in the tetragonal phase of $CH_3NH_3PbI_3$ due to increased thermal vibrations of $CH_3NH_3^+$ cations as well as continuous tilting of the average lead-iodine-lead bond angle towards 180° [47]. The temperature dependence of E_t was fitted with a model which takes into account phonon-induced disorder and a phonon energy E_{ph} of 150 ± 40 was obtained.

CHAPTER 7

Summary and Outlook

In this thesis, selected electronic, structural and optical properties of hybrid organic-inorganic lead halide perovskite ($CH_3NH_3Pb(I_{1-X}Br_X)_3$) were studied as functions of preparation conditions, interfaces and degradation. The band gap, the characteristic energy of the exponential tails and the diffusion length changed depending on time of storage in different ambient and light soaking, on substrates and coatings and on temperature treatments, which are important factors for the stability of perovskite solar cells. Modulated surface photovoltage (SPV) spectroscopy was used as the main method to characterize the electronic properties related to E_g, E_t and L. The SPV measurements were performed in nitrogen atmosphere in a home-made chamber. SPV analysis does not require a preparation of contacts and can be performed ex-situ after different stages of layer preparation and/or treatments or in-situ, for example, during light soaking.

Thin layers of $CH_3NH_3Pb(I,Br)_3$ films were fabricated by spin coating of a solution onto various substrates at room temperature in a glove box. The formation of the $CH_3NH_3Pb(I,Br)_3$ films depended on solvents, additives, temperature and substrates. The samples were in air for 1 – 2 min during the transfer from the glove box into the measurement chamber. In some experiments, E_g and E_t determined by SPV were correlated with E_g and the Urbach tails (E_u), which were obtained from UV-Vis spectroscopy and PDS measurements. GIXRD was used for the determination of the phase composition and of the stoichiometry of $CH_3NH_3Pb(I_{1-x}Br_x)_3$ films. Vegard's law was used to obtain the composition of $CH_3NH_3Pb(I_{1-X}Br_X)_3$ films since the lattice constant decreases linearly with increasing x in $CH_3NH_3Pb(I_{1-X})Br_X)_3$ composition.

The variation of E_g with the composition of bromide (x) in $CH_3NH_3Pb(I_{1-X}Br_X)_3$ perovskite films was investigated by modulated SPV and UV-Vis spectroscopies. E_g of $CH_3NH_3Pb(I_{1-X}Br_X)_3$ films was tuned from (1.56) 1.59 eV to 2.30 eV by varying the stoichiometry of the perovskite. E_g of $CH_3NH_3Pb(I_{1-X}Br_X)_3$ films blue shifted with increasing content of bromide whereas the bowing parameter was 0.36 eV. The blue shift can be attributed to different spin-orbit interactions between lead-iodide and lead-bromide ions. The lowest values of E_t of up to about 15 meV were obtained for the pure $CH_3NH_3PbI_3$ and $CH_3NH_3PbBr_3$ films.

The values of E_g and E_t depended sensitively on the kind of interface as shown by modulated SPV spectroscopy. $CH_3NH_3PbI_3$ deposited on double layers of TiO_2-PCBM and SnO_2-PCBM showed a constant band gap of 1.58 eV and low scatter in the value of E_t. This was attributed to the modification of the TiO_2 or $SnO_2/CH_3NH_3PbI_3$ interfaces by the PCBM

which allowed for efficient charge separation and transfer. In contrast, $CH_3NH_3PbI_3$ deposited on TiO_2 showed relatively large values of E_t which was correlated to the significant density of shallow traps in the TiO_2 that allowed for the excitation of charge carriers from the valence band of perovskite into defect states at the interface with TiO_2.

The diffusion or transport length was measured for $CH_3NH_3PbI_3$ layers by the method after Goodman. *L* was studied as a function of degradation under light soaking. For the investigation of *L*, the modulated SPV signals were kept constant by varying the light intensity and the light intensity was plotted as a function of the absorption length. A decrease of *L* with increasing time of light soaking was observed. The decrease was attributed to light-induced degradation which arises due to trap states and charging- discharging effect at the TiO_2/ $CH_3NH_3PbI_3$ interface. After 12 h of light soaking, *L* depended on the value of the modulated SPV signal, i.e. on the generation rate. The strong variation of *L* with modulated SPV signals was an indication of defects and/or inhomogeneity of the films which led to changes in the quasi Fermi levels over the whole range of film thickness. As remark, the analysis of L after Goodman was not for all samples straight forward, i.e. the development of a model including inhomogeneity due to combined diffusion and drift, variation of built-in electric fields and changes in the composition would be useful in the future.

The temperature dependence of E_g and E_t was investigated for $CH_3NH_3PbI_3$ layers by modulated SPV spectroscopy. In order to avoid degradation of $CH_3NH_3PbI_3$ in vacuum during temperature dependent SPV measurements, a poly (methyl methacrylate) (PMMA) layer was deposited on $CH_3NH_3PbI_3$ films and optimized for stabilization of $CH_3NH_3PbI_3$ films. The stabilization of $CH_3NH_3PbI_3$ with PMMA was necessary since a stable perovskite sample was required for temperature-dependent measurements over a wide temperature range. E_g and E_t of $CH_3NH_3PbI_3$ increased with increasing temperature. The value of E_t increased monotonously with increasing temperature from 13 meV at -160 °C to 24 meV at 0°C but scattered between 25 and 30 meV in the temperature range between 20 and 60 °C. The scatter can be related to stress at the PMMA / $CH_3NH_3PbI_3$ interface. Furthermore, with increasing temperature, disorder can increase in the tetragonal phase of $CH_3NH_3PbI_3$ due to increased thermal vibrations of $CH_3NH_3^+$ cations as well as continuous tilting of the average Pb-I-Pb bond angle towards 180° [47]. In addition, the temperature dependence of E_t was fitted with a model taking into account phonon-induced disorder and a phonon energy E_{ph} of 150 ± 40 was obtained.

In comparison to covalent semiconductors, unusual behavior of the increase in E_g of the tetragonal phase of $CH_3NH_3PbI_3$ layers with increasing temperature is attributed to lattice dilation which occurred due to thermal expansion. The lattice dilation is produced by thermal vibrations of the ions around their mean position which increases due to increased thermal energy. The effect can be quantified by the positive temperature coefficient of the energy band

gap [64]. In contrast, in covalent semiconductors such as silicon and gallium arsenide, the electron-phonon interaction is the dominant factor which leads to a decrease of E_g with increasing temperature [79, 60]. A jump in the value of E_g near the region of phase transition has been observed and was related to the phase transition from the tetragonal to the cubic phases.

It has been shown that modulated SPV spectroscopy is a well suitable method for very efficient, sensitive and reliable characterization of hybrid organic-inorganic metal halide perovskites. In this context, modulated SPV spectroscopy can be well applied for the characterization of perovskites with respect to preparation technologies and treatments, for the monitoring and analysis of degradation processes and for the investigation of fundamental dependencies of parameters.

The reproducibility of $CH_3NH_3PbI_3$ and other perovskite layers is rather challenging in relation to the preparation conditions and stability of solar cells based on related absorbers. For example, the continued evaporation of CH_3NH_3, HI and degradation to PbI_2 makes the reproducibility of $CH_3NH_3PbI_3$ layers a challenge. One way to get higher stability is to form a dense interface between the $CH_3NH_3PbI_3$ absorber layer and charge selective contacts. This implies the preparation of interfacial materials which can enhance the growth of perovskite, passivate defects and offer protective barriers for $CH_3NH_3PbI_3$ perovskites. Another way to stabilize perovskites is to use perovskites with mixed cations and halides (i.e. the so- called triple cations which contains Cs^+, MA^+ and FA^+). Solar cells based on mixed cations and halides are much better reproducible and thermally and structurally stable at higher efficiencies in comparison to bare $CH_3NH_3PbI_3$. The further improvement of the materials and combinations of materials with perovskites requires a further optimization of the compositional design of the perovskite. This is beneficial for tandem solar cell applications. Furthermore, it would be interesting to determine L after Goodman [32] using SPV spectroscopy for mixed perovskites based on cations and halides. For this purpose, however, the layer shall be homogeneous in the composition and the absorption spectra shall be measured with high precision.

References

1. Quaschning, V. Understanding renewable energy systems; Carl Hanser Verlag GmbH & Co KG: London, 2005; Vol. 67; ISBN 1844071286.
2. Kaizuka,I. and Masson, G. Trends in photovoltaic applications; Report IEA PVPS T1-32:**2017**; ISBN 9783906042688.
3. Monier, V.; Hestin, M. Study on photovoltaic panels supplementing the impact assessment for a recast of the WEEE Directive. *BIO Intell. Serv.* **2011**, 1–86.
4. Green, M. A.; Hishikawa, Y.; Dunlop, E. D.; Levi, D. H.; Hohl-Ebinger, J.; Ho-Baillie, A. W. Y. Solar cell efficiency tables (version 51). *Prog. Photovoltaics Res. Appl.* **2018**, *26*, 3–12, doi:10.1002/pip.2978.
5. National renewable energy laboratory efficiency_chart. *Http://Www.Nrel.Gov/Ncpv/Images/Efficiency_Chart.Jpg* 2016.
6. Fthenakis, V. M. and Kim, H. C. CdTe photovoltaics: Life cycle environmental profile and comparisons. Presented at the european material research society meeting, symposium O, Nice, France, May 29-June 2, **2006**
7. Grätzel, M. Dye-sensitized solar cells. J. Photochem. Photobiol. C Photochem. Rev. **2003**, *4*, 145–153, doi:10.1016/S1389-5567(03)00026-1.
8. Shockley, W.; Queisser, H. J. Detailed balance limit of efficiency of p-n junction solar cells. *J. Appl. Phys.* **1961**, *32*, 510–519, doi:10.1063/1.1736034.
9. Saliba, M.; Matsui, T.; Seo, J.-Y.; Domanski, K.; Correa-Baena, J.-P.; Nazeeruddin, M. K.; Zakeeruddin, S. M.; Tress, W.; Abate, A.; Hagfeldt, A.; Grätzel, M. Cesium-containing triple cation perovskite solar cells: improved stability, reproducibility and high efficiency. *Energy Environ. Sci.* **2016**, *9*, 1989–1997, doi:10.1039/C5EE03874J.
10. Kagan, C. R. Organic-inorganic hybrid materials as semiconducting channels in thin-film field-effect transistors. *Science (80-.).* **1999**, *286*, 945–947, doi:10.1126/science.286.5441.945
11. Mitzi, D.B; Feild, C.A;Schlesinger, Z and Laibowitz, R. Transport, optical, and magnetic properties of the conducting perovskite $CH_3NH_3SnI_3$ 1994, 159–163.
12. Kojima, A.; Teshima, K.; Shirai, Y.; Miyasaka, T. Organometal halide perovskites as visible-light sensitizers for photovoltaic cells. *J. Am. Chem. Soc.* **2009**, *131*, 6050–6051, doi:10.1021/ja809598r.
13. Wolf, S. de; Holovsky, J.; Moon, S.-J.; Löper, P.; Niesen, B.; Ledinsky, M.; Haug, F.; Yum, J.; Ballif, C. Organometallic halide perovskites: sharp optical absorption edge and its relation to photovoltaic performance. *J. Phys. Chem. Lett.* **2014**, *5*, 1035–1039, doi:10.1021/jz500279b.
14. Herz, L. M. Charge-carrier mobilities in metal halide perovskites: Fundamental mechanisms and limits. *ACS Energy Lett.* **2017**, *2*, 1539–1548,

doi:10.1021/acsenergylett.7b00276.

15. Stranks, S. D.; Eperon, G. E.; Grancini, G.; Menelaou, C.; Alcocer, M. J. P.; Leijtens, T.; Herz, L. M.; Petrozza, A.; Snaith, H. J. Electron-hole diffusion lengths exceeding 1 micrometer in an organometaltrihalide perovskite absorber. *Science* **2014**, *342*, 341–344, doi:10.1126/science.1243982.
16. Kim, J.; Lee, S. H.; Lee, J. H.; Hong, K. H. The role of intrinsic defects in methylammonium lead iodide perovskite. *J. Phys. Chem. Lett.* **2014**, *5*, 1312–1317, doi:10.1021/jz500370k.
17. Hao, F.; Stoumpos, C. C.; Chang, R. P. H.; Kanatzidis, M. G. Anomalous band gap behavior in mixed Sn and Pb perovskites enables broadening of absorption spectrum in solar cells. *J. Am. Chem. Soc.* **2014**, *136*, 8094–8099, doi:10.1021/ja5033259.
18. Edri, E.; Kirmayer, S.; Kulbak, M.; Hodes, G.; Cahen, D. Chloride inclusion and hole transport material doping to improve methyl ammonium lead bromide perovskite-based high open-circuit voltage solar cells. *J. Phys. Chem. Lett.* **2014**, *5*, 429–433, doi:10.1021/jz402706q.
19. Noh, J. H.; Im, S. H.; Heo, J. H.; Mandal, T. N.; Seok, S. Il Chemical management for colorful, efficient, and stable inorganic − organic hybrid nanostructured solar cells. *Nano Lett.* **2013**, *13*, 1764–1769, doi:dx.doi.org/10.1021/nl400349b.
20. Hoke, E. T.; Slotcavage, D. J.; Dohner, E. R.; Bowring, A. R.; Karunadasa, H. I.; McGehee, M. D. Reversible photo-induced trap formation in mixed-halide hybrid perovskites for photovoltaics. *Chem. Sci.* **2015**, *6*, 613–617, doi:10.1039/C4SC03141E.
21. Jordan, D.C; Kurtz, S.R;VanSant, K. and Newmiller, J. Compendium of photovoltaic degradation rates. *Prog. Photovolt Res. Appl* **2016**, *24*, 978–989, doi:DOI: 10.1002/pip.2744.
22. Kronik, L.; Shapira, Y. Surface photovoltage phenomena : theory , experiment , and applications. *Surf. Sci. Rep.* **1999**, *37*, 1–206.
23. Duzhko, V.; Timoshenko, V. Y.; Koch, F.; Dittrich, T. Photovoltage in nanocrystalline porous TiO_2. *Phys. Rev. B* **2001**, *64*, 75204, doi:10.1103/PhysRevB.64.075204.
24. Liu, Y.-T.; Chen, Y.; Lin, C.; Fan, C.; Liu, J.; Tung, Y.; Tsai, S.-Y. Modeling and simulation of band-gap profiling with planar heterojunction of hole-transporting layer-free perovskite solar cells. *Mater. Res. Express* **2017**, *4*, 75505, doi:10.1088/2053-1591/aa77ee.
25. Longo, G.; Momblona, C.; La-Placa, M. G.; Gil-Escrig, L.; Sessolo, M.; Bolink, H. J. Fully vacuum-processed wide band gap mixed-halide perovskite solar cells. *ACS Energy Lett.* **2018**, *3*, 214–219, doi:10.1021/acsenergylett.7b01217.
26. Foley, B. J.; Marlowe, D. L.; Sun, K.; Saidi, W. A.; Scudiero, L.; Gupta, M. C.; Choi, J.

J. Temperature dependent energy levels of methylammonium lead iodide perovskite. *Mater. Eng. Sci. Div. Core Program,* **2015**, *243904*, 581–586, doi:10.1063/1.4922804.

27. Naikaew, A.; Prajongtat, P.; Lux-Steiner, M. C.; Arunchaiya, M.; Dittrich, T. Role of phase composition for electronic states in $CH_3NH_3PbI_3$ prepared from $CH_3NHI/PbCl_2$ solution. *Appl. Phys. Lett.* **2015**, *106*, 232104-1-4, doi:10.1063/1.4922554.
28. Prajongtat, P.; Dittrich, T. Precipitation of $CH_3NH_3PbCl_3$ in $CH_3NH_3PbI_3$ and Its impact on modulated charge separation. *J. Phys. Chem. C* **2015**, 150416112311000, doi:10.1021/acs.jpcc.5b01667.
29. Supasai, T.; Rujisamphan, N.; Ullrich, K.; Chemseddine, A.; Dittrich, T.; Supasai, T.; Rujisamphan, N.; Ullrich, K.; Chemseddine, A.; Dittrich, T. Formation of a passivating $CH_3NH_3PbI_3$ / PbI_2 interface during moderate heating of $CH_3NH_3PbI_3$ layers. **2013**, *183906*, doi:10.1063/1.4826116.
30. Varshni, Y. P. Temperature dependence of the energy gap in semiconductors. *Physica* **1967**, *34*, 149–154, doi:10.1016/0031-8914(67)90062-6.
31. Yu, C.; Chen, Z.; Wang, J.; Pfenninger, W.; Vockic, N.; Kenney, J. T.; Shum, K. Temperature dependence of the band gap of perovskite semiconductor compound $CsSnI_3$. *J. Appl. Phys.* **2011**, *110*, doi:10.1063/1.3638699.
32. Goodman, A. M. A method for the measurement of short minority carrier diffusion lengths in semiconductors. *J. Appl. Phys.* **1961**, *32*, 2550–2552, doi:10.1063/1.1728351.
33. Jesper Jacobsson, T.; Correa-Baena, J.-P.; Pazoki, M.; Saliba, M.; Schenk, K.; Grätzel, M.; Hagfeldt, A. Exploration of the compositional space for mixed lead halogen perovskites for high efficiency solar cells. *Energy Environ. Sci.* **2016**, *9*, 1706–1724, doi:10.1039/C6EE00030D.
34. Kegelmann, L.; Wolff, C. M.; Omondi, C. A.; Lang, F.; Unger, E. L.; Korte, L.; Dittrich, T.; Neher, D.; Rech, B.; Albrecht, S. It takes two to tango – double-layer selective contacts in perovskite solar cells for improved device performance and reduced hysteresis. *ACS Appl. Mater. Interfaces* **2017**, acsami.7b00900, doi:10.1021/acsami.7b00900.
35. Lee, M. ;Teuscher, J.;Miyasaka, T.;Murakami, T.N.;Snaith, H. J. Efficient hybrid solar cells based on meso-superstructured organometal halide perovskites. *Science (80-.).* **2012**, *338*, 643–647, doi:10.1126/science.1225053.
36. Hendon, C. H.; Yang, R. X.; Burton, L. A.; Walsh, A. Assessment of polyanion (BF_4^- and PF_6^-) substitutions in hybrid halide perovskites. *J. Mater. Chem. A* **2015**, *3*, 9067–9070, doi:10.1039/C4TA05284F.
37. Jiang, Q.; Rebollar, D.; Gong, J.; Piacentino, E. L.; Zheng, C.; Xu, T. Pseudohalide-induced moisture tolerance in perovskite $CH_3NH_3Pb(SCN)_2I$ Thin Films. *Angew.*

Chemie **2015**, *127*, 7727–7730, doi:10.1002/ange.201503038.

38. Chen, Q.; De Marco, N.; Yang, Y.; Song, T. Bin; Chen, C. C.; Zhao, H.; Hong, Z.; Zhou, H.; Yang, Y. Under the spotlight: The organic-inorganic hybrid halide perovskite for optoelectronic applications. *Nano Today* **2015**, *10*, 355–396, doi:10.1016/j.nantod.2015.04.009.
39. Goldschmidt, V. M. Die Gesetze der Krystallochemie. *Naturwissenschaften* **1926**, *14*, 477–485, doi:10.1007/BF01507527.
40. Kieslich, G.; Sun, S.; Cheetham, A. K. Solid-state principles applied to organic–inorganic perovskites: new tricks for an old dog. *Chem. Sci.* **2014**, *5*, 4712–4715, doi:10.1039/C4SC02211D.
41. Poglitsch, A.; Weber, D. Dynamic disorder in methylammoniumtrihalogenoplumbates (II) observed by millimeter-wave spectroscopy. *J. Chem. Phys.* **1987**, *87*, 6373–6378, doi:10.1063/1.453467.
42. Li, Z.; Yang, M.; Park, J. S.; Wei, S. H.; Berry, J. J.; Zhu, K. Stabilizing perovskite structures by tuning tolerance factor: formation of formamidinium and cesium lead iodide solid-state alloys. *Chem. Mater.* **2016**, *28*, 284–292, doi:10.1021/acs.chemmater.5b04107.
43. Wasylishen, R. E.; Knop, O.; Macdonald, J. B. Cation rotation in methylammonium lead halides. *Solid State Commun.* **1985**, *56*, 581–582, doi:10.1016/0038-1098(85)90959-7.
44. Onoda-Yamamuro, N.; Matsuo, T.; Suga, H. Calorimetric and IR spectroscopic studies of phase transitions in methylammonium trihalogenoplumbates (II). *J. Phys. Chem. Solids* **1990**, *51*, 1383–1395, doi:10.1016/0022-3697(90)90021-7.
45. Milot, R. L.; Eperon, G. E.; Snaith, H. J.; Johnston, M. B.; Herz, L. M. Temperature-dependent charge-carrier dynamics in $CH_3NH_3PbI_3$ perovskite thin films. *Adv. Funct. Mater.* **2015**, *25*, 6218–6227, doi:10.1002/adfm.201502340.
46. Swainson, I. P.; Hammond, R. P.; Soullière, C.; Knop, O.; Massa, W. Phase transitions in the perovskite methylammonium lead bromide, $CH_3NH_3PbBr_3$. *J. Solid State Chem.* **2003**, *176*, 97–104, doi:10.1016/S0022-4596(03)00352-9.
47. Weller, M. T.; Weber, O. J.; Henry, P. F.; Di Pumpo, A. M.; Hansen, T. C. Complete structure and cation orientation in the perovskite photovoltaic methylammonium lead iodide between 100 and 352 K. *Chem. Commun.* **2015**, *51*, 4180–4183, doi:10.1039/C4CC09944C.
48. Park, N.-G.; Grätzel, M.; Tsutomu, M. *Organic- inorganic halide perovskite photovoltaics*; 2016; isbn 9783319351124.
49. Vegard,L. Die Konstitution der Mischkristalle und die Raumffillung der Atome . Zeitschrift für physik Bd. V. Julius springer, Berlin. **1921**, *17-26*,

doi:10.1007/BF00549722.

50. Kittel, C. Introduction To Solid State Physics-1 edition, 1953, 223–252.
51. Yamada, Y.; Nakamura, T.; Endo, M.; Wakamiya, A.; Kanemitsu, Y. Near-band-edge optical responses of solution-processed organic–inorganic hybrid perovskite $CH_3NH_3PbI_3$ on mesoporous TiO_2 electrodes. *Appl. Phys. Express* **2014**, *7*, 32302, doi:10.7567/APEX.7.032302.
52. Green, M. A.; Ho-Baillie, A.; Snaith, H. J. The emergence of perovskite solar cells. *Nat. Photonics* **2014**, *8*, 506–514, doi:10.1038/nphoton.2014.134.
53. Hutter, E. M.; Gélvez-Rueda, M. C.; Osherov, A.; Bulović, V.; Grozema, F. C.; Stranks, S. D.; Savenije, T. J. Direct–indirect character of the bandgap in methylammonium lead iodide perovskite. *Nat. Mater.* **2016**, *16*, 115–120, doi:10.1038/nmat4765.
54. Zheng, F.; Tan, L. Z.; Liu, S.; Rappe, A. M. Rashba spin-orbit coupling enhanced carrier lifetime in $CH_3NH_3PbI_3$. *Nano Lett.* **2015**, *15*, 7794–7800, doi:10.1021/acs.nanolett.5b01854.
55. Ndione, P. F.; Li, Z.; Zhu, K. Effects of alloying on the optical properties of organic–inorganic lead halide perovskite thin films. *J. Mater. Chem. C* **2016**, *4*, 7775–7782, doi:10.1039/C6TC02135B.
56. Kitazawa, N.; Watanabe, Y.; Nakamura, Y. Optical properties of $CH_3NH_3PbX_3$ (X = halogen) and their mixed-halide crystals. *J. Mater. Sci.* **2002**, *37*, 3585–3587, doi:10.1023/A:1016584519829.
57. Unger, E. L. Bandgap tuneability for high-voltage lead-halide perovskite materials bandgap tuneability for high-voltage lead-halide perovskite materials. Online proceedings of the 29th Workshop on Quantum Solar Energy Conversion (QUANTSOL) **2017**, 3–4, doi:10.1039/C5NR07739G.
58. Wang, M.; Fei, G. T.; Zhang, Y. G.; Kong, M. G.; De Zhang, L. Tunable and predetermined bandgap emissions in alloyed ZnS_xSe_{1-x} nanowires. *Adv. Mater.* **2007**, *19*, 4491–4494, doi:10.1002/adma.200602919.
59. Donnell, K. P. O.; Chen, X.; Chen, X. Temperature dependence of semiconductor band gaps. **1991**, *2924*, 67–70, doi:10.1063/1.104723.
60. Bludau, W.; Onton, A. and Heinke, W. Temperature dependence of the band gap of silicon. *Appl. Phys. Lett.* **1974**, *45*, 1846–1848, doi:10.1063/1.3242026.
61. Sturge, M. D. Optical absorption of gallium arsenide between 0.6 and 2.75 eV. *Phys. Rev.* **1962**, *127*, 768–773, doi:10.1103/PhysRev.127.768.
62. Turner, W. J.; Reese, W. E.; Pettit, G. D. Exciton absorption and emission in InP. *Phys. Rev.* **1964**, *136*, 1955–1958, doi:10.1103/PhysRev.136.A1467.
63. Cody, G. D.; Tiedje, T.; Abeles, B.; Moustakas, T. D.; Brooks, B.; Goldstein, Y. Disorder and the optical absorption edge of hydrogenated amorphous silicon.

Phys.Rev.Lett. **1981**, *47*, 20 1480-1483, doi:10.1051/jphyscol:1981463.

64. Singh, S.; Li, C.; Panzer, F.; Narasimhan, K. L.; Graeser, A.; Gujar, T. P.; Köhler, A.; Thelakkat, M.; Huettner, S.; Kabra, D. Effect of thermal and structural disorder on the electronic structure of hybrid perovskite semiconductor $CH_3NH_3PbI_3$. *J. Phys. Chem. Lett.* **2016**, *7*, 3014–3021, doi:10.1021/acs.jpclett.6b01207.
65. Keffer, C.; Hayes, T. M.; Bienenstock, A. PbTe Debye-Waller factors and band-gap temperature dependence. *Phys. Rev. Lett.* **1968**, *21*, 1676–1678, doi:10.1103/PhysRevLett.21.1676.
66. Lian, H. J.; Yang, A.; Thewalt, M. L. W.; Lauck, R.; Cardona, M. Effects of sulfur isotopic composition on the band gap of PbS. *Phys. Rev. B* **2006**, *73*, 233202, doi:10.1103/PhysRevB.73.233202.
67. Choyke, W. J.; Patrick, L. Exciton recombination radiation and phonon spectrum of 6H SiC. *Phys. Rev.* **1962**, *127*, 1868–1877, doi:10.1103/PhysRev.127.1868.
68. Lautenschlager, P.; Garriga, M.; Logothetidis, S.; Cardona, M. Interband critical points of CsaAs and their temperature dependence. *Phys. Rev. B* **1987**, *35*, 9174–9189, doi:10.1103/PhysRevB.35.9174.
69. Oelgart, G.; Orschel, B.; Proctor, M.; Martin, D.; Morier-Genoud, F.; Reinhart, F. K. Temperature dependence of the Γ8v-Γ6c gap of GaAs. *J. Appl. Phys.* **1993**, *74*, 2742–2747, doi:10.1063/1.354674.
70. Pejova, B.; Abay, B.; Bineva, I. Temperature dependence of the band-gap energy and sub-band-gap absorption tails in strongly quantized ZnSe nanocrystals deposited as thin films. *J. Phys. Chem. C* **2010**, *114*, 15280–15291, doi:10.1021/jp102773z.
71. Sarswat, P. K.; Free, M. L. A Study of energy band gap temperature relationships for Cu_2ZnSnS_4 thin films. *Phys. Status Solidi Appl. Mater. Sci.* **2011**, *208*, 2861–2864, doi:10.1002/pssa.201127216..
72. Pässler, R.; Oelgart, G. Appropriate analytical description of the temperature dependence of exciton peak positions in GaAs/$Al_xGa_{1-x}As$ multiple quantum wells and the Γ_{8v} - Γ_{6c} gap of GaAs. *J. Appl. Phys.* **1997**, *82*, 2611–2616, doi:10.1063/1.366098.
73. Pässler, R. Alternative analytical descriptions of the temperature dependence of the energy gap in cadmium sulfide. *Phys. Status Solidi* **1996**, *193*, 135–144, doi:10.1002/pssb.2221930114.
74. Cardona, M.; Meyer, T. A.; Thewalt, M. L. W. Temperature dependence of the energy gap of semiconductors in the low-temperature limit. *Phys. Rev. Lett.* **2004**, *92*, 196403, doi:10.1103/PhysRevLett.92.196403.
75. Grüneisen, E. Theorie des festen Zustandes einatomiger Elemente. *Ann. Phys.* **1912**, *344*, 257–306, doi:10.1002/andp.19123441202.
76. Tsang, Y. W. and Cohen, M. L. Band ordering in PbTe. Solid state

communications,**1971**, *9*, 261–264.

77. Oszwałldowski, M.; Zimpel, M. Temperature dependence of intrinsic carrier concentration and density of states effective mass of heavy holes in InSb. *J. Phys. Chem. Solids* **1988**, *49*, 1179–1185, doi:10.1016/0022-3697(88)90173-4.
78. Even, J.; Pedesseau, L.; Dupertuis, M. A.; Jancu, J. M.; Katan, C. Electronic model for self-assembled hybrid organic/perovskite semiconductors: Reverse band edge electronic states ordering and spin-orbit coupling. *Phys. Rev. B - Condens. Matter Mater. Phys.* **2012**, *86*, 3–6, doi:10.1103/PhysRevB.86.205301.
79. Fan, H. Y. Temperature dependence of the energy gap in semiconductors. *Phys. Rev.* **1951**, *82*, 900–905, doi:10.1103/PhysRev.82.900.
80. Hameed, K.S. and AL-Sheikh, A. M. Theoretical study of energy gap for silicon and germanium under high pressure. Raf. Jou. Sci., **2011**, *22*, 56–68.
81. Camassel, J.; Auvergne, D. Temperature dependence of the fundamental edge of germanium and zinc-blende-type semiconductors. *Phys. Rev. B* **1975**, *12*, 3258–3267, doi:10.1103/PhysRevB.12.3258.
82. Nakwaski, W. Effective masses of electrons and heavy holes in GaAs , InAs , AlAs and their ternary compounds. **1995**, *210*, 1–25.
83. Bouarissa, N.; Aourag, H. Effective masses of electrons and heavy holes in InAs , InSb , GaSb , GaAs and some of their ternary compounds. **1999**.
84. Adachi, S. Band gaps and refractive indices of AlGaAsSb, GaInAsSb, and InPAsSb: Key properties for a variety of the 2-4 μm optoelectronic device applications. Journal of Applied Physics 61, 4869, **1987**.
85. Camassel, J.; Auvergne, D.; Mathieu, H. Temperature dependence of the band gap and comparison with the threshold frequency of pure GaAs lasers. *J. Appl. Phys.* **1975**, *46*, 2683–2689, doi:10.1063/1.321903.
86. Schneider, D.; Rürup, D.; Schönfelder, B.; Schlachetzki, A. Effective mass and energy-band parameters in InP by magnetophonon effect. *Z. Phys. B 100, 33—38,***1996**, doi:10.1007/s002570050090.
87. Pavesi, I.; Piazza, F.; Micro, I. De; Carlin, F.; Ilegems, M. Temperature dependence of the InP band gap from a photolurninescence study. Phys. Rev. B., **1991**, *44*, 9052–9055.
88. Wei, J.; Murray, J. M.; Barnes, J.; Gonzalez, L. P.; Uha, S. Determination of the temperature dependence of the band gap energy of semiconductors from transmission spectra. *J. Electron. Mater.* **2012**, *41*, 2857–2866, doi:10.1007/s11664-012-2055-0.
89. Rössler, U. (Ed. . *II-VI and I-VII Compounds; Semimagnetic Compounds*; Springer: Berlin, 1999;
90. Chukwuocha, E.; Onyeaju, M. Effect of quantum confinement on the wavelength of CdSe, ZnS And GaAs Quantum Dots (Qds). *Int. J. Sci. Technol. Res.* **2012**, *1*, 21–24.

91. Lipatova, Z. O.; Kolobkova, E. V.; Babkina, A. N.; Nikonorov, N. V. On the size and temperature dependence of the energy gap in cadmium-selenide quantum dots embedded in fluorophosphate glasses. *Semiconductors* **2017**, *51*, 326–328, doi:10.1134/S1063782617030150.
92. Marple, D. T. F. Effective electron mass in CdTe. *Phys. Rev.* **1963**, *129*, 2466–2470, doi:10.1103/PhysRev.129.2466.
93. Giorgi, G.; Fujisawa, J. I.; Segawa, H.; Yamashita, K. Small photocarrier effective masses featuring ambipolar transport in methylammonium lead iodide perovskite: A density functional analysis. *J. Phys. Chem. Lett.* **2013**, *4*, 4213–4216, doi:10.1021/jz4023865.
94. Jiang, Y.; Soufiani, A. M.; Gentle, A.; Huang, F.; Ho-baillie, A.; Green, M. A. Temperature dependent optical properties of $CH_3NH_3PbI_3$ perovskite by spectroscopic ellipsometry. **2016**, *61905*, 3–8, doi:10.1063/1.4941710.
95. Urbach, F. The long-wavelength edge of photographic sensitivity and of the electronic Absorption of Solids [8]. *Phys. Rev.* **1953**, *92*, 1324, doi:10.1103/PhysRev.92.1324.
96. Studenyak, I.; Kranj, M.; Kurik, M. Urbach Rule in Solid State Physics. *Int. J. Opt. Appl.* **2014**, *4*, 76–83, doi:10.5923/j.optics.20140403.02.
97. Carretero-Palacios, S.; Calvo, M. E.; Míguez, H. Absorption enhancement in organic-inorganic halide perovskite films with embedded plasmonic gold nanoparticles. *J. Phys. Chem. C* **2015**, *119*, 18635–18640, doi:10.1021/acs.jpcc.5b06473.
98. Zhang, B.; Zhang, M. J.; Pang, S. P.; Huang, C. S.; Zhou, Z. M.; Wang, D.; Wang, N.; Cui, G. L. Carrier transport in $CH_3NH_3PbI_3$ films with different thickness for perovskite solar cells. *Adv. Mater. Interfaces* **2016**, *3*, doi:10.1002/admi.201600327.
99. Carlson, D. E.; Wronski, C. R. Amorphous silicon solar cell. *Appl. Phys. Lett.* **1976**, *28*, 671–673, doi:10.1063/1.88617.
100. Asar, T.; Özçelik, S.; Özbay, E. Structural and electrical characterizations of $In_xGa_{1-x}As$/InP structures for infrared photodetector applications. *J. Appl. Phys.* **2014**, *115*, 104502, doi:10.1063/1.4868056.
101. Dong, Q.; Fang, Y.; Shao, Y.; Mulligan, P.; Qiu, J.; Cao, L.; Huang, J. Electron-hole diffusion lengths > 175 um in solution-grown $CH_3NH_3PbI_3$ single crystals. *Science* **2015**, *347*, 967–970, doi:10.1126/science.aaa5760.
102. Dittrich, T.; Lang, F.; Shargaieva, O.; Rappich, J.; Nickel, N. H.; Unger, E.; Rech, B. Diffusion length of photo-generated charge carriers in layers and powders of $CH_3NH_3PbI_3$ perovskite. *Appl. Phys. Lett.* **2016**, *109*, 73901, doi:10.1063/1.4960641..
103. Xing, G.; Mathews, N.; Lim, S. S.; Lam, Y. M.; Mhaisalkar, S.; Sum, T. C. Long-range balanced electron- and hole-transport lengths in organic-inorganic $CH_3NH_3PbI_3$. Science. **2013**, *342,* 344–347.
104. Barugkin, C.; Cong, J.; Duong, T.; Rahman, S.; Nguyen, H. T.; Macdonald, D.; White,

T. P.; Catchpole, K. R. Ultralow absorption coefficient and temperature dependence of radiative recombination of $CH_3NH_3PbI_3$ perovskite from photoluminescence. *J. Phys. Chem. Lett.* **2015**, *6*, 767–772, doi:10.1021/acs.jpclett.5b00044.

105. Löper, P.; Stuckelberger, M.; Niesen, B.; Werner, J.; Filipič, M.; Moon, S.-J.; Yum, J.-H.; Topič, M.; De Wolf, S.; Ballif, C. Complex refractive index spectra of $CH_3NH_3PbI_3$ perovskite thin films determined by spectroscopic ellipsometry and spectrophotometry. *J. Phys. Chem. Lett.* **2015**, *6*, 66–71, doi:10.1021/jz502471h.
106. Green, M. A. Self-consistent optical parameters of intrinsic silicon at 300 K including temperature coefficients. *Sol. Energy Mater. Sol. Cells* **2008**, *92*, 1305–1310, doi:10.1016/j.solmat.2008.06.009.
107. Elbersen, R.; Tiggelaar, R. M.; Milbrat, A.; Mul, G.; Gardeniers, H.; Huskens, J. Controlled doping methods for radial p/n junctions in silicon. *Adv. Energy Mater.* **2015**, *5*, 1–8, doi:10.1002/aenm.201401745.
108. Walzer, K.; Männig, B.; Pfeiffer, M.; Leo, K. Highly efficient organic devices based on electrically doped transport layers. *Chem. Rev.* **2007**, *107*, 1233–1271, doi:10.1021/cr050156n.
109. Wang, Q.; Shao, Y.; Xie, H.; Lyu, L.; Liu, X.; Gao, Y.; Huang, J. Qualifying composition dependent p and n self-doping in $CH_3NH_3PbI_3$. Appl. Phys. Lett. **2014**, 105,*163508*, doi:10.1063/1.4899051.
110. Li, Y.; Yi, Y.; Coropceanu, V.; Brédas, J. L. Optical conductivity and optical effective mass in a high-mobility organic semiconductor: Implications for the nature of charge transport. *Phys. Rev. B - Condens. Matter Mater. Phys.* **2014**, *90*, 1–8, doi:10.1103/PhysRevB.90.245112.
111. Sze, S. M. and Kwok. K. NG. *Physics of Semiconductor Devices*; Third Edit.; a John Wiley & Sons, Jnc., publication: New Jersey and canada, 2007; ISBN 0471143235..
112. Podzorov, V. Organic single crystals: Addressing the fundamentals of organic electronics. *MRS Bull.* **2013**, *38*, 15–24, doi:10.1557/mrs.2012.306.
113. Valverde-Chávez, D. A.; Ponseca, C.; Stoumpos, C.; Yartsev, A.; Kanatzidis, M. G.; Sundström, V.; Cooke, D. G. Intrinsic femtosecond charge generation dynamics in a single crystal organometal halide perovskite. **2015**, 3700–3707, doi:10.1039/c5ee02503f.
114. Brenner, T. M.; Egger, D. A.; Rappe, A. M.; Kronik, L.; Hodes, G.; Cahen, D. Are mobilities in hybrid organic-inorganic halide perovskites actually “high”? *J. Phys. Chem. Lett.* **2015**, *6*, 4754–4757, doi:10.1021/acs.jpclett.5b02390.
115. Mante, P. A.; Stoumpos, C. C.; Kanatzidis, M. G.; Yartsev, A. Electron-acoustic phonon coupling in single crystal $CH_3NH_3PbI_3$ perovskites revealed by coherent acoustic phonons. *Nat. Commun.* **2017**, *8*, 1–7, doi:10.1038/ncomms14398.

116. Motta, C.; Sanvito, S. Electron-phonon coupling and polaron mobility in hybrid perovskites from first-principles. School of physics, Amber and Crann institute, Trinity College, Dublin 2, Ireland **2017**, 1–16.

117. Charriau, P. and Desbrosses,N. Is energy transition on the right path? Energydata, Global Energy Trends , **2017** edition.

118. ASTM Solar Constant and Zero Air Mass Solar Spectral Irradiance. *Annu. B. ASTM Stand.* **2006**, *15.03*, 1–16, doi:10.1520/E0490-00AR06.2.

119. S Stratford, C. Oriel product training - Solar Simulation. *New port* **2016**, 5. www.newport.com/oriel • oriel.sales@newport.com

120. ASTM International Standard Am0 and Am1.5 Spectra. **2003**.www.knovel.com.

121. Kahn, A. Fermi level, work function and vacuum level. *Mater. Horiz.* **2016**, *3*, 7–10, doi:10.1039/C5MH00160A.

122. Lang, P. F.; Smith, B. C. Ionization Energies of Atoms and Atomic Ions. *J. Chem. Educ.* **2003**, *80*, 938, doi:10.1021/ed080p938.

123. Helander, M. G.; Greiner, M. T.; Wang, Z. B.; Tang, W. M.; Lu, Z. H. Work function of fluorine doped tin oxide. *J. Vac. Sci. Technol. A Vacuum, Surfaces, Film.* **2011**, *29*, 11019, doi:10.1116/1.3525641.

124. Andersson N Broms, P Yu, N Lupo, D Salaneck, WR, a J. Fluorine tin oxide as an alternative to indium tin oxide in polymer LEDs. *Adv. Mater.* **1998**, *10*, doi:10.1002/(SICI)1521-4095(199808)10:11<859::AID-ADMA859>3.0.CO;2-1.

125. Farhan, M. S.; Zalnezhad, E.; Bushroa, A. R.; Sarhan, A. A. D. Electrical and optical properties of indium-tin oxide (ITO) films by ion-assisted deposition (IAD) at room temperature. *Int. J. Precis. Eng. Manuf.* **2013**, *14*, 1465–1469, doi:10.1007/s12541-013-0197-5.

126. Zuo, C. and Ding, L. Modified PEDOT layer makes a 1 . 52 V Voc for perovskite / PCBM Solar Cells. *Adv. Energy Mater.* **2016**, *1601193*, 1–6, doi:10.1002/aenm.201601193.

127. Groenendaal, B. L.; Jonas, F.; Freitag, D.; Pielartzik, H.; Reynolds, J. R. Poly(3,4-ethylendioxythiophene) and its derivatives : past , present , and future. *Adv. Funct. Mater.* **2000**, *12*, 481–494.

128. Fakhouri, H.; Arefi-khonsari, F.; Jaiswal, A. K.; Pulpytel, J. Enhanced visible light photoactivity and charge separation in TiO_2 / TiN bilayer thin films. *"Applied Catal. A, Gen.* **2015**, *492*, 83–92, doi:10.1016/j.apcata.2014.12.030.

129. Feucht, D. L. Heterojunctions in photovoltaic devices. *J. Vac. Sci. Technol.* **1977**, *14*, 57, doi:10.1116/1.569153.

130. Meng, L.; You, J.; Guo, T.-F.; Yang, Y. Recent advances in the inverted planar structure of perovskite solar cells. *Acc. Chem. Res.* **2015**, acs.accounts.5b00404, doi:10.1021/acs.accounts.5b00404.

131. Xu, Z.; Chen, L.; Chen, M.; Li, G.; Yang, Y. Energy level alignment of poly(3-hexylthiophene): [6,6]-phenyl C-61 butyric acid methyl ester bulk heterojunction. *Appl. Phys. Lett.* **2008**, *95*, 13301, doi:10.1063/1.3163056.
132. Wei, M.; Li, C. F.; Deng, X. R.; Deng, H. Surface work function of transparent conductive ZnO Films. *Energy Procedia* **2012**, *16*, 76–80, doi:10.1016/j.egypro.2012.01.014.
133. Shan, F. K.; Yu, Y. S. Band gap energy of pure and Al-doped ZnO thin films. *J. Eur. Ceram. Soc.* **2004**, *24*, 1869–1872, doi:10.1016/S0955-2219(03)00490-4.
134. Nakanishi, R.; Nogimura, A.; Eguchi, R.; Kanai, K. Electronic structure of fullerene derivatives in organic photovoltaics. *Org. Electron.* **2014**, *15*, 2912–2921, doi:10.1016/j.orgel.2014.08.013.
135. Greiner, M. T.; Chai, L.; Helander, M. G.; Tang, W. M.; Lu, Z. H. Metal/metal-oxide interfaces: How metal contacts affect the work function and band structure of MoO_3. *Adv. Funct. Mater.* **2013**, *23*, 215–226, doi:10.1002/adfm.201200993.
136. Ryu, S.; Noh, J. H.; Jeon, N. J.; Chan Kim, Y.; Yang, W. S.; Seo, J.; Seok, S. Il Voltage output of efficient perovskite solar cells with high open-circuit voltage and fill factor. *Energy Environ. Sci.* **2014**, *7*, 2614, doi:10.1039/C4EE00762J.
137. Khadka, D. B.; Shirai, Y.; Yanagida, M.; Ryan, J. W.; Miyano, K. Exploring the effects of interfacial carrier transport layers on device performance and optoelectronic properties of planar perovskite solar cells. *J. Mater. Chem. C* **2017**, *5*, 8819–8827, doi:10.1039/C7TC02822A.
138. Ashton, Q. *Cyclic Hydrocarbons—Advances in Research and Application: 2013 Edition*
139. Peumans, P.; Bulović, V.; Forrest, S. R. Efficient photon harvesting at high optical intensities in ultrathin organic double-heterostructure photovoltaic diodes. *Appl. Phys. Lett.* **2000**, *76*, 2650, doi:10.1063/1.126433.
140. Dymshits, A.; Henning, A.; Segev, G.; Rosenwaks, Y.; Etgar, L. The electronic structure of metal oxide/organo metal halide perovskite junctions in perovskite based solar cells. *Sci. Rep.* **2015**, *5*, 8704, doi:10.1038/srep08704.
141. Schulz, P.; Edri, E.; Kirmayer, S.; Hodes, G.; Cahen, D.; Kahn, A. Interface energetics in organo-metal halide perovskite-based photovoltaic cells. *Energy Environ. Sci.* **2014**, *7*, 1377–1381, doi:10.1039/C4EE00168K.
142. Deepa, M.; Salado, M.; Calio, L.; Kazim, S.; Shivaprasad, S. M.; Ahmad, S. Cesium power: low Cs+ levels impart stability to perovskite solar cells. *Phys. Chem. Chem. Phys.* **2017**, *19*, 4069–4077, doi:10.1039/C6CP08022G.
143. Albrecht, S.; Saliba, M.; Correa Baena, J. P.; Lang, F.; Kegelmann, L.; Mews, M.; Steier, L.; Abate, A.; Rappich, J.; Korte, L.; Schlatmann, R.; Nazeeruddin, M. K.;

Hagfeldt, A.; Grätzel, M.; Rech, B. Monolithic perovskite/silicon-heterojunction tandem solar cells processed at low temperature. *Energy Environ. Sci.* **2016**, *9*, 81–88, doi:10.1039/C5EE02965A.

144. Meillaud, F.; Shah, A.; Droz, C.; Vallat-Sauvain, E.; Miazza, C. Efficiency limits for single-junction and tandem solar cells. *Sol. Energy Mater. Sol. Cells* **2006**, *90*, 2952–2959, doi:10.1016/j.solmat.2006.06.002.
145. Park, N. G. Perovskite solar cells: An emerging photovoltaic technology. *Mater. Today* **2015**, *18*, 65–72, doi:10.1016/j.mattod.2014.07.007.
146. Zhao, D.; Yu, Y.; Wang, C.; Liao, W.; Shrestha, N.; Grice, C. R.; Cimaroli, A. J.; Guan, L.; Ellingson, R. J.; Zhu, K.; Zhao, X.; Xiong, R.-G.; Yan, Y. Low-bandgap mixed tin–lead iodide perovskite absorbers with long carrier lifetimes for all-perovskite tandem solar cells. *Nat. Energy* **2017**, *2*, 17018, doi:10.1038/nenergy.2017.18.
147. Eperon, G. E.; Leijtens, T.; Bush, K. A.; Prasanna, R.; Green, T.; Wang, J. T.-W.; McMeekin, D. P.; Volonakis, G.; Milot, R. L.; May, R.; Palmstrom, A.; Slotcavage, D. J.; Belisle, R. A.; Patel, J. B.; Parrott, E. S.; Sutton, R. J.; Ma, W.; Moghadam, F.; Conings, B.; Babayigit, A.; Boyen, H.-G.; Bent, S.; Giustino, F.; Herz, L. M.; Johnston, M. B.; McGehee, M. D.; Snaith, H. J. Perovskite-perovskite tandem photovoltaics with optimized band gaps. *Science (80-.).* **2016**, *354*, 861–865, doi:10.1126/science.aaf9717.
148. Wang, D.L.; Cui, H.-J.; Hou, G.-J.; Zhu, Z.-G.; Yan, Q.-B.; Su, G. Highly efficient light management for perovskite solar cells. *Sci. Rep.* **2016**, *6*, 18922, doi:10.1038/srep18922.
149. You, J.; Meng, L.; Song, T.-B.; Guo, T.-F.; Yang, Y. M; Chang, W.-H.; Hong, Z.; Chen, H.; Zhou, H.; Chen, Q.; Liu, Y.; De Marco, N.; Yang, Y. Improved air stability of perovskite solar cells via solution-processed metal oxide transport layers. *Nat. Nanotechnol.* **2015**, 1–8, doi:10.1038/nnano.2015.230.
150. Leijtens, T.; Eperon, G. E.; Noel, N. K.; Habisreutinger, S. N.; Petrozza, A.; Snaith, H. J. Stability of metal halide perovskite solar cells. *Adv. Energy Mater.* **2015**, *5*, 1–23, doi:10.1002/aenm.201500963.
151. Ahn, N.; Kwak, K.; Jang, M. S.; Yoon, H.; Lee, B. Y.; Lee, J.-K.; Pikhitsa, P. V.; Byun, J.; Choi, M. Trapped charge-driven degradation of perovskite solar cells. *Nat. Commun.* **2016**, *7*, 13422, doi:10.1038/ncomms13422.
152. You, J.; Yang, Y. M; Hong, Z.; Song, T.-B.; Meng, L.; Liu, Y.; Jiang, C.; Zhou, H.; Chang, W.-H.; Li, G.; Yang, Y. Moisture assisted perovskite film growth for high performance solar cells. *Appl. Phys. Lett.* **2014**, *105*, 183902, doi:10.1063/1.4901510.
153. Ferreira da Silva, A.; Veissid, N.; An, C. Y.; Pepe, I.; Barros de Oliveira, N.; Batista da Silva, A. V. Optical determination of the direct bandgap energy of lead iodide crystals.

Appl. Phys. Lett. **1996**, *69*, 1930–1932, doi:10.1063/1.117625.

154. Leijtens, T.; Eperon, G. E.; Pathak, S.; Abate, A.; Lee, M. M.; Snaith, H. J. Overcoming ultraviolet light instability of sensitized TiO_2 with meso-superstructured organometal tri-halide perovskite solar cells. *Nat. Commun.* **2013**, *4*, 28885.1-8, doi:10.1038/ncomms3885.
155. Nickel, N.; Lang, F.;Brus, V.; Shargaieva, O.; Rappich, J. Unraveling the light-induced degradation mechanisms of $CH_3NH_3PbI_3$ perovskite films. *Adv. Electron. Mater.* **2017**, *3*, 1700158, doi:10.1002/aelm.201700158.
156. Gibbs, H. D. The boiling-points of ammonia, methyl amine, methyl chloride and sulphur dioxide. *J. Am. Chem. Soc.* **1905**, *27*, 851–865, doi:10.1021/ja01985a003.
157. Manshor, N. A.; Wali, Q.; Wong, K. K.; Muzakir, S. K.; Fakharuddin, A.; Schmidt-Mende, L.; Jose, R. Humidity versus photo-stability of metal halide perovskite films in a polymer matrix. *Phys. Chem. Chem. Phys.* **2016**, *18*, 21629–21639, doi:10.1039/C6CP03600G.
158. Christians, J. A.; Miranda Herrera, P. A.; Kamat, P. V. Transformation of the excited state and photovoltaic efficiency of $CH_3NH_3PbI_3$ perovskite upon controlled exposure to humidified air. *J. Am. Chem. Soc.* **2015**, *137*, 1530–1538, doi:10.1021/ja511132a.
159. Zhang, H.; Qiao, X.; Shen, Y.; Moehl, T.; Zakeeruddin, S. M.; Grätzel, M.; Wang, M. Photovoltaic behaviour of lead methylammonium triiodide perovskite solar cells down to 80 K. *J. Mater. Chem. A* **2015**, *3*, 11762–11767, doi:10.1039/C5TA02206A.
160. Habisreutinger, S. N.; Leijtens, T.; Eperon, G. E.; Stranks, S. D.; Nicholas, R. J.; Snaith, H. J. Carbon nanotube / polymer composite as a highly stable charge collection layer in perovskite solar cells. *Nano Lett.* **2014**, *14*, 5561, doi:10.1021/nl501982b.
161. Kim, N.-K.; Min, Y. H.; Noh, S.; Cho, E.; Jeong, G.; Joo, M.; Ahn, S.-W.; Lee, J. S.; Kim, S.; Ihm, K.; Ahn, H.; Kang, Y.; Lee, H.-S.; Kim, D. Investigation of thermally induced degradation in $CH_3NH_3PbI_3$ perovskite solar cells using in-situ synchrotron radiation analysis. *Sci. Rep.* **2017**, *7*, 4645, doi:10.1038/s41598-017-04690-w.
162. Snaith, H. J.; Abate, A.; Ball, J. M.; Eperon, G. E.; Leijtens, T.; Noel, N. K.; Stranks, S. D.; Wang, J. T. W.; Wojciechowski, K.; Zhang, W. SP: Anomalous hysteresis in perovskite solar cells. *J. Phys. Chem. Lett.* **2014**, *5*, 1511–1515, doi:10.1021/jz500113x.
163. Correa Baena, J. P.; Steier, L.; Tress, W.; Saliba, M.; Neutzner, S.; Matsui, T.; Giordano, F.; Jacobsson, T. J.; Srimath Kandada, A. R.; Zakeeruddin, S. M.; Petrozza, A.; Abate, A.; Nazeeruddin, M. K.; Grätzel, M.; Hagfeldt, A. Highly efficient planar perovskite solar cells through band alignment engineering. *Energy Environ. Sci.* **2015**, *8*, 2928–2934, doi:10.1039/C5EE02608C.

164. Anaraki, E. H.; Kermanpur, A.; Steier, L.; Domanski, K.; Matsui, T.; Tress, W.; Saliba, M.; Abate, A.; Grä, M.; Hagfeldt, A.; Correa-Baena, J.-P. Highly efficient and stable planar perovskite solar cells by solution-processed tin oxide. *Energy Environ. Sci. Energy Environ. Sci* **2016**, *3128*, 3128–3134, doi:10.1039/c6ee02390h.
165. Barnea-Nehoshtan, L.; Kirmayer, S.; Edri, E.; Hodes, G.; Cahen, D. Surface photovoltage spectroscopy study of organo-lead perovskite solar cells. *J. Phys. Chem. Lett.* **2014**, *5*, 2408–2413, doi:10.1021/jz501163r.
166. Dittrich, T. Principle of Surface Photovoltage (SPV) Techniques and Applications on Solar Cell Materials. **2010**. https://www.helmholtz-berlin.de
167. Dittrich, T.; Fengler, S.; Franke, M. Transient surface photovoltage measurement over 12 orders of magnitude in time. *Rev. Sci. Instrum.* **2017**, *88*, 53904, doi:10.1063/1.4983079.
168. Somsongkul, V.; Lang, F.; Jeong, A. R.; Rusu, M.; Arunchaiya, M.; Dittrich, T. Hole blocking $PbI_2/CH_3NH_3PbI_3$ interface. *Phys. Status Solidi - Rapid Res. Lett.* **2014**, *8*, 763–766, doi:10.1002/pssr.201409292.
169. Prajongtat, P.; Dittrich, T.; Hinrichs, K.; Rappich, J. Thickness of AVA + controls the direction of charge transfer at TiO_2 /PbI_2 Interfaces. *J. Phys. Chem. C* **2018**, acs.jpcc.8b00579, doi:10.1021/acs.jpcc.8b00579.
170. Th. Dittrich, O. Shargaieva, F. Lang, N. H. Nickel, B. Rech, J. R. Dependence of the transport length in $CH_3NH_3PbI_3$ powders on light soaking: A surface photovoltage study. *32nd Eur. Photovolt. Sol. Energy Conf. Exhib.* **2016**, 1104–1107.
171. Shargaieva, O.; Lang, F.; Rappich, J.; Dittrich, T.; Klaus, M.; Meixner, M.; Genzel, C.; Nickel, N. H. The influence of the grain size on the properties of $CH_3NH_3PbI_3$ thin films. *ACS Appl. Mater. Interfaces* **2017**, *9*, 38428–38435, doi:10.1021/acsami.7b10056.
172. Prajongtat, P.; Wargulski, D. R.; Unold, T.; Dittrich, T. Photochemically driven modulated charge transfer at local contacts between $CH_3NH_3PbI_3$ and carboxylated multiwalled carbon nanotubes. *J. Phys. Chem. C* **2016**, *120*, 3876–3881, doi:10.1021/acs.jpcc.5b11854.
173. Pineda, S. S. Analysis of high impedance buffers and design of a vacuum chamber for characterization of photoactive materials by surface photovoltage . Master thesis 2018, 24–31
174. Mesa, F.; Chamorro, W.; Vallejo, W.; Baier, R.; Dittrich, T.; Grimm, A.; Lux-Steiner, M. C.; Sadewasser, S. Junction formation of Cu_3BiS_3 investigated by Kelvin probe force microscopy and surface photovoltage measurements. *Beilstein J. Nanotechnol.* **2012**, *3*, 277–284, doi:10.3762/bjnano.3.31.
175. Owino Juma, A.; Azarpira, A.; Steigert, A.; Pomaska, M.; Fischer, C. H.; Lauermann, I.; Dittrich, T. Role of chlorine in In_2S_3 for band alignment at nanoporous-TiO_2/In_2S_3

interfaces. *J. Appl. Phys.* **2013**, *114*, 2–7, doi:10.1063/1.4817766.

176. Lagowski, J.; Jastrzebski, L.; Cullen, G. W. Electronic characterization of heteroepitaxial silicon-on-sapphire by surface photovoltage spectroscopy. *J. Electrochem. Soc. Solid-State Sci. Technol.* **1981**, *128*, 2665–2670, doi:10.1149/1.2127325.
177. Lassabatere, C. Alibert, J. B. and L. S. The use of surface properties for determining semiconductor band gaps. *J. Phys. E.* **1976**, *9*, 773–775.
178. Tauc, J. Optical properties and electronic structure of amorphous Ge and Si. *Mater. Res. Bull.* **1968**, *3*, 37–46, doi:10.1016/0025-5408(68)90023-8.
179. Kroto, H.W. Heath, J.R. O'Brien, S.C. ,Curl, R. F.and Smalley,R. E. C60: Buckministerfullerene. *Nature* **1985**, *318*.
180. Wojciechowski, K. Stranks, S.D, Abate,A., Sadoughi,G., Sadhanala, A, Kopidakis, N., Rumbles, G., Li, C., Friend, R.H., Jen, A.K.-Y and Snaith, H.J. Heterojunction modification for highly efficient organic and inorganic perovskite Solar Cells. ACS Nano, **2014**, 12701–12709, doi:10.1021/nn505723h.
181. Ke, W.; Fang, G.; Liu, Q.; Xiong, L.; Qin, P.; Tao, H.; Ke, W.; Fang, G.; Liu, Q.; Xiong, L.; Qin, P.; Tao, H.; Wang, J. Low-temperature solution processed tin oxide as an alternative electron transporting layer for efficient perovskite solar cells. *Communication* **2015**, 1–7, doi:10.1021/jacs.5b01994..
182. Choi, M. S.; Kim, T. M.; Shim, H. S.; Kim, B. S.; Kim, H. J.; Kim, J. J. Enhancement of the fill factor through an increase of the crystallinity in fullerene-based small-molecule organic photovoltaic cells. *ACS Appl. Mater. Interfaces* **2015**, *7*, 9134–9138, doi:10.1021/acsami.5b01166.
183. Bi, C.; Shao, Y.; Yuan, Y.; Xiao, Z.; Wang, C.; Gao, Y.; Huang, J. Understanding the formation and evolution of interdiffusion grown organolead halide perovskite thin films by thermal annealing. *J. Mater. Chem. A* **2014**, *2*, 18508–18514, doi:10.1039/C4TA04007D.
184. Heo, J. H.; Im, S. H.; Noh, J. H.; Mandal, T. N.; Lim, C.-S.; Chang, J. A.; Lee, Y. H.; Kim, H.; Sarkar, A.; Nazeeruddin, M. K.; Grätzel, M.; Seok, S. Il Efficient inorganic–organic hybrid heterojunction solar cells containing perovskite compound and polymeric hole conductors. *Nat. Photonics* **2013**, *7*, 486–491, doi:10.1038/nphoton.2013.80.
185. Jeon, N. J.; Noh, J. H.; Kim, Y. C.; Yang, W. S.; Ryu, S.; Seok, S. Il Solvent engineering for high-performance inorganic–organic hybrid perovskite solar cells. *Nat Mater* **2014**, *13*, 897–903,doi:10.1038/nmat4014
186. Burschka, J.; Pellet, N.; Moon, S.-J.; Humphry-Baker, R.; Gao, P.; Nazeeruddin, M. K.; Grätzel, M. Sequential deposition as a route to high-performance perovskite-sensitized

solar cells. *Nature* **2013**, *499*, 316–320, doi:10.1038/nature12340.

187. Xiao, Z.; Dong, Q.; Bi, C.; Shao, Y.; Yuan, Y.; Huang, J. Solvent annealing of perovskite-induced crystal growth for photovoltaic-device efficiency enhancement. *Adv. Mater.* **2014**, *26*, 6503–6509, doi:10.1002/adma.201401685.
188. Zhou, H.; Chen, Q.; Yang, Y. Vapor-assisted solution process for perovskite materials and solar cells. *MRS Bull.* **2015**, *40*, 667–673, doi:10.1557/mrs.2015.171.
189. Conings, B.; Baeten, L.; De Dobbelaere, C.; D'Haen, J.; Manca, J.; Boyen, H. G. Perovskite-based hybrid solar cells exceeding 10% efficiency with high reproducibility using a thin film.
190. Mitzi, D. B. Templating and structural engineering in organic–inorganic perovskites. *J. Chem. Soc. Dalt. Trans.* **2001**, 1–12, doi:10.1039/b007070j.
191. Unger, E. L.; Bowring, A. R.; Tassone, C. J.; Pool, V.; Gold-Parker, A.; Cheacharoen, R.; Stone, K. H.; Hoke, E. T.; Toney, M. F.; McGehee, M. D. Chloride in lead-chloride derived organo-metal halides for perovskite-absorber solar cells. *Chem. Mater.* **2014**, *26*, 7158–7165, doi:10.1021/cm503828b.
192. Yu, H.; Wang, F.; Xie, F.; Li, W.; Chen, J.; Zhao, N. The role of chlorine in the formation process of "$CH_3NH_3PbI_{3-x}Cl_x$" perovskite. *Adv. Funct. Mater.* **2014**, *24*, 7102–7108, doi:10.1002/adfm.201401872.
193. Wang, J.; Zhong, X.; Wang, J. Significant roughness enhancement of fluorine-doped tin oxide films with low resistivity and high transparency by using HNO_3 addition. *RSC Adv.* **2015**, *5*, 52174–52182, doi:10.1039/C5RA08270F.
194. Armin Segmüller.Characterization of epitaxial films by grazing incidence x-ray diffraction *. *Thin Solid Films* **1987**, *154*, 33–42.
195. Marra, W. C.; Eisenberger, P.; Cho, A. Y. X-ray total-external-reflection-Bragg diffraction: A structural study of the GaAs-Al interface. *J. Appl. Phys.* **1979**, *50*, 6927–6933, doi:10.1063/1.325845.
196. Huang, T. C.; Predecki, P. K. Grazing-incidence x-ray technique for surface, interface and thin-film analysis. *Denver X-ray Conf. Appl. X-ray Anal.* **1997**, 1–12.
197. Deretzis, I.; Alberti, A.; Pellegrino, G.; Smecca, E.; Giannazzo, F.; Sakai, N.; Miyasaka, T.; La Magna, A. Atomistic origins of $CH_3NH_3PbI_3$ degradation to PbI_2 in vacuum. *Appl. Phys. Lett.* **2015**, *106*, doi:10.1063/1.4916821.
198. Niemann, R. G.; Kontos, A. G.; Palles, D.; Kamitsos, E. I.; Kaltzoglou, A.; Brivio, F.; Falaras, P.; Cameron, P. J. Halogen effects on ordering and bonding of $CH_3NH_3^+$ in $CH_3NH_3PbX_3$ (X = Cl, Br, I) hybrid perovskites: A vibrational spectroscopic study. *J. Phys. Chem. C* **2016**, *120*, 2509–2519, doi:10.1021/acs.jpcc.5b11256.
199. Goris, L.; Haenen, K.; Nesládek, M.; Wagner, P.; Vanderzande, D.; De Schepper, L.; D'haen, J.; Luisen, L.; Manca, J. V. Absorption phenomena in organic thin films for

solar cell applications investigated by photothermal deflection spectroscopy. *J. Mater. Sci.* **2005**, *40*, 1413–1418, doi:10.1007/s10853-005-0576-0.

200. Ilahi, S.; Saidi, F.; Hamila, R.; Yacoubi, N.; Auvray, L.; Maaref, H. Photothermal deflection spectroscopy (PDS) investigation of optical and thermal properties of BGaAs/GaAs alloys. *Curr. Appl. Phys.* **2013**, *13*, 610–613, doi:10.1016/j.cap.2012.11.002.
201. Jackson, W. B.; Amer, N. M.; Boccara, A. C.; Fournier, D. Photothermal deflection spectroscopy and detection. *Appl. Opt.* **1981**, *20*, 1333, doi:10.1364/AO.20.001333.
202. Skvortsov, L. A. Laser photothermal spectroscopy of light-induced absorption. *Quantum Electron.* **2013**, *43*, 1–13, doi:10.1070/QE2013v043n01ABEH014912.
203. Dittrich, T.; Gonzáles, a; Rada, T.; Rissom, T.; Zillner, E.; Sadewasser, S.; Lux-Steiner, M. Comparative study of Cu(In,Ga)Se_2/CdS and Cu(In,Ga)Se_2/In_2S_3 systems by surface photovoltage techniques. *Thin Solid Films* **2013**, *535*, 357–361, doi:10.1016/j.tsf.2012.12.078.
204. Awino, C.; Odari, V.; Sakwa, T. Investigation of structural and electronic properties of $CH_3NH_3PbI_3$ stabilized by varying concentrations of poly(Methyl Methacrylate) (PMMA). *Coatings* **2017**, *7*, 115, doi:10.3390/coatings7080115.
205. Juma.A.O Copper diffusion in In_2S_3 and charge separation. *Thesis* **2013**.
206. Wenger, B.; Nayak, P. K.; Wen, X.; Kesava, S. V.; Noel, N. K.; Snaith, H. J. Consolidation of the optoelectronic properties of $CH_3NH_3PbBr_3$ perovskite single crystals. *Nat. Commun.* **2017**, *8*, 590, doi:10.1038/s41467-017-00567-8.
207. Leguy, A.; Azarhoosh, P.; Alonso, M. I.; Campoy-Quiles, M.; Weber, O. J.; Yao, J.; Bryant, D.; Weller, M. T.; Nelson, J.; Walsh, A.; van Schilfgaarde, M.; Barnes, P. R. F. Experimental and theoretical optical properties of methylammonium lead halide perovskites. *Nanoscale* **2015**, *8*, 6317–6327, doi:10.1039/C5NR05435D.
208. Mali, S. S.; Shim, C. S.; Hong, C. K. Highly stable and efficient solid-state solar cells based on methylammonium lead bromide ($CH_3NH_3PbBr_3$) perovskite quantum dots. *NPG Asia Mater.* **2015**, *7*, e208, doi:10.1038/am.2015.86.
209. Dittrich, T.; Awino, C.; Prajongtat, P.; Rech, B.; Lux-Steiner, M. C. Temperature Dependence of the Band Gap of $CH_3NH_3PbI_3$ Stabilized with PMMA: A Modulated Surface Photovoltage Study. *J. Phys. Chem. C* **2015**, *119*, 23968–23972, doi:10.1021/acs.jpcc.5b07132.
210. Giesbrecht, N.; Schlipf, J.; Oesinghaus, L.; Binek, A.; Bein, T.; Müller-Buschbaum, P.; Docampo, P. Synthesis of perfectly oriented and micrometer-sized $MAPbBr_3$ perovskite crystals for thin-film photovoltaic applications. *ACS Energy Lett.* **2016**, 150–154, doi:10.1021/acsenergylett.6b00050.
211. Sadhanala, A.; Deschler, F.; Thomas, T. H.; Dutton, S. E.; Goedel, K. C.; Hanusch, F.

C.; Lai, M. L.; Steiner, U.; Bein, T.; Docampo, P.; Cahen, D.; Friend, R. H. Preparation of single phase films of $CH_3NH_3Pb(I_{1-x}Br_x)_3$ with sharp optical band edges. *J. Phys. Chem. Lett.* **2014**, 140709102712008, doi:10.1021/jz501332v.

212. Ashhab, S.; Voznyy, O.; Hoogland, S.; Sargent, E. H.; Madjet, M. E. Effect of disorder on transport properties in a tight-binding model for lead halide perovskites. **2017**, 1–24, doi:10.1038/s41598-017-09442-4.
213. Misra, R. K.; Ciammaruchi, L.; Aharon, S.; Mogilyansky, D.; Etgar, L.; Visoly-Fisher, I.; Katz, E. A. Effect of halide composition on the photochemical stability of perovskite photovoltaic materials. *ChemSusChem* **2016**, *9*, 2572–2577, doi:10.1002/cssc.201600679.
214. Tahara, H.; Endo, M.; Wakamiya, A.; Kanemitsu, Y. Experimental evidence of localized shallow states in orthorhombic phase of $CH_3NH_3PbI_3$ perovskite thin films revealed by photocurrent beat spectroscopy. *J. Phys. Chem. C* **2016**, *120*, 5347–5352, doi:10.1021/acs.jpcc.6b01283.
215. Lin, X. Z.; Dittrich, T.; Fengler, S.; Lux-Steiner, M. C.; Ennaoui, a. Correlation between processing conditions of $Cu_2ZnSn(S_xSe_{1-x})_4$ and modulated surface photovoltage. *Appl. Phys. Lett.* **2013**, *102*, 143903, doi:10.1063/1.4801463.
216. Hill, R. Energy-gap variations in semiconductor alloys. *J. Phys. C Solid State Phys.* **1974**, *7*, 521–526, doi:10.1088/0022-3719/7/3/009.
217. Wang, C.; Ecker, B. R.; Wei, H.; Huang, J.; Gao, Y. Environmental surface stability of the $MAPbBr_3$ single crystal. *J. Phys. Chem. C* **2018**, acs.jpcc.7b12740, doi:10.1021/acs.jpcc.7b12740.
218. Hanusch, F. C.; Wiesenmayer, E.; Mankel, E.; Binek, A.; Angloher, P.; Fraunhofer, C.; Giesbrecht, N.; Feckl, J. M.; Jaegermann, W.; Johrendt, D.; Bein, T.; Docampo, P. Efficient planar heterojunction perovskite solar cells based on formamidinium lead bromide. *J. Phys. Chem. Lett.* **2014**, *5*, 2791–2795, doi:10.1021/jz501237m.
219. Visoly-fisher, I.; Misra, R. K.; Ciammaruchi, L.; Aharon, S.; Li, B.; Mogilyanski, D.; Katz, E. A.; Physics, E. Accelerated stability testing of perovskite photovoltaic materials reveals dependence on the halide composition. **2015**, *134*, 1–2.
220. Fang, X.; Zhang, K.; Li, Y.; Yao, L.; Zhang, Y.; Wang, Y.; Zhai, W.; Tao, L.; Du, H.; Ran, G. Effect of excess $PbBr_2$ on photoluminescence spectra of $CH_3NH_3PbBr_3$ perovskite particles at room temperature. *Appl. Phys. Lett.* **2016**, *108*, 71109, doi:10.1063/1.4942410.
221. Belarbi, E.; Marta Vallé s-Pelarda, ab; Clasen Hames, B.; Sanchez, R. S.; Barea, E. M.; Maghraoui-Meherzi, H.; Mora-Seró, I. Transformation of PbI_2 , $PbBr_2$ and $PbCl_2$ salts into $MAPbBr_3$ perovskite by halide exchange as an effective method for recombination reduction. *Phys. Chem. Chem. Phys. Phys. Chem. Chem. Phys* **2017**,

19, 10913–10921, doi:10.1039/c7cp01192j.

222. Jiang, Q.; Zhang, L.; Wang, H.; Yang, X.; Meng, J.; Liu, H.; Yin, Z.; Wu, J.; Zhang, X.; You, J. Enhanced electron extraction using SnO_2 for high-efficiency planar-structure $HC(NH_2)_2PbI_3$-based perovskite solar cells. *Nat. Energy* **2016**, *2*, 16177, doi:10.1038/nenergy.2016.177.
223. Chen, W.-Y.; Deng, L.-L.; Dai, S.-M.; Wang, X.; Tian, C.-B.; Zhan, X.-X.; Xie, S.-Y.; Huang, R.-B.; Zheng, L. Low-cost solution-processed copper iodide as an alternative to PEDOT: PSS hole transport layer for efficient and stable inverted planar heterojunction perovskite solar cells. *J. Mater. Chem. A* **2015**, *3*, 19353–19359, doi:10.1039/C5TA05286F.
224. Liu, G.; Yang, B.; Liu, B.; Zhang, C.; Xiao, S.; Yuan, Y.; Xie, H.; Niu, D.; Yang, J.; Gao, Y.; Zhou, C. Irreversible light-soaking effect of perovskite solar cells caused by light-induced oxygen vacancies in titanium oxide. *Appl. Phys. Lett.* **2017**, *111*, 1–6, doi:10.1063/1.4994085.
225. Patel, J. B.; Wong-Leung, J.; Van Reenen, S.; Sakai, N.; Wang, J. T. W.; Parrott, E. S.; Liu, M.; Snaith, H. J.; Herz, L. M.; Johnston, M. B. Influence of interface morphology on hysteresis in vapor-deposited perovskite solar cells. *Adv. Electron. Mater.* **2017**, *3*, 1–6, doi:10.1002/aelm.201600470.
226. Kedem, N.; Brenner, T. M.; Kulbak, M.; Schaefer, N.; Levcenko, S.; Levine, I.; Abou-Ras, D.; Hodes, G.; Cahen, D. Light-induced increase of electron diffusion length in a p-n Junction Type $CH_3NH_3PbBr_3$ perovskite solar cell. *J. Phys. Chem. Lett.* **2015**, *6*, 2469–2476, doi:10.1021/acs.jpclett.5b00889.
227. Aristidou, N.; Sanchez-Molina, I.; Chotchuangchutchaval, T.; Brown, M.; Martinez, L.; Rath, T.; Haque, S. A. The role of oxygen in the degradation of methylammonium lead trihalide perovskite photoactive layers. *Angew. Chemie - Int. Ed.* **2015**, *54*, 8208–8212, doi:10.1002/anie.201503153.
228. Fan, Z.; Xiao, H.; Wang, Y.; Zhao, Z.; Lin, Z.; Cheng, H. C.; Lee, S. J.; Wang, G.; Feng, Z.; Goddard, W. A.; Huang, Y.; Duan, X. Layer-by-Layer degradation of methylammonium lead tri-iodide perovskite microplates. *Joule* **2017**, *1*, 548–562, doi:10.1016/j.joule.2017.08.005.
229. Tang, X.; Brandl, M.; May, B.; Levchuk, I.; Hou, Y.; Richter, M.; Chen, H.; Chen, S.; Kahmann, S.; Osvet, A.; Maier, F.; Steinrück, H.-P.; Hock, R.; Matt, G. J.; Brabec, C. J. Photoinduced degradation of methylammonium lead triiodide perovskite semiconductors. *J. Mater. Chem. A* **2016**, *4*, 15896–15903, doi:10.1039/C6TA06497C.
230. Wang, F.; Shimazaki, A.; Yang, F.; Kanahashi, K.; Matsuki, K.; Miyauchi, Y.; Takenobu, T.; Wakamiya, A.; Murata, Y.; Matsuda, K. Highly efficient and stable perovskite solar cells by interfacial engineering using solution-processed polymer

layer. *J. Phys. Chem. C* **2017**, *121*, 1562–1568, doi:10.1021/acs.jpcc.6b12137.

231. Gao, Z. Silicon based heterojunction solar cells and photodetectors. **2017**.
232. Fuhs, W.; Korte, L.; Schmidt, M. Heterojunctions of hydrogenated amorphous silicon and monocrystalline silicon. *J. Optoelectron. …* **2006**, *8*, 1989–1995.
233. Condeles, J. F.; Lofrano, R. C. Z.; Rosolen, J. M.; Mulato, M. Stoichiometry , surface and structural characterization of lead iodide thin films. *Brazilian J. Phys.* **2006**, *36*, 320–323, doi:10.1590/S0103-97332006000300023.
234. Oku, T. Crystal structures of $CH_3NH_3PbI_3$ and related perovskite compounds used for solar cells. *Sol. cells-New approaches Rev.* **2016**, 77–101, doi:10.5772/59284.
235. Acuña, D.; Krishnan, B.; Shaji, S.; Sepúlveda, S.; Menchaca, J. L. Growth and properties of lead iodide thin films by spin coating. *Bull. Mater. Sci.* **2016**, *39*, 1453–1460, doi:10.1007/s12034-016-1282-z.
236. Frost, J. M.; Butler, K. T.; Brivio, F.; Hendon, C. H.; Van Schilfgaarde, M.; Walsh, A. Atomistic origins of high-performance in hybrid halide perovskite solar cells. *Nano Lett.* **2014**, *14*, 2584–2590, doi:10.1021/nl500390f.
237. Ferreira da Silva, A.; Veissid, N.; An, C. Y.; Pepe, I.; Barros de Oliveira, N.; Batista da Silva, A. V. Optical determination of the direct bandgap energy of lead iodide crystals. *Appl. Phys. Lett.* **1996**, *69*, 1930, doi:10.1063/1.117625.
238. Schaeffer, R.W; and Ardelean, M. POwder X-ray diffraction of oriented and intercalated lead iodide. *JCPDS-ICDD* **2000**, *16*, 16–19.
239. Moustafa, M.; Wasnick, A.; Janowitz, C.; Manzke, R. Temperature shift of the absorption edge and Urbach tail of Zr Sx S e2-x single crystals. *Phys. Rev. B* **2017**, *95*, 1–7, doi:10.1103/PhysRevB.95.245207.
240. Gesi, K. Effect of hydrostatic pressure on the structural phase transitions in $CH_3NH_3PbX_3$ (X = Cl, Br, I). *Ferroelectrics* **1997**, *203*, 249–268, doi:10.1080/00150199708012851.
241. Singh, P.; Singh, S. N.; Lal, M.; Husain, M. Temperature dependence of I-V characteristics and performance parameters of silicon solar cell. *Sol. Energy Mater. Sol. Cells* **2008**, *92*, 1611–1616, doi:10.1016/j.solmat.2008.07.010.
242. Wolf, C.; Kim, J.-S.; Lee, T.-W. Structural and thermal disorder of solution-processed $CH_3NH_3PbBr_3$ hybrid perovskite thin films. *ACS Appl. Mater. Interfaces* **2017**, *9*, 10344–10348, doi:10.1021/acsami.6b15694.
243. Ledinsky et al . The Urbach tails of organic-inorganic hybrid halide perovskites. *to be Publ.* **2018**.
244. Bardeen, J.; Shockley, W. Scattering of electrons in crystals in the presence of large electric fields. *Phys. Rev.* **1950**, *80*, 69–71, doi:10.1103/PhysRev.80.69.
245. Borriello, I.; Cantele, G.; Ninno, D. Ab initio investigation of hybrid organic-inorganic

perovskites based on tin halides. *Phys. Rev. B - Condens. Matter Mater. Phys.* **2008**, *77*, 1–9, doi:10.1103/PhysRevB.77.235214.

246. Fang, H. H.; Raissa, R.; Abdu-Aguye, M.; Adjokatse, S.; Blake, G. R.; Even, J.; Loi, M. A. Photophysics of organic-inorganic hybrid lead iodide perovskite single crystals. *Adv. Funct. Mater.* **2015**, *25*, 2378–2385, doi:10.1002/adfm.201404421.
247. Kawamura, Y.; Mashiyama, H.; Hasebe, K. Structural study on cubic–tetragonal transition of $CH_3NH_3PbI_3$. *J. Phys. Soc. Japan* **2002**, *71*, 1694–1697, doi:10.1143/JPSJ.71.1694.

Publications

Journal articles

Thomas Dittrich, Celline Awino, Pongthep Prajongtat, Bernd Rech, and Martha Ch. Lux-Steiner, Temperature dependence of the band gap of $CH_3NH_3PbI_3$ stabilized with PMMA: A modulated surface photovoltage study. *J. Phys. Chem. C*, **2015**, 119, 23968−23972.

Lukas Kegelmann, Christian M. Wolff, Celline Awino Omondi, Felix Lang, Eva Lisa Unger, Lars Korte, Thomas Dittrich, Dieter Neher, Bernd Rech, and Steve Albrech. It takes two to tango – double-layer selective contacts in perovskite solar cells for improved device performance and reduced hysteresis. *ACS Appl. Mater. Interfaces*, **2017**, *9* (20), pp 17245–17255.

Celline Awino, Thomas Dittrich, Lukas Kegelmann, Steve Albrecht. Effects of light soaking on the transport length of $CH_3NH_3PbI_3$, **2018**, to be submitted.

Conference presentations

Celline Awino, Thomas Dittrich, Eva Unger, Lukas Kegelmann, Steve Albrecht, Bernd Rech. Modulated surface photovoltage spectroscopy of $CH_3NH_3Pb(I,Br)_3$ thin films. DPG Spring meeting, 19-24 March 2017 Dresden Germany.

Celline Awino,Thomas Dittrich, Eva Unger, Lukas Kegelmann, Steve Albrecht, Bernd Rech. Characterization of lead halide perovskites. European material research society (EMRS 2017 spring meeting), Strasbourg France May 2017

List of abbreviations and symbols

Abbreviation	description
AE	activation energy
Ag	silver
A.M 1.5 G	air mass of 1.5 global
a-Si-H	hydrogenated amorphous silicon
ASTM	American society for testing of materials
Au	gold
c-Si	crystalline silicon
BA	butyl acetate
°C	Degrees centigrade
CB	conduction band
CdSe	cadmium selenide
CdTe	cadmium tellurium
$CH_3NH_3PbI_3$	methyl ammonium lead iodide
$CH_3NH_3PbBr_3$	methyl ammonium lead bromide
$CsSnI_3$	cesium tin iodide
Cm^2	squared centimeter
D	charge carrier diffusion coefficient
dE_g/dT	temperature coefficient
DFT	density functional theory
E_c	conduction band minimum
E_F	Fermi energy
E_g	energy band gap
$E_{g\text{-}ip}$	energy band gap due to inflexion point
$E_{g\text{-}Tauc}$	Tauc gap energy
E_{offset}	offset energy
$E_{on\text{-}X}$	onset energy of the x- or in-phase signal
$E_{on\text{-}Y}$	onset energy of the y- or phase shifted by 90° signal
E_{ph}	electron phonon energy
E_t	exponential tail states
E_v	maximum of valence band
eV	electron volt
eV/K	electron volt per kelvin

E_{vac}	vacuum level
f_{mod}	modulated frequency
FTPS	Fourier transform photoelectron spectroscopy
FTO	fluorine doped tin oxide
GaAs	gallium Arsenide
Ge	germanium
GIXRD	grazing incidence x-ray diffraction
EA	electron affinity
h	hour
HOMO	highest occupied molecular orbital
I	iodine
InP	indium phosphide
IE	ionization energy
Isc	short circuit current
J	joules
K_B	Boltzmann constant (~ 26 meV) or 8.62×10^{-5} eV/K
KWh	killo-watt hour
L	diffusion length
LUMO	lowest unoccupied molecular orbital
meV	milli-electron volt
mg	milli-gram
min	minute
ml	milli-litre
mg/ml	milli-gram per milli-litre
Mo	molybdenum
M_o	effective mass
MPa	mega-pascal
mV	milli-volt
Pb	lead
PCE	power conversion efficiency
PEDOT: PSS	poly (3, 4-ethylenedioxythiophene)polystyrene sulfonate
PL	photoluminescence
PDS	photo-thermal deflection spectroscopy
Pb-I-Pb	lead-iodine-lead
PMMA	poly (methyl methacrylate)
PTAA	poly (triaryl amine)
SCs	solar cells

SEM	scanning electron microscopy
SPV	Surface photovoltage
VB	valence band
Voc	open circuit voltage
VS	volt-second
rad	radians
R_{max}	maximum amplitude
RT	reflection and transmission
t	time
T	absolute temperature
T_o	phase transition temperature
tan h	hyperbolic tangent function
TCO	transparent conducting oxide
T_{max}	maximum temperature
TW	tella Watt
TWh	tella Watt hour
X_{max}	maximum in-phase signal
Y_{max}	maximum phase shifted by 90° signal
$Wm^{-2}eV^{-1}$	Watts per squared meter per electron volt
%	percent
σ	steepness parameter in relation to absorption
σ_o	material dependent steepness parameter
μ	charge carrier mobility
τ	charge carrier lifetime
q	electronic charge (1.6×10^{-19}) J
Φ	work-function
Φ	Angle of rotation of the position detector in relation to PDS
Φph	photon flux
hv	photon energy
h+	hole
e-	electron

Acknowledgements

I am very grateful to Prof. Dr. Bernd Rech for giving me the opportunity to perform my PhD studies and research at the Institut für Silizium-photovoltaik at the Helmholtz-Zentrum Berlin für Materialien und Energie GmbH and for taking the responsibility as the first reviewer of my thesis. I am also grateful to Prof. Dr. Roland Scheer, the external reviewer of my thesis, from the Martin Luther Universität, Halle. Special thanks goes to my supervisor and mentor PD Dr. Thomas Dittrich for accepting me as his student and for his tireless, professional guidance and training during my entire studies. I am also grateful to Prof. Dr. Martha Lux-Steiner for giving me the opportunity to perform experiments at her former Institut für Heterogene Materialien and for the exciting and interesting experience at the ISU energy 2015 (International Summer University of renewable energy, Falera).

I am grateful to Prof. Dr. Nobert Nickel and Dr. Jörg Rappich for support of my research at the Institut für Silizium-photovoltaik; Dr. Eva Unger and Steve Albrecht for their open minded support within the young investigator groups. I am also grateful to Lukas Kegelmann and Katrin Hirselandt for fruitful collaboration and for some technical support. I am also very grateful to PD Dr. Thomas Dittrich, Prof. Dr. Pongthep Prajongtat and Dr. Attitaya Naikeaw for introducing me to the world of perovskites and surface photovoltage at the former Institut für Heterogene Materialien.

Thanks to Dr. Steffen Fengler and Santiago Pineda Solano for enlightening discussions about SPV. Many thanks goes to Dr. Karolina Mack of the Kompetenz-zentrum Dünnschicht- und Nanotechnologie für Photovoltaik Berlin (PVcomB) for the introduction into UV-vis spectroscopy and the assistance in interpretation. Thanks to Dr. Eva Unger for some PDS measurements and for discussions. I thank Dr. Michael Tovar for introduction to XRD measurements at the Abteilung Struktur und Dynamik von Energiematerialien of the HZB and Carola Klimm for sample characterization by SEM. Special thanks also goes to Dr. Ruslan Muydinov of Technologie für Dünnschicht-Bauelemente (TU Berlin - Fakultät IV) and Kompetenz-zentrum Dünnschicht-und Nanotechnologie für Photovoltaik Berlin (PVcomB) for collaboration and support.

I also thank Marion Krusche for assistance and patience with administrative work. Thanks also to Dr. Sonya Calnan, Dr. Albert Juma and Lydia Radoli for corrections and feedback.

My PhD studies would not be possible without the financial support from the Catholic academic exchange service (KAAD) and the Helmholtz Zentrum Berlin. I am grateful for the scholarships.

Last but not least, special thanks goes to my husband Charles Ogoma and children; Noela Atieno, Marvin Ochieng, Wilson Maguma and Jeremy Monyi for their patience, motivation and understanding over the whole period of my PhD studies.